NASA/TP–2015–218482

Experimental and Computational Sonic Boom Assessment of Boeing N+2 Low Boom Models

Donald A. Durston[*]
Alaa A. Elmiligui[†]
Susan E. Cliff[*]
Courtney S. Winski[†]
Melissa B. Carter[†]
Eric L. Walker[†]

[*] *NASA Ames Research Center, Moffett Field, California*
[†] *NASA Langley Research Center, Hampton, Virginia*

February 2015

NASA STI Program ... in Profile

Since its founding, NASA has been dedicated to the advancement of aeronautics and space science. The NASA scientific and technical information (STI) program plays a key part in helping NASA maintain this important role.

The NASA STI program operates under the auspices of the Agency Chief Information Officer. It collects, organizes, provides for archiving, and disseminates NASA's STI. The NASA STI program provides access to the NTRS Registered and its public interface, the NASA Technical Reports Server, thus providing one of the largest collections of aeronautical and space science STI in the world. Results are published in both non-NASA channels and by NASA in the NASA STI Report Series, which includes the following report types:

- TECHNICAL PUBLICATION. Reports of completed research or a major significant phase of research that present the results of NASA Programs and include extensive data or theoretical analysis. Includes compilations of significant scientific and technical data and information deemed to be of continuing reference value. NASA counterpart of peer-reviewed formal professional papers but has less stringent limitations on manuscript length and extent of graphic presentations.

- TECHNICAL MEMORANDUM. Scientific and technical findings that are preliminary or of specialized interest, e.g., quick release reports, working papers, and bibliographies that contain minimal annotation. Does not contain extensive analysis.

- CONTRACTOR REPORT. Scientific and technical findings by NASA-sponsored contractors and grantees.

- CONFERENCE PUBLICATION. Collected papers from scientific and technical conferences, symposia, seminars, or other meetings sponsored or co-sponsored by NASA.

- SPECIAL PUBLICATION. Scientific, technical, or historical information from NASA programs, projects, and missions, often concerned with subjects having substantial public interest.

- TECHNICAL TRANSLATION. English-language translations of foreign scientific and technical material pertinent to NASA's mission.

Specialized services also include organizing and publishing research results, distributing specialized research announcements and feeds, providing information desk and personal search support, and enabling data exchange services.

For more information about the NASA STI program, see the following:

- Access the NASA STI program home page at http://www.sti.nasa.gov

- E-mail your question to help@sti.nasa.gov

- Phone the NASA STI Information Desk at 757-864-9658

- Write to:
  NASA STI Information Desk
  Mail Stop 148
  NASA Langley Research Center
  Hampton, VA 23681-2199

NASA/TP–2015–218482

Experimental and Computational Sonic Boom Assessment of Boeing N+2 Low Boom Models

Donald A. Durston[*]
Alaa A. Elmiligui[†]
Susan E. Cliff[*]
Courtney S. Winski[†]
Melissa B. Carter[†]
Eric L. Walker[†]

[*] *NASA Ames Research Center, Moffett Field, California*
[†] *NASA Langley Research Center, Hampton, Virginia*

National Aeronautics and
Space Administration

Ames Research Center
Moffett Field, California

February 2015

Acknowledgements

The authors would like to thank Linda Bangert, the Technical Lead in the High Speed Project overseeing this work, for her support and valuable input throughout the course of this work. We are grateful for the work done by the Boeing Seattle and Huntington Beach teams for their design of the QEVC concept and the wind tunnel models, for their leadership in the testing, and their CFD analyses. We appreciate the untiring efforts of the crews at the Ames 9- by 7-Foot Supersonic Wind Tunnel and the Glenn 8- by 6-Foot Supersonic Wind Tunnel for running the tests that provided all the experimental data herein. We are thankful for the CFD support of Mike Park and Michael Aftosmis, for adjoint-based solution adapted analyses with *Cart3D*, and we thank Edward Parlette, Sudheer Nayani, and Norma Farr for developing Euler and Navier-Stokes surface and volume grids.

Summary

Near-field pressure signatures were measured and computational predictions made for several sonic boom models representing Boeing's Quiet Experimental Validation Concept (QEVC) supersonic transport, as well as three axisymmetric calibration models. Boeing developed the QEVC under a NASA Research Announcement (NRA) contract for Experimental Systems Validations for N+2 Supersonic Commercial Transport Aircraft, which was led by the NASA High Speed Project under the Fundamental Aeronautics Program. The concept was designed to address environmental and performance goals given in the NRA, specifically for low sonic boom loudness levels and high cruise efficiency, for an aircraft anticipated to enter service in the 2020 timeframe. Wind tunnel tests were conducted on the aircraft and calibration models during Phases I and II of the NRA contract from 2011 to 2013 in the NASA Ames 9- by 7-Foot and NASA Glenn 8- by 6-Foot Supersonic Wind Tunnels. Sonic boom pressure signatures were acquired primarily at Mach 1.6 and 1.8, and force and moment data were acquired from Mach 0.8 to 1.8.

The sonic boom test data were obtained using a 2-in. flat-top pressure rail and a 14-in. round-top tapered "reflection factor 1" (RF1) pressure rail. Both rails capture an entire pressure signature in one data point, and successive signatures at varying positions along or above the rail were used to improve data quality through spatial averaging. The sonic boom data obtained by the rails were validated with high-fidelity numerical simulations of off-body pressures using the CFD codes *USM3D, Cart3D,* and *OVERFLOW*. The test results from the RF1 rail showed good agreement between the computational and experimental data when a variety of testing techniques including spatial averaging of a series of pressure signatures were employed, however, reflections off the 2-in. flat-top rail caused distortions in the signatures that did not agree with the CFD predictions. The 9x7 and 8x6 wind tunnels generally produced comparable data.

Table of Contents

List of Figures

List of Tables

Nomenclature

b_{Ref}	Model reference span, in.
CAD	Computer-Aided Design
CFD	Computational Fluid Dynamics
CoR	Center of Rotation
C_{Ref}	Model reference chord length, also mean aerodynamic chord, in.
Duration	Sampling duration for single data point (sequence number), sec
EI NOx	Emissions index of NOx (nitrogen oxides), grams of NO_2 per kg of fuel
EPNdB	Effective perceived noise level in decibels
h, h_nose	Model altitude at model nose, in.
h/L, h_nose_L	Model altitude non-dimensionalized by model length
HumidAvg	Average humidity from wind tunnel sensors, ppm by weight
L_{Ref}	Model reference length, in.
LM	Lockheed-Martin
L/D	Lift-to-drag ratio
M	Mach number
MAC	Mean Aerodynamic Chord, in.
NaN	Not a Number
P	Rail static pressure or ground overpressure (increment over ambient pressure), psfa
P_∞	Free stream static pressure, psfa
P_T	Free stream total pressure, psfa
PLdB	Perceived sound level in decibels
psfa	Pounds/square foot absolute
q	Dynamic pressure, psf
QEVC	Quiet Experimental Validation Concept
Re	Reynolds number, non-dimensional, $\rho VL/\mu$
Re_L	Reynolds number per unit length, 1/foot
RF1	Reflection Factor 1, name of 14-in. pressure rail
RBOS	Retro-reflective Background-Oriented Schlieren
S_{Ref}	Model reference area, sq ft
SWT	Supersonic Wind Tunnel
X	Longitudinal coordinate, positive aft, in.
X_{Ram}	Longitudinal extension of linear actuator ram, in.
Z	Coordinate in tunnel angle-of-attack plane: lateral in 9x7, vertical in 8x6, positive “above” rail, in.
α	Angle of attack, degrees
β	Angle of sideslip, degrees
$\Delta P/P$	Overpressure coefficient, $(P - P_\infty)/P_\infty$
ϕ	Off-track angle, or model roll angle relative to the rail, degrees

Subscripts

Data	Data run, where model pressure signature was measured on the rail
Ref	Reference run “empty” tunnel measurement, where model pressure signature was *not* on the rail; also a reference parameter for model geometry
∞	ambient, or freestream, flow conditions

1. Introduction

Flight at speeds greater than the speed of sound is currently not permitted over land, primarily because of the sonic boom annoyance and potential structural damage caused by sonic boom pressure waves generated by supersonic aircraft. Mitigation of the sonic boom is a key focus area of the High Speed Project under NASA's Fundamental Aeronautics Program. The project is focusing on technologies to enable future civilian aircraft to fly efficiently with reduced sonic boom, engine and aircraft noise, and emissions. One major objective is the improvement of both computational and experimental capabilities for design of low boom aircraft. NASA and industry partners are developing improved wind tunnel testing techniques and new pressure instrumentation to measure the weak sonic boom pressure signatures of modern vehicle concepts. In parallel, computational methods are being developed to provide rapid design and analysis of supersonic aircraft with improved meshing techniques that provide efficient, robust, and accurate off-body pressures at several body lengths from vehicles with very low sonic boom overpressures. The maturity of these critical parallel efforts is necessary before low-boom flight can be demonstrated and commercial supersonic flight can be realized.

The measurement of the sonic boom pressure signatures of modern low-boom supersonic vehicles in wind tunnels is challenging. Historically, these signatures were measured in a wind tunnel using needle-like conical probes that measure static pressure at a single point in the flow-field.[1] This technique requires axial translation of the model past the probe to obtain a complete pressure signature of the model (or translation of the probe past the model). Traditional methods used a move-pause data acquisition technique requiring between 40-60 minutes per signature, although a recent effort[2] has shown that near continuous model translation with environmentally-controlled pressure transducers and shortened pressure lines can significantly speed up data acquisition time using a probe. However, the single-probe technique is still prone to reduced data accuracy because of small changes in tunnel flow conditions even over short data acquisition times. Humidity, turbulence, ambient pressure variations and stream angle changes during model translation all contribute to reduced data quality.

Unlike single-point conical probes, pressure rails with hundreds of closely-spaced pressure orifices measure a model's entire sonic boom pressure signature at one location of the model in the tunnel. Rails offer significant gains in efficiency and precision compared with conventional conical probe testing. Several rails with different cross-sectional shapes have been investigated in the 9- by 7-Foot Supersonic Wind Tunnel at NASA Ames Research Center since 2008.[3] Initial rail concepts had flat or large-diameter rounded tips that resulted in unknown and inconsistent reflection (i.e., amplification of the pressure signal due to the shock reflection off the surface) of a model's pressure signature. A pressure rail that effectively eliminates shock reflection and boundary layer growth effects on the tip of rail was designed in 2010 using CFD analyses.[3] This rail, designated the "reflection factor 1" (RF1) rail, is 14-in. tall and tapered toward the tip to a 0.05-in. radius, and was used in some of the tests discussed in this report. Another rail used in these tests was a 2-in. tall flat-top rail, but reflection of the model shocks off the surface of this rail caused some parts of the model signature to be amplified.

When NASA first used pressure rails for sonic boom testing in 2008, it was envisioned that model translation would be unnecessary since the rails capture an entire model signature at once. However, further testing with rails showed that spatially averaging a series of pressure signatures from a number of model positions significantly improved measurement accuracy.[4,5] Small ambient pressure oscillations and disturbances caused by small shocks emanating from the tunnel structure are nearly eliminated by spatial averaging techniques.

In 2009, NASA published a NASA Research Announcement (NRA)[6] requesting proposals for "System-Level Experimental Validations for Supersonic Commercial Transport Aircraft Entering Service

in the 2018–2020 Time Period." The aircraft concepts were to be designed to second generation "N+2" supersonic vehicle technology with a focus on providing system-level solutions capable of overcoming the efficiency, environmental, and performance barriers to practical supersonic flight. The N+2 environmental and performance goals are given in Table 1.

Table 1. N+2 Supersonic Transport (2020) Goals

Environmental Goals	
Sonic Boom	85 PLdB up to 20° off-track
Airport Noise (cumulative below stage 3)	10–20 EPNdB
Cruise Emissions	< 10 EI NOx
Performance Goals	
Cruise Speed	Mach 1.6–1.8 low-boom flight
Range	4000 nm
Payload (passengers)	35–70 passengers
Fuel Efficiency (passenger-nm per lb of fuel)	3.0

The NRA contractors were to independently design N+2 concepts to meet these goals, and then build and test wind tunnel models to validate the sonic boom and aerodynamic performance estimates. Two companies were awarded the NRA contracts: Lockheed-Martin Aeronautics Company (LMAC) and The Boeing Company (TBC). This report covers the experimental measurements and CFD predictions for the concepts developed by Boeing, and a companion report covers the same for the concepts developed by Lockheed-Martin.[7]

The contracts with both companies were executed in two phases, each concluding with wind tunnel test validation of the sonic boom characteristics of their design efforts. The first phase[8,9] of Boeing's efforts was focused on design of a low boom airliner (Figure 1–1), the reduction of on-track (directly below aircraft in straight-and-level flight) sonic boom signatures, and assessment of aerodynamic performance in light of the environmental and performance goals specified in the NRA. The second phase[10-12] focused on nacelle integration with the airframe in terms of its effects on the boom signatures and aerodynamic performance, as well as inlet performance.

NASA provided Computational Fluid Dynamics (CFD) predictions of sonic boom pressure signatures of test articles prior to wind tunnel testing so that the experimentalists would have a firm understanding of the expected wind tunnel test results. Predicting accurate sonic boom pressure signatures of weak signals is challenging and significant improvements in the accuracy of sonic boom characteristics have been realized during the High Speed Project. Accurate CFD simulations can be obtained in many ways. One is by providing dense meshes within the sonic boom pressure disturbance along with mesh rotation

Figure 1–1. Artist's concept of Boeing N+2 QEVC supersonic transport

techniques to align the mesh with the Mach angle.[13] Another is to provide unstructured mesh adaptation with effective refinement criterion but without cell alignment.[14] A clever method that provides dense unstructured meshes, by grid sourcing and stretching at the Mach angle, tends to align the cells through the stretching and shearing process.[15] Solution-adaptive techniques using node-centered unstructured mixed-element meshes,[16-18] or Cartesian-adaptive refinement methods with domain rotation for Euler solutions[19-21] have proven successful. A method that provides anisotropic adapted unstructured mesh optimization for shock capturing has also been successfully used for the compressible Euler equations.[22] Also, structured overset grid methods,[23] or hybrid methods[24-26] that utilize an unstructured flow solutions in the near-field and structured grid solutions in the far-field can also provide accurate on-track calculations. Grid generation tools that allow stretching of the mesh in addition to alignment to the Mach cone angle[27-30] offer smaller meshes that maintain density in the axial direction and reduce the effects of dissipation along characteristic lines. The CFD computations provided here use Mach cone aligned prism meshes.[27] Some solution-adaptive (Cartesian and tetrahedral) results[18-21] and new overset grid computations will also be shown.

2. Test Objectives and Overview

There were three primary objectives for conducting the tests in this experimental validations program:

1. Obtain data to evaluate sonic boom and aerodynamic performance of the Boeing configurations, including the effects of nacelle changes and varying mass flows
2. Improve wind tunnel test techniques for acquiring such data
3. Provide a large, high-quality experimental validation database for CFD tool development and improvement of low-boom design methods

The overall purpose of the experimental validations program was to design a viable low-boom supersonic transport aircraft that would meet the NRA environmental and performance goals. Boeing designed their N+2 transport to meet these goals, but needed high-quality experimental data to evaluate the merits of their design. Boeing worked with NASA in developing a wind tunnel test program that would meet their needs. Past experience and lessons learned were applied to the test program to get the best data possible, and additional valuable experience was gained for further improvement of the test techniques. The result was a large dataset that Boeing used to assess their multidisciplinary design and analysis methods for their Phase I transport design,[8] and their final N+2 design at the completion of Phase II of the NRA contract.[10] These data also provided NASA and industry the information needed to validate their CFD codes.

A total of five tests were conducted with The Boeing Company (TBC) in pursuit of the NRA goals:

Phase I:

1. TBC1: Ames 9x7-ft wind tunnel, April 2011, Test 97-0229
2. TBC2: Ames 11x11-ft wind tunnel, June 2012, Test 97-0249
3. TBC3: Glenn 8x6-ft wind tunnel, September 2012, Test 86-12-002

Phase II:

4. TBC4: Ames 9x7-ft wind tunnel, April 2013, Test 97-0259
5. TBC5: Glenn 8x6-ft wind tunnel, March 2013, Test 86-13-001

This report will cover data only from the TBC3 and TBC4 tests, where the data were spatially averaged, and also from a 9x7 “parametric” test (April 2012, Test 97-0250, also referred to herein as “97p”). No spatial averaging was done in TBC1, so this test will not be covered herein because the data quality is poorer without spatial averaging. TBC2 data were compromised by high lateral dynamics in the 11x11-ft wind tunnel, and TBC5 data were acquired for inlet performance and recovery, which is not the

subject of this report. Various combinations of the Boeing N+2 "Boom" models, a "Performance" model, and axisymmetric calibration models were run in the above tests, which will be described in detail in the Models section below.

3. Facilities

Wind tunnel tests for the data presented herein were conducted at the NASA Ames 9- by 7-Foot and the NASA Glenn 8- by 6-Foot Supersonic Wind Tunnels. Brief descriptions of the wind tunnel facilities are presented in this section.

3.1. Ames 9- by 7-Foot Supersonic Wind Tunnel

The Ames 9- by 7-Foot Supersonic Wind Tunnel is part of the Unitary Plan Wind Tunnel[31,32] complex at NASA Ames Research Center at Moffett Field, California. It is a continuous-flow, closed-circuit, variable-density tunnel equipped with an asymmetric sliding-block nozzle for setting Mach number. The floor of the wind tunnel test section is part of the nozzle block. It translates axially (streamwise) to vary the nozzle throat area while the contoured tunnel ceiling remains stationary. This combination provides a Mach number range from 1.55 to 2.5. The sidewalls are flat and parallel through the nozzle and test section. The asymmetric nozzle results in slightly larger stream angle variations in the vertical plane, on the order of 0.25 to 0.5 degrees, whereas stream angle in the horizontal plane is generally less than 0.2 degrees. The angle-of-attack plane is therefore horizontal, and the model support strut at the rear of the test section is oriented this way. Models are thus normally mounted wings vertical, and the strut's side-to-side heave compensation keeps the model in the center of the tunnel as the pitch angle is changed. The forward end of the strut centerbody pivots by means of a mechanical joint

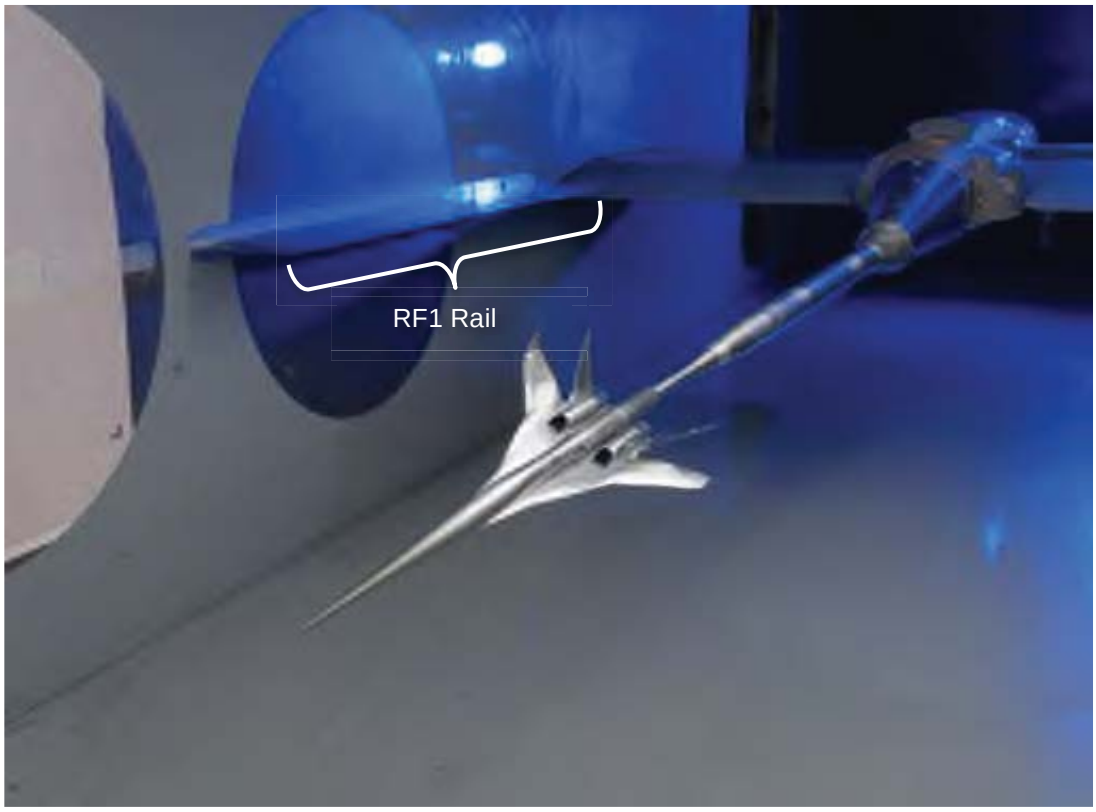

Figure 3–1. Boeing Performance model installed in Ames 9x7-ft wind tunnel

(knuckle-sleeve system) to achieve any combination of angle of attack or sideslip within a 15° cone angle. Throughout this report, the model distance from the rail on the sidewall of the tunnel is referred to as "height," even though in reality it is a horizontal distance in the 9x7 wind tunnel.

The tunnel is driven by an 11-stage axial compressor powered by four wound-rotor motors totaling 216,000 hp. The tunnel operates at total pressures between 634 and 3600 psfa with corresponding unit Reynolds numbers between 0.8 and 5.7 million per foot. For the subject series of sonic boom tests, the Mach number and total pressure have been prescribed in the tunnel control system, rather than Mach and Reynolds number, because it is more productive for the 9x7 to run in constant-pressure mode, allowing temperature to float.

Figure 3–2. Boeing Performance model in Ames 9x7-ft wind tunnel with NASA (N) and Boeing (B) research and test staff

Kneeling L–R: Eric Adamson (B), Michael Treese (N), Ross Flach (N), Don Durston (N)
Standing L–R: Courtney Winski (N), Laura Kushner (N), Eric Walker (N), Ed Schairer (N), Nicole Mendoza (B), Spencer Fugal (B), Tom Romer (N), Susan Cliff (N), Stephen Shaw (B), Alaa Elmiligui (N)

Most types of testing in the 9x7 wind tunnel do not require very low humidity and fine control of it, but sonic boom testing is an exception because static pressure measurements are sensitive to humidity. Humidity is normally brought down to operational levels (less than 500 ppm by weight, depending on test requirements) by purging the tunnel of wet air and pumping back up with dry air, but for best data quality in sonic boom testing, this purging is supplemented by continuously injecting dry, high-pressure air to keep the humidity below ~300 ppm. Modulation of this dry-air injection has proven capable of

maintaining humidity within ±5 ppm, which has allowed more consistent static pressure measurements relative to earlier tests where humidity was not so tightly controlled.

An installation photograph of the Boeing Performance model in the 9x7 tunnel is shown in Figure 3–1. The model, RF1 pressure rail, strut and centerbody are visible in the photograph (the model is shown rolled approximately 60° from its normal wings-vertical orientation to better show the model's upper surface features). The RF1 pressure rail is mounted on the north sidewall of the test section to measure the pressure signatures below the model. The wind tunnel strut movement controls the distance from the model to the top of the rail.

A similar photograph of the Performance model in the tunnel surrounded by many (but not all) of the NASA and Boeing research and test staff associated with this test is shown in Figure 3–2.

3.2. Glenn 8- by 6-Foot Supersonic Wind Tunnel

The Glenn 8- by 6-Foot Supersonic Wind Tunnel[33,34] is an atmospheric facility with a test section Mach number range from 0.25 to 2.0 (at discrete Mach numbers). It has dual-cycle operation in that it can operate closed-loop in an aerodynamic cycle, or open-loop in a propulsion cycle when combustion products are being introduced into the air stream. The tunnel is driven by a 7-stage axial compressor powered by three wound-rotor motors totaling 87,000 hp. Total pressure in the tunnel is a function of Mach number and temperature since the tunnel is not pressurized. High temperatures from the heat of compression are cooled by a heat exchanger on the leg of the tunnel opposite to the compressor and 8x6 test section, but with the test section being immediately downstream of the compressor, temperatures in the 8x6 typically reach 200° F at speeds of Mach 1.8 and higher. The range of total pressure from minimum to maximum Mach number is roughly 2150 to 3625 psfa, with corresponding unit Reynolds numbers between 1.7 to 5.1 million per foot. A balance chamber surrounds the test section and is used to provide boundary layer and Mach number control of the airflow in the test section through slanted holes in the walls.

Humidity is controlled by an air dryer in the tunnel circuit that consists of activated alumina in multiple beds. Each bed is two feet thick, through which all the wind tunnel air is continuously passed when not in bypass mode. On days when the outside humidity is high, the dryer beds can reach saturation during or by the end of an operating shift in the tunnel. At this point, they can no longer maintain a low dew point (upper limit is typically -15° F, an approximate humidity of 320 ppm by weight) to continue running without sacrificing data quality. The time it takes to reach saturation is dependent on the humidity of the outside air, as the tunnel is an atmospheric tunnel. During multiple-day test operations, the dryer beds are put through a heating and cooling cycle on a non-running shift to remove the excess moisture, as there is no active humidity control other than the dryer beds.

The test section of this facility is 8 ft. high by 6 ft. wide and 23.5 ft long. The nozzle upstream of the test section consists of flexible walls that are moved inward by hydraulic jacks for supersonic flow, and the floor and ceiling of the tunnel through the nozzle and test section areas are flat and parallel. The test section is divided into two sections: a supersonic section, 9.08 ft long starting from the end of the nozzle, and a transonic section 14.42 ft long from the end of the supersonic section. The walls around the supersonic section are solid, and they are porous around the transonic section with 1-in. diameter holes at 60° angles through the walls.

Several different strut arrangements are available for the tunnel, but the one used in sonic boom testing is a supersonic strut that raises and lowers through the tunnel floor with a pitch capability of -5° to 20°. Models are mounted wings-horizontal since the angle-of-attack plane is vertical.

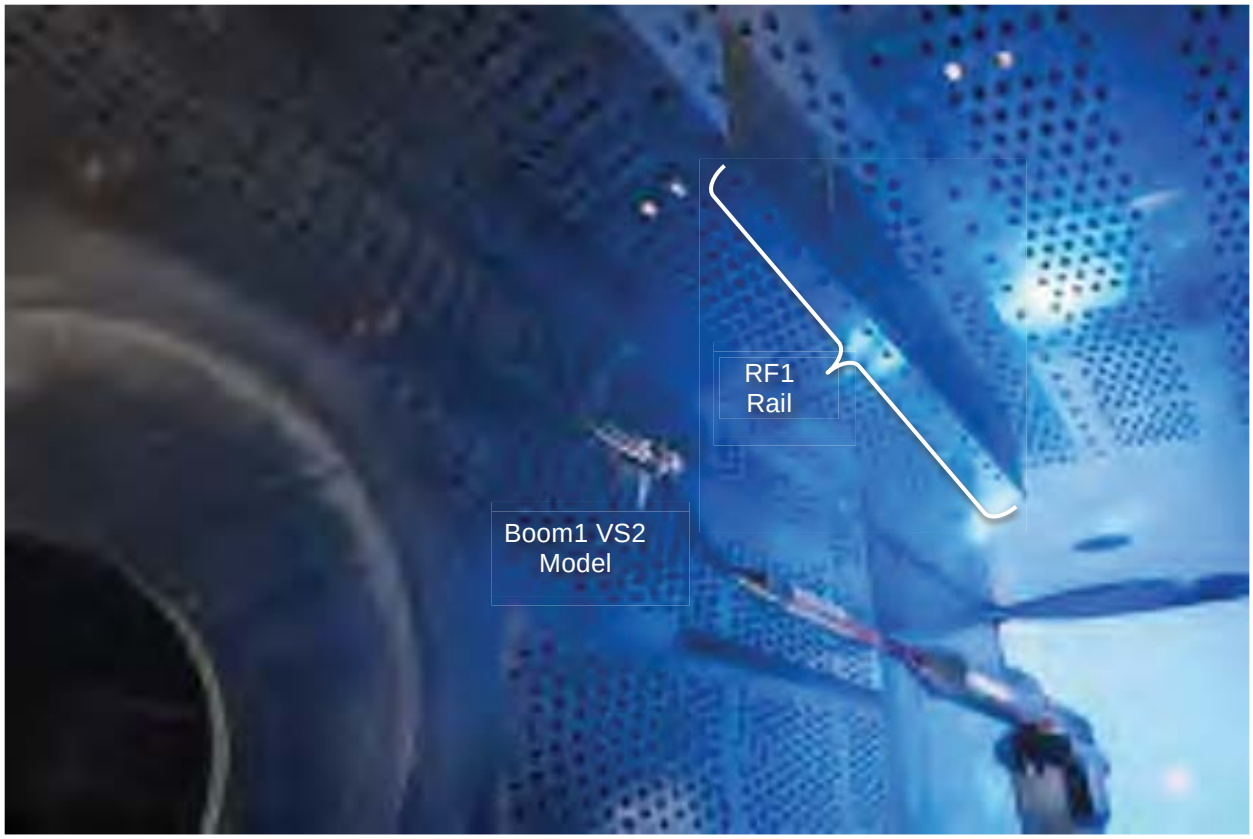

Figure 3–3. Boeing Boom1 model installed in Glenn 8x6-ft wind tunnel

For the TBC3 test, the RF1 pressure rail was mounted on the top wall of the transonic (porous wall) section to measure the pressure signatures of the models, which were thus required to be mounted upside-down on the strut so the rail would see the model lower-surface pressures. The distance from the model to the rail was controlled by adjusting the height of the wind tunnel strut. A photograph of one of the Boeing Boom models in the 8x6 tunnel and the RF1 rail on the ceiling is shown in Figure 3–3.

Two additional photographs of the 8x6 wind tunnel are shown in Figures 3–4 and –5 that show the positions of the windows in the tunnel side walls. In the first week of the TBC3 test, the tunnel was configured with porous window blanks in the upstream window frame and Schlieren windows in the downstream frames (Figure 3–4). This was done to accommodate Schlieren imaging of the models, as the strut and model mounting hardware positioned the models in line with the downstream windows. For the second week of testing, it was desired to have smoother flow at the model and over the pressure rail, so the Schlieren windows were moved forward and the porous blanks moved aft (Figure 3–5). The impacts of this move on the data will be discussed later.

A short table summarizing the operational characteristics of the Ames 9x7 and the Glenn 8x6 wind tunnels is given in Table 2, and a plot of the pressure and temperature conditions experienced during the subject tests is presented in Figure 3–6. Throughout this report, data from the 9x7 are presented at Mach numbers of 1.6 and 1.8, but the corresponding Mach numbers obtained in the 8x6 were 1.56 and 1.78, respectively, because the tunnel only operates at discrete Mach numbers. These slight differences in Mach number are believed to be not significant for the comparisons made in this report.

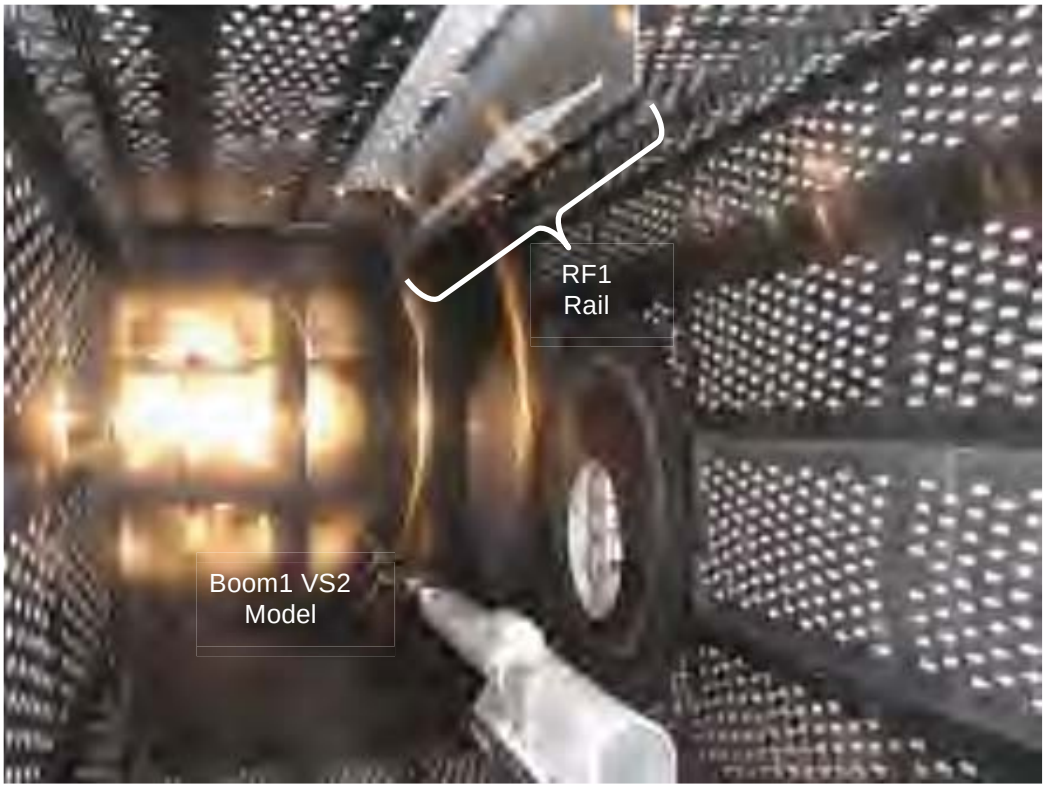

Figure 3–4. Boeing Performance model in 8x6-ft wind tunnel, with view of porous window blank in upstream window frame and Schlieren window in downstream frame during week 1 of test

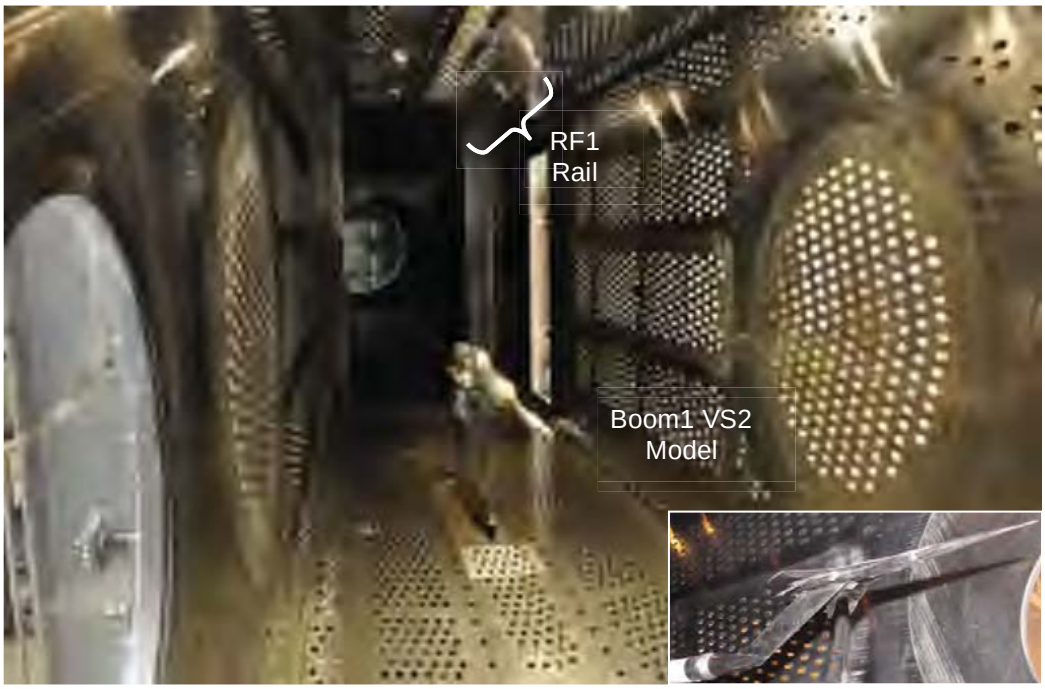

Figure 3–5. Boeing Boom1 model in Glenn 8x6-ft wind tunnel, with view of porous window blank in downstream window frame and Schlieren window in upstream frame during week 2 of test

Table 2. Tunnel Operational Characteristics

	Ames 9x7-Ft Supersonic Wind Tunnel	Glenn 8x6-Ft Supersonic Wind Tunnel
Mach Range	1.55 – 2.5, continuously variable	0.36 – 2, discrete
Pressure Control	Range of 634 to 3600 psf	Atmospheric; P_T varies with Mach
Temperature Control	Heat exchanger removes most heat of compression	Heat exchanger partially effective, T_T dependent on Mach number
Humidity Control	Humidity control continuously available by make-up air and high-pressure air	Humidity controlled by dryer beds, run time dependent on weather
Nozzle Design	Asymmetric sliding block (floor) nozzle	Symmetric vertical flex walls

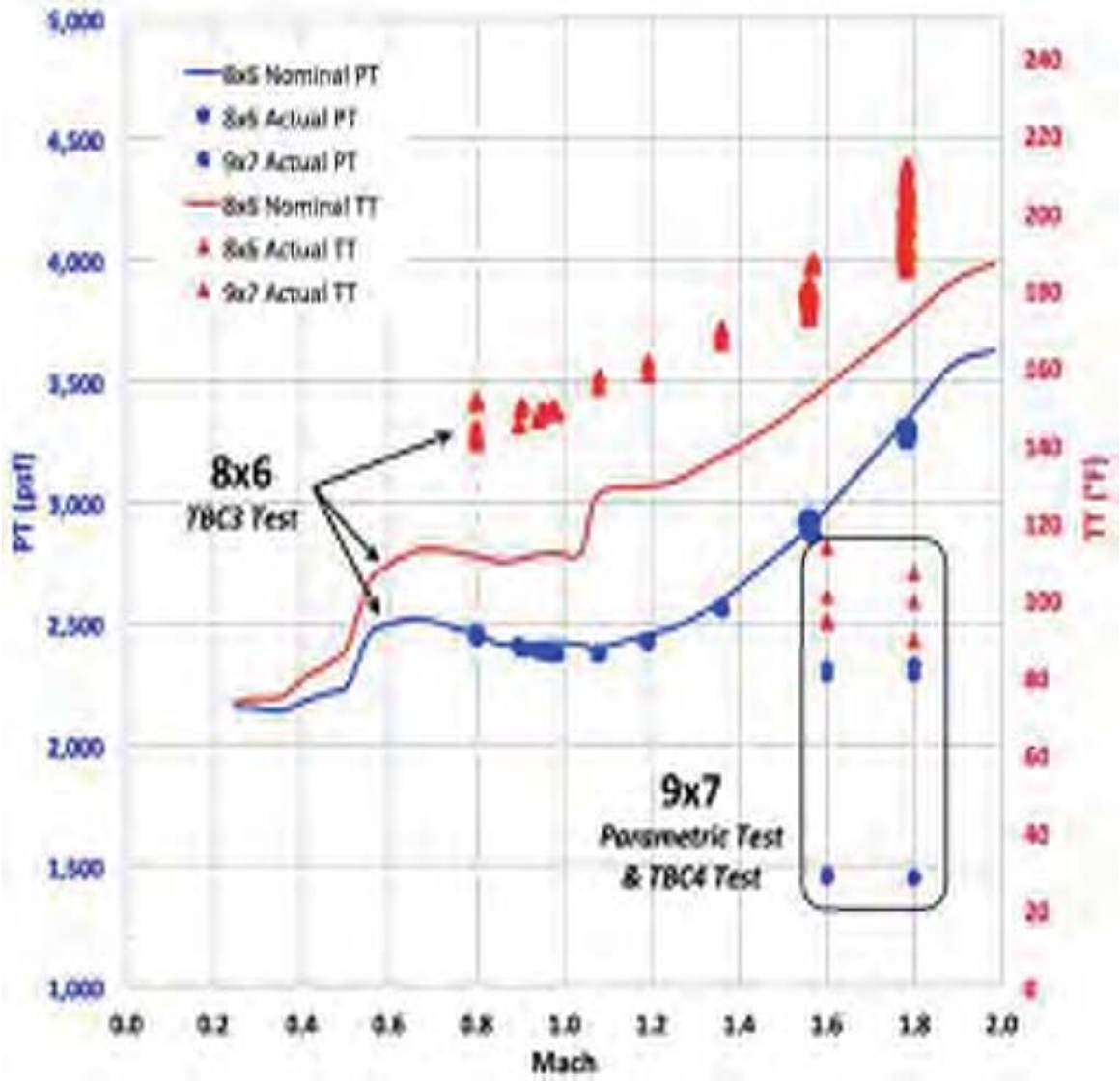

Figure 3–6. Variation of total pressure and total temperature versus Mach number in 9x7 and 8x6 wind tunnels (actual values from tests indicated by symbols)

4. Full Scale Configuration and Wind Tunnel Models

4.1. Quiet Experimental Validation Concept (QEVC)

The Boeing Quiet Experimental Validation Concept (QEVC) supersonic transport configuration was developed during Phase I of the Supersonic Experimental Validations NRA contract with Boeing. It was designed to the NASA N+2 goals (Table 1) for low sonic boom loudness levels and high cruise efficiency as an airliner feasible for entry into service in the in the 2018 to 2020 timeframe. It was designated by Boeing as their 6007 configuration after an extensive design study, and its design cruise flight conditions were *Mach* 1.8, C_L = 0.104, and an angle of attack of 3.28 degrees.

A three-view drawing of the configuration is shown in Figure 4–1, and the flight vehicle attributes are given in Table 3. It is a twin-engine design with the nacelles on top of the wing, and V-tails mounted outboard of the nacelles. The nacelles were placed on the upper surface to minimize their effect on the sonic boom signature, but this location creates potential problems with inlet recovery and distortion. The inlet performance, the effects of nacelles on the sonic boom, and the aerodynamic performance were investigated in Phase II of the study contract.

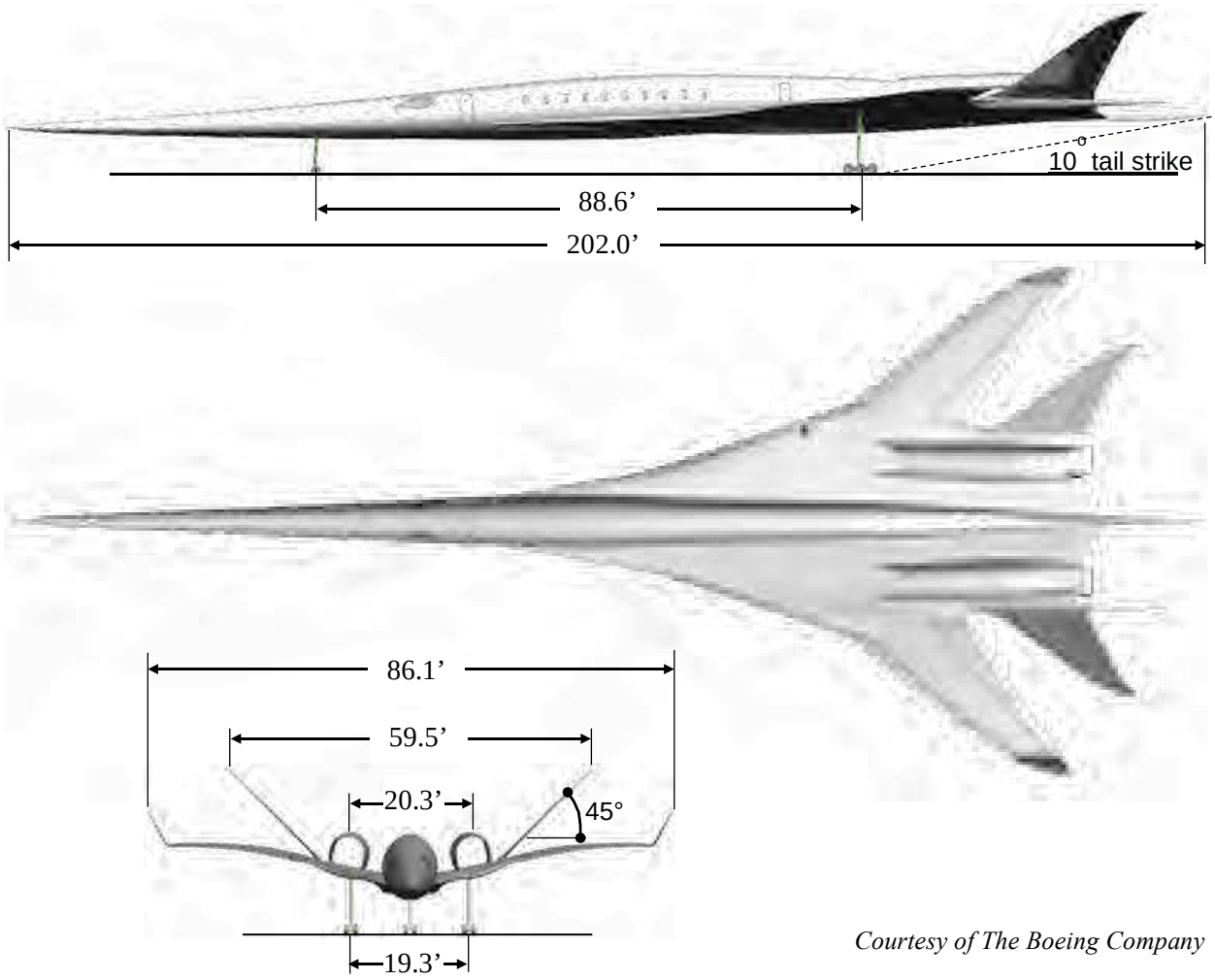

Courtesy of The Boeing Company

Figure 4–1. Boeing QEVC supersonic transport three-view drawing

Table 3. Boeing QEVC N+2 Flight Vehicle Attributes

Length (ft)	202.0
Span (ft)	86.1
Reference area (sq ft)	2,592
Flight altitude (ft)	47,500
Cruise Mach number	1.8
Cruise L/D	11.6
Aspect ratio	2.86
Taper ratio	0.17
LE sweep angles (inbd/mid/outbd)	80°/71°/52°
MAC (ft)	34.1

4.2. Wind Tunnel Models

4.2.1. Performance Model

The Performance model is a 43.31-in.-long, 1.79%-scale model of the QEVC. This model was sized primarily for good resolution in measuring aerodynamic performance, with some reduced capability to measure off-body sonic boom pressure signatures as its length sometimes prevented fitting the entire signature on the rail, depending on position. It is sting-mounted, with a 1-in. diameter six-component

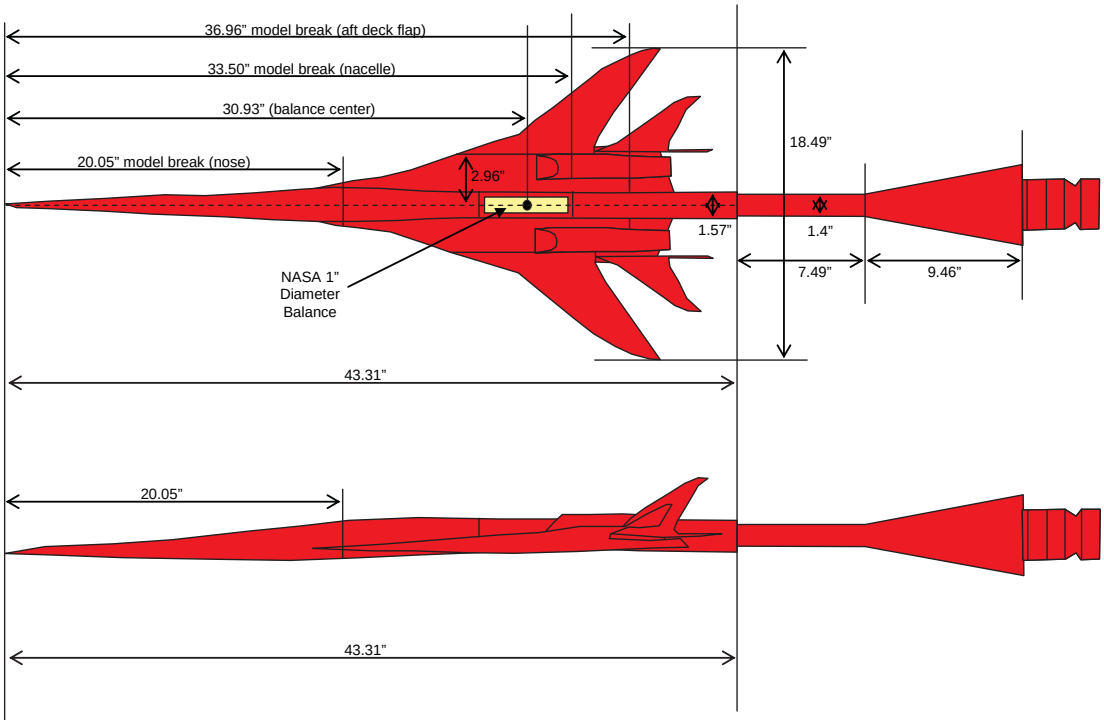

Courtesy of The Boeing Company

Figure 4–2. Phase I Performance model top- and side-view drawings

balance located in the center of the model. To accommodate the sting and the balance, the aft body of the model had to be made with a constant cross section, thus unavoidably compromising the boom signature from this part of the model. In addition, the edges of the wings, V-tails, and nacelle inlets and nozzles were thickened to a minimum of 0.004 in. at model scale for manufacturability and durability. Other changes from the full-scale configuration necessitated by model manufacturing requirements were that the nacelles had to be moved inboard 5 in., the support pod thickness needed to be increased by 50%, and the V-tail wing tips and winglet thicknesses needed to be increased from an original t/c = 3% to 4.5%.

Courtesy of The Boeing Company

Figure 4–3. CAD views of Performance model components

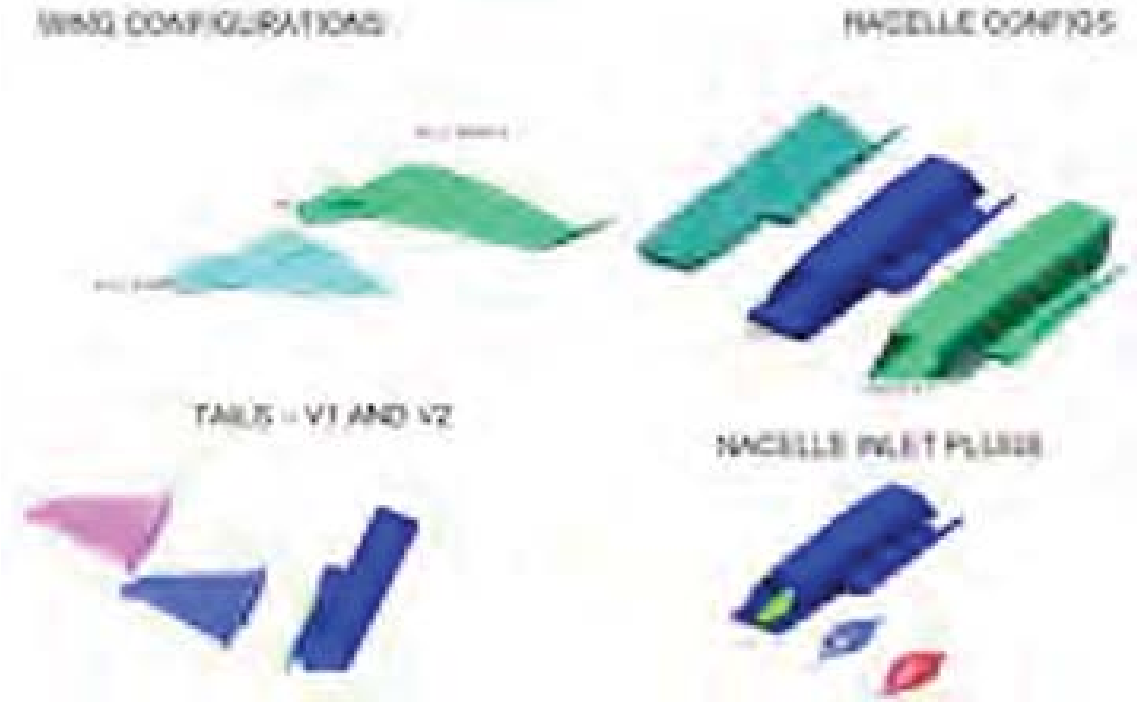

Figure 4–4. CAD views of Performance model modular parts *Courtesy of The Boeing Company*

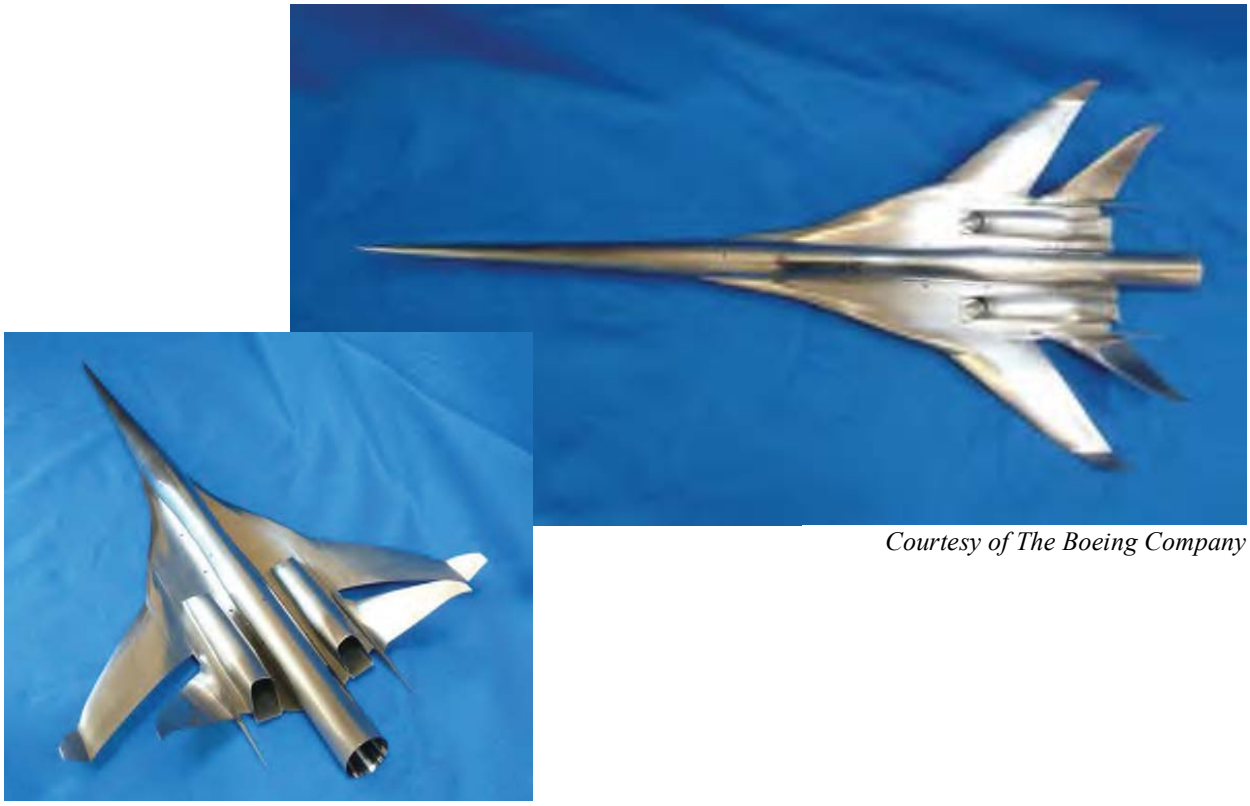

Courtesy of The Boeing Company

Figure 4–5. Photographs of assembled Performance model with sting can at aft end

Top- and side-view drawings of the model with sting are shown in Figure 4–2, and color-coded CAD representations of the model components are shown in Figures 4–3 and –4. The parts of the model that have interchangeable options are the wings, V-tails, and nacelles, and there are also three different sets of nacelle inlet plugs that can be inserted in the flow-through nacelles. Photographs of the assembled Performance Model are shown in Figure 4–5, and the model with all of its interchangeable parts and a check-loading frame is shown in Figure 4–6.

Courtesy of The Boeing Company

Figure 4–6. Photograph of Performance model and interchangeable parts

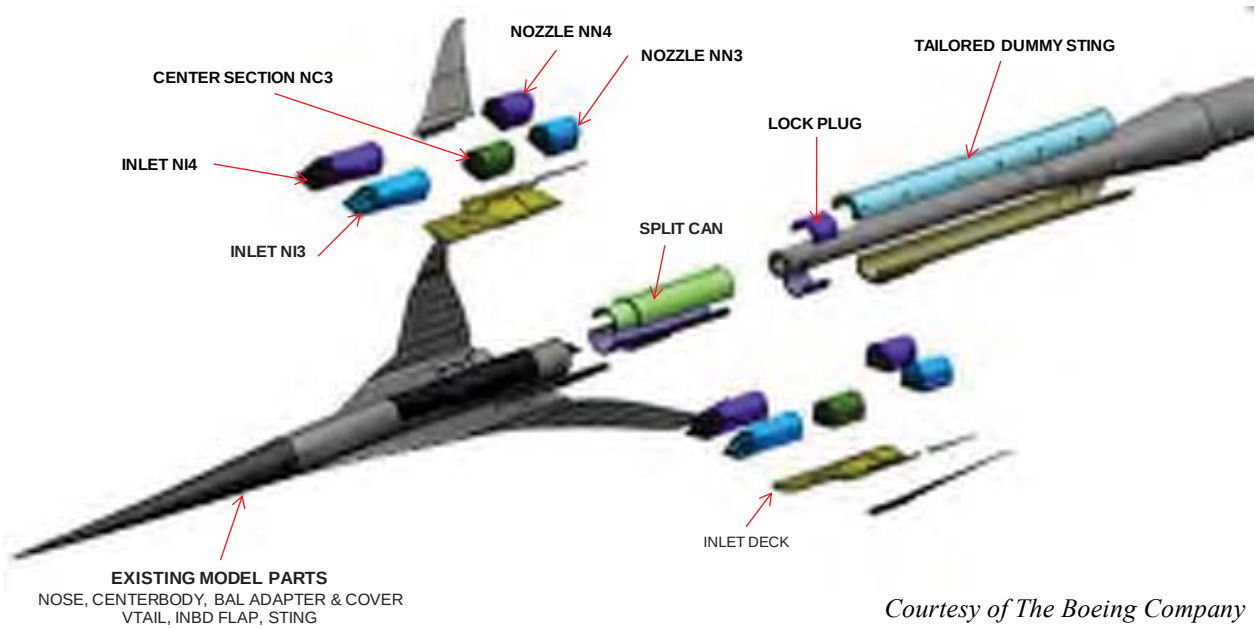

Courtesy of The Boeing Company

Figure 4–7. CAD views of Performance model, interchangeable parts, and sting with tailored dummy sting covers

Courtesy of The Boeing Company

Figure 4–8. Photograph of Performance model new parts, and tailored sting covers

As previously stated, Phase II of the NRA contract focused on (1) nacelle effects on the sonic boom signatures, (2) aerodynamic performance of the vehicle, and (3) inlet performance. New parts were made for the Performance model that would allow these investigations, namely, inlet sections NI3 and NI4 and nozzle sections NN3 and NN4. These are shown in the CAD views in Figure 4–7 and in a photograph in Figure 4–8. New nacelle center sections were also made so that parametric inlet and nozzle sections could be tested in various combinations. The primary differences between the new nacelle parts and the nacelles used in Phase I are that the new parts have contoured lower inside surfaces, simulating the inlet and nozzle throats. All of the nacelle options for this model and the Boom models are strictly flow-through—no external suction or blowing was applied in the tests to the inlets and nozzles to simulate propulsion effects.

The model is shown in Figures 4–2, –3, –5, and –6 with a "sting can" at the rear of the model, which extends the cylindrical body 6-in. aft to minimize the influence of the sting on the sonic boom pressures and the aerodynamic performance. It was found during the TBC1 and TBC3 tests, however, that the aft-facing cavity area between the sting can and the sting was adversely affecting the aft part of the pressure signature, so sting covers (two clamshell halves) were made prior to the TBC4 test to replace the sting can and continue the cylindrical cross section of the aft body as far back as possible along the sting, to the point where it tapers up in size to meet strength requirements. The assembly of these sting covers on the sting is referred to as the "tailored dummy sting," and this, along with the sting can (in a split view), are shown in the exploded CAD views in Figure 4–7. A lock plug was inserted into the back end of the model just ahead of the dummy sting to prevent the model from rotating about the balance and causing steps and gaps when deflecting under aerodynamic loads. Note that this plug and the attachment of the dummy sting to the model bridge the balance, thus rendering the balance readings invalid. During the TBC4 test, the Performance model was run with the tailored dummy sting for all boom signature measurements, and with the sting can for force and moment measurements.

Various views of the Performance model installed in the 9x7 and 8x6 wind tunnels are provided in Figures 4–9 and –10.

Figure 4–9. Boeing Performance model installed in Ames 9x7-ft wind tunnel

Figure 4–10. Boeing Performance model installed in Glenn 8x6-ft wind tunnel

4.2.2. Boom1 Model

The Boom1 model is a 15.748-in.-long model of the QEVC at 0.65% scale. It has the same aerodynamic lines as the Performance model (which is 2.75 times the size of the Boom models) aside from the differences for the mounting provisions. Boeing sized the Boom1 model to provide the best compromise of model fidelity and the ability to measure off-body sonic boom pressure signatures in a large wind tunnel. The small size was selected to measure the full signature of model on the pressure rail with room to spare for various sting or strut mounting configurations at various positions and sweeps relative to the rail. As with the Performance model, the sharp edges of the wings, V-tails, and nacelle inlets and nozzles had to be thickened relative to their true scaled-down thicknesses to a minimum of 0.004 in.

Drawings of the model are shown in Figure 4–11, which show that the model was attached to the balance by a swept blade strut and a balance adapter. The same 1-in. diameter six-component balance that was used for the Performance model was also used for this and all the other Boeing models. Two blade struts were made in Phase I of the NRA study for this model and the Boom2 model (discussed in next section): a short one, VS1 (10.028-in. long), and a long one, VS2 (11.652-in. long). VS1 is the one shown in Figure 4–11, and also in the left-side view of the colored model components in Figure 4–12. VS2 is shown in the right-side view of Figure 4–12. They both attach to the model at the same mounting location, so the longer length of VS2 places the model nose 1.625 in. further forward in the tunnel than VS1. The longer strut was preferred for minimizing strut effects on the model signature, but the shorter

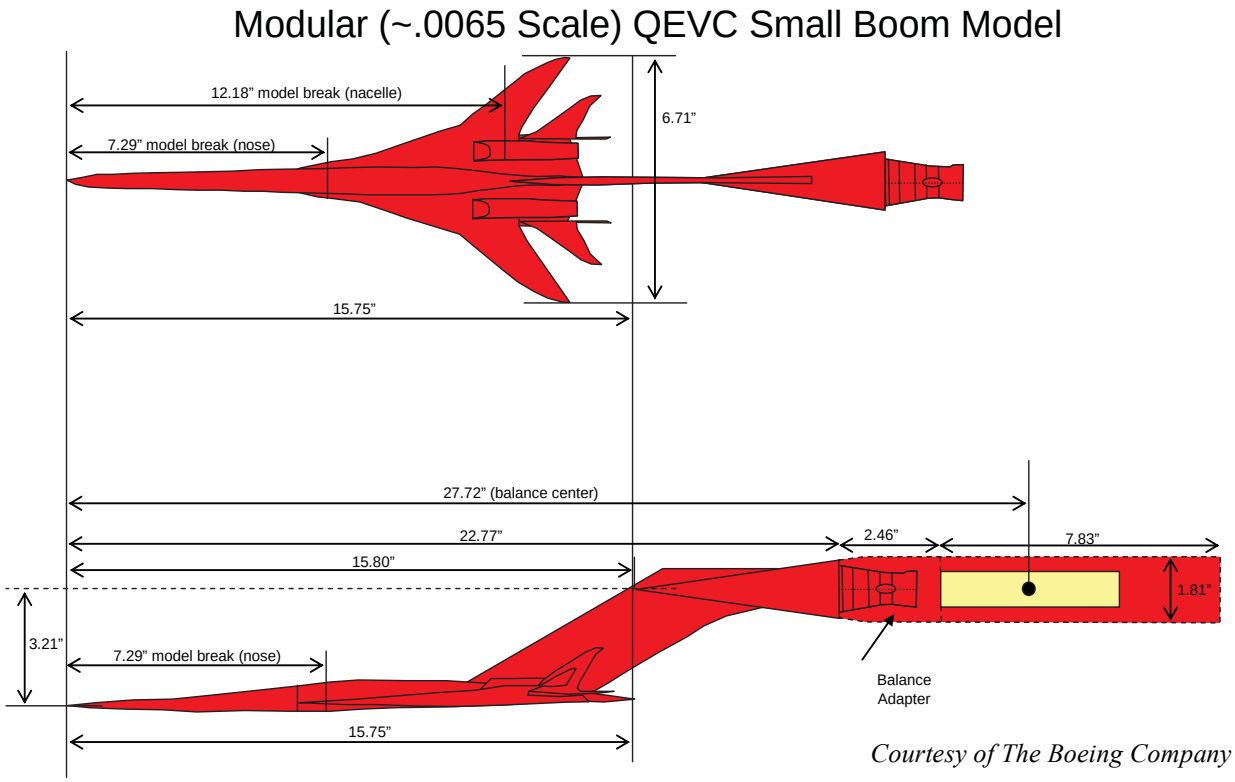

Figure 4–11. Boom1 model top and side view drawings

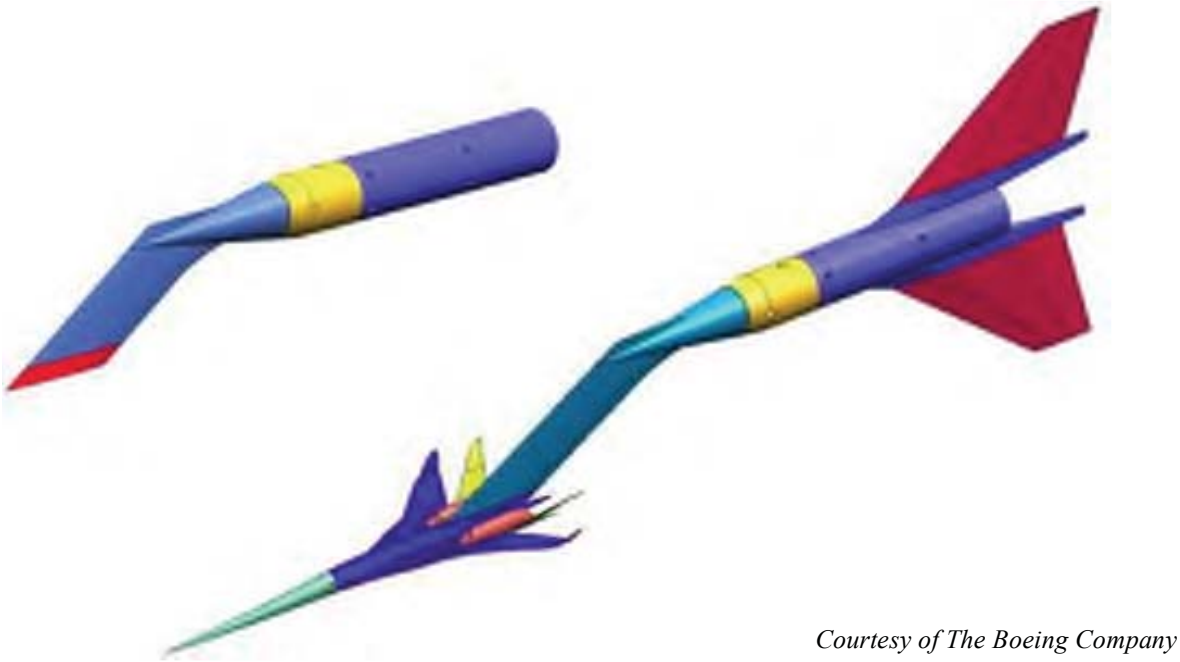

Figure 4–12. CAD views of VS1 strut (left) and Boom1 model with VS2 strut (right)

one was tested first to determine whether the cantilevered model would have high lateral dynamics in the wind tunnel. After this was determined to be a non-issue, VS2 was run with the Boom1 model from then on with no significant dynamics. The large fins attached to the rear of the balance adapter, shown in the right-side image of Figure 4–12, were built just as a standby measure in case the lateral dynamics were too severe with either strut, but they were never needed.

Color-coded CAD representations of the Boom1 model components are shown in Figure 4–13, where an alternate nacelle/V-tail (one-piece) part is shown, as well as a nacelle-off/V-tail-only part. The small teardrop-shaped mass flow plug is shown in the nacelle inlet, but a flat-bottomed fully-open nacelle component was also available. Photographs of the assembled Boom1 Model are shown in Figure 4–14, and two views of this model with the VS2 strut in the 9x7 wind tunnel are shown in Figure 4–15.

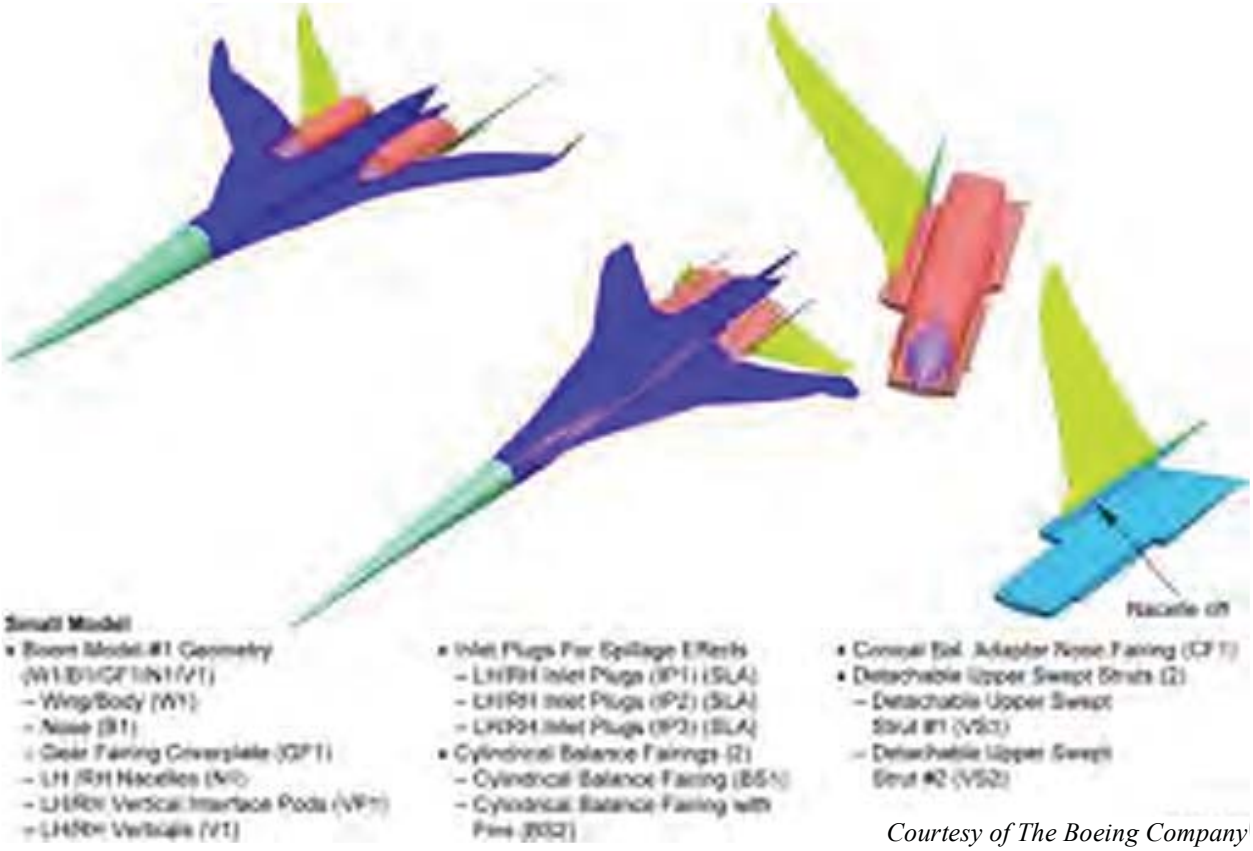

Courtesy of The Boeing Company

Figure 4–13. CAD views of Boom1 model modular parts

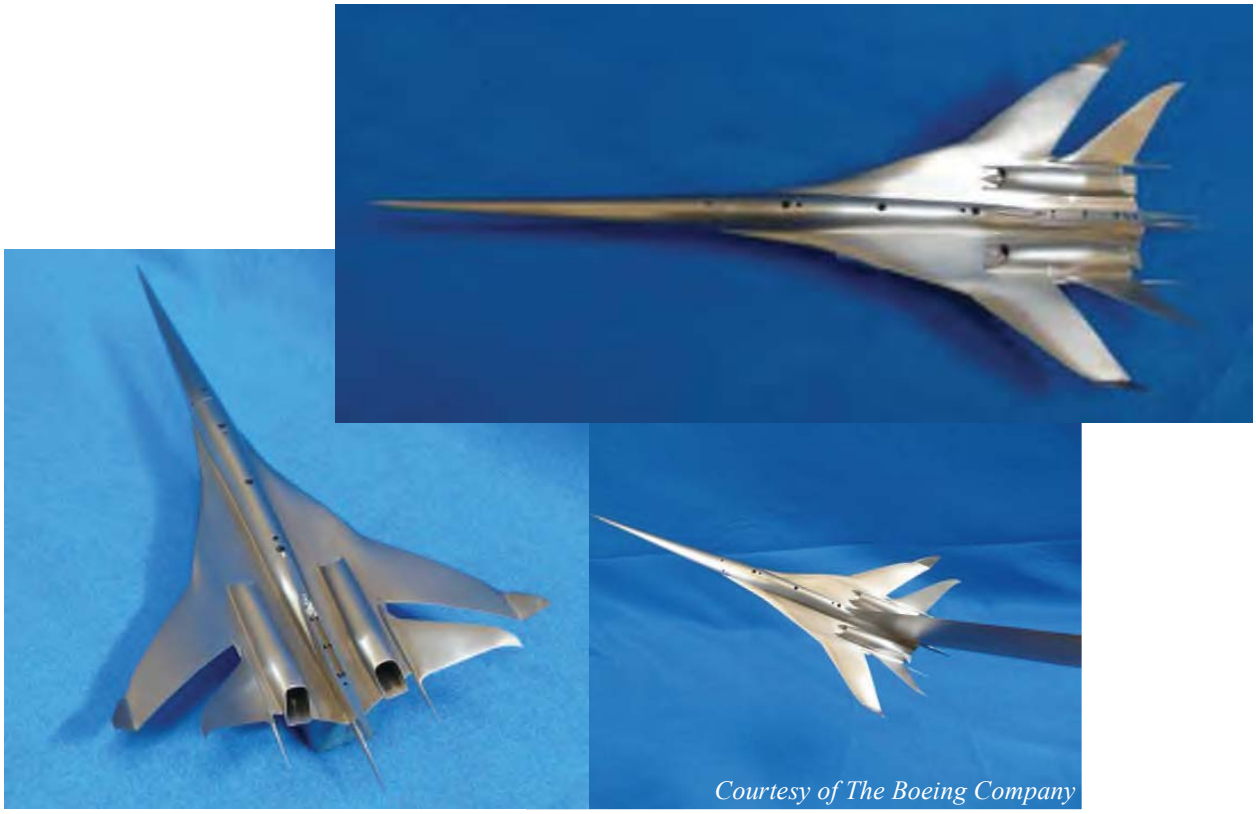

Figure 4–14. Photographs of assembled Boom1 model

Figure 4–15. Photographs of Boom1 model with VS2 strut mounted in 9x7 wind tunnel

4.2.3. Boom2 Model

The Boom2 model is an alternate low-boom design with the same breakdown and general features as the Boom1 model. It was designed for a free stream Mach number of 1.6 and C_L = 0.14, and the focus in the design was more on drag and pitching moment rather than on the near-field signature shape. It did result in significantly lower drag than Boom1, with a lower pitching moment and an under-track signature comparable to Boom1. The off-track signatures were somewhat worse for Boom2, however.

The differences between Boom1 and Boom2 are in minor tweaks of the OML, particularly on the underside body contours which will be discussed in the next section. The two models with their inter-changeable parts, the VS1 and VS2 struts, balance adapter, and adapter fins, are shown in Figure 4–16.

Figure 4–16. Photograph of Boom1 (left) and Boom2 (right) models with interchangeable parts, VS1 and VS2 struts, balance adapter, and adapter fins

4.2.4. Boom3 Model

The Boom3 model was made during Phase II of the NRA contract, and has nearly the same aerodynamic lines as the Boom1 model aside for provisions for mounting on the new VS3 and VS4 struts. CAD views of the Boom3 model with its alternate nacelles and VS3 and VS4 struts are shown in Figure 4–17, and a photograph of this model and parts are shown in Figure 4–18.

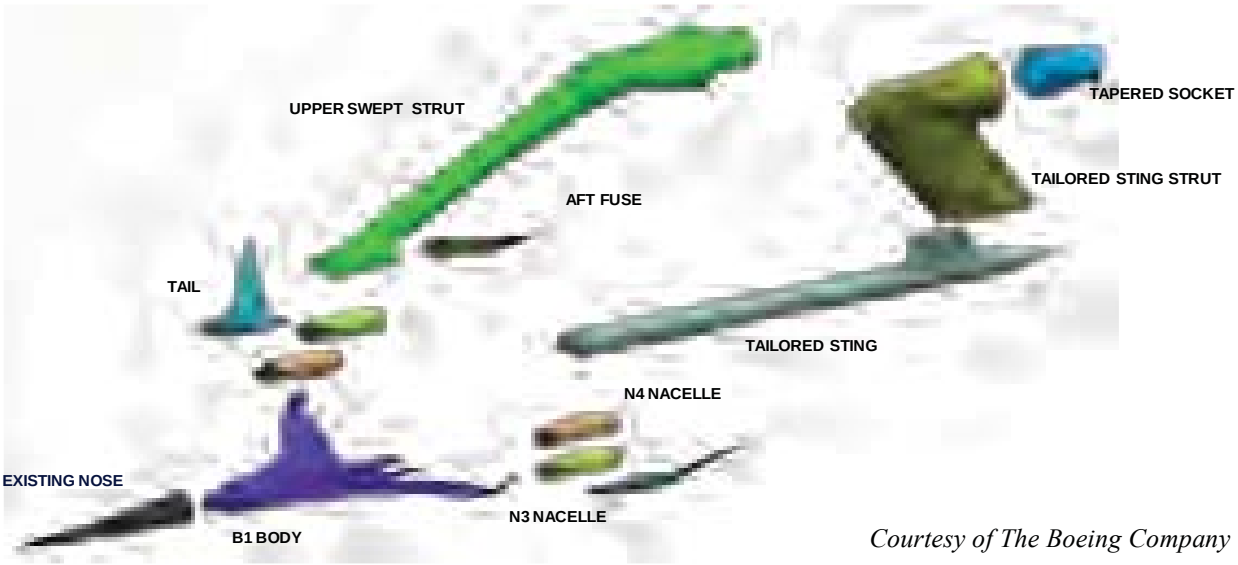

Figure 4–17. CAD views of Boom3 model, interchangeable parts, and VS3 and VS4 struts

Figure 4–18. Photograph of Boom3 model, interchangeable parts, and VS3 and VS4 struts

Figure 4–19 shows side-by-side comparison photographs of all three Boom models, both upright and inverted. The models-upright photo (a) shows the mounting interface pylon for the VS1/VS2 struts at the rear of the Boom1 and Boom2 (left and center) models in between the nacelles. The mounting interface, in the rear fuselage cut-away area, for the VS3/VS4 struts on the Boom3 (right) model extends further forward than on the other two models since the VS3 strut was made to attach near the center of the Boom3 model. The VS4 strut has a straight sting that covers this mounting interface from the rear up to the center section of the body.

A subtle difference among the undersides of the three models is evident in Figure 4–19(b). Boom1 and Boom3 are intended to be aerodynamically similar aside from the mounting strut location, and a slightly raised area under the aft fuselage between the wings can be seen on these models that is much flatter on Boom2. This shape difference is likely the main contributor to the small drag and pitching moment differences between Boom2 and the other models.

(a) Models upright

(b) Models inverted

Figure 4–19. Photographs of Boom1, Boom2, and Boom3 (left to right) models

Drawings of the VS1 through VS4 struts are provided in Figure 4–20, and photographs of the three Boom models mounted on these struts are provided in Figure 4–21. VS3 is a forward-swept strut similar to VS1 and VS2, but it is significantly longer than VS2 (14.365 vs 11.652 in.), though its attachment location is closer to the center of the model so that the nose remains the same distance from the balance center as with VS2. VS4 is an aft-swept strut that supports a straight, rear-entry sting for the Boom3 model. As with VS3, it too is designed to place the model nose at the same station as the VS2 strut.

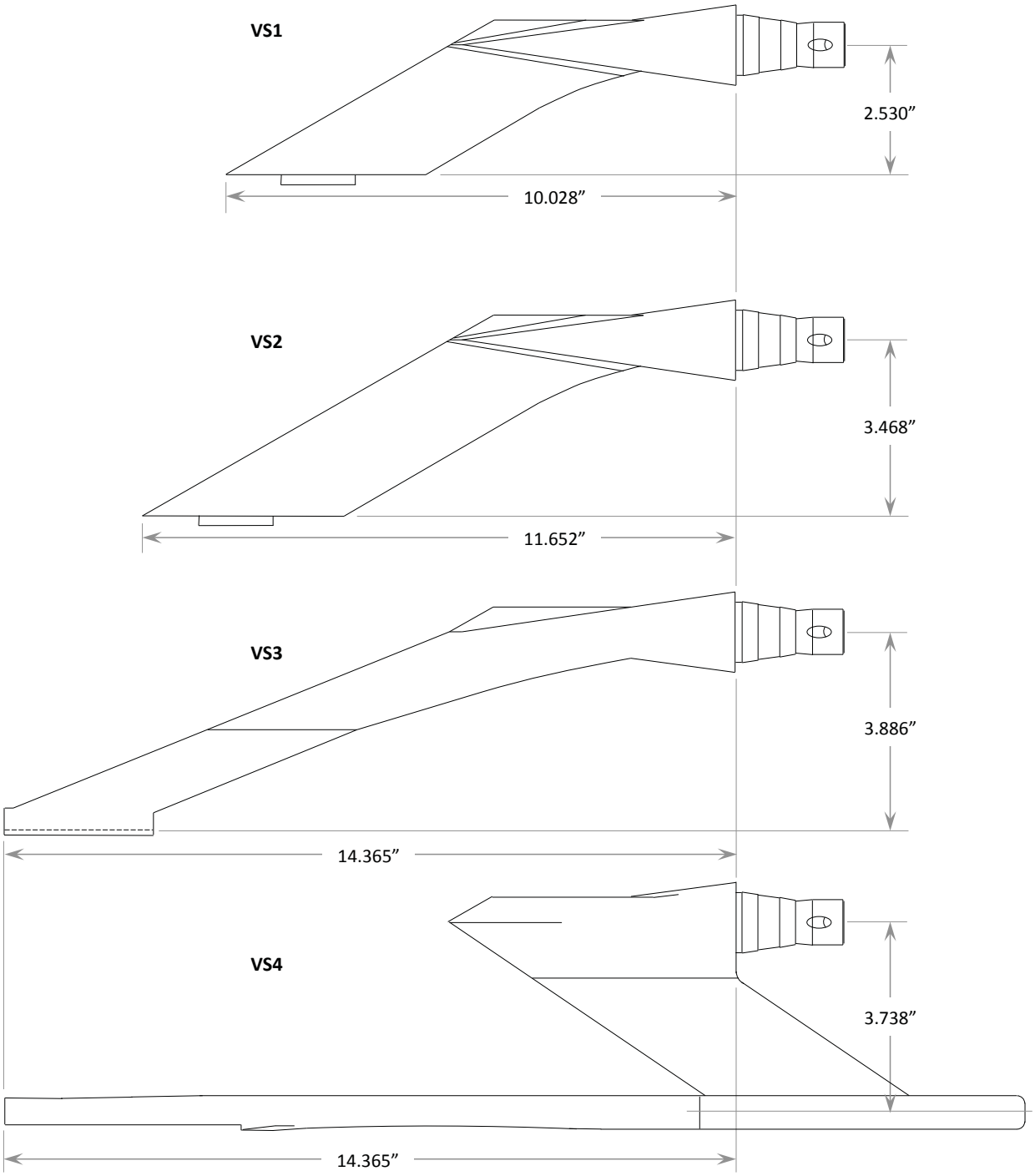

Figure 4–20. Drawings of VS1, VS2, VS3, and VS4 struts

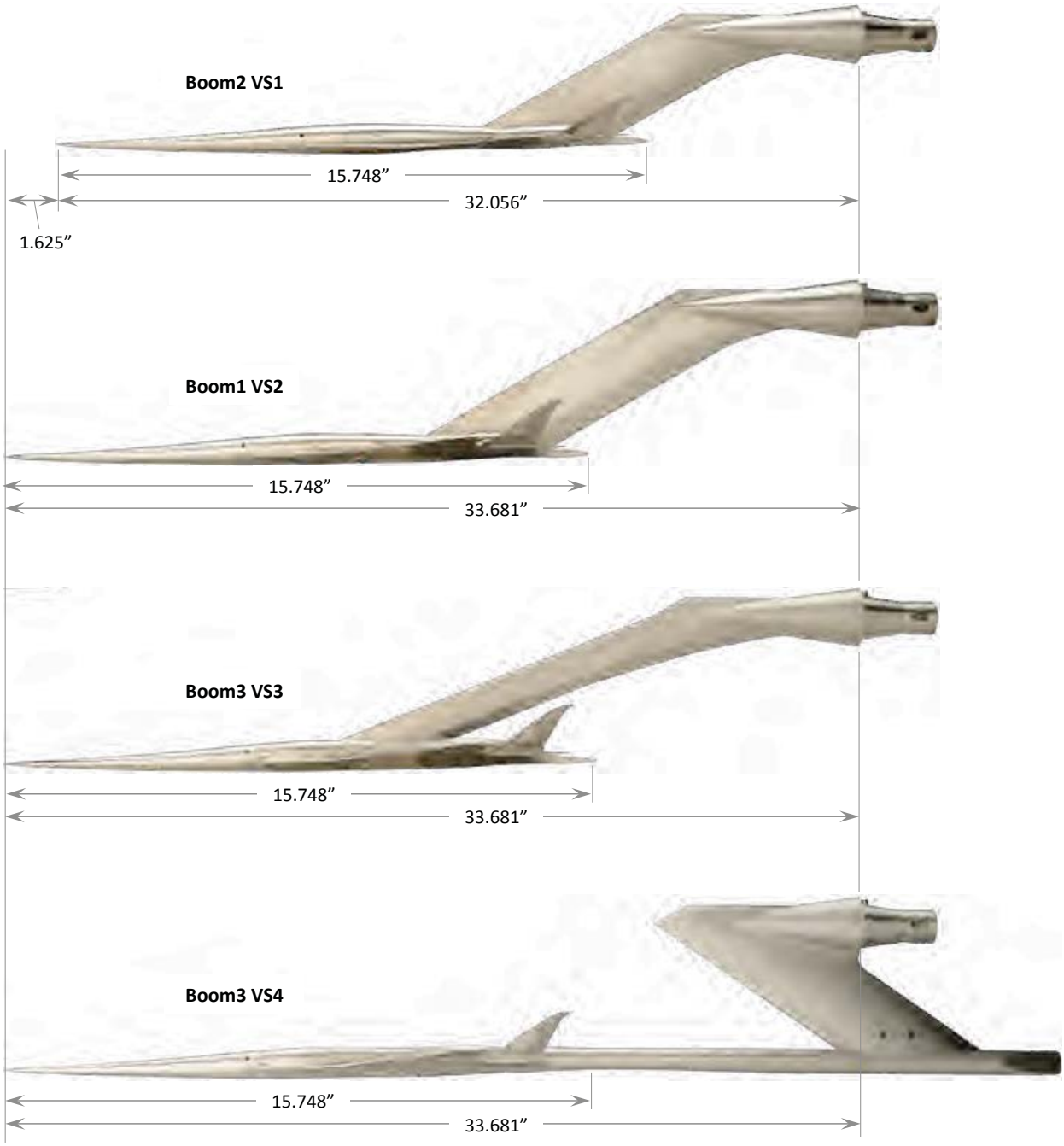

Figure 4–21. Photographs of Boom1, Boom2, and Boom3 models with VS1, VS2, VS3, and VS4 struts

4.2.5. Axisymmetric Models AS1, AS2, AS3

Three axisymmetric calibration models were tested to calibrate the pressure rail signature and provide data for CFD validation. The three models were designated AS1, AS2, and AS3. Boom results will only be presented for the AS2 model in this report because it was used as the common calibration body in the various Boeing tests, and data from AS1 and AS3 are not pertinent to this report. The attributes of the AS2 model are provided in Table 4, where the diameter listed is that of the long cylindrical portion of the model. A close-up photograph of the AS2 model is given in Figure 4–22, and a photograph of it mounted in the 9x7 tunnel is shown in Figure 4–23. The AS-2 model is a true "Seeb" configuration designed after the work of George, Seebass, and Darden.[35,36] It was designed without alteration of the aft signature and was designed to produce a sonic boom pressure signature with a small 2-in. flat pressure region behind the nose shock.

Figure 4–22. Photograph of AS2 model

Figure 4–23. Photograph of AS2 model in 9x7 wind tunnel with RF1 rail mounted on forward window blank

Important geometry parameters for all of the Boeing models are given in Table 4.

Table 4. Wind Tunnel Model Geometry

Model	*AS2*[*]	*Boom Models on VS1*	*Boom Models on VS2,3,4*	*Performance*
Scale	—	0.65%	0.65%	1.79%
L_{Ref} (in)	18.611	15.748	15.748	43.307
S_{Ref} (sq in)	—	15.322	15.322	115.891
C_{Ref} (in)	—	2.6714	2.6714	7.3465
b_{Ref} or Dia. (in)	0.965	6.7111	6.7111	18.4555
X_{Ref} (in)	—	11.4706	11.4706	31.5441
Z_{Ref} (in)	—	0	0	0
X_{Nose} to BMC (in)	24.024	26.854	28.478	31.345
Z_{Nose} to BMC (in)	0	3.201	4.139	1.053

[*] *Reference parameters for AS models were set equal to those for Boom models for consistency in test data reduction; actual AS2 model dimensions are given here*

5. Instrumentation and Model Positioning

Sonic boom pressure signatures in the various tests were measured using either the tapered RF1 (14-in.) pressure rail or the flat-top 2-in. pressure rail, and a few selected signatures were measured on both rails (one at a time) in a given test for direct comparisons.

5.1. RF1 (14-in.) Pressure Rail

The RF1 rail, also known as the 14-in. rail, has a small rounded tip and is blade-like with a small 3.5° angle from the tip to the base. A cross sectional cut through the pressure measuring center section of the rail is shown in Figure 5–1 and a CAD drawing of the design is shown in Figure 5–2. The rail is shown attached to two window blanks (54-in. diameter steel plates that replace the windows in the 9x7 wind tunnel) in the drawing. The rail stands off the wall 14 in., has a 0.05-in. radius tip, and a 1-in. base width, and is 90 in. long with an instrumented section 66 in. long. The rail height was selected to prevent contamination of the aft part of a model's signature measured on the rail by reflections off the tunnel wall of model shock waves from the forward part of the model. The height of 14 in. provides reflection-free data for model lengths of 35 and 43 in. at Mach 1.6 and 1.8, respectively.

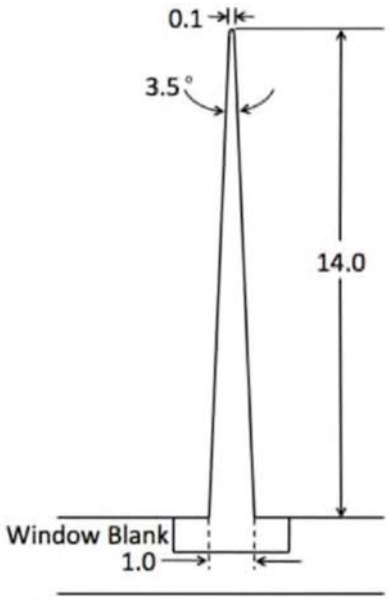

Figure 5–1. Cross section of RF1 rail (dimensions in inches)

The rail has 420 pressure orifices of 0.015-in. diameter, spaced 4 mm (approximately 0.1575 in.) apart along its tip. Prefabricated ferrules were used to accommodate the small orifice size, and were connected to metal pressure tubes that

were routed through seven machined grooves on one side of the rail. Covers over these grooves are shown in purple in the CAD images of Figure 5–2, which lead the tubes through the rail footpads mounted in the 9x7 window blanks. The mounting location of the rail in this figure is referred to as the forward location, since most of the pressure orifices are over the forward window blank, and all the pressure tubing runs through this blank. The rail can also be mounted on the aft window blank, where the aft end of the rail is secured to the tunnel wall downstream of the aft blank. In the 8x6 tunnel, the rail was just mounted in one position in the ceiling, so no "forward" or "aft" designation is given for the mounting position in the 8x6 in the figures presented herein.

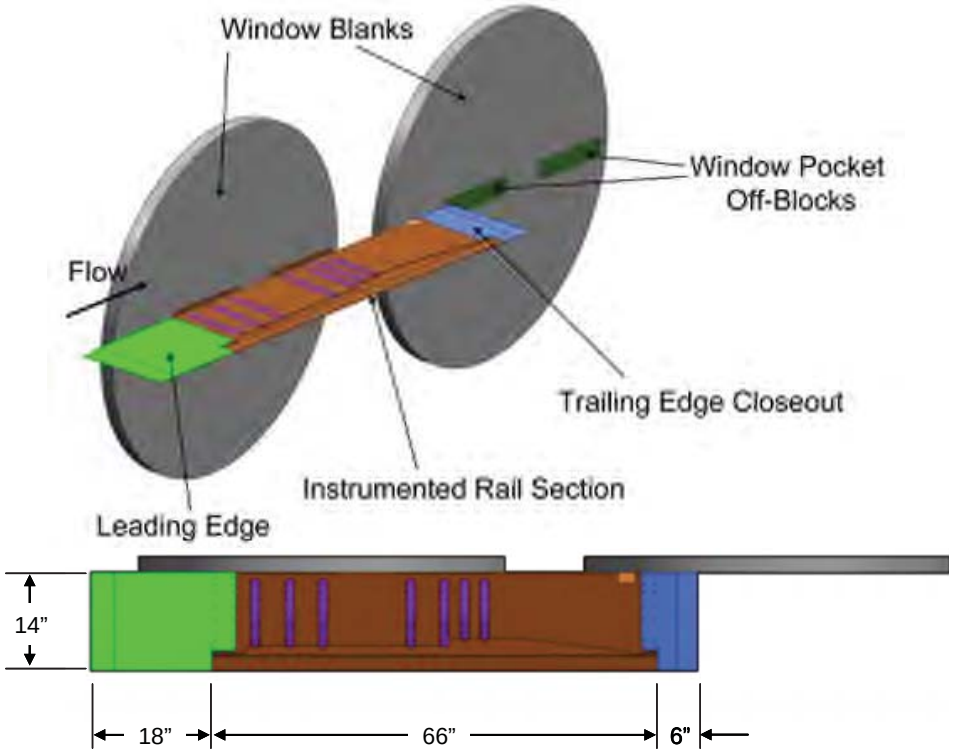

Figure 5–2. CAD views of RF1 14-in. rail mounted on forward window blank of 9x7 wind tunnel

A flow field simulation of the rail with shocks generated by the Lockheed Seeb body-of-revolution model[37] (similar to AS2 but with a longer nose) is shown in Figure 5–3. Shocks from the nose of the model (the small red tip in the center of the figure, indicating compression) pass over the rail surface and reflect off the tunnel wall to the region indicated as the reflected signature. The computation was performed with *Cart3D*[19-21,38] in conjunction with the Adjoint Error Optimization *(AERO)* module. The computation utilized mesh adaptation to minimize errors along a line sensor placed 0.1 in. above the tip of the RF1 rail. The simulation provides visualization of the pressure field in the symmetry plane of the rail. The mesh is colored by pressure coefficient and was rotated to nearly align with the Mach angle of the flow. The model is one body length (17.68 in.) from the rail in the computation. Here it is evident that the model's leading shock reflects from the wall far downstream of the model pressure signature on the rail. The figure marks the model's signature and reflected signature regions on the rail, and it is clear that there are nearly two body lengths behind the model's signature that offer no contamination from reflected model shocks. Details of the computational assessment of the rail are provided by Cliff.[3]

The RF1 rail was used in conjunction with the 2-in. rail during the TBC3 and 9x7 parametric tests and exclusively during the TBC4 test.

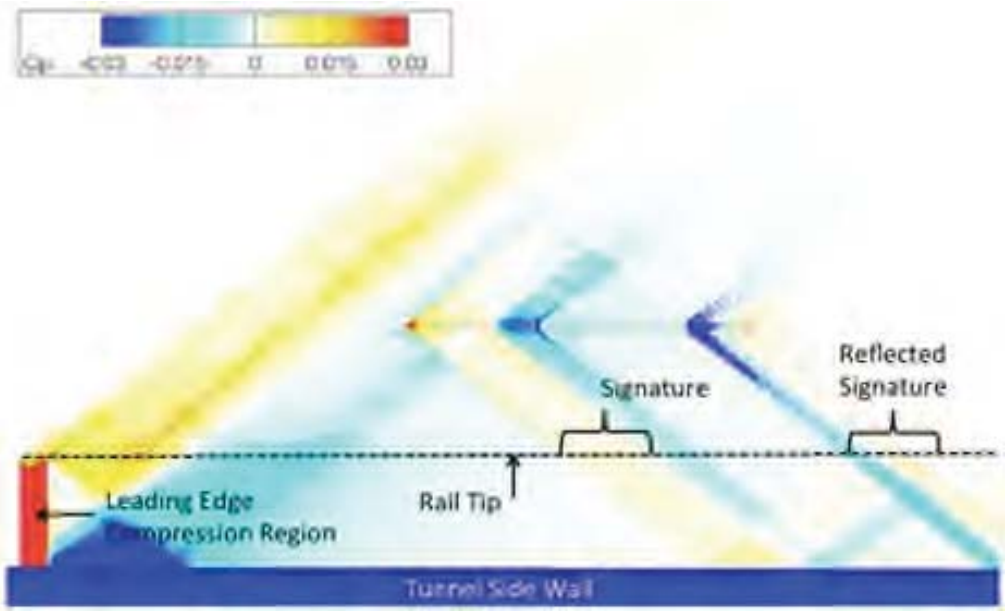

Figure 5–3. CART3D-AERO computation of the Seeb-ALR model, RF1 rail, and tunnel wall *Mach* = 1.6, α = 0 deg, *h* = 17.68 in.

5.2. 2-in. Pressure Rail

The RF1 rail was used in the Lockheed Phase I test before the first Boeing test in the 9x7 wind tunnel, but it was desired to build and test a more conventional 2-in. pressure rail for the Boeing TBC1 test. Instead of a tapered cross section like the RF1 rail, it has a rectangular cross section, being 1.5 in. wide and 2 in. tall with a flat top. The flat surface of the rail caused shock reflections that were known to artificially amplify some parts of the model signatures. The rail is 96 in. long with a 72-in. instrumented section used for boom signature measurement. The leading- and trailing-edge sections, 18 in. and 6 in. long, respectively, are wedge-shaped as shown in the CAD view of the rail on the aft window blank in Figure 5–4. The rail consists of 458 pressure orifices spaced 4 mm (approximately 0.1575 in.) apart, each with an internal diameter of 0.015 in. Pressure tubes from the orifices were routed from the rail through the rail foot pads and tunnel window blank to the 64-port PSI modules located just outside of the test section. Photographs of the rail installation in the 9x7 test section are shown in Figure 5–5.

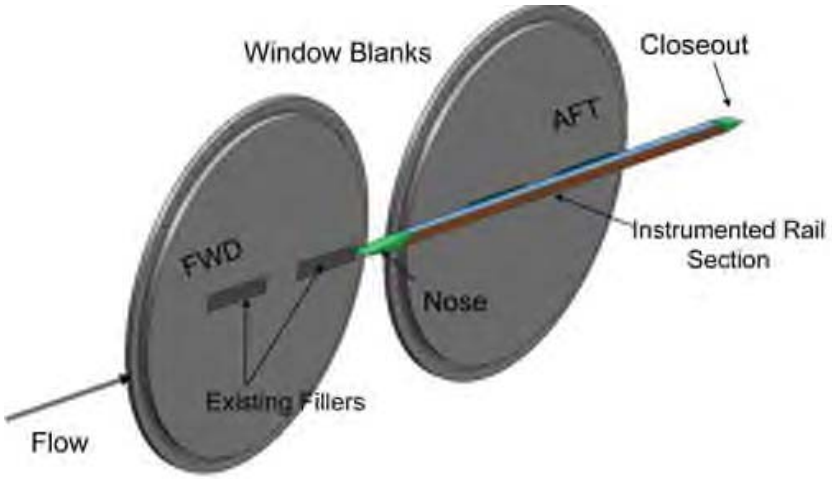

Figure 5–4. CAD view of 2” pressure rail on aft window blank of 9x7 wind tunnel

The 2-in. rail was used exclusively during the TBC1 test, and in conjunction with the RF1 rail during the TBC3 and 9x7 parametric tests.

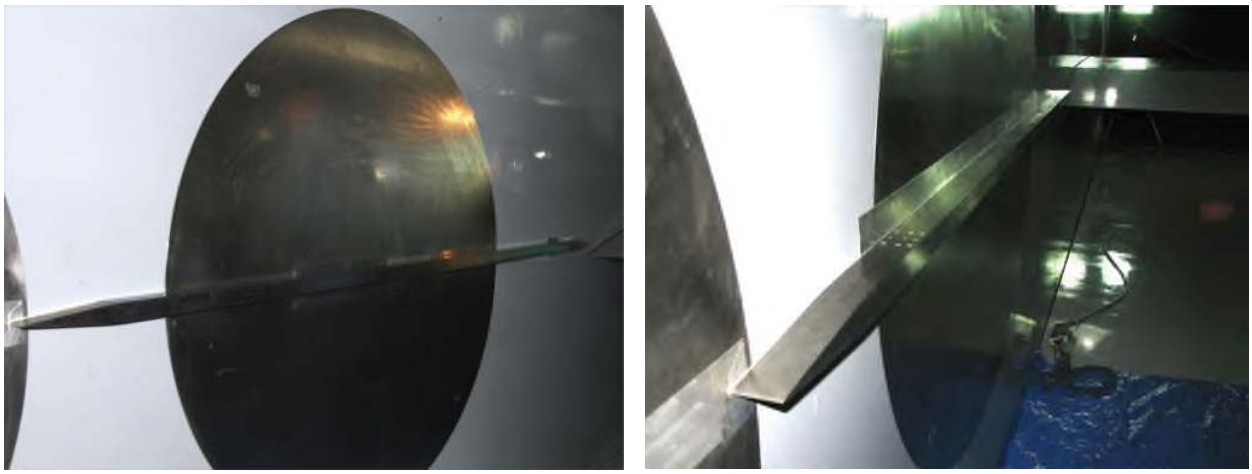

Figure 5–5. Photographs of 2-in pressure rail on aft window blank of 9x7 wind tunnel

5.3. Pressure Transducers

The rail pressures were measured using a series of 64-port, 5-psid ESP electronic pressure scanners deranged to 1.67 psid. The ESP pressure scanners are miniature electronic differential pressure measurement units that contain an array of 64 pressure sensors, one for each of 60 rail ports plus 4 monitor ports (*not* plumbed to the rail). Seven ESP scanners were used with the RF1 rail (420 orifices), and eight scanners were used with the 2-in. rail (458 orifices). The accuracy of these scanners was determined to be 0.08% of the deranged value, which equates to about 0.0013 psi or 0.187 psf. The measured pressures are converted to pressure coefficients using the tunnel freestream static pressure computed from the Mach number and freestream total pressure measured in the plenum upstream of the test section.

5.4. Model Balance and Additional Instrumentation

All Boeing models run in the Phase I and II tests used the Ames 1.0-in. Task Mk XIV-C six-component force balance. Upright and inverted runs were conducted in the first test (TBC1) to correct the angles of attack and sideslip for tunnel flow angularity. These angle corrections turned out to be not significant in their impact on the sonic boom data, so the flow angularity was not measured or applied in subsequent tests.

In the Performance model the balance was located inside the model close to the center, but for the Boom and axisymmetric models the balance was located in a balance adapter with one of the VS1

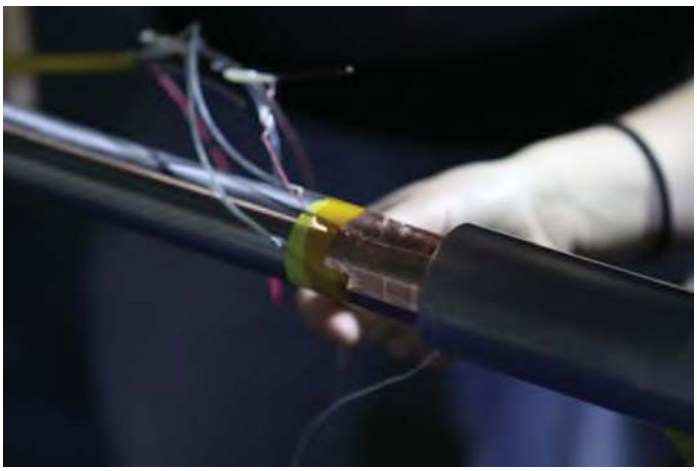

Figure 5–6. Fouling strip, cavity pressure tubes, and thermocouple wires attached to sting behind Performance model

through 4 struts in between. The axi-symmetric models were directly attached to the balance adapter. The use of the adapter was required because there was insufficient room for a balance inside the smaller models without compromising the outer mold lines, but the downstream location of the balance meant that the resolution of the model forces was not as good. The recorded force data were not adjusted for aerodynamic tares from the blade strut or balance adapter.

Figure 5–7. Fouling strip, cavity pressure tubes, and thermocouple wires on sting behind balance adapter

A fouling strip was wrapped around the forward end of the model sting to detect fouling from the back end of the Performance model, or the balance adapter when the Boom or axisymmetric models were being run. An exception, however, in the use of the fouling strip was with the Performance model in the TBC4 test, where the tailored dummy sting covers were attached to the rear of the model and the sting. Since this cover was attached both to the sting and to the model, the balance was fouled and the force measurements were not reliable, so the fouling strip was not used. The model angle was therefore set only by angle of attack and not by lift coefficient for the sonic boom measurements.

Cavity pressure measurements were recorded just inside the aft end of the Performance model and the aft end of the balance adapter for the other models in order to make cavity drag corrections. A thermocouple was also installed at the forward end of the sting just behind the balance to measure balance temperature at its back end. A photograph showing the fouling strip, cavity pressure tubes, and thermocouple wires attached to the sting behind the Performance model is shown in Figure 5–6, and the same behind the balance adapter is shown in Figure 5–7.

5.5. Roll Mechanism

The Ames small model roll mechanism (SMRM) was used for off-ground-track boom signature measurements in the 9x7 parametric and TBC4 tests, but not at the 8x6 in the TBC3 test. The SMRM has a fixed 7.5° bend in it to further accommodate offset angle-of-attack and -sideslip ranges desired by particular tests. This bend has been useful in sonic boom tests in that it allows a model to be moved closer to the rail (mounted on the north wall) or further from the rail (toward the south wall) than would be possible without it, though the bend has not been required for some of the recent sonic boom testing in the 9x7.

5.6. Linear Actuator

A linear actuator was used in the 9x7 parametric and TBC3 tests to translate the model longitudinally in the wind tunnel. This allowed acquisition of multiple pressure signatures at small increments in the *X* direction over a specified distance, such as 26 positions spaced 0.63 in. apart (~4 rail orifices) in a typical *X* sweep conducted in the 9x7 parametric test. In the TBC4 test, the linear actuator was not installed, so the only sweeps were in the *Z* direction, accomplished by translating the tunnel strut. Both *X* and *Z* sweeps in the various tests were successfully used in improving the quality of the signatures through spatial averaging.

The linear actuator is remotely controlled and its ram translates forward and aft at a rate of 0.7 in. per second over a 24-in. traverse distance. The minimum and maximum (retracted and extended) lengths of the linear actuator plus ram are 44 in. and 68 in., respectively. The linear actuator mounts into the roll mechanism with a 2.875-in. diameter male taper, and accommodate the model sting in the linear actuator with a 1.05-in. diameter female taper.

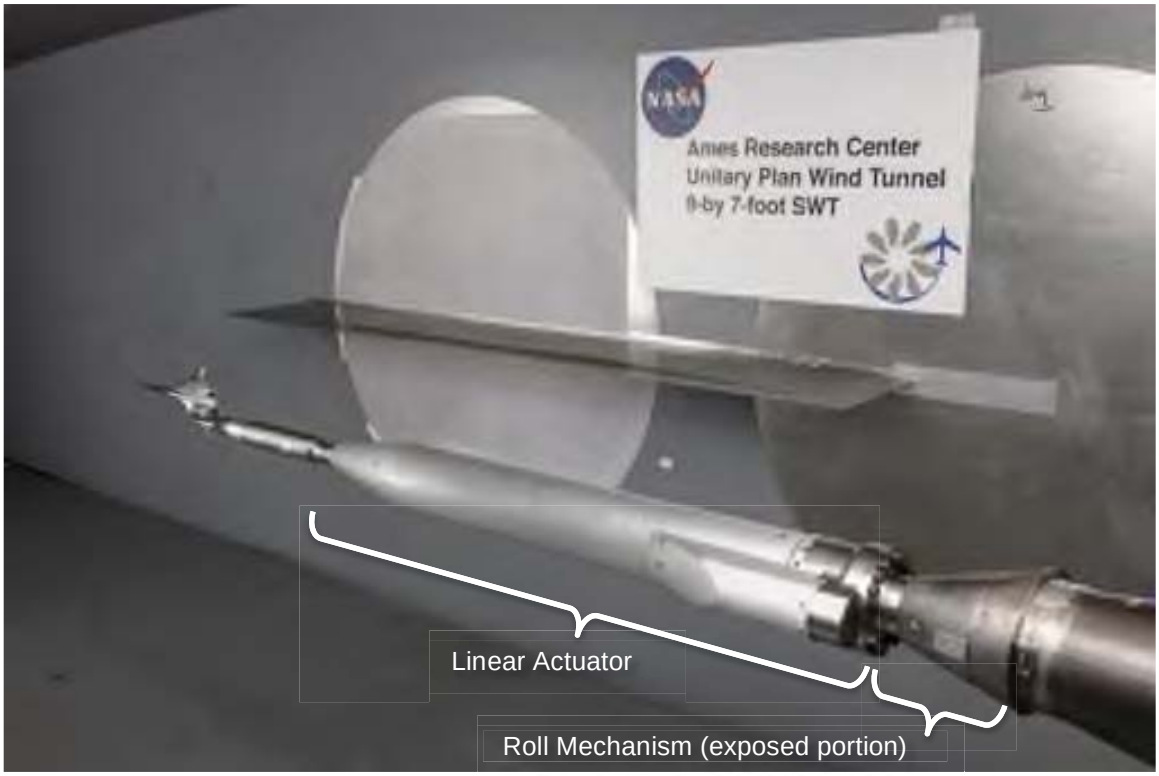

Figure 5–8. View of linear actuator and roll mechanism in 9x7 wind tunnel, with Boom1 model mounted on blade strut and balance adapter and RF1 pressure rail in background

A photograph showing the linear actuator and exposed portion of the roll mechanism in the 9x7 wind tunnel is provided in Figure 5–8. The ram of the actuator is shown in its retracted position, where the minimum of 2.625 in. of it is exposed at the front end of the actuator. The tilted-cone-shaped head of the roll mechanism is visible between the primary adapter (at right, partially hidden) and the rear of the linear actuator. The non-rotating cylindrical body of the roll mechanism is secured in the forward end of the primary adapter.

6. Wind Tunnel Flow Quality and Test Techniques

6.1. Wind Tunnel Flow Quality

Ideally, a wind tunnel flow field surrounding a model would be completely uniform and steady for all model positions in the tunnel. However, this is rarely the case in supersonic wind tunnels, and in the 9x7 wind tunnel, there are spatial variations in terms of undesired flow angularity and Mach number variation throughout the test section, as well as temporal variations. These variations are caused in large part by the asymmetric sliding-block nozzle, and the fixed nozzle contours of the floor and ceiling, which result in a design that is optimized for one Mach number and not ideal for the others. Therefore, it is not surprising that unsteady characteristic waves emanate from the nozzle through the test section, affecting flow angles,

Mach number, and steadiness of the flow. It is not possible to completely correct for these issues, but spatial and temporal averaging have been used to minimize their effects on the sonic boom signatures. To illustrate some of these flow features in the tunnel, Schlieren and shadowgraph images of the flow in the 9x7 and some plots of the variation of model forces and angle of attack will be presented.

6.1.1. Schlieren and Shadowgraph Imaging

Undesired facility-generated shock waves within a wind tunnel become significant in a sonic boom test when the shock waves from a low-sonic-boom design are generally weaker than those from the facility. This is evident in viewing Schlieren images that reveal both the ambient tunnel pressure waves and the model shock waves. Figure 6–1 presents Schlieren images of three Boeing models (AS2, Boom1, and Performance) in the Glenn 8x6 wind tunnel. The red arrows point to some of the facility-generated shock waves in the tunnel, which, in some cases, appear as strong if not stronger than the model shocks. The effect of these shocks on the model forces or boom characteristics could not be measured however, because there was insufficient flexibility in placement of the model to allow gathering data with the model clear of the tunnel-generated shock waves. Figure 6-1 shows the facility shock waves visible through the windows; it is very likely that such shocks persist downstream of the tunnel nozzle and through the entire test section.[39]

In the AS2 model image at Mach 1.8 (Figure 6–1(a)), the nose shocks are clearly visible against the background, and do appear stronger and more clearly defined than the tunnel ambient shocks. However, in the Boom1 model image at the same Mach number (Figure 6–1(b); the model is mounted upside-down for reasons stated above), the nose shock is much less visible than in the AS2 image, primarily because the nose tip is more slender. Additional shocks along the length of the model are very weak and difficult to see, with the exception of the shocks emanating from the vertical blade strut where it attaches near the rear of the upper surface of the model. For the Performance model at Mach 1.6 (Figure 6–1(c)), the nose shocks appear a little stronger than those of the Boom1 model, as expected because of the almost 3x larger model size. The rest of the Performance model behind the nose is not visible in the RBOS image because it is too large for the viewing window.

Schlieren-like images of the Boeing Boom1 model in the Ames 9x7 wind tunnel are shown in Figure 6–2. These were not made with the conventional through-tunnel Schlieren technique, but with a technique known as retro-reflective background-oriented Schlieren (RBOS).[40] This technique is used when optical access is limited, such as in sonic boom tests where window blanks are installed on one side of the tunnel to accommodate the pressure rail. For the tests of the Boeing models in the 9x7, cameras and lights were placed on the south side of the tunnel, and a highly reflective material (3M Scotchlite brand film 900X) was placed on the north side window blanks behind the model. This was then speckled with ink in order to provide a background against which image-processing techniques would highlight density gradients in the field of view, due to the apparent movement of the speckles between wind-on and wind-off images.

In the Boom1 model RBOS images in Figure 6–2, the first image is at Mach 1.6 and the model is shown in the wings-horizontal orientation. The second image is at Mach 1.8 and the model is shown wings-vertical. The RF1 rail is the black horizontal band across each of the images, and the model and strut are also masked out. At first glance, it appears that the background shocks in the 9x7 are much stronger than in the 8x6, but this is not necessarily the case. The darkness of the 9x7 images are a result of higher contrast obtained in the RBOS technique, as the gray scale was compressed to make the model shocks stand out more.

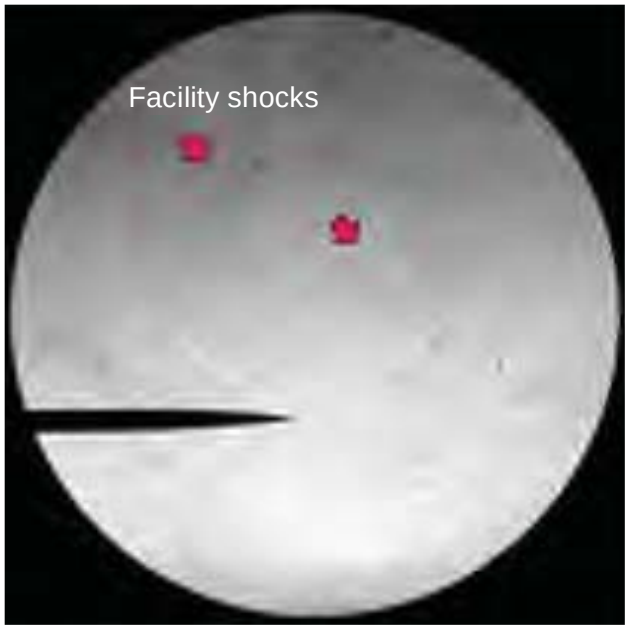

(a) AS2 model, Mach 1.8

(b) Boom1 model, Mach 1.8

(c) Performance model, Mach 1.6

Figure 6–1. Schlieren images of Boeing Models in NASA Glenn 8x6 wind tunnel, taken through aft Schlieren windows

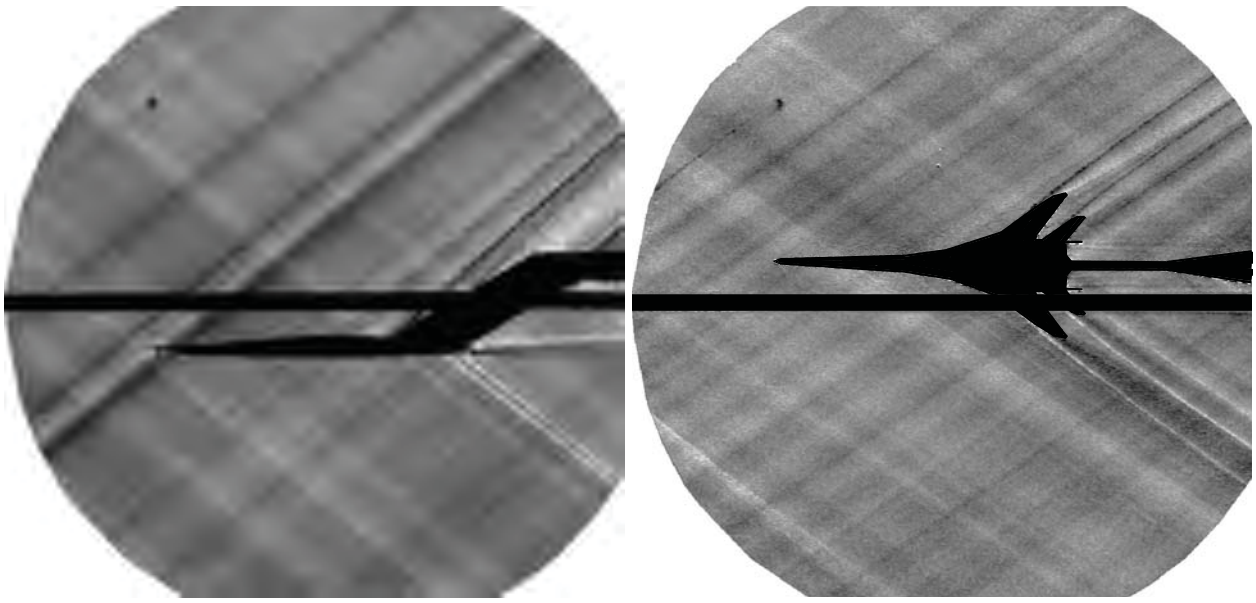

(a) Mach 1.6 **(b) Mach 1.8**

Figure 6–2. RBOS images of Boeing Boom1 Model with VS2 strut in 9x7 wind tunnel, taken through the forward south side Schlieren window

In the Mach 1.6 9x7 image, it is apparent that there is a pair of strong facility-generated shock waves that cross the model nose from the lower left to the upper right, along with quite a few weaker shocks and Mach lines throughout the window view. The source of these waves was not able to be determined during the test as there were no steps or bumps on the tunnel floor in line with these waves—they could be characteristic waves from the nozzle bouncing between the floor and ceiling. A shadowgraph image through the forward windows of the 9x7 in Figure 6–3(a) taken with the tunnel empty shows the same strong shock waves, confirming that they are independent of the presence of the model. The Mach 1.8 images in Figure 6–2(b) and 6–3(b) also show similar background shock wave patterns.

The Boom1 model nose shock is very difficult to see in Figure 6–2(a) because both above and below the nose the shock is nearly coincident with facility shocks, which may or may not be at the same spanwise position in the tunnel as the model. Shock waves further aft on the model are more evident in both the Mach 1.6 and 1.8 images, such as those coming off the wings, tails, and nacelles. Also, the wake coming off the back of the model in the streamwise direction is clearly evident. Note that the shocks from the model appear as dark bands going upward and light bands going downward; this is because the density gradients resolved by the RBOS technique are measured by the vertical deflection of the light path, equivalent to a horizontal knife edge in conventional Schlieren.

All of these images show the shock wave patterns in the tunnel at an instant in time, but time-resolved video (not shown herein) using Schlieren, shadowgraph, and RBOS reveals that the tunnel ambient pressure waves randomly shift positions by small amounts. This shifting covers distances on the order of one-quarter of an inch on the average, and occurs both in short-term temporal variations (at frequencies on the order of 100 Hz or more) and in long-term variations (several seconds or more). The short-term variations are averaged out in the data samples, but the long-term variations cause differences to be seen in the force and pressure data for the short data samples (~2 second durations).

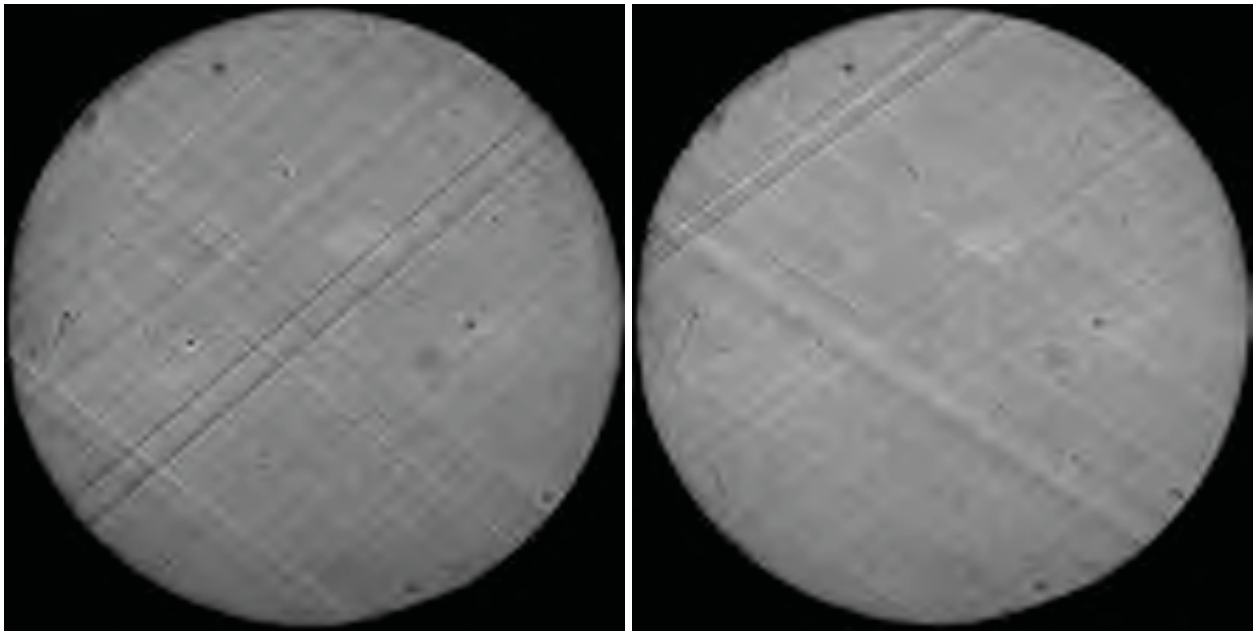

(a) Mach 1.6 **(b) Mach 1.8**

Figure 6–3. Shadowgraph images of empty 9x7 wind tunnel, taken through forward Schlieren windows

6.1.2. Lift, Angle of Attack, and Pitching Moment Variations During Sweeps

The Ames 9x7 and the Glenn 8x6 wind tunnels have stream angle variations throughout the test sections which result in variations in the model forces, moments, and angles when the model is moved in the *X* or *Z* direction to acquire multiple signatures. Figures 6–4 through –7 show plots of lift, angle of attack, and pitching moment variations during selected *X* and *Z* sweeps for the Boom1 VS2 model in the 9x7 and 8x6 tunnels, and Table 5 lists the average ranges of these variations among the all the curves on each of the plots. Data at nominal Mach numbers of 1.6 and 1.8 are presented in the first three figures, but only at Mach ~1.8 (1.78 in 8x6) in the last figure since no *Z* sweeps were acquired for the Boom1 model in the 8x6 wind tunnel at Mach ~1.6 (1.56 in 8x6).

Note that for some of the runs, the configuration is the Boom1 VS2 model with nacelles and vertical tails off ("n/v off") since valid comparison runs with these components *on* the model were not available in some cases. While the nacelles and verticals do affect the lift and pitching moment, the focus in this section is just on the *variation* of these coefficients over the ranges of the sweeps conducted, and the effect of the nacelles and verticals on the average variation is believed to be small.

Table 5. Average ranges of variations of lift, angle of attack, and pitching moment during *X* or *Z* sweeps

	9x7 X Sweeps	***8x6 X Sweeps***	***9x7 Z Sweeps***	***8x6 Z Sweeps***
Figure	**6–4**	**6–5**	**6–6**	**6–7**
C_L	0.019	0.004	0.011	0.004
α	0.030	0.055	0.007	0.018
C_M	0.057	0.017	0.056	0.021

One of the notable differences among the four sets of plots is that the angle of attack increased by an average of more than 0.030° over the length of the various *X* sweeps in the 9x7 and 8x6 wind tunnels, while it varied extremely little during *Z* sweeps. This is a clear indication that the stream angle in the angle-of-attack plane varies with longitudinal position in both tunnels, and thus could be expected to cause small differences in the pressure signatures over the length of the *X* sweeps. In the 9x7 *Z* sweeps, the average angle-of-attack variation was only 0.007°, indicating that the α stream angle is fairly uniform across the width of the tunnel within the range of heights tested: 26- to 34-in. "above" the rail, or 40- to 48-in. horizontally away from the north wall.

Very few *Z* sweeps were run in the 8x6 test (Figure 6–7) because it was learned early in the test that moving the tunnel strut vertically had an intolerable effect on the rail pressures. The strut was located directly under the aft part of the rail, and while any shocks from the strut fell behind the rail at the Mach numbers tested, the porous walls in the transonic part of the test section (where the rail was located) allowed changes in the air exiting through the tunnel walls due to strut movement, and this had a significant effect on the rail pressures. The three curves shown in Figure 6–7 for *Z*-sweep runs in the 8x6 tunnel at Mach 1.78 show some angle-of-attack variation with model height, but it is not consistent as it was for *X* sweeps in either tunnel or for *Z* sweeps in the 9x7.

In regards to the fairly uniform angle-of-attack variation observed in *X* sweeps in both tunnels, it is interesting to note that there are generally *not* the commensurate uniform changes in lift or pitching moment that one would expect with the α changes. The lift or pitching moment curves are mostly flat over the ranges of ram positions tested, with the exception of a few of the sweeps in the 9x7 tunnel (signature "sig" sets 53, 45, and 51).

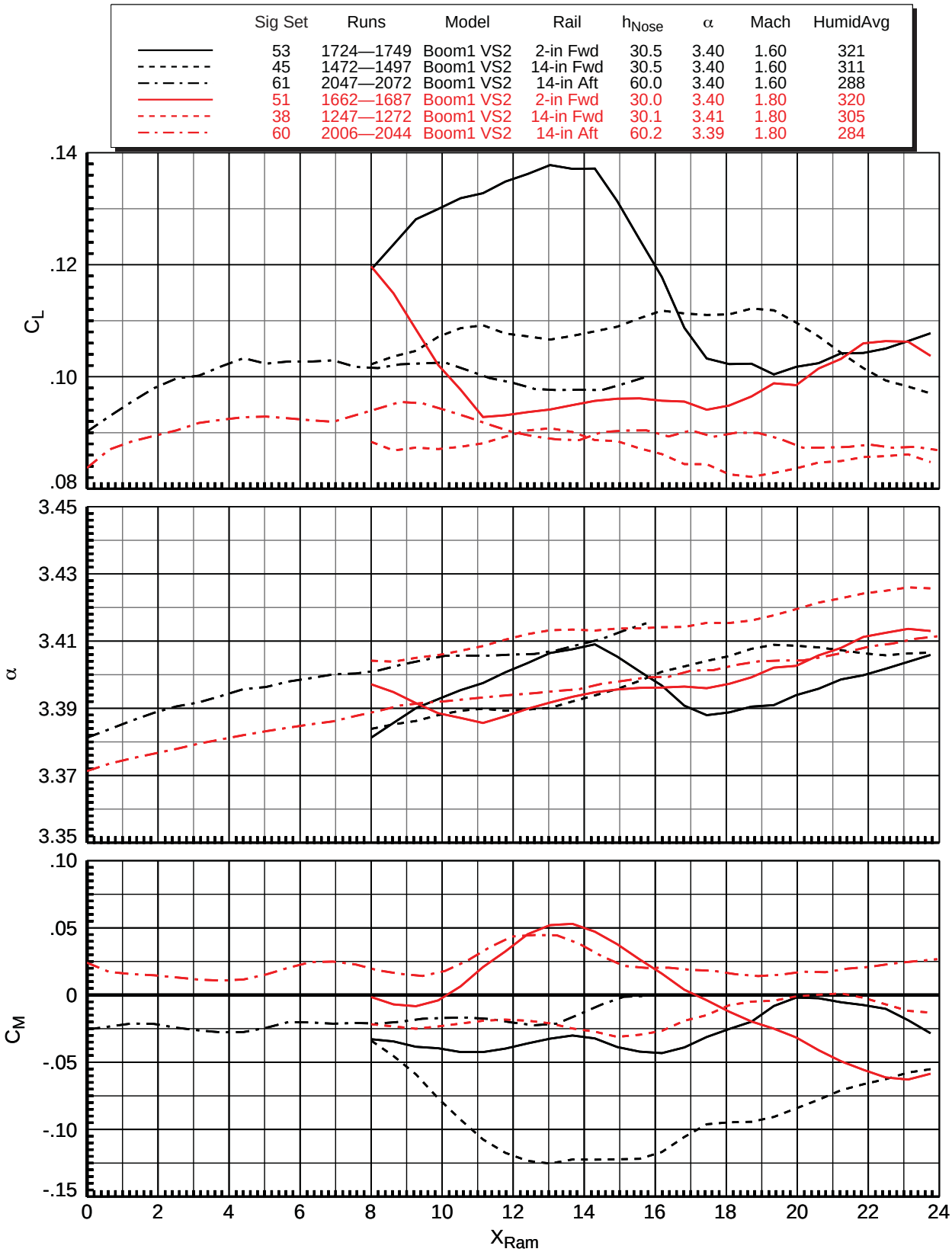

Figure 6–4. Boom1 VS2 model lift, angle of attack, and pitching moment variations during *X* sweeps, 9x7 parametric test

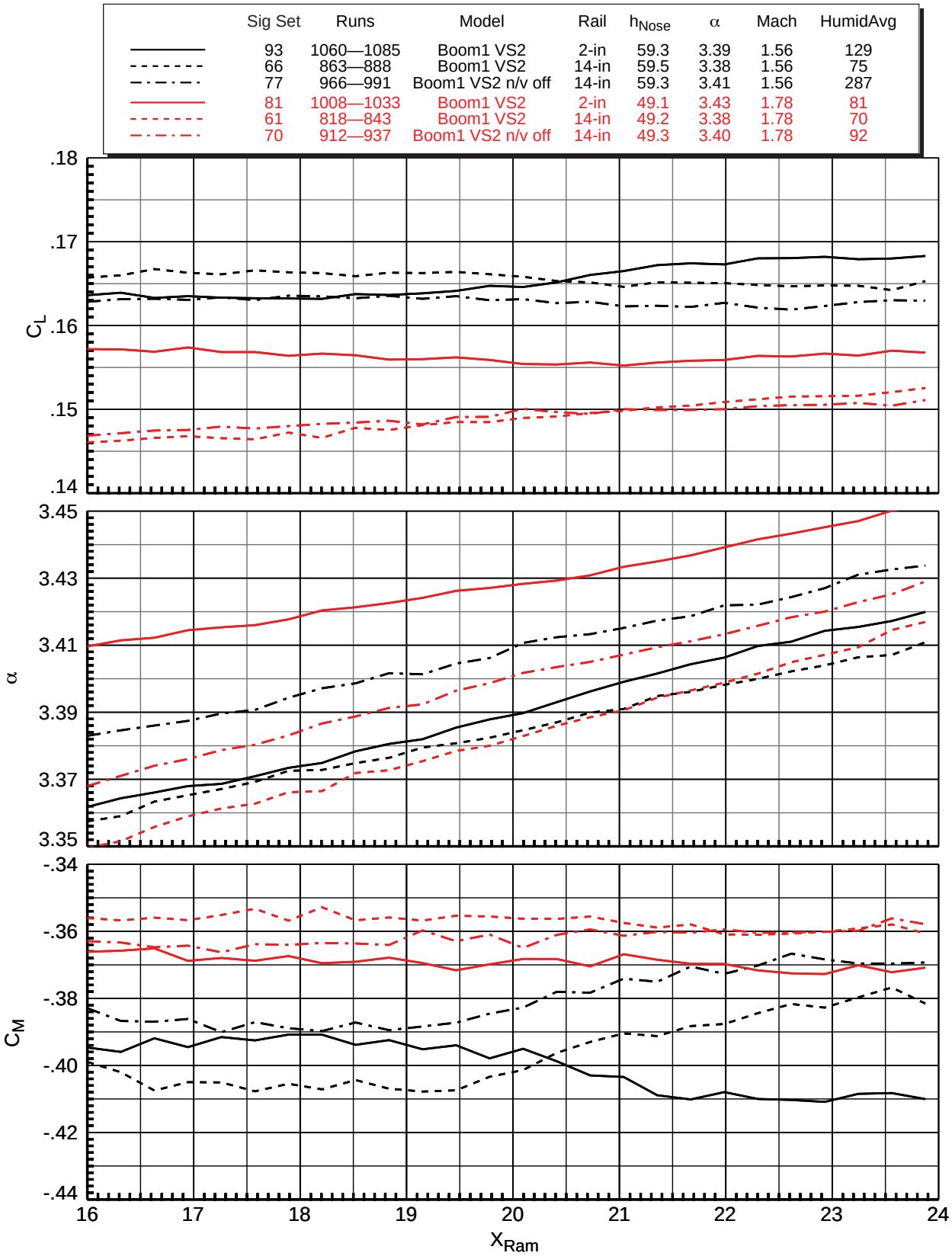

Figure 6–5. Boom1 VS2 model lift, angle of attack, and pitching moment variations during *X* sweeps, 8x6 TBC3 test

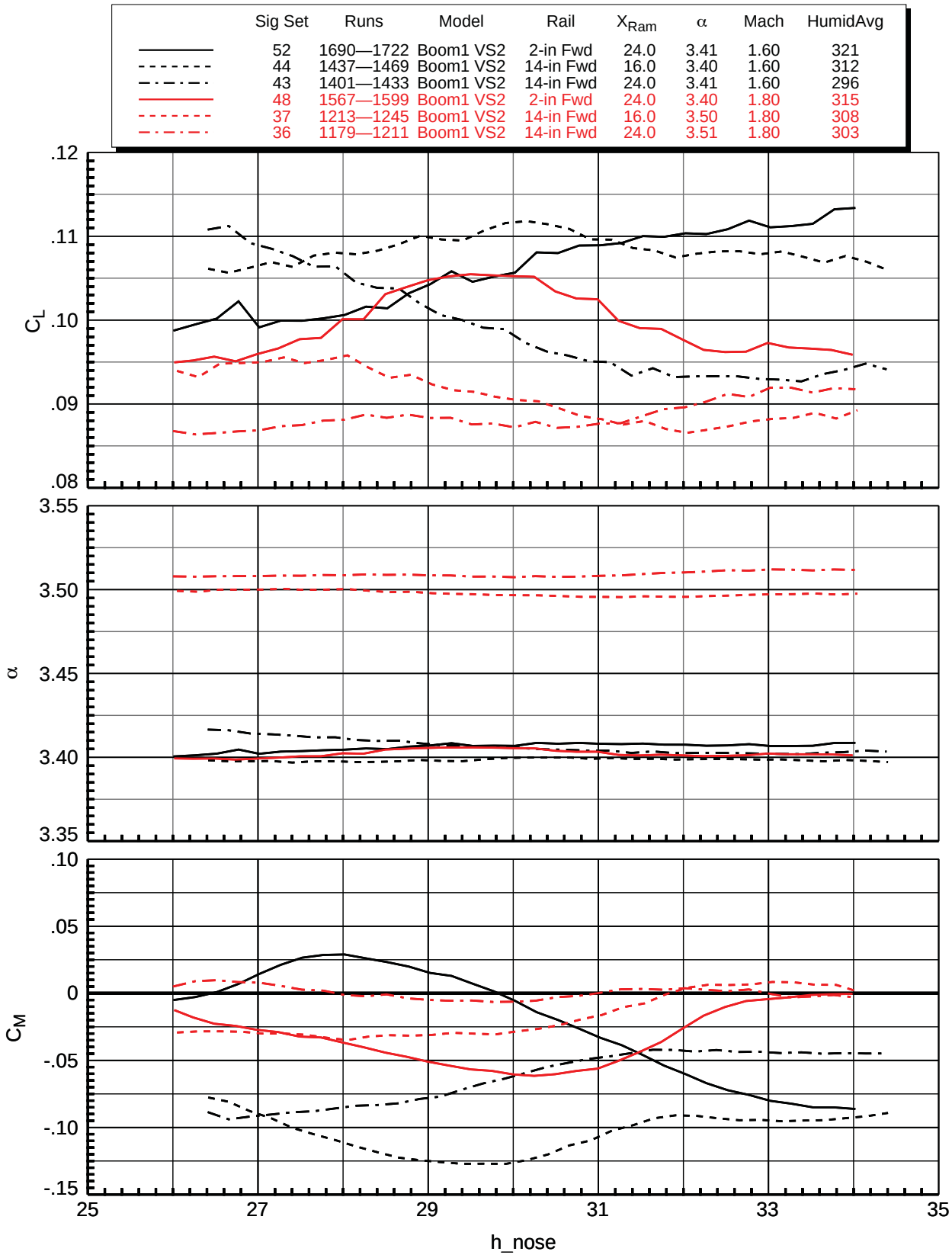

Figure 6–6. Boom1 VS2 model lift, angle of attack, and pitching moment variations during *Z* sweeps, 9x7 parametric test

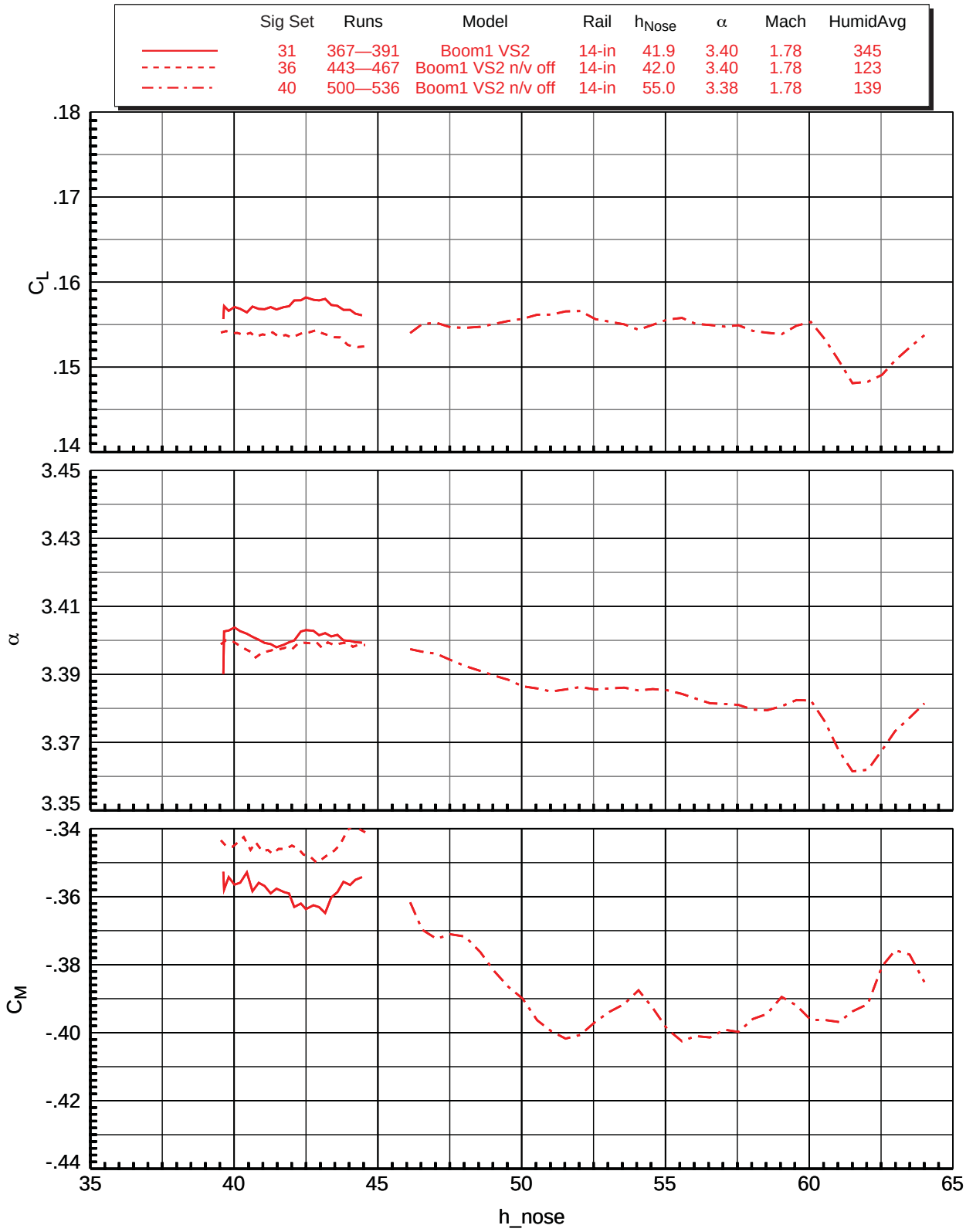

Figure 6–7. Boom1 VS2 model lift, angle of attack, and pitching moment variations during *Z* sweeps, 8x6 TBC3 test

What these variations in the model data during *X* or *Z* sweeps mean for the boom signature data is that not all of the signatures measured in a sweep are at constant model conditions, resulting in a somewhat incorrect averaging of the signature data. It is possible to reprocess the data using only those *X* or *Z* positions where the model conditions are fairly constant, but that has not been done as of the writing of this report, since it would reduce the number of signatures used in the average and could reduce data quality more so than any improvement due to consistent model and tunnel conditions.

6.2. Corrections for Reference Runs

The standard technique for acquiring sonic boom data using a pressure rail is to subtract a reference run from a data run, so that the difference yields only the model's signature and none of the ambient freestream signature from the tunnel flow. The reference run is taken in a "clean" tunnel, where the model shocks (if the model is present) are either off the rail or behind where they will be in the data run. Truly clean-tunnel runs can also be used, where the model and support components are physically out of the tunnel, but this is usually not necessary as long as the model shocks from the reference run do not overlap with those from the data run.

Model locations for typical reference and data runs in the 9x7 wind tunnel are illustrated in Figure 6–8, where the Boom1 VS2 model and test set up are shown schematically using an Excel-based layout diagram. The red model is in the reference run position (nose 52 in. above rail, alpha 3.4°, ram retracted), and its shocks (dashed lines drawn at the Mach line angle as an approximation) pass just behind the rail at the 14-in. height of the rail orifices above the wall. For the data runs (a sweep from X_{Ram} = 8 to 24 in.), the blue model is 30 in. above the rail at an alpha of 3.4°. Note that the model shocks for these data runs fall on the instrumented section of the rail—from tunnel station -84 to -116 in. It is clear from this figure that the data-run model shocks are far enough ahead of those from the reference run to produce valid measurements, given that in supersonic flow there is no appreciable influence ahead of a model leading shock wave, aside from miniscule influences that might feed forward through the thin boundary layer of the rail tip.

In contrast to the reference run for the small Boom model, the 43-in. Performance model is too long to acquire a reference run and leave enough room ahead of the nose shock for data runs to be acquired. Figure 6–9 shows a layout for this model with it positioned as far from the rail as possible (while leaving adequate clearance—at least 6 in.—between the model and the south wall of the tunnel, at the top of the figure), and even with the model tail shock aft of the rail orifices, the nose shock falls just 30-in. behind the first orifice on the rail. This clearly does not leave a sufficient length of uncontaminated orifices to get a clean signature for this model, so in the TBC4 test, reference runs were acquired at the beginning of the test without the model installed, each of the two Mach numbers, 1.6 & 1.8. A simple cone fairing was attached to the male taper at the front of the tunnel strut for these runs, which, with positioning away from the rail, assured that no shock waves from anything attached to the strut fell anywhere close to the rail.

A typical layout diagram for the Boom1 VS2 model in the 8x6 wind tunnel is shown in Figure 6–10. As stated in Section 3.2, the model was mounted upside down since the rail was mounted on the ceiling to allow use of the tunnel strut which translates up and down through the floor and pitches about a center of rotation below the floor. Throughout this report, the height of the model "above" the rail in the 8x6 is physically a vertical distance *upward* from the nose of the model to the rail tip. The rail position shown is the only position used in the 8x6 test; it was not moved to either a forward or aft position as it was in the 9x7 test. The rail position in the 8x6 tunnel was determined by assuring that the model shocks would fall on the rail when the model was positioned between the pair of downstream Schlieren windows in the side walls of the tunnel (refer to Figures 3–3 through –5).

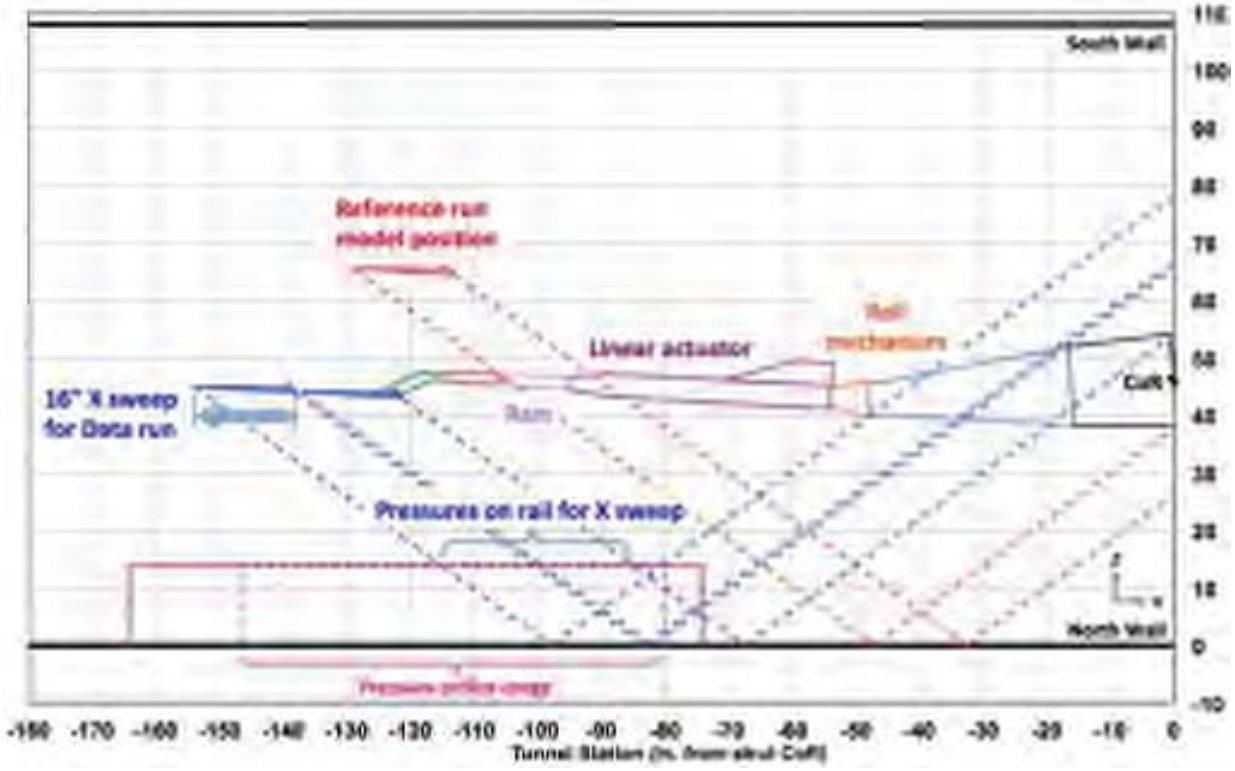

Figure 6–8. Layout of reference and data runs in 9x7 wind tunnel for Boom1 VS2 model (view as from floor of tunnel looking up)

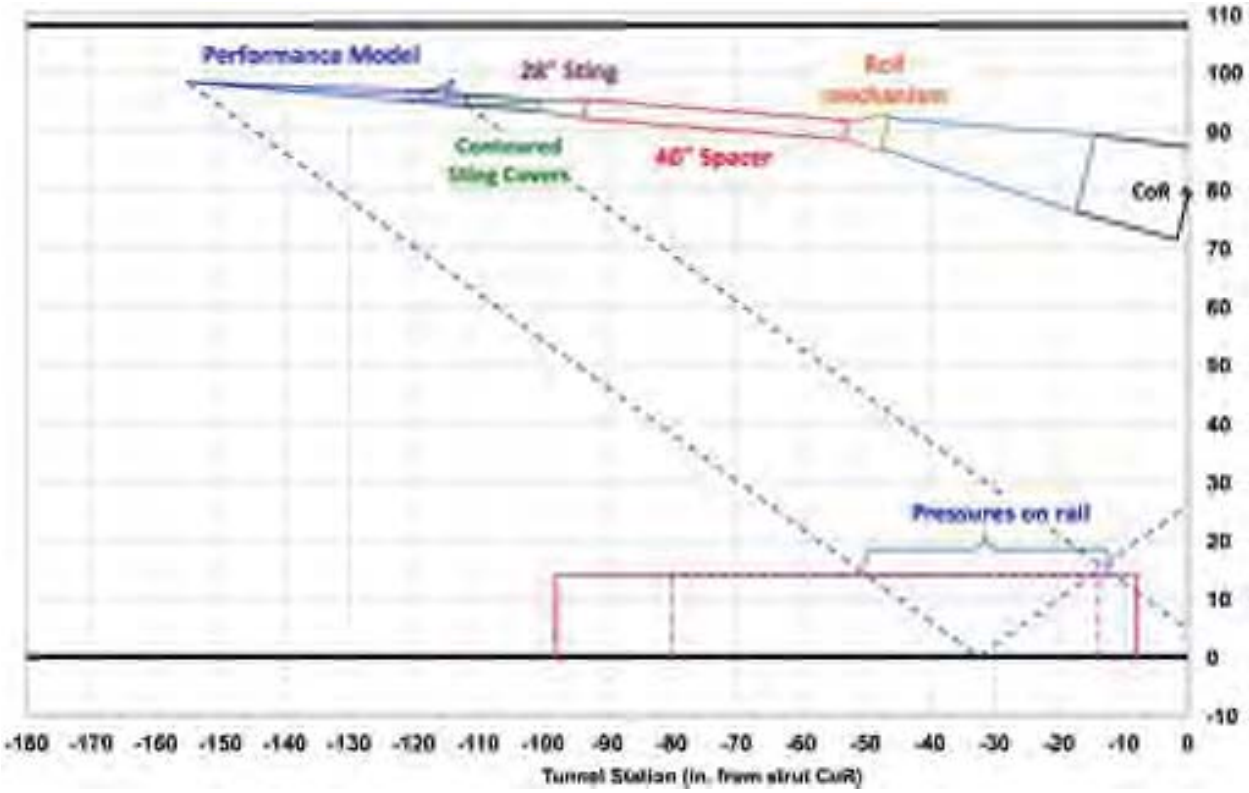

Figure 6–9. Layout of highest possible position of Performance model in 9x7 wind tunnel

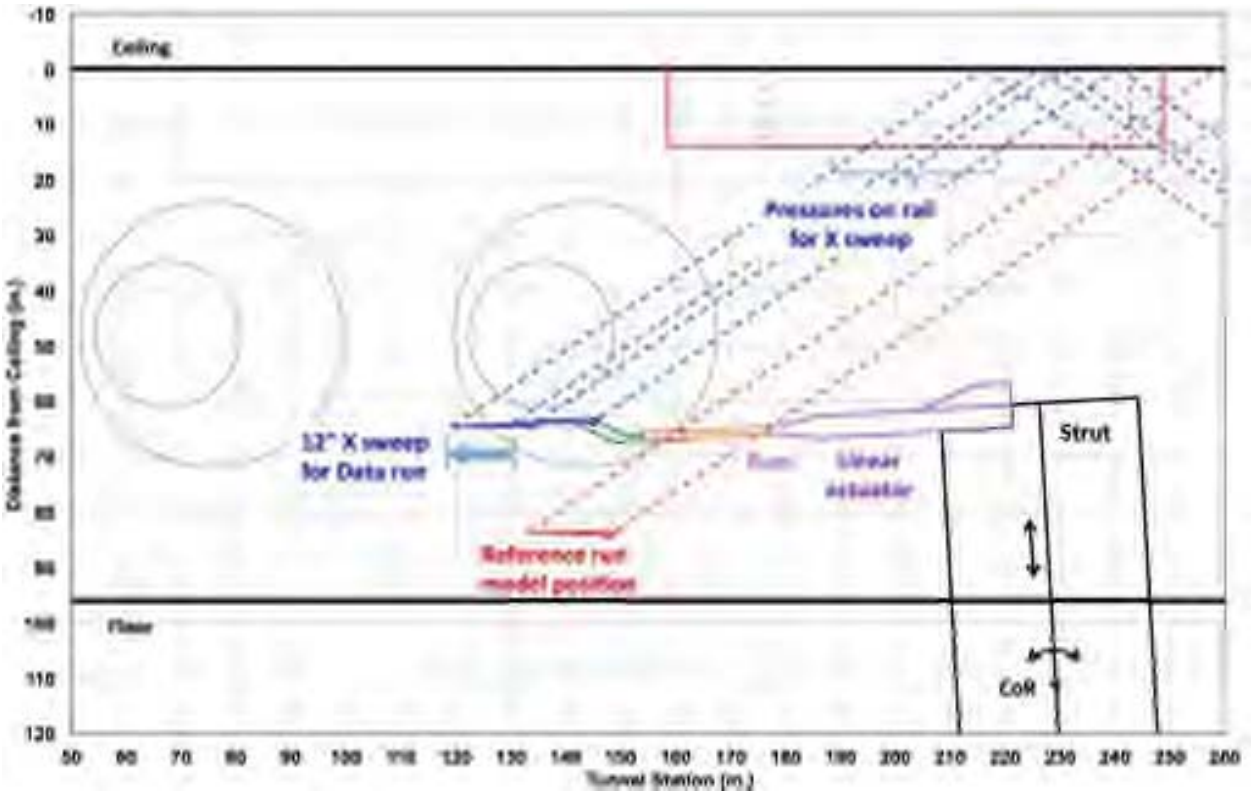

Figure 6–10. Layout of reference and data runs in 8x6 wind tunnel for Boom1 VS2 model

The reference run shown in the layout of Figure 6–10 is positioned as low as possible in order to keep the model shocks as far back as possible on the rail so that they would not interfere with the rail pressure measurements for the data run. A number of runs were acquired this way, but it was observed in the data that the reference run pressures were strongly dependent on the exposed height of the tunnel strut above the floor. The decision was therefore made to use in-line reference runs only; that is, the strut height for the reference run was selected to be at the same height as for the data run, even though there would likely be some signature overlap on the rail for the reference and data runs. This probably caused some compromise in data quality relative to using reference and data runs *without* any overlap, though it was not entirely clear in the data. Comparisons of various signatures from the 9x7 and 8x6 wind tunnels will be presented in the Experimental Results section.

Pressure signatures measured on the RF1 rail for the Boom1 model reference and data runs of the layout in Figure 6-8 are shown in Figure 6–11. In the top of the plot, the reference and data runs are plotted as $\Delta P/P$, where $\Delta P = P - P_\infty$, and the P in the denominator is P_∞. The red curve is the reference run, which is the tunnel's ambient pressure signature on the rail. The variance of the pressures over the length of the rail is due to the non-uniformity of the tunnel flow (including various facility shocks as discussed above) and the influence of the rail on the ambient flow as it passes over the 18-in. leading-edge section of the rail and establishes itself over the instrumented section. The black curve is the signature from a single data run (X_{Ram} = 8 in.), visible mostly in the region where the model shocks fall on the rail at tunnel stations approximately from -84 to -105 in. Where the black curve appears slightly separated from the red curve *ahead* of the model shocks is indicative of small temporal variations in the tunnel flow between the reference and data runs. The corrected pressure signature of the model is shown in the figure as the blue curve (offset in the plot by -0.04 in $\Delta P/P$ for clarity), obtained by subtracting the reference signature from the data signature.

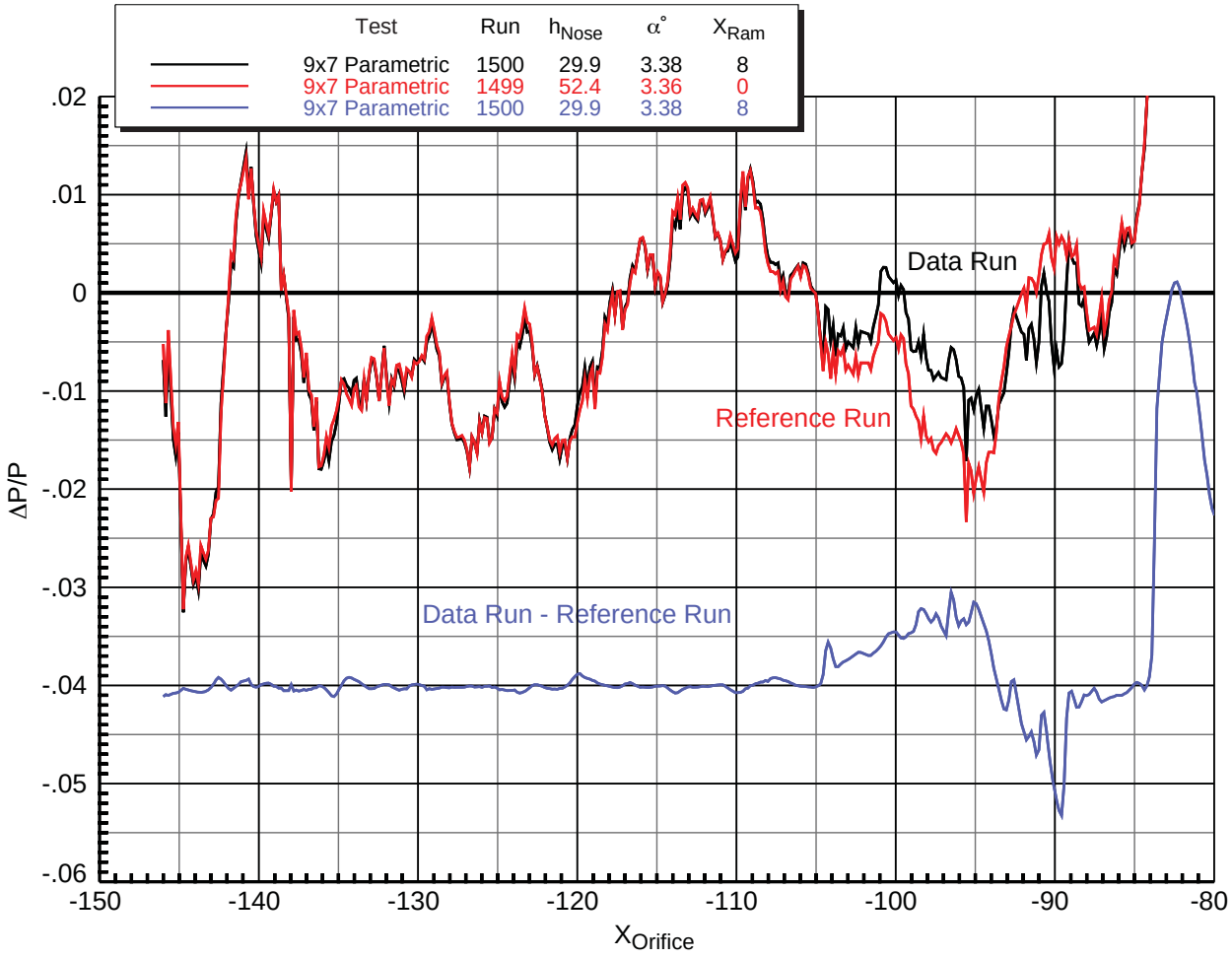

Figure 6–11. Differencing technique to isolate model pressure signature on the rail 9x7 Parametric test, Boom1 VS2 model, M = 1.60, P_T = 2292 psf, *HumidAvg* = 314 ppm

6.3. Test Technique Improvements

NASA and its NRA contract partners found that some changes employed in the current tests to some former test techniques resulted in improved accuracy and repeatability of the sonic boom pressure data. These changes included:

- Spatially average the data over limited model movements in the X or Z direction
- Operate the 9x7 tunnel at a higher total pressure (2300 psf) than in previous sonic boom tests
- Reduce the freestream humidity to less than 250 ppm and maintain within 4 ppm
- Position the model upstream of the leading edge shocks from the rails
- Optimize the sampling duration of the reference and data runs

Details of these changes and their effects on the data are discussed in the following sections.

6.3.1. Spatial Averaging and Error Analysis

The spatial averaging technique was developed to reduce the effect of tunnel flow field spatial distortions on the data at single model positions during supersonic wind tunnel testing.[4,5] In sonic boom testing in the 9x7 wind tunnel, the non-uniform flow field causes pressure signatures on the rail to be different for different model positions in the test section. To enable the spatial averaging technique, the model is typically translated a short distance longitudinally (*X* direction) or vertically (*Z* direction, away from the rail), and a number of sonic boom signatures are acquired at multiple positions as shown in the waterfall plot in Figure 6–12(a). The *X* locations at each point on the individual signatures need to be aligned in order to enable averaging of the signatures. For an *X* sweep, the *X* values of the rail orifice locations are aligned by simply adding the ram position, as shown in Figure 6–12(b):

$$X_{Aligned} = X_{Orif} + X_{Ram}$$

For a *Z* sweep, the *X* values of the rail orifice locations are adjusted by subtracting the height of the model nose at each *Z* position multiplied by the Mach number beta parameter:

$$X_{Aligned} = X_{Orif} - h_{Nose}\sqrt{M^2 - 1}$$

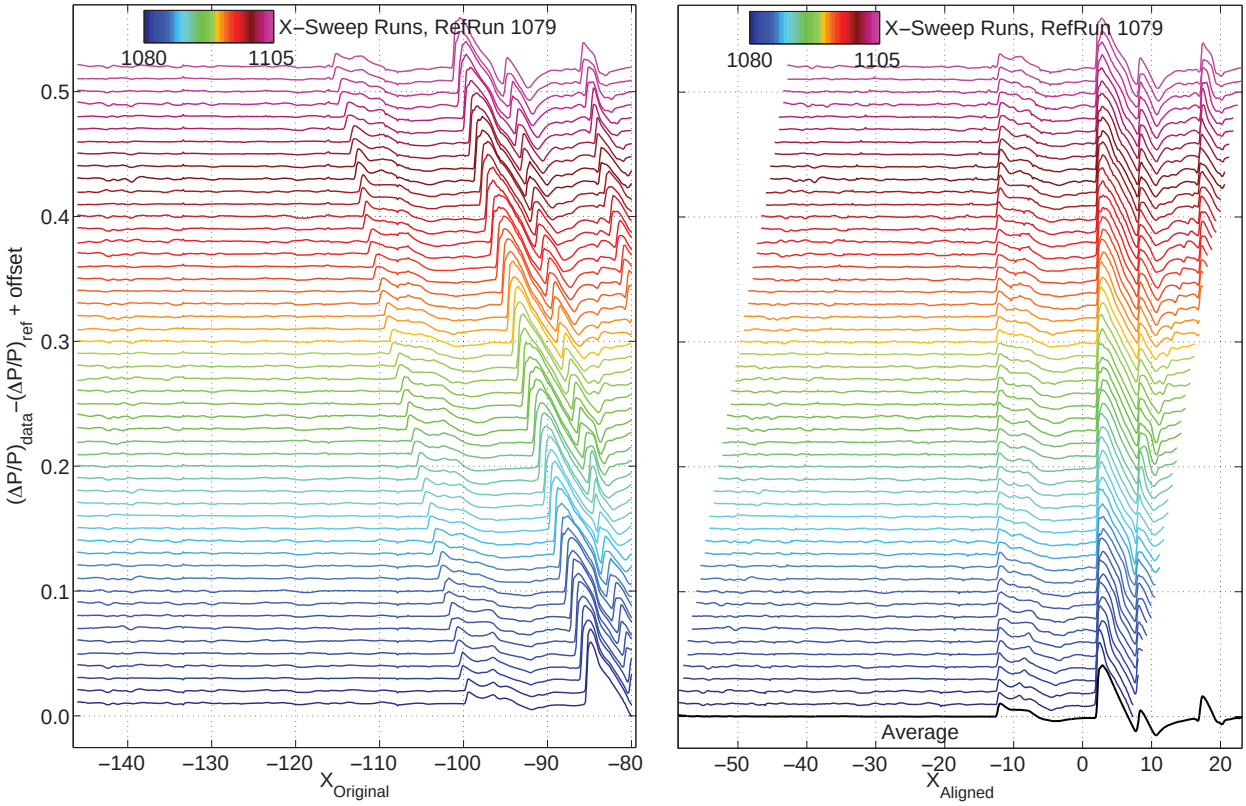

(a) Model signatures not aligned **(b) Model signatures aligned**

Figure 6–12. Non-aligned and aligned waterfall plots for 9x7 parametric test *X* sweeps for AS2 model

An individual signature after alignment is represented by the function $\overline{f}_i(X_{Aligned})$, and the grand averaged signature $\overline{\overline{f}}(X)$, is obtained by summing individual temporally averaged signatures, $\overline{f}_i(X_{Aligned})$, at each port X_{Orif} and dividing by *N*, the number of positions:

$$\overline{\overline{f}}(X) = \frac{\sum_{i=1}^{N} \overline{f}_i(X_{Aligned})}{N}$$

where

$$\overline{f_i}(X_{Aligned}) = \frac{\sum_{j=1}^{k_1} f_{ij}(X_{Orif})}{k_1} - \overline{f}_{Ref}(X_{Orif})$$

$$\overline{f}_{Ref}(X_{Orif}) = \frac{\sum_{j=1}^{k_2} f_{0j}(X_{Orif})}{k_2}$$

and

i is the counter for the ram positions
j is the counter for data point samples (acquired over the sampling duration)
f_i is the i^{th} temporal average at rail position X_{Orif}
X_{Ram} is the i^{th} position of the linear actuator
$\bar{f}_{ref}$ is the temporal average of the reference signature(s) f_{0j}
k_1, k_2 are the intervals of the temporal average for the data run signatures, f_i, and reference run signatures, f_{Ref}, respectively

Theoretically, the mean signature is obtained at each port where the shifted signatures align perfectly. In practice, interpolation is required between the port measurements on the rail to properly align the signatures with minimal setpoint error. Figure 6–12(b) shows aligned pressure signatures for the run series, which are the result of adjusting for the linear actuator position or X shift from the model nose height to each pressure signature.

To begin estimation of uncertainties for the spatial averaging technique, it is necessary to compute several components of variation from the test data. For the purpose of understanding the behavior of the test technique a relative uncertainty analysis is performed. This analysis is useful for the comparison of spatially averaged signatures and is not necessarily indicative of the total uncertainty of the final averaged signature.

Using the method described by Walker[41] for developing a dispersion relationship for equations with multiple levels of variation, the dispersion σ^2 of the grand averaged signature $\overline{\overline{f}}(x)$ can be written as

$$\sigma^2_{\overline{\overline{f}}(x)} = \frac{\sum_{i=1}^{N} \left[\sigma^2_{sp} + \sigma^2_{\overline{f}_i(X_{Orif})} + \sigma^2_{\overline{f}_{ref}(X_{Orif})} \right]}{N}$$

where

$$\sigma^2_{sp} = \sigma^2_{ar} - \sigma^2_{\overline{f}_i(X_{Orif})}$$

$$\sigma^2_{ar} = \frac{1}{N} \sum_{i=1}^{N} \left[\overline{f}_i\left(X_{Orif}\right) - \overline{\overline{f}}(X) \right]^2$$

σ^2_{sp} is the spatial standard deviation of the i^{th} model position at rail position X_{Orif}

$\sigma^2_{\bar{f}_i(X_{Orif})}$ is the temporal standard deviation of the i^{th} model position at rail position X_{Orif}

$\sigma^2_{\bar{f}_{Ref}(X_{Orif})}$ is the temporal standard deviation of the reference run at rail position X_{Orif}

σ^2_{ar} is the spatial standard deviation *across runs* of the i^{th} model position at rail position X_{Orif}, where a run is a measurement of rail pressures at a given model position i

The reported uncertainty band applied to the grand mean sonic boom pressure signature is $2\sigma^2_{\bar{\bar{f}}(x)}$. Since the primary application of the uncertainty band was to compare signatures, no fossilized uncertainty (from tunnel or instrument calibration errors) was included in the uncertainty buildup. Some of the fossilized uncertainty due primarily to calibration of the pressure measurement devices may also be mitigated by subtraction of the reference signatures. At best, the uncertainty bands or intervals provided should be deemed to represent a minimum level of uncertainty. The interval is set to a width of four standard deviations with no statement of the associated distribution. This corresponds to 95 percent coverage for a normal distribution. However, given the low sample sizes for the experimental data it is best to not assume a distribution.

Some assumptions are made for the uncertainty calculations of the RF1 rail. It is assumed that the average performance of the ports across the rail are similar. While this may be a valid assumption, the experimental data show that different regions of the signature have different levels of variation. It is not known if these differences are caused by non-uniformities in the rail surface (unlikely) or just fixed non-uniformities in the tunnel flow in the vicinity of the rail (more likely). The uncertainty calculations currently do not include the variation due to reproducibility of the signature.[3]

Temporal variance is the variance of the reference run pressures (each reference run includes a number of 2-second points which are used in the reference uncertainty calculations) multiplied by the duration of the reference points. Spatial variance is the difference between the variance of the averaged data run and the average variance of the reference run data. The total variance is the data run variance divided by the number of points included in the run variance added to the reference run variance divided by the number of points. The square root of the total variance is taken to get the standard deviation, and multiplied by two, for the two-sigma uncertainty.

Figure 6–13 shows the temporal and spatial uncertainty components and the total composite uncertainty for the 9x7 and 8x6 wind tunnels, where σ is shown as *ΔP/P*. The center plot represents 8x6 data and the left and right plots are of the 9x7 data. Each of the three run series are shown with the *X* sweep data processed by the beginning reference runs (a; top) and the ending reference runs (b; bottom). The temporal uncertainties are almost the same for all three cases. These would be higher if computed from single runs or just a few runs each, but the data were averaged over 26 runs in each of the *X* sweeps. The spatial uncertainties increase substantially from left to right with height of the model above the rail (30, 49, and 60 in.), which makes sense because the pressure gradients are weaker at the greater distances from the model, and they have traveled through more of the wind tunnel turbulent flow field on their way to the rail. The total composite uncertainties for the three cases are fairly similar, though slightly higher for the 9x7 and definitely higher for the 60-in. model height case.

The computed uncertainty and/or the scatter observed among the individual pressure signatures computed with a given reference run are often used as figures of merit to determine the best reference run to use. Reference runs were usually taken just before and just after each series of data runs for an *X* or *Z* sweep. When deciding which reference run to use in forming the spatially averaged signature, the one with the least scatter or smallest average standard deviation over the entire signature is typically selected. Figure 6–14 shows the individual, average, and $\pm 1\sigma$ signatures for an AS2 model *X* sweep from runs

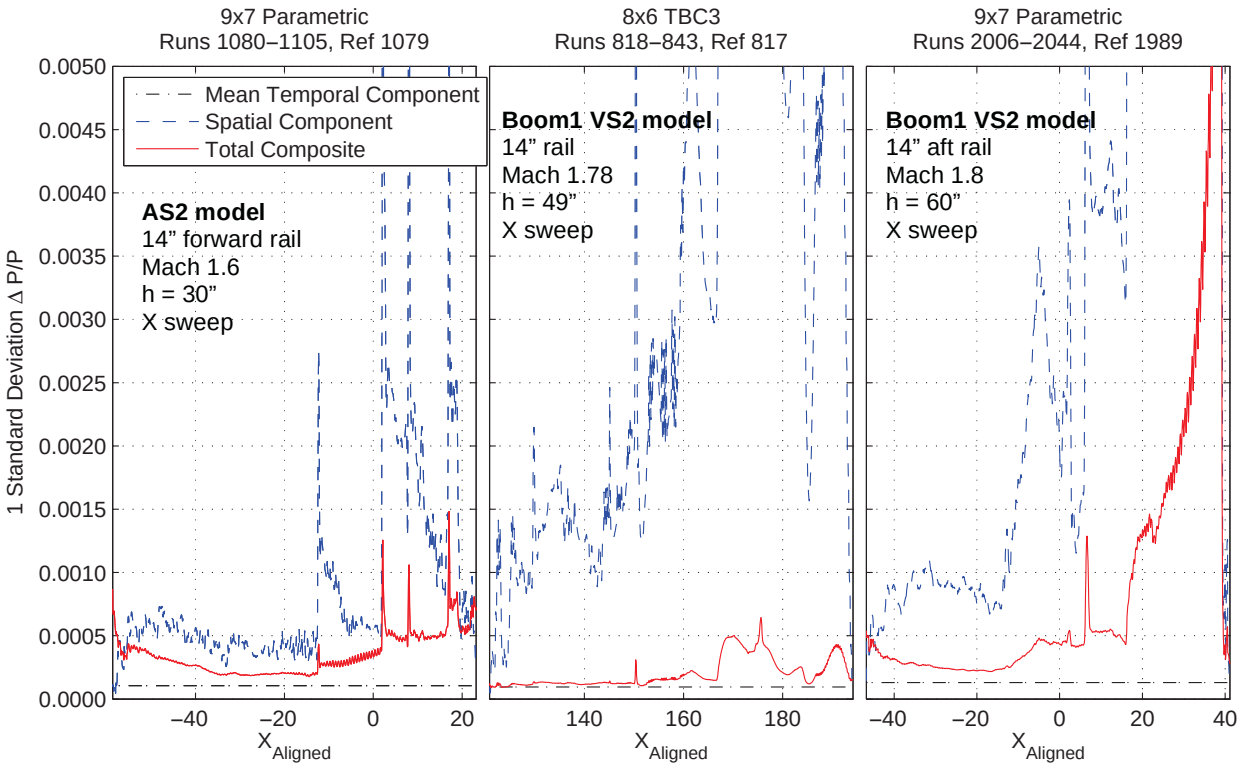

(a) Sweep data processed using *beginning* reference runs

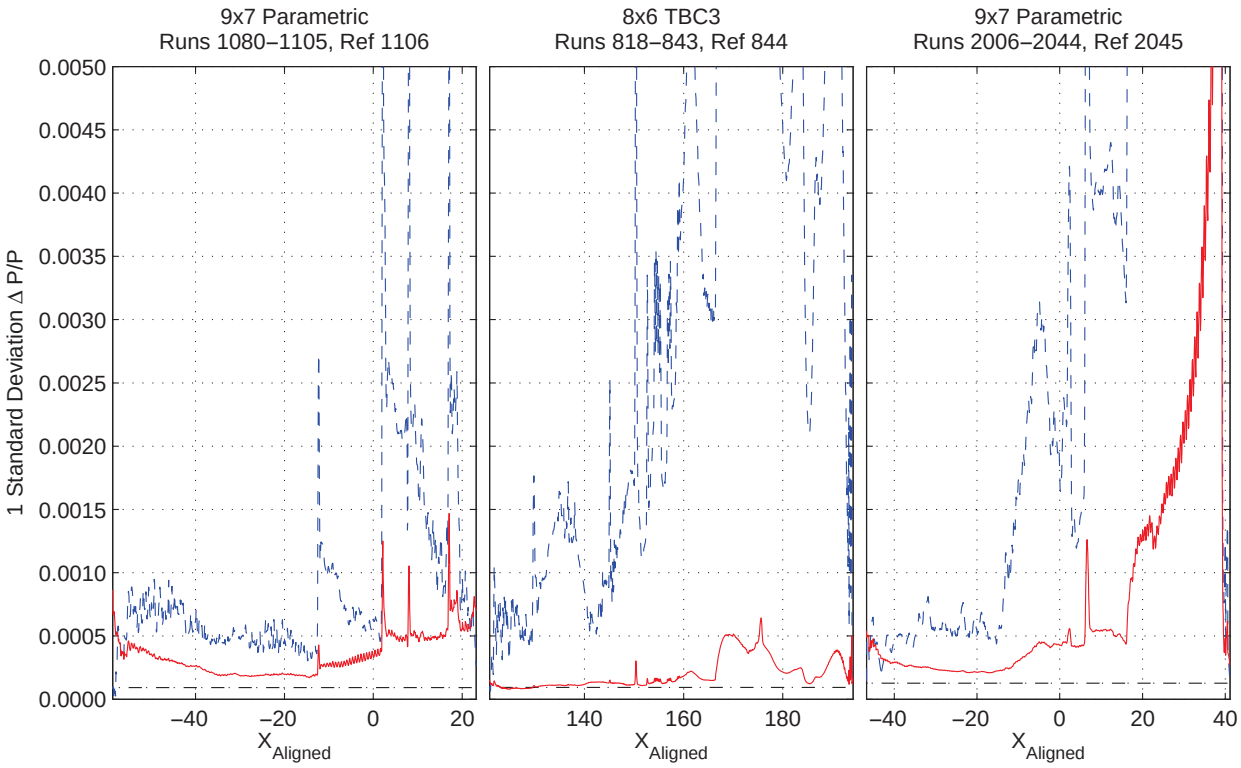

(b) Sweep data processed using *ending* reference runs

Figure 6–13. Temporal and spatial uncertainty for the 9x7 and 8x6 wind tunnels

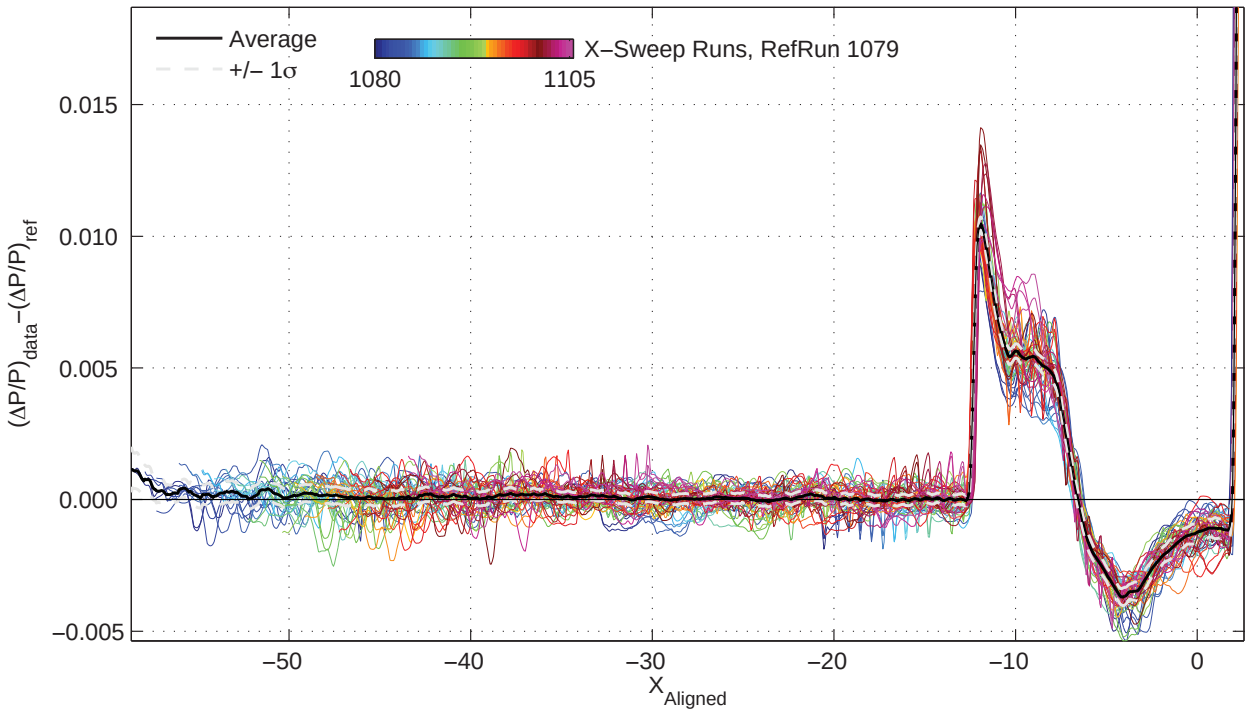

(a) Beginning reference run 1079

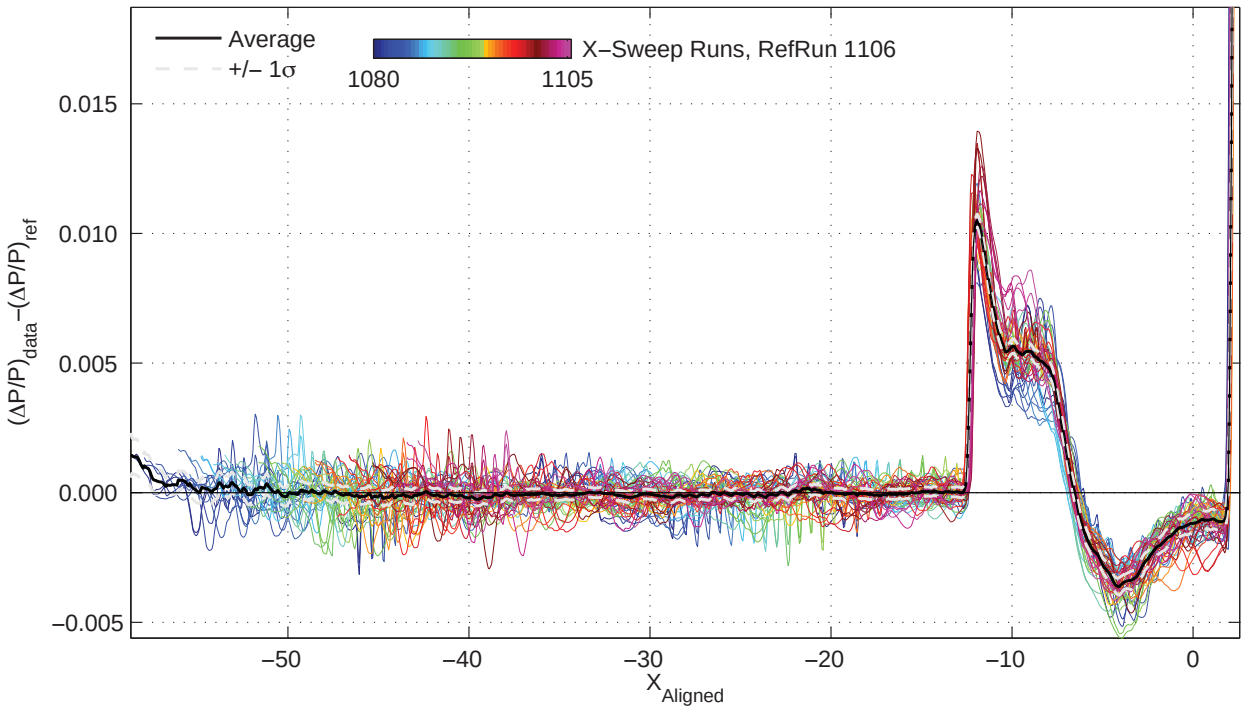

(b) Ending reference run 1106

Figure 6–14. Individual and averaged signatures for AS2 model runs 1010-1043 processed with either beginning or ending reference runs, 9x7 parametric test, 14-in. fwd rail, *M* = 1.6

1080 to 1105 of the 9x7 parametric test, where the signatures computed from the *before* reference run (1079) are shown in (a), and those computed from the *after* reference run (1106) are shown in (b). While the amount of scatter of the individual signatures, and the spread of the $\pm 1\sigma$ signatures around the average, appear to be about the same between the two plots, the average curve in (b) drops slightly below the $\Delta P/P = 0$ line well forward of the model nose shock, indicating that in this case, the *before* reference run is probably the better choice. This can be seen a little more clearly in Figure 6–15, where the plot of just the two averaged curves shows the separation in the leading zero points. Note, however, that the curves for the model signatures lie right on top of each other. A plot of the two reference runs, 1079 and 1106, by themselves is shown in Figure 6–16, and the differences between them are very slight, essentially insignificant. This was the case with most reference runs taken within a short period of time throughout the tests, with the exceptions being among those which were taken at substantially different humidity levels.

6.3.2. Tunnel Pressure

Operating the 9x7 wind tunnel slightly above atmospheric condition at a total pressure of 2300 psf rather than 1450 psf as was used in some earlier tests has significant advantages. At Mach 1.6 a higher Reynolds number per foot of 4.5×10^6 is obtained compared with 2.8×10^6 at 1450 psf. Testing at a higher Reynolds number reduces the likelihood of flow separation from the model or blade mounting surfaces. Also, the settling time of the rail static pressures is reduced by nearly a factor of two compared with operation at 1450 psf. And operating at 2300 psf also reduces the quantity of dry (~50 ppm) high-pressure air needed to stabilize the humidity, and lower humidity levels are more easily obtained, thus reducing time to get on condition.

6.3.3. Humidity Levels

Maintaining a reasonably low humidity level for data and reference runs is of utmost importance to obtain high quality sonic boom data. Higher levels of humidity can cause rounding of the shocks in the signatures, shifts in the overall $\Delta P/P$ level, and also random variations in the pressure data. The effects of humidity on sonic boom single probe data as well as pressure rail data in a 2008 test in the 9x7 wind tunnel, and methods to correct for these effects, are discussed by Durston[1] and Cliff.[3] In sonic boom tests in the 9x7 since 2008, very dry high-pressure air has been pumped into the wind tunnel to reduce and stabilize the humidity levels. Typically, approximately 5 to 10 lbs/sec of dry air is continuously pumped into the tunnel via a single pipe exiting through the bottom of the wind tunnel strut and pointed downstream. Humidity levels in the tests reported herein have been set generally below 300 ppm by weight and stabilized to within about 4 ppm within each run series (between reference runs). This has resulted in significantly higher-quality data in that there are almost no variations of the pressures due to humidity differences.

6.3.4. Sampling Duration

Short-, medium-, and long-term variations in the wind tunnel flow cause temporal uncertainties in the measured signatures. In the present work, short-term is defined as the time required to take one data point (aka one “sequence” in Ames wind tunnels), which is often just one or two seconds, but longer if more temporal averaging is desired. Medium-term is defined here as periods of minutes, in which multiple data points are taken, and large-scale flow structures or turbulence have had a chance to move around the wind tunnel circuit at least several times. Long-term refers to intervals of hours or days, where a repeat run may be taken after completing several run series, model changes, and/or tunnel stops and starts since the

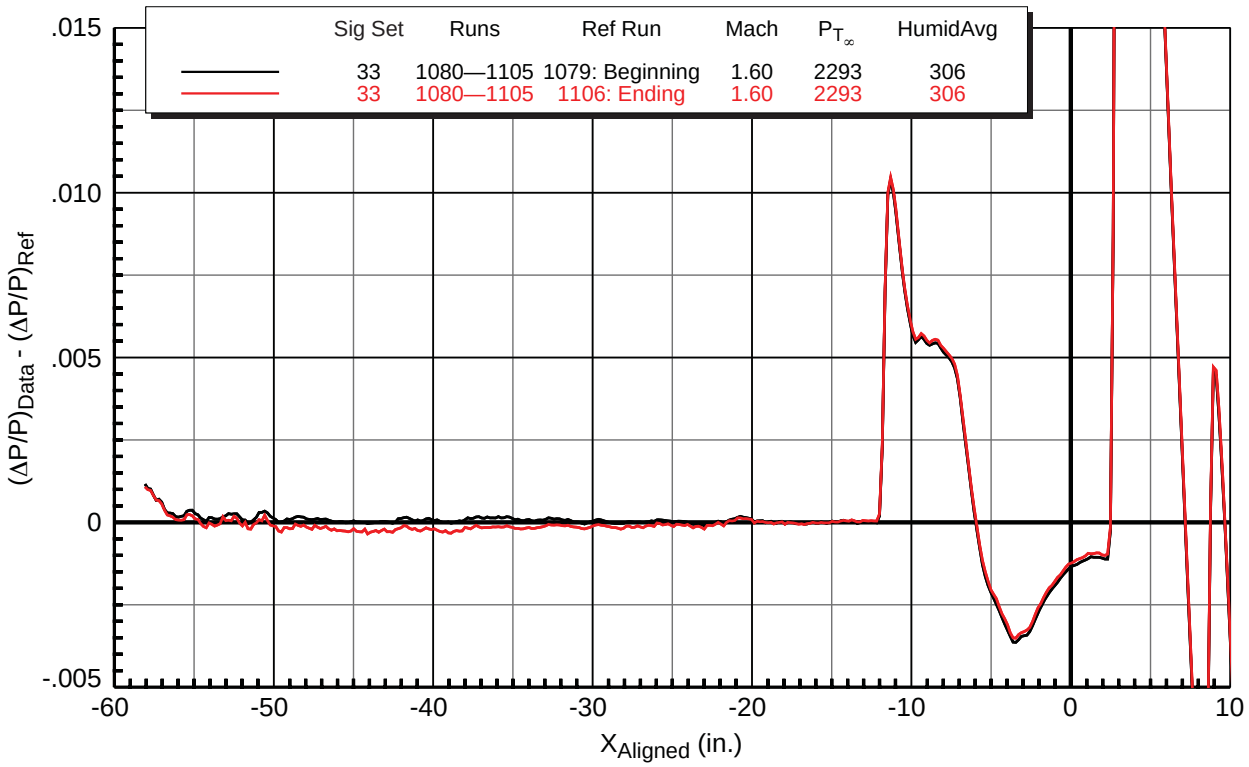

Figure 6–15. Averaged signatures for runs 1080 to 1105 processed with beginning and ending reference runs. 9x7 Parametric test, AS2 model, 14-in. forward rail, M = 1.60, α = 0°, h_{Nose} = 30 in.

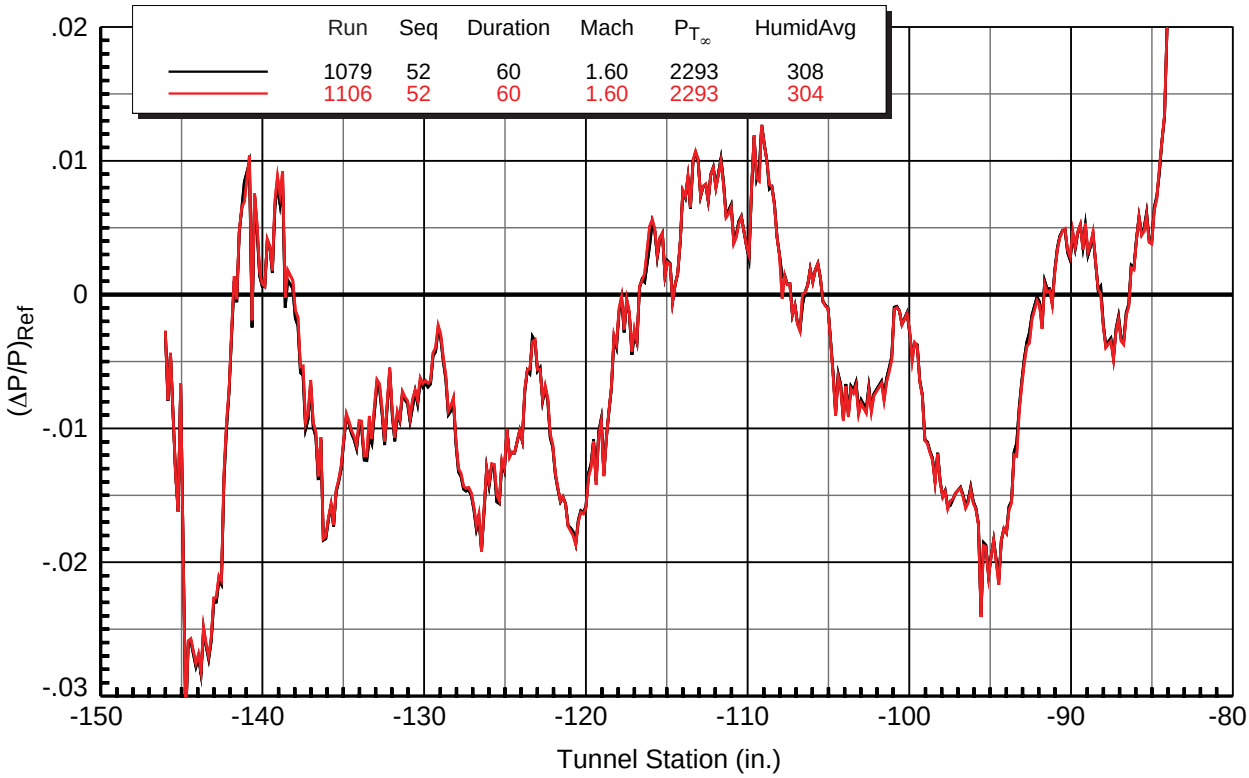

Figure 6–16. Beginning and ending reference run comparisons for run series 1080 to 1105 9x7 Parametric test, AS2 model, 14-in. forward rail, M = 1.60, α = 0°, h_{Nose} = 50 in.

original run being repeated was acquired. The present discussion regarding sampling duration pertains to the short- and medium-term flow variations only.

The spatial averaging technique described above helps to reduce the uncertainties due to the long-term variations by having multiple signatures acquired over a period of five or ten minutes. For each individual signature (one "run" as defined for the present studies), multiple data points are normally taken, each of which has its own sampling duration. In the series of sonic boom wind tunnel tests conducted for Boeing and Lockheed-Martin in support of their NRA contracts, various combinations of number of seconds of sampling duration per data point and number of data points per run were implemented during various *X* and *Z* sweeps and reference runs to determine which would give the best results while maintaining good productivity. Factors contributing to "best" results were 1) allowing sufficient lag time for the pressures passing through the tubing from the rail to settle at the measurement transducers, and 2) taking a number of data points over a specified time interval that could be averaged to give a final result for a run.

In the 9x7 parametric test in particular, a number of sampling studies were done, with reference run durations from 10 to 90 seconds and data run (for signature sweeps) sampling durations from 2 to 16 seconds. In the TBC3 test, durations of 16 seconds were used for both reference and data runs, allowing for 6 seconds of pressure lag in which data were not acquired and 10 seconds of data recording. In TBC4, durations of 8 seconds were used for most reference runs and all data runs, but the empty-tunnel reference runs acquired in the beginning of the test for the Performance model (including runs 116, Mach 1.8, and 119, Mach 1.6 used for the data plotted herein) had durations of 30 seconds. The sampling durations in each test eventually converged to those used in TBC4 as the best compromise between data quality and productivity.

7. Experimental Results

Selected experimental data from the Boeing AS2, Boom1, Boom3, and Performance models run in the 9x7 wind tunnel parametric and TBC4 tests and in the 8x6 wind tunnel TBC3 test are presented in this section. Sample composite plots of individual pressure signatures taken during *X* or *Z* sweeps and their resulting averages are given first to illustrate the averaging procedure. Then the remainder of the plots—up to but not including the reference run plots—consisting only of the *averaged signatures* will be shown to isolate various comparisons among the data, such as repeat runs, rail comparisons, *X* vs. *Z* sweeps, model variations, Mach effects, angle-of-attack effects, etc. Note that a "sig set" (signature set) number is included in the listing and in the legends of the plots—this is a sequential count of the *X* or *Z* sweeps (referring to a run range) within a test, and the sig set numbers were restarted at 1 for each test.

A listing of all of the run sweeps plotted in this section and the figure numbers in which they appear is given in Appendix A, and a listing of all of the reference runs plotted and the figure numbers in which they appear is given in Appendix B.

7.1. Composite Plots of *X*- and *Z*-Sweep Individual and Averaged Signatures

Sample composite plots of selected *X* and *Z* sweeps for three Boeing models (AS2, Boom1, and Performance) are shown in Figures 7–1 through –5. Each composite plot consists of four plots: an aligned waterfall plot (upper left) showing individual pressure signatures (offset in small $\Delta P/P$ increments, in various colors) obtained within a sweep, along with the spatially-averaged signature (in black, at the bottom); a similar plot of the individual and averaged signatures but collapsed to the same $\Delta P/P$ scale (lower left); a zoomed-in plot of just the average model signature (lower right); and a small layout diagram showing the reference and sweep positions for the model (upper right). Average values and ranges of the model parameters for the sweep represented by the plots are given in the table at the top of each plot.

The waterfall plots are shown after alignment of the signatures. Prior to alignment, the ends of the signatures line up vertically in the waterfall plot (as in Figure 6–12(a); representing the first and last orifices on the rail at their fixed *X* positions in the tunnel), and the locations of the model shocks vary throughout the sweep. The alignment allows the signatures to be averaged together, but note that the ends of the averaged signature do not use all of the individual signatures in computing the average because of the forward-sweeping (in viewing from bottom to top) signature edges in the aligned waterfall plot. The goal in the testing was to keep the model shocks far enough from the ends of the rail orifices so that as many as possible, if not all, of the signatures in the sweep could be used in the average. This was generally easy to do for the smaller models, but the large 43-in.-long Performance model required careful planning to make sure its signature was sufficiently centered on the rail. The dynamic layout diagrams shown on these composite plots and in Figures 6–8 through –10 were created in Excel by the author to permit the researchers to estimate shock locations on the rail for any given model and position in the tunnel.

The variation of the corrected pressures from one model position to the next can be seen in the waterfall plot (albeit at a very compressed vertical scale). These variations are seen at their normal scale in the plot below the waterfall plot. The ambient flow upstream of the wind tunnel model should produce a pressure signature of exactly zero as a result of subtracting the reference run from the data run. The cause of these corrected pressures not being zero is due to temporal variations in the wind tunnel flow between the reference and data runs. The flatness of these "leading zero" pressures upstream of the model is a good indication of the quality of the pressure signature of the model—if the tunnel flow variations are small enough that these leading zero pressures are close to zero, then the temporal effects

on the model signature will be slight. Other contributors to errors in the model signature measurements are tunnel turbulence (temporal variations that are short term and small scale) and model vibration. Also, the discrete spacing (4 mm) of the pressure taps on the rail can lead to rounding of the model signatures if the shock peaks mostly fell between the rail orifices during the sweeps.

Figure 7–1 shows the experimental pressures for the AS2 model from the 9x7 parametric test 97-0250 for the run series 1010–1043. A *Z* sweep was conducted in this series, consisting of an 8-in. vertical traverse with 0.25-in. spacing in the *Z* direction (roughly equivalent to 2-orifice, 0.31-in., spacing in *X*). Within the whole range of rail pressures shown, the AS2 model pressure signature runs from the first shock wave at approximately $X = -12$, followed by a short flat region, then a recovery at negative $\Delta P/P$ and back to ambient pressure at $X = 2$, before the large shock wave from the balance adapter aft of that point. The signatures show slight pressure variations at each *Z* position in the tunnel due to non-uniformities in the tunnel flow, and some of these can be identified by small bumps or spikes in the signatures at constant orifice locations on the rail.

Figure 7–2 shows the aligned pressure signatures for an *X* sweep from the 8x6 TBC3 test, in run series 1162–1187, consisting of an 8-in. horizontal traverse with 0.31-in. (2 orifices) spacing. Note that with this *X* sweep, the ends of the signatures in the waterfall plot sweep *aft* from the bottom to the top, in contrast to the *forward*-swept edges of the *Z* sweep in the previous figure. As model height above the rail is increased, the model shocks move *aft* on the rail, whereas in an *X* sweep, the model shocks move *forward* on the rail, and the alignment process shifts the edges of the signatures on the waterfall plots in the opposite direction to get the model shocks to line up at constant *X* values.

The portion of the rail pressures showing the AS2 model signature is from approximately $X = 143$ to 155 (the *X* values are different for the 8x6 wind tunnel because the origin is at the forward end of the test section). The model signature in this figure looks similar to that in the previous figure, though the flat region behind the nose shock is lower in magnitude, primarily because the model is twice as far from the rail (60 in. vs. 30 in.).

Composite signature plots for the Boom1 and Boom3 models in the 97p and TBC4 tests are shown in Figures 7–3 and –4, respectively. Note that the entire Boom1 model signature ($X = -15$ to 7) was captured for every position in the *X* sweep in Figure 7–3, allowing a number of leading zero points before the start of the model signature at approximately $X = -12$, but in Figure 7–4 the front of the model signature was not even captured until higher in the *Z* sweep. This caused enough smearing of the model nose shock that it is not even recognizable in the averaged signature, rendering this data set unusable as a full signature. This run series was chosen to show here to illustrate the importance of positioning the model properly in the wind tunnel in order to acquire usable signatures. It is likely that this position was believed to be acceptable at the time of the running, but the missing front of the signature was noticed only after the data were taken.

Performance model data from the 9x7 TBC4 test are shown in Figure 7–5. These data are at a nominal height of 60 in., and the model signature covers an *X* range from approximately -32 to 15. Significant variations among the individual signatures are evident in the waterfall plot, and the average curves show some unexpected undulations between the nose shock and the highest peak from the wing shock. These are most likely the result of the large (60-in.) distance from the model to the rail. The spatial and temporal tunnel flow irregularities affect the shock wave patterns coming from the model to the rail, and make it difficult to consistently acquire high-quality data at these distances.

X_{ram}, in	h, in	h/L
16.00 (16.00–16.00)	30.02 (26.02–34.01)	1.61 (1.40–1.83)
α, deg	β, deg	ϕ, deg
0.04 (0.04–0.04)	0.01 (0.01–0.01)	–0.15 (–0.18– –0.13)
C_L	C_D	C_M
0.006 (–0.003–0.010)	0.04470 (0.04180–0.04972)	–0.021 (–0.052–0.047)

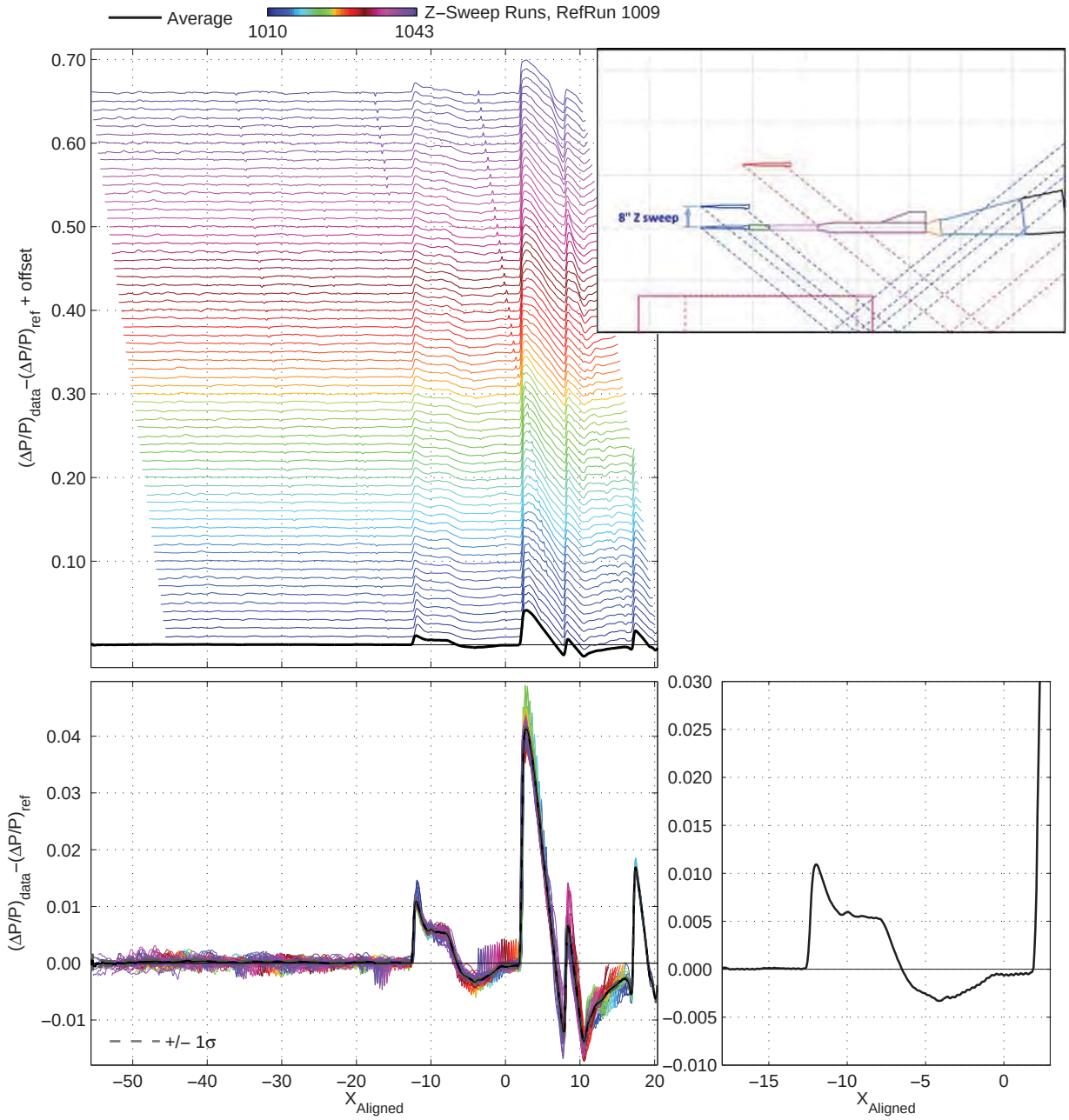

Figure 7–1. AS2 model aligned waterfall plot and averaged signature plots for *Z* sweep from 26” to 34” at X_{Ram} = 16 in., 9x7 parametric test, *M* = 1.6, 14-in. forward rail

X_{ram}, in	h, in	h/L
19.94 (16.00–23.88)	59.15 (59.12–59.18)	3.76 (3.75–3.76)
α, deg	β, deg	ϕ, deg
–0.02 (–0.04–0.00)	0.00 (0.00–0.00)	0.00 (0.00–0.00)
C_L	C_D	C_M
0.070 (0.069–0.071)	0.03953 (0.03933–0.03986)	0.130 (0.129–0.132)

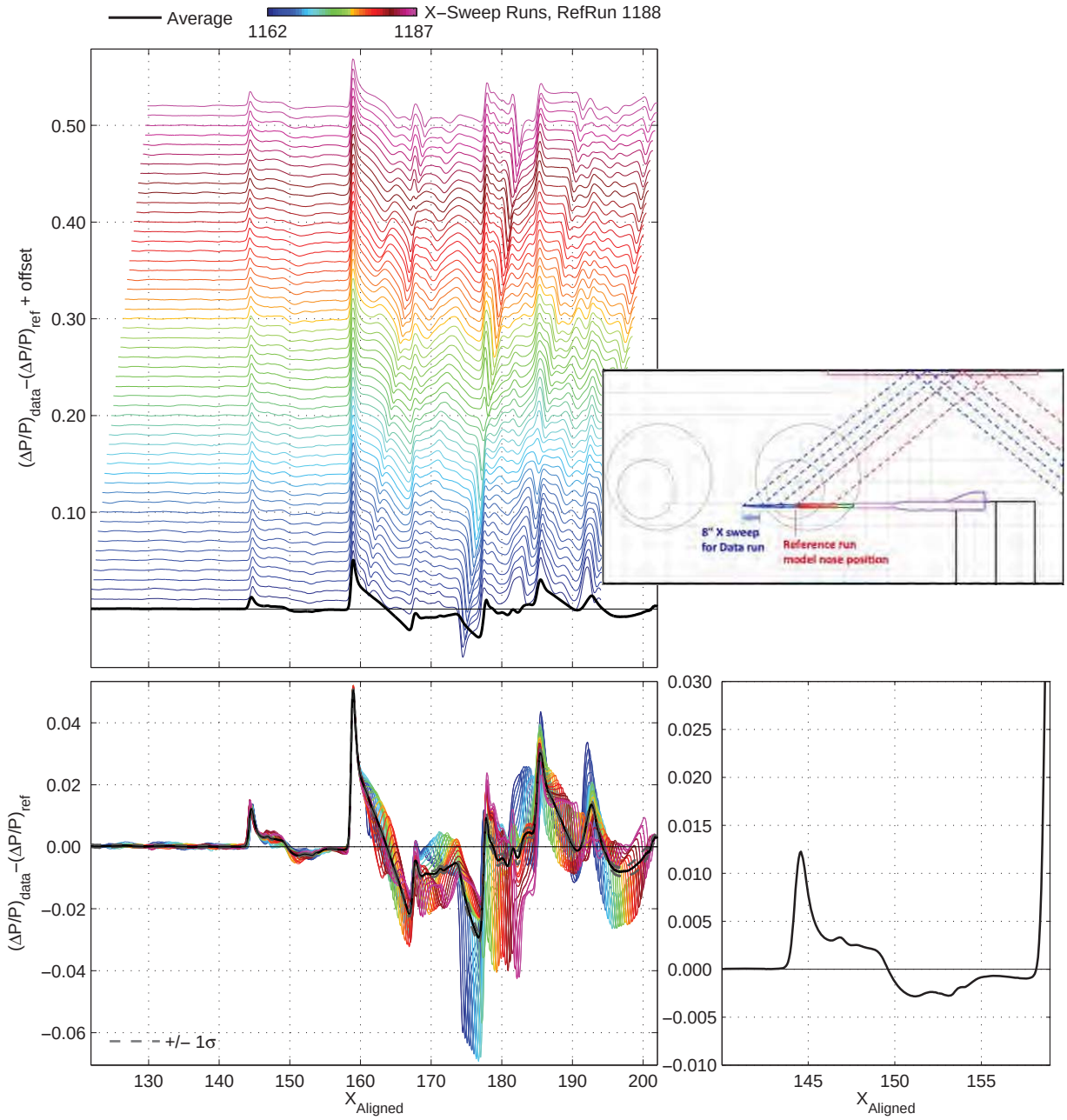

Figure 7–2. AS2 model aligned waterfall plot and averaged signature plots for *X* sweep from 0" to 8" at h_{Nose} = 59 in., 8x6 TBC3 test, *M* = 1.56, 2-in. rail

X_{ram}, in	h, in	h/L
7.87 (–0.00–15.75)	59.59 (59.10–60.08)	3.78 (3.75–3.82)
α, deg	β, deg	ϕ, deg
3.40 (3.38–3.42)	0.21 (0.20–0.22)	0.39 (0.34–0.43)
C_L	C_D	C_M
0.100 (0.090–0.104)	0.07165 (0.06711–0.07379)	–0.019 (–0.028–0.000)

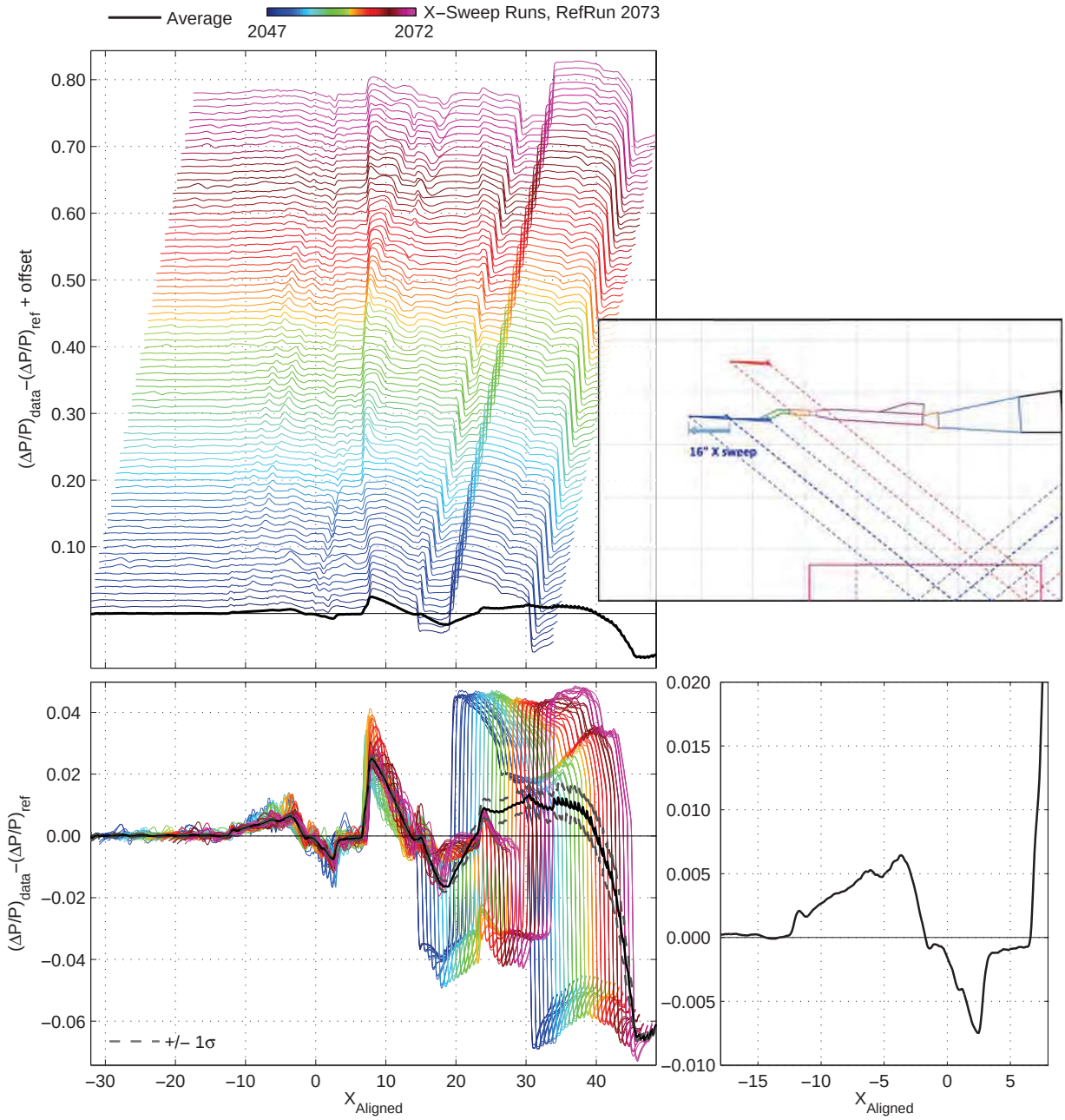

Figure 7–3. Boom1 VS2 model aligned waterfall plot and averaged signature plots for *X* sweep from 0" to 16" at h_{Nose} = 60 in., 9x7 parametric test, *M* = 1.6, 14-in. aft rail

X_{ram}, in	h, in	h/L
(–)	61.66 (58.63–64.69)	3.92 (3.72–4.11)
α, deg	β, deg	ϕ, deg
2.57 (2.55–2.57)	0.23 (0.23–0.23)	0.19 (0.18–0.20)
C_L	C_D	C_M
0.060 (0.054–0.065)	0.06502 (0.06397–0.06554)	0.005 (–0.010–0.028)

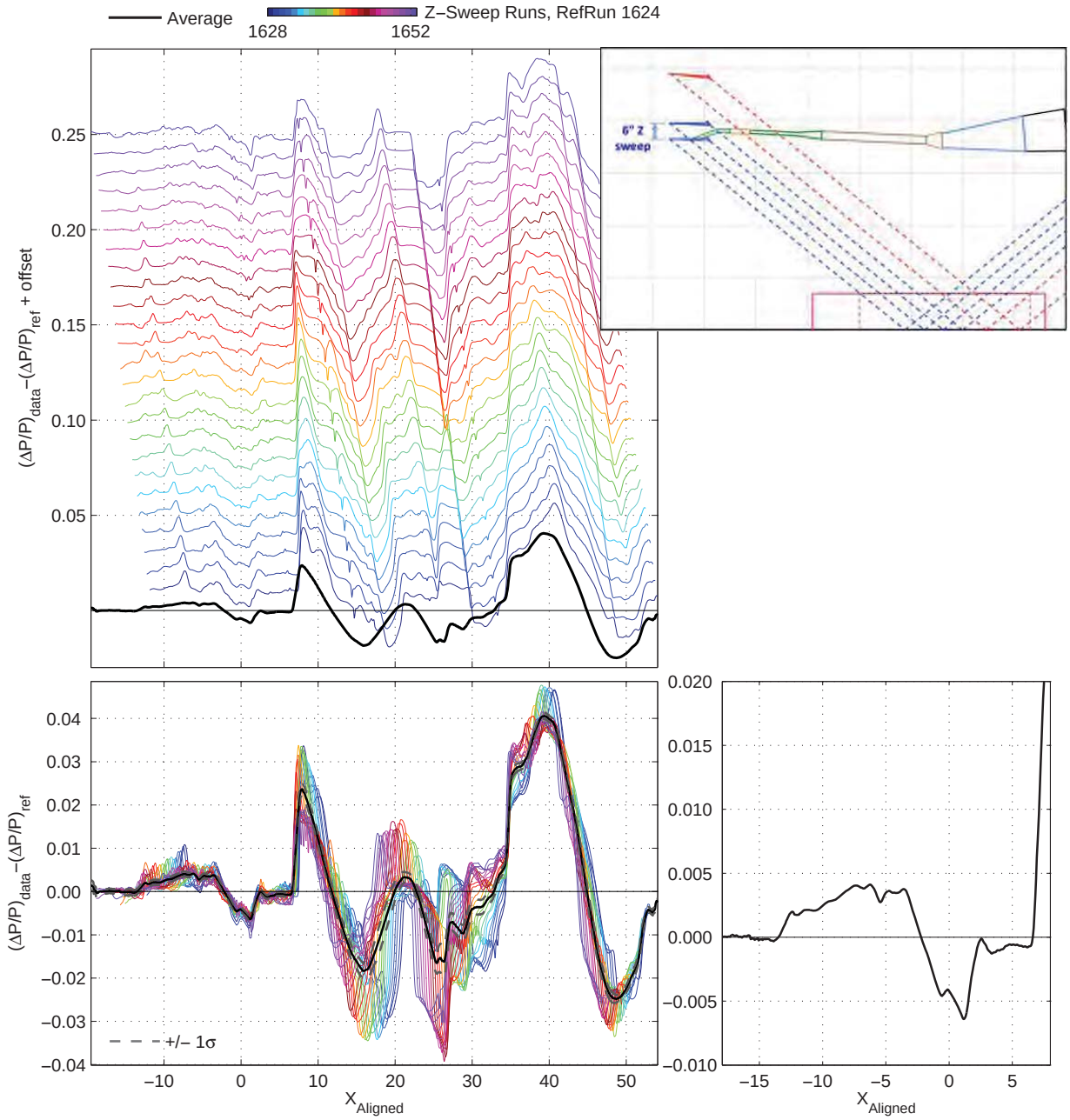

Figure 7–4. Boom3 VS3 model aligned waterfall plot and averaged signature plots for *Z* sweep from 59" to 65", 9x7 TBC4 test, *M* = 1.6, 14-in. aft rail

X_{ram}, in (–)	h, in 60.87 (57.87–63.88)	h/L 1.41 (1.34–1.48)
α, deg 3.40 (3.39–3.40)	β, deg –0.19 (–0.20– –0.19)	ϕ, deg 45.46 (45.03–45.85)
C_L 0.064 (0.063–0.066)	C_D 0.01109 (0.01044–0.01166)	C_M –0.014 (–0.014– –0.014)

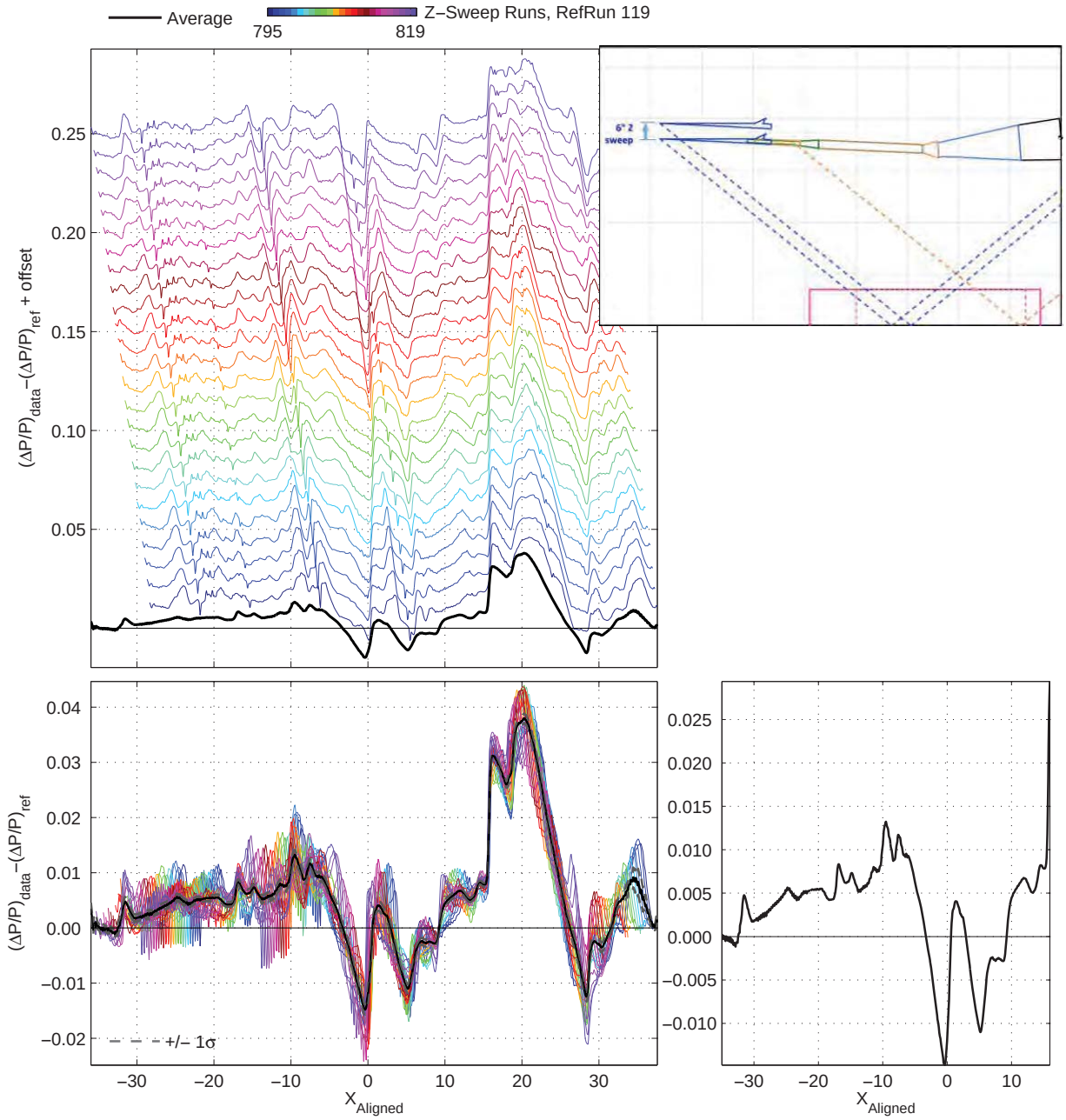

Figure 7–5. Performance model aligned waterfall plot and averaged signature plots for *Z* sweep from 59” to 65”, 9x7 TBC4 test, *M* = 1.6, 14-in. aft rail

7.2. Repeatability

The plots in the remainder of the report showing experimental model signature data will now consist only of the *spatially averaged* pressure signatures, as opposed to those of the previous subsection which included the individual signatures that were used to generate the average. It should be noted that the Mach, total pressure, and humidity values in the second title lines of each of the following plots are the *average* values of those parameters for all of the runs shown in the plots. On plots where these parameters vary among the runs, the plot legends will show those values for each set of runs.

Short-term repeatability of signature measurements for several models in the 9x7 tests are shown in Figures 7–6 through –9. (Long-term repeat runs were not acquired because of limitations on test time.) Back-to-back *Z* sweeps followed by *X* sweeps from the 9x7 parametric test for the AS2 model at heights of 30 and 31.8 in. are shown in Figure 7–6, where the four signatures are almost identical except for a roughly 10% difference in the $\Delta P/P$ levels in the flat part of the signatures behind the nose shock. This difference could be due to the slight differences in model height or due to the type of sweep (more on these effects later), but considering the variation in individual signatures seen in Figures 7–1 and –2, it could also be considered within the scatter of the data. Boom1 VS2 model signatures in Figure 7–7 show similar very good repeatability.

Repeatability for various *Z* sweeps with the Performance model in the TBC4 test are shown in Figures 7–8 and –9. The agreement in the forward part of the signatures, aside from the nose shock, is quite good ahead of X = -65 in., but aft of that it is worse in the vicinity of wing, nacelle, and tail shocks (in particular, at X = -61, -55, and -41 in.), with differences up to ~0.0025 in $\Delta P/P$. Average humidity for the three runs is displayed in the legend to see if there is any correlation between any humidity differences and the data mismatches, but the trends are not consistent. The humidity for runs in sig set 2 is over 100 ppm higher than in the other sig sets, and yet it is sig set 4 that has the greatest deviations among the runs. (Average humidity differences between each pair of runs in Figures 7–6 and –7 were within 2 ppm, so humidity is likely not the cause of the slight differences in those repeat runs.)

The other comparison of repeat runs for the Performance model is shown in Figure 7–9. In these runs, the entire model signature was captured, and the repeatability is only slightly better than in the previous figure—there are several places with differences up to ~0.0020 in $\Delta P/P$. The deviations in both of these plots are probably a fair representation of the repeatability that can be expected for sonic boom measurements in the 9x7, and are most likely due to model fluctuations or variations in tunnel flow conditions over time.

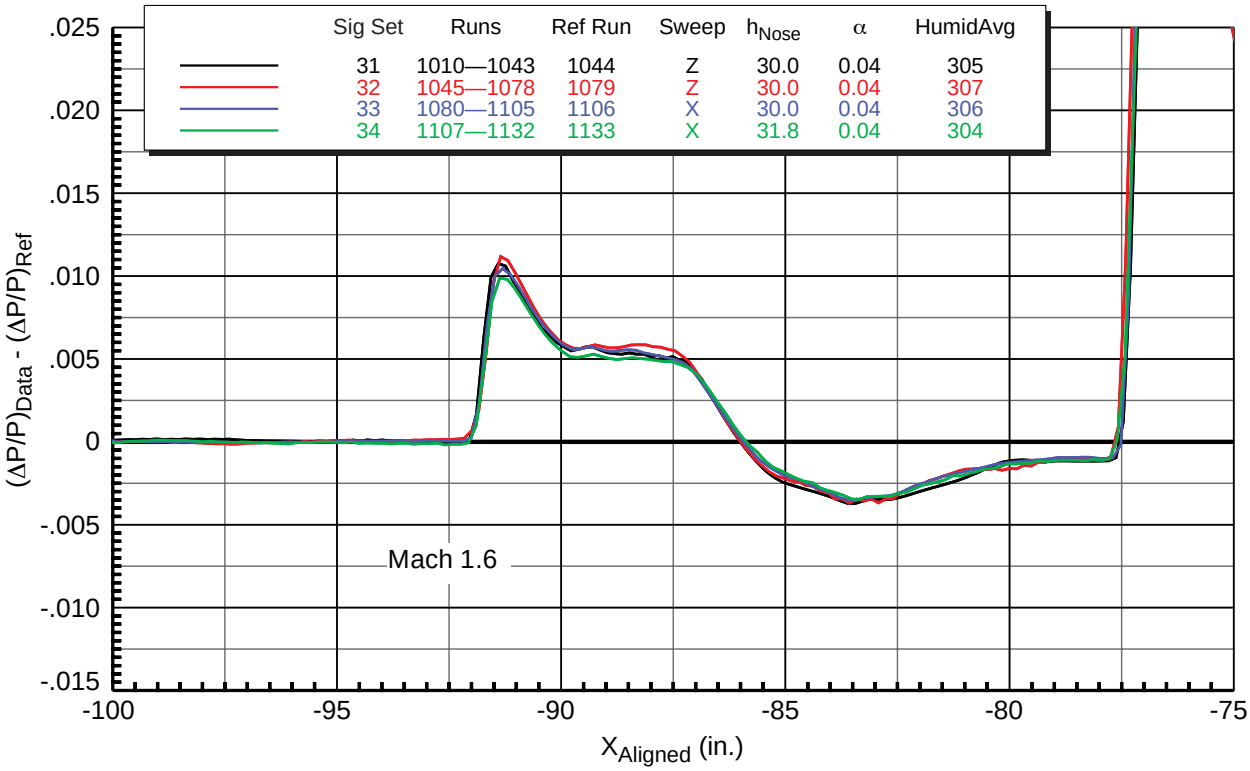

Figure 7–6. Repeatability, *X* and *Z* sweeps
9x7 parametric test, AS2 model, 14-in. forward rail, *M* = 1.60

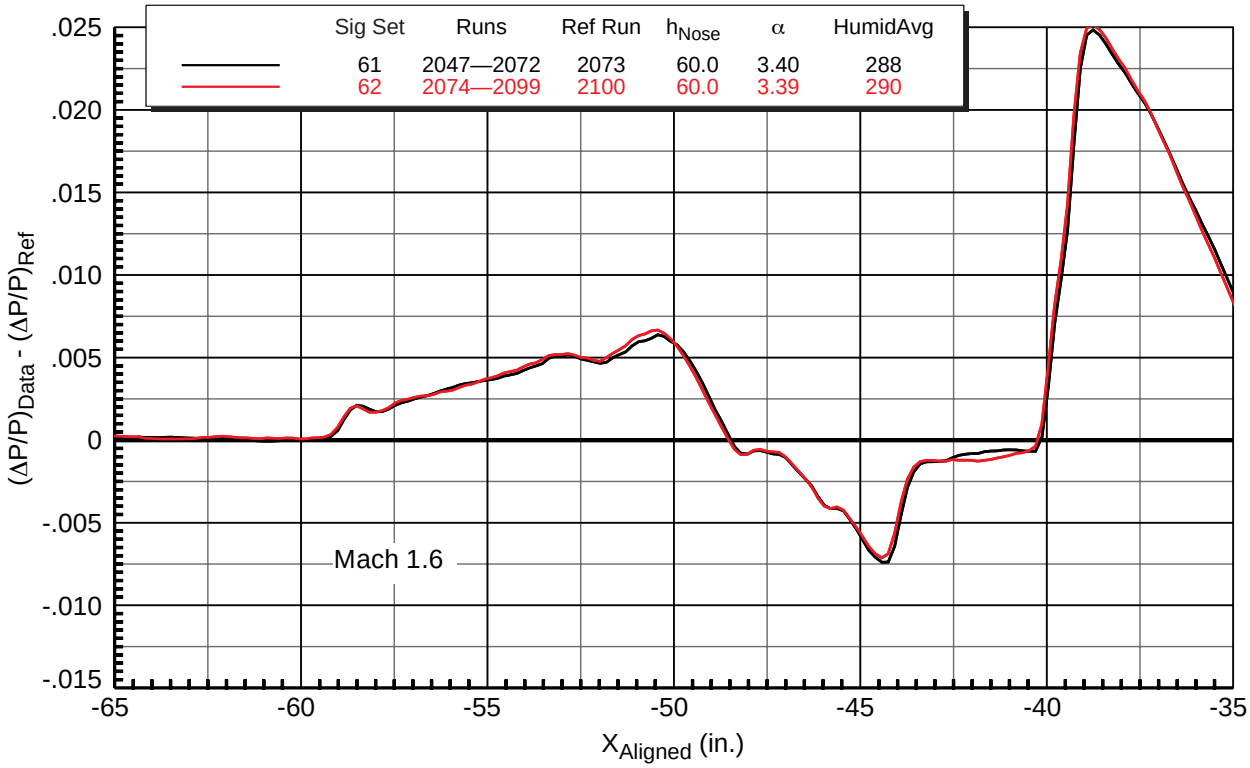

Figure 7–7. Repeatability, *X* sweeps (0” to 16”)
9x7 parametric test, Boom1 VS2 model, 14-in. aft rail, *M* = 1.60

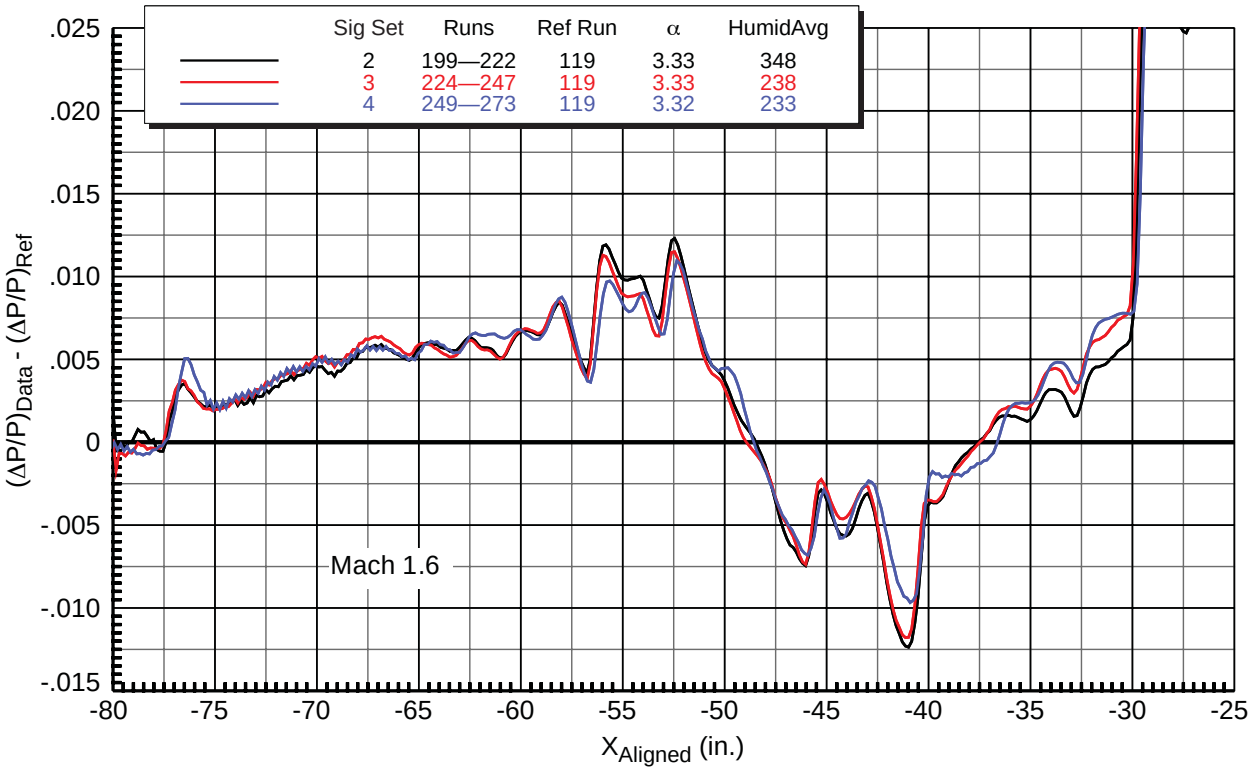

Figure 7–8. Repeatability, *Z* sweeps (59" to 64")
9x7 TBC4 test, Performance sting+contour model, 14-in. aft rail, *M* = 1.60

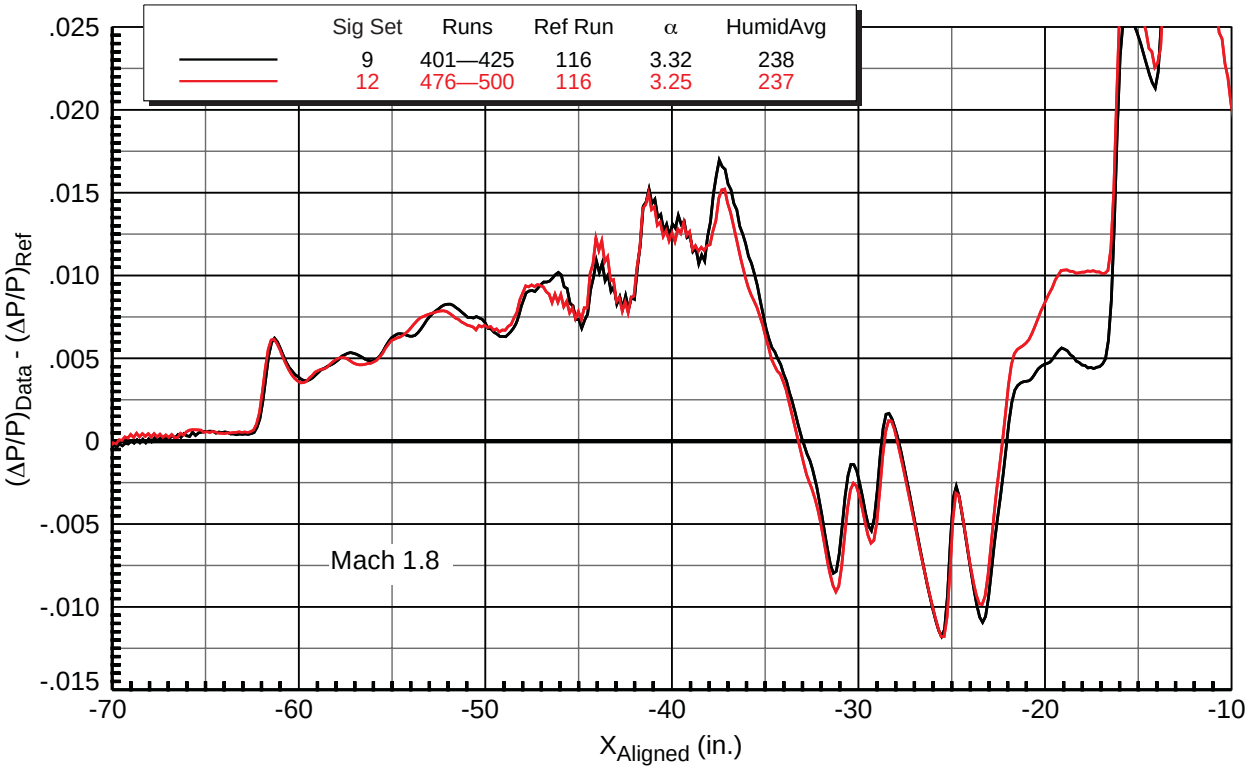

Figure 7–9. Repeatability, *Z* sweeps (59" to 64")
9x7 TBC4 test, Performance sting+contour model, 14-in. aft rail, *M* = 1.80

7.3. Effect of Adjusting Height During *X* Sweeps

All of the Boeing models were mounted on the struts/balance adapter/balance at zero incidence angle; that is, the model was "level" when the balance was "level" (speaking of the *Z*, or "height" orientation). The linear actuator was colinear with the balance, so in order to run the Boom models at a positive angle of attack, the wind tunnel strut had to be pitched up by this angle. This meant that as the ram of the linear actuator was extended, it was driving the model higher, away from the rail during *X* sweeps. For a model angle of attack of 3.4° and a 16-in. *X* sweep, the model nose would move up in *Z* by 0.95 in. There was concern during the test as to whether this height change would affect the pressure signature, so some comparison runs were obtained in the 9x7 to investigate this.

The model height for the Boom1 VS2 sig set 45 was adjusted to try to keep the height within 0.33 in. of the target value, and in sig sets 46 and 47, the height was not adjusted but allowed to drift. The resulting signatures are shown in Figure 7–10 at Mach 1.6, where the changes in height for the three run sets, designated by Δh_{Nose}, were 0.42 in., 0.96 in., and 0.97 in., respectively. The three signatures are nearly identical, and the very minor variations among them are well within the repeatability of the data.

A similar comparison of runs where the heights were and were not adjusted is presented in Figure 7–11 at Mach 1.8. The model height during the *X* sweep was adjusted for sig set 38 (Δh_{Nose}, = 0.21 in.), but allowed to drift up for sig set 39 (Δh_{Nose}, = 0.97 in.). As on the previous plot, the signatures are very close, but the one which was allowed to drift is very slightly lower overall than the adjusted one, though within expected repeatability.

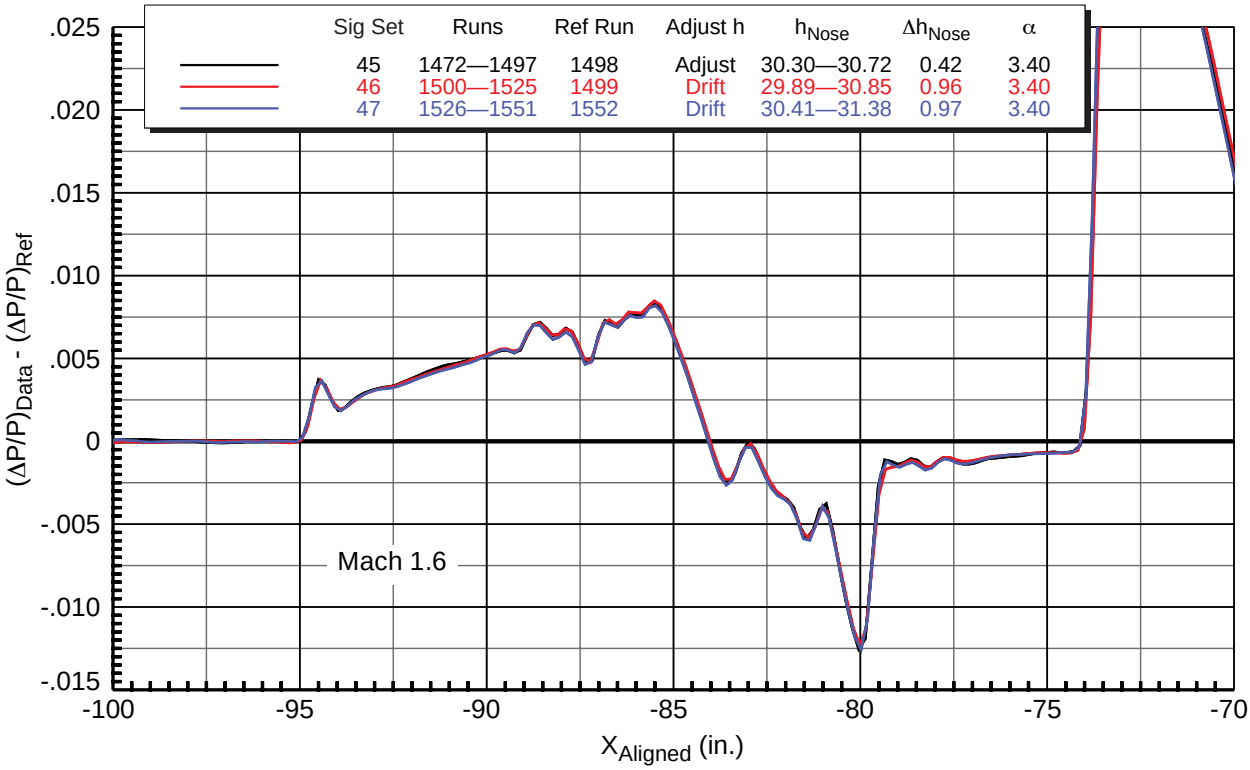

Figure 7–10. Effect of adjusting height in *X* sweeps (8" to 24")
9x7 parametric test, Boom1 VS2 model, 14-in. fwd rail, *M* = 1.60, *HumidAvg*=314 ppm

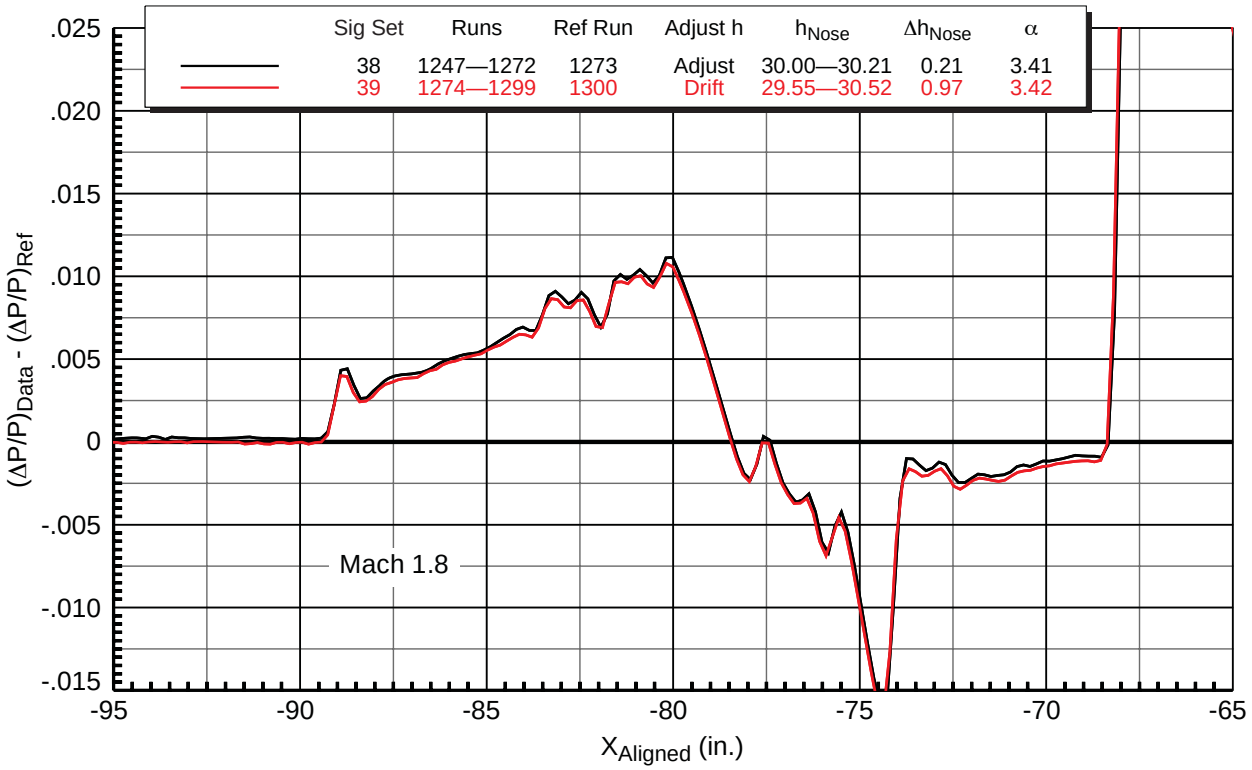

Figure 7–11. Effect of adjusting height in *X* sweeps (8" to 24")
9x7 parametric test, Boom1 VS2 model, 14-in. fwd rail, *M* = 1.80, *HumidAvg*=306 ppm

These two plots clearly indicate that adjusting model height during an *X* sweep has essentially negligible effects on the measured signatures—the differences appear to be well within the expected uncertainty, and these plots can be considered as repeatability plots, which show very good repeatability.

7.4. Effect of Model Height

For a given rail and mounting position on the wall of the 9x7 tunnel, there are allowable ranges of model *X* and *Z* positions where the model shocks stay within the instrumented section of the rail (refer to Figure 6–8 for a typical layout). For the Boom1 model with the VS2 strut at Mach 1.6, $\alpha = 3.4°$ in the 9x7 tunnel, with the rail on the forward window blank, the model height range (estimated by the Excel layout) that allows for at least an 8-in. *X* sweep without overlap between the reference and data runs is from 10 to 38 in. With the rail on the aft window blank, the model height range that allows for at least an 8-in. *X* sweep is from 52 to 68 in. The rail could also be mounted to span the two window blanks to cover the middle range, but this position was not used in any of the tests in the interest of time.

In the 9x7 parametric test, the RF1 rail was run in both the forward and aft window blank positions, and signature measurements of the Boom1 VS2 model were acquired at heights of 30 and 60 in. Comparisons of these signatures from *X* sweeps at Mach 1.6 and 1.8 are shown in Figure 7–12 and –13, respectively. The signatures at both Mach numbers at 30 in. have much more clearly defined shock peaks than those at 60 in., and the magnitude of the overall pressure levels are higher at 30 in., as one would expect. At 60 in., the small shocks aft of the primary expansion have already coalesced.

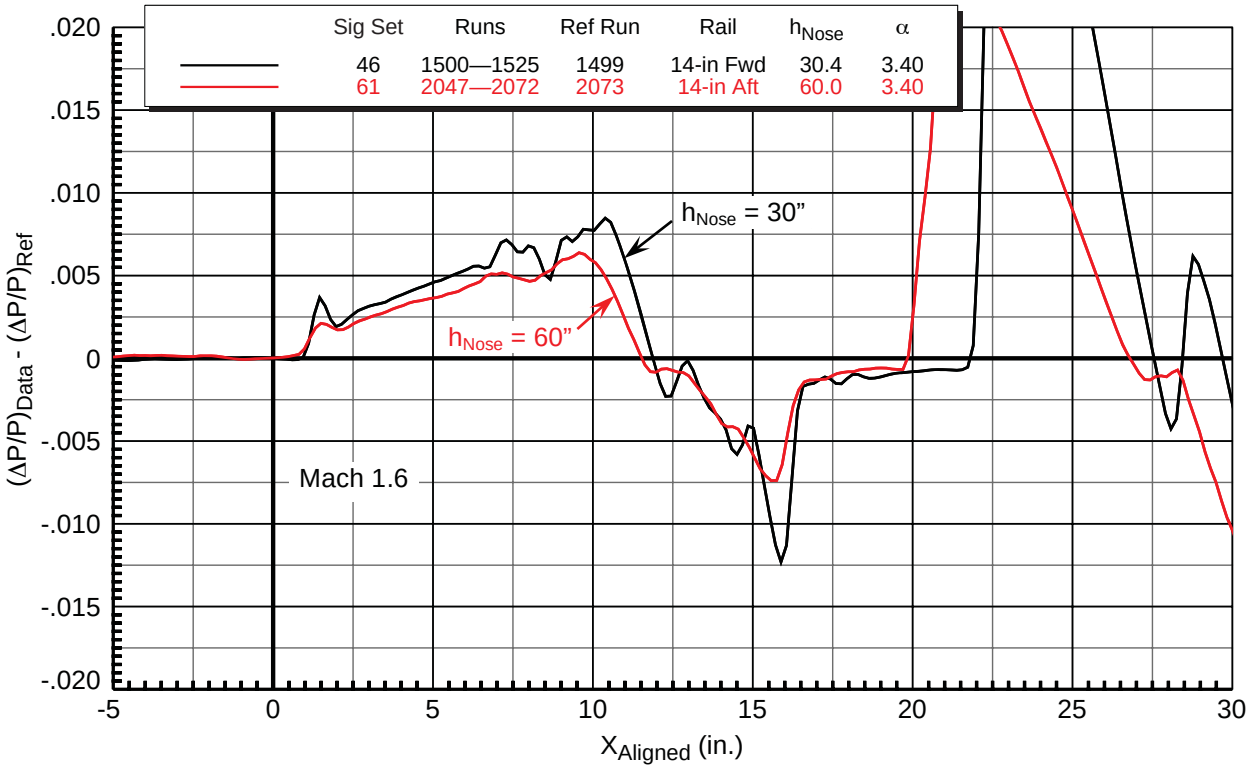

Figure 7–12. Effect of model height, *X* sweeps (8” to 24”, 0” to 16”) 9x7 parametric test, Boom1 VS2 model, *M* = 1.60, *HumidAvg* = 301 ppm

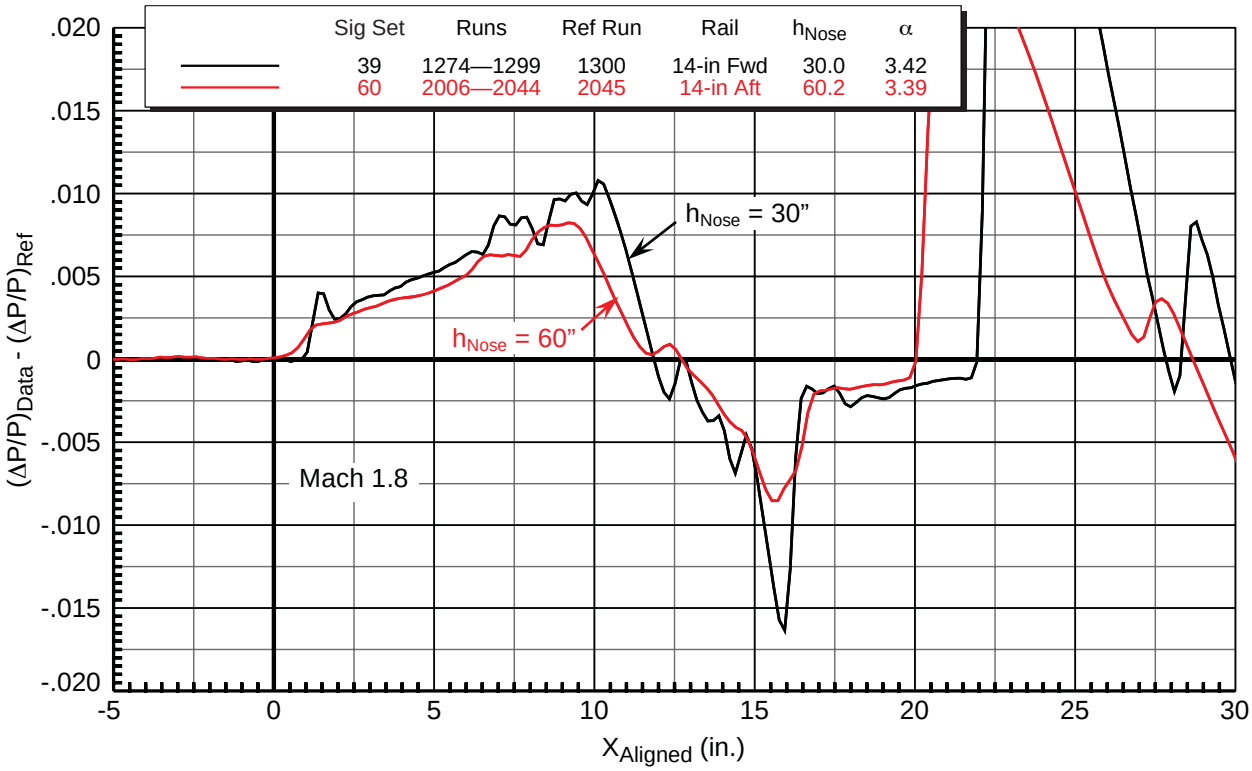

Figure 7–13. Effect of model height, *X* sweeps (8” to 24”, 0” to 16”) 9x7 parametric test, Boom1 VS2 model, *M* = 1.80, *HumidAvg* = 295 ppm

7.5. Comparison of *X* vs. *Z* Sweeps

Spatial averaging of model pressure signatures can be accomplished by moving the model over small ranges in either the *X* or *Z* direction such that the signatures fall on different regions of the pressure rail. The first sweeps done to accomplish this in the series of tests were in the *X* direction, and were made possible by extension of the ram of the linear actuator. At the time of the 9x7 parametric test, it was anticipated that a future test might not include the linear actuator, but it needed to be established first that *Z* sweeps over small ranges would give equally valid data as *X* sweeps. Hence a few direct comparisons of signatures obtained with both types of sweeps for the AS2 and Boom1 VS2 models were run in both the 9x7 parametric and the 8x6 TBC3 tests.

AS2 body of revolution signatures from one *X* sweep and two *Z* sweeps at nominally 30-in. heights above the 14-in. rail in the 9x7 are shown in Figure 7–14. The agreement is generally excellent among all three signatures, though slight differences appear, unexpectedly, between the two *Z* sweeps, where the latter one (sig set 32) with X_{Ram} = 24 in. has a slightly higher initial shock peak and the aft flat area before the main expansion is higher. It is possible that the 8-in.-further-forward position in the tunnel (X_{Ram} = 24 in. vs. 16 in.) for the second *Z* sweep could account for this difference, if there was a slightly different flow angle or static pressure in the tunnel for this position. Or the differences could be just random scatter in the data as they are not atypical in light of the measured repeatability.

Four different *X* vs. *Z* sweep comparisons for the Boom1 VS2 model in the 9x7 are shown in Figures 7–15 through –18, two with the 14-in. rail and two with the 2-in. rail, all at nominally 30-in. heights above the rails. The first comparison, at Mach 1.6 in Figure 7–15, shows very good agreement over the entire length of the signatures, with minor differences in various positions along the signatures. The next comparison, at Mach 1.8 in Figure 7–16, shows that the *Z* sweep has an overall slightly higher pressure level than the *X* sweep, ranging from 0 to 0.001 $\Delta P/P$ difference. This difference exists even in the leading zero points, though very small, and if the leading zero points just ahead of the model's front shock were made to align by an overall lowering of the *Z* sweep curve, then the two sweeps would have a more favorable comparison. The *Z* sweep curve has a little more rounding, or smearing, of the shock peaks relative to the *X* sweep curve. Nonetheless, it seems that there must have been some variation in the tunnel flow between these two sets of runs to cause the differences that are apparent.

The other two comparisons of sweep types with the Boom1 VS2 model are in Figures 7–17 and –18, with the 2-in. rail. The two signatures at Mach 1.6 in Figure 7–17 show good agreement up to (X = -88) but not including the highest pressure peak, where the differences from this point through the aft expansion (X = -82) are fairly significant, up to 0.003 in $\Delta P/P$. At Mach 1.8, Figure 7–18, the differences between the two sweeps are more in line with those at the same Mach number from the 14-in. rail (Figure 7–16). However, at this Mach number, the *Z* sweep pressures are *higher* than those from the *X* sweep in the 14-in. rail data, but *lower* in the 2-in. rail data at both Mach numbers.

The reasons for the pressure signature differences between the two types of sweeps are not understood, but from these data and data from other tests not reported herein the two types of sweeps were considered equally valid for acquiring sonic boom data for spatial averaging.

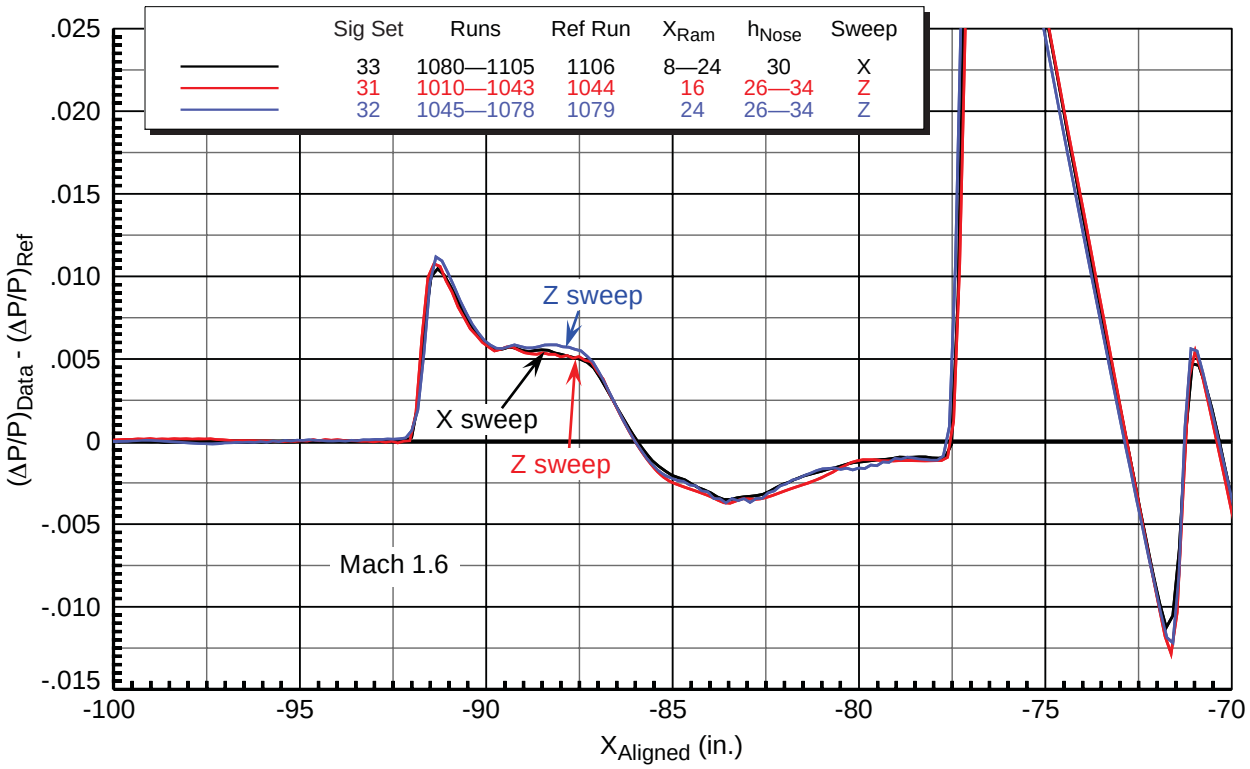

Figure 7–14. *X* vs *Z* sweep comparisons
9x7 parametric test, AS2 model, 14-in. forward rail, *M* = 1.60, *HumidAvg* = 306 ppm

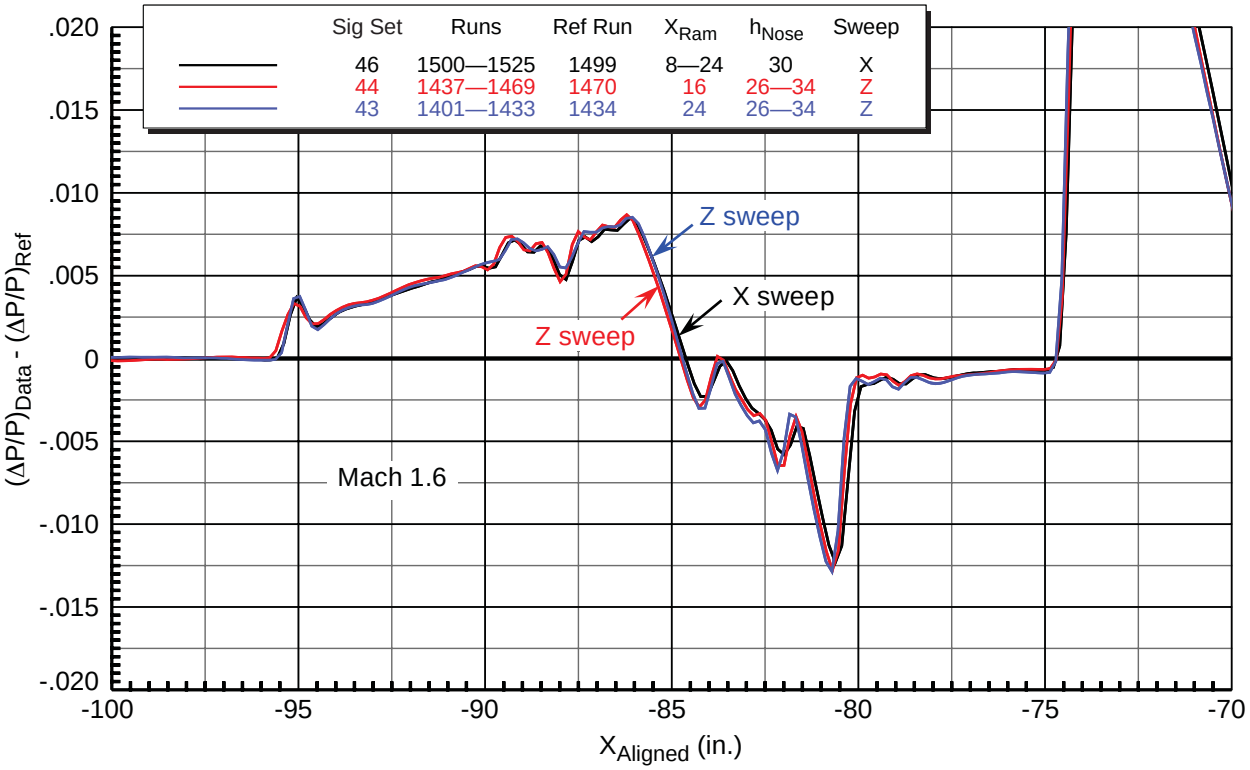

Figure 7–15. *X* vs *Z* sweep comparisons
9x7 parametric test, Boom1 VS2 model, 14-in. fwd rail, *M* = 1.60, *HumidAvg*=308 ppm

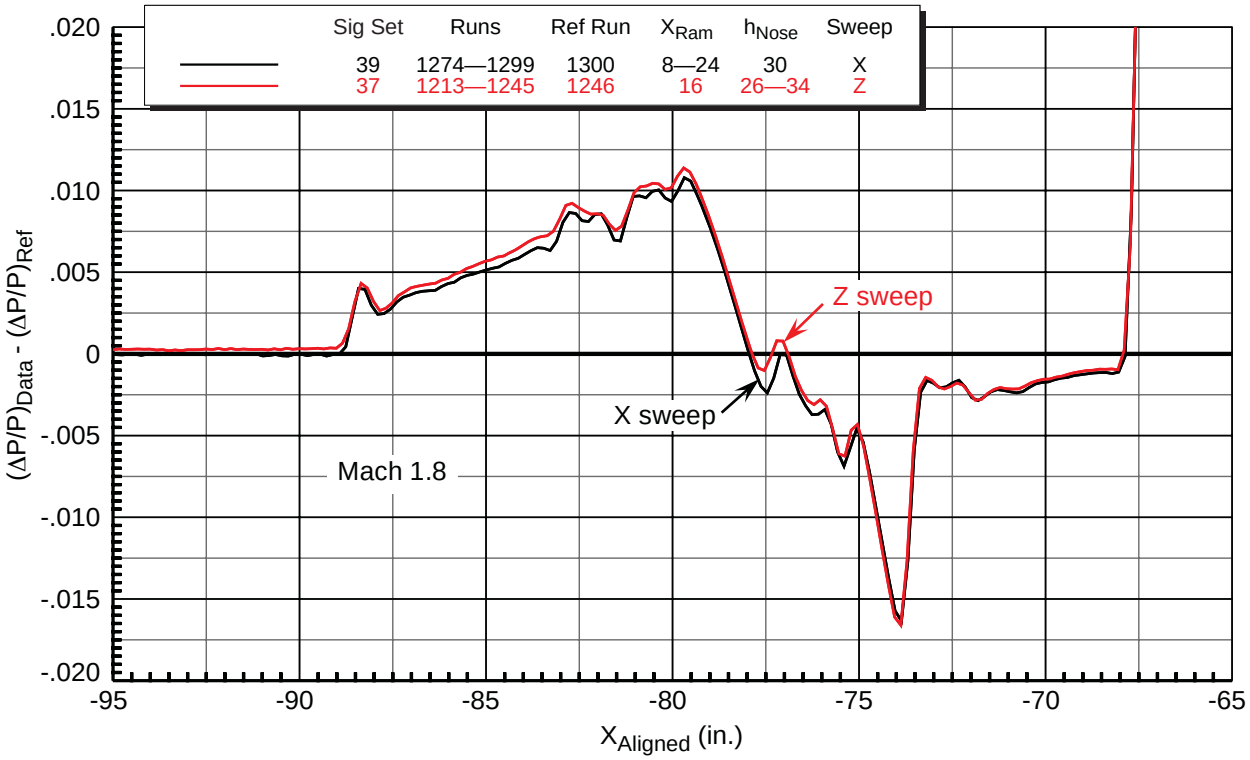

Figure 7–16. *X* vs *Z* sweep comparisons
9x7 parametric test, Boom1 VS2 model, 14-in. fwd rail, *M* = 1.80, *HumidAvg*=307 ppm

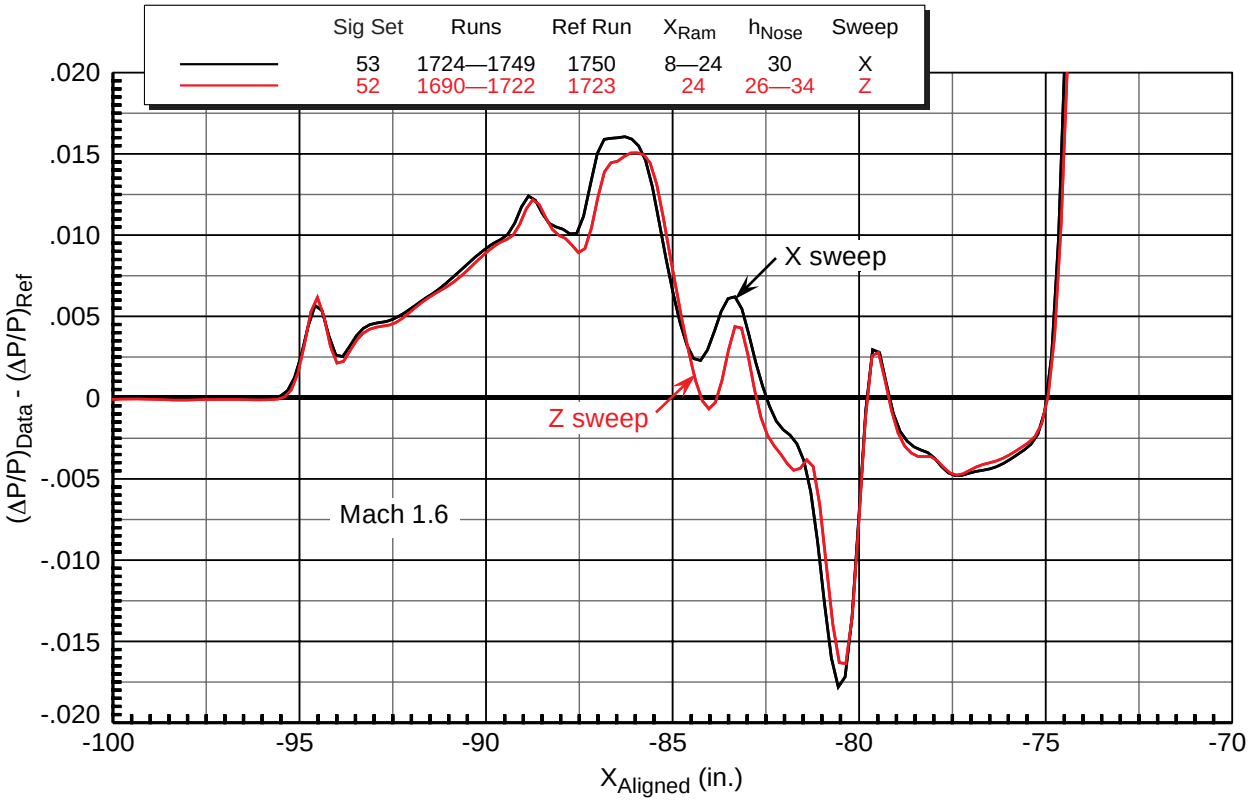

Figure 7–17. *X* vs *Z* sweep comparisons
9x7 parametric test, Boom1 VS2 model, 2-in. fwd rail, *M* = 1.60, *HumidAvg* = 321 ppm

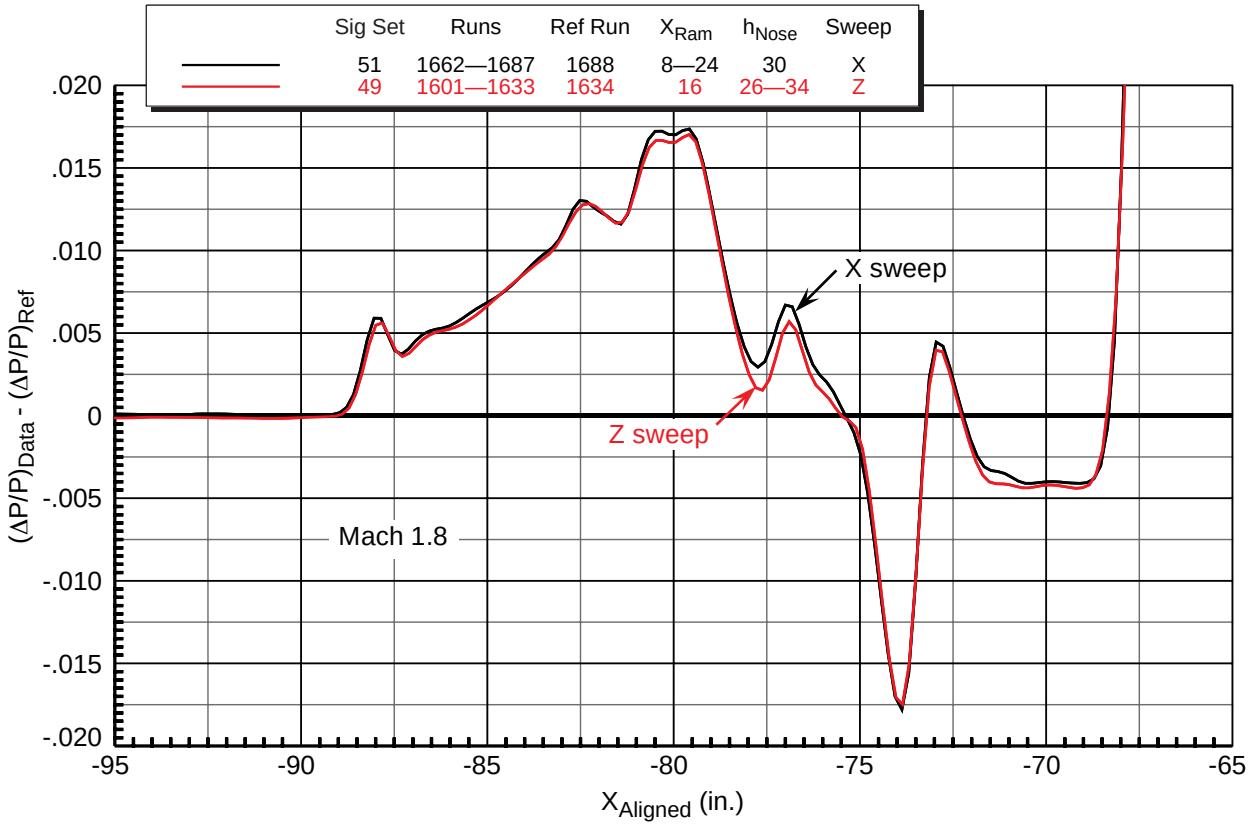

Figure 7–18. *X* vs *Z* sweep comparisons
9x7 parametric test, Boom1 VS2 model, 2-in. fwd rail, *M* = 1.80, *HumidAvg* = 317 ppm

7.6. Effect of Ram Position for *Z* Sweeps

It is well known that the flow in the 9x7 test section is curved in the vertical plane due to the asymmetric nozzle, and this impacts the measurement of sonic boom data because the model is in different flow environments in different locations in the test section. The subtraction of an ambient pressure signature on the rail from a data run is intended to reduce or eliminate the effects of the different flow environments, but that is not always a given.

In the 9x7 parametric test, a few runs were conducted with the AS2 and Boom1 VS2 models to investigate these possible effects. *Z* sweeps centered on a 30-in. height for the AS2 model were run at X_{Ram} positions of 16 and 24 in., and the signatures for these sweeps taken at Mach 1.6 are shown in Figure 7–19. There are some minor differences in the nose shock peak and the aft flat area, but these differences are no greater than those observed in Figure 7–8 showing repeatability and in Figure 7–15 showing the comparison of *X* vs. *Z* sweeps.

Similar insignificant differences between *Z* sweeps at X_{Ram} positions of 16 and 24 in. for the Boom1 VS2 model are seen in Figures 7–20 and –21 at Mach 1.6 and 1.8, respectively. There are some minor variations among the curves, but not any greater than those observed in the plots showing repeatability or comparison of sweep types. Perhaps greater differences could have been seen between sweeps at the extremes of the ram positions—0 and 24 in.—but there were other higher-priority test objectives that precluded getting additional comparable signatures at X_{Ram} = 0 in.

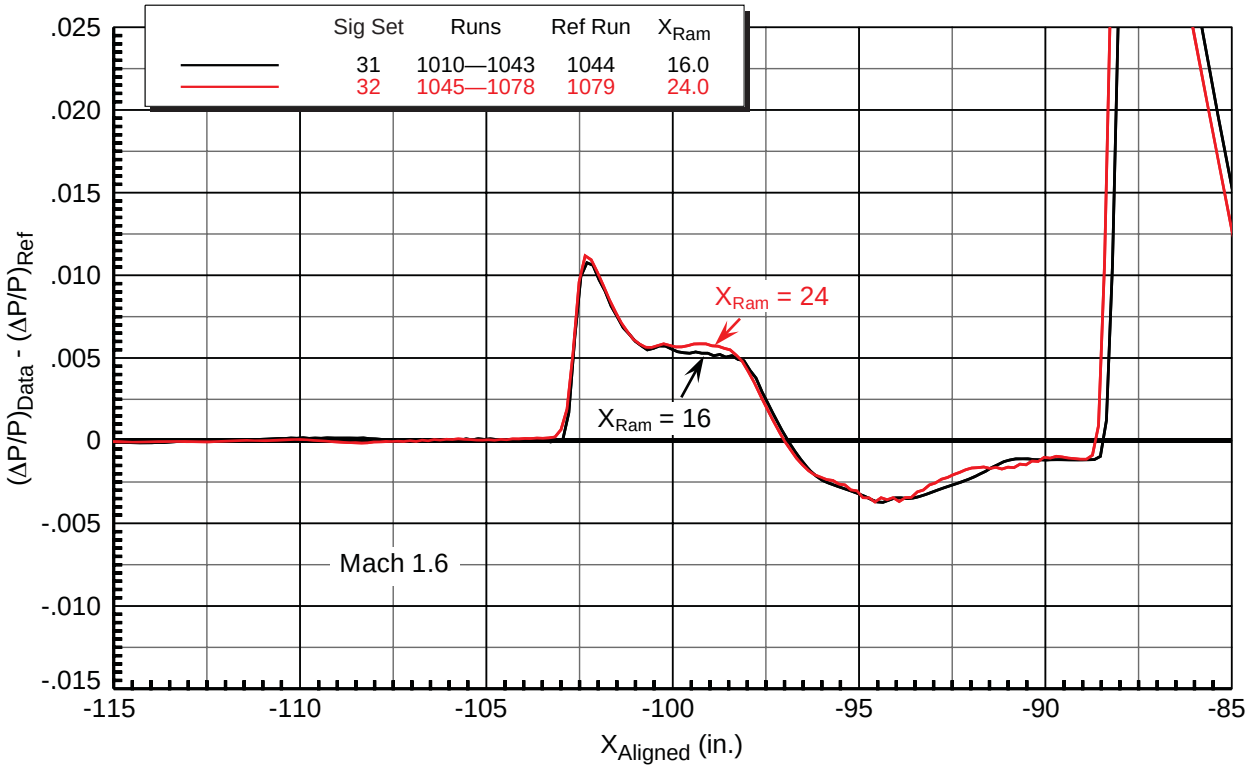

Figure 7–19. Effects of ram position for *Z* sweeps (26” to 34”)
9x7 parametric test, AS2 model, 14-in. fwd rail, *M* = 1.60, *HumidAvg* = 306 ppm

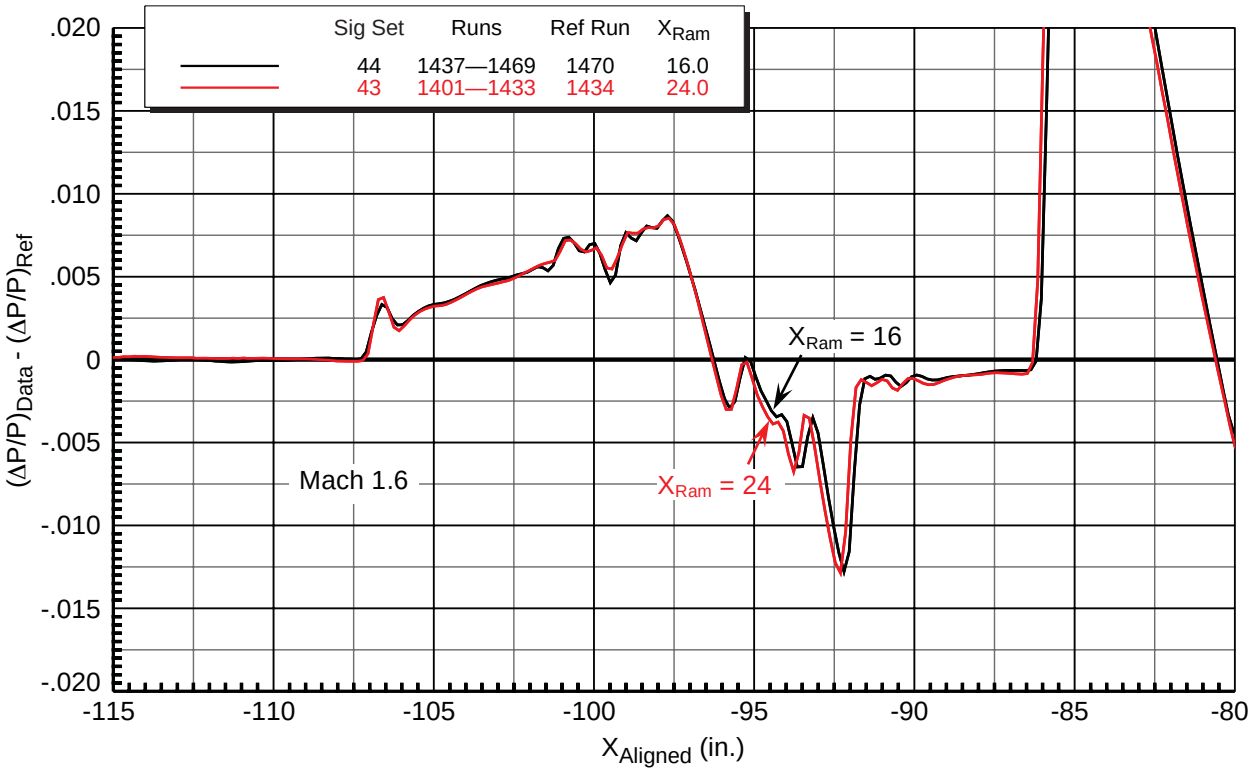

Figure 7–20. Effects of ram position for *Z* sweeps (26” to 34”)
9x7 parametric test, Boom1 VS2 model, 14-in. fwd rail, *M* = 1.60, *HumidAvg*=304 ppm

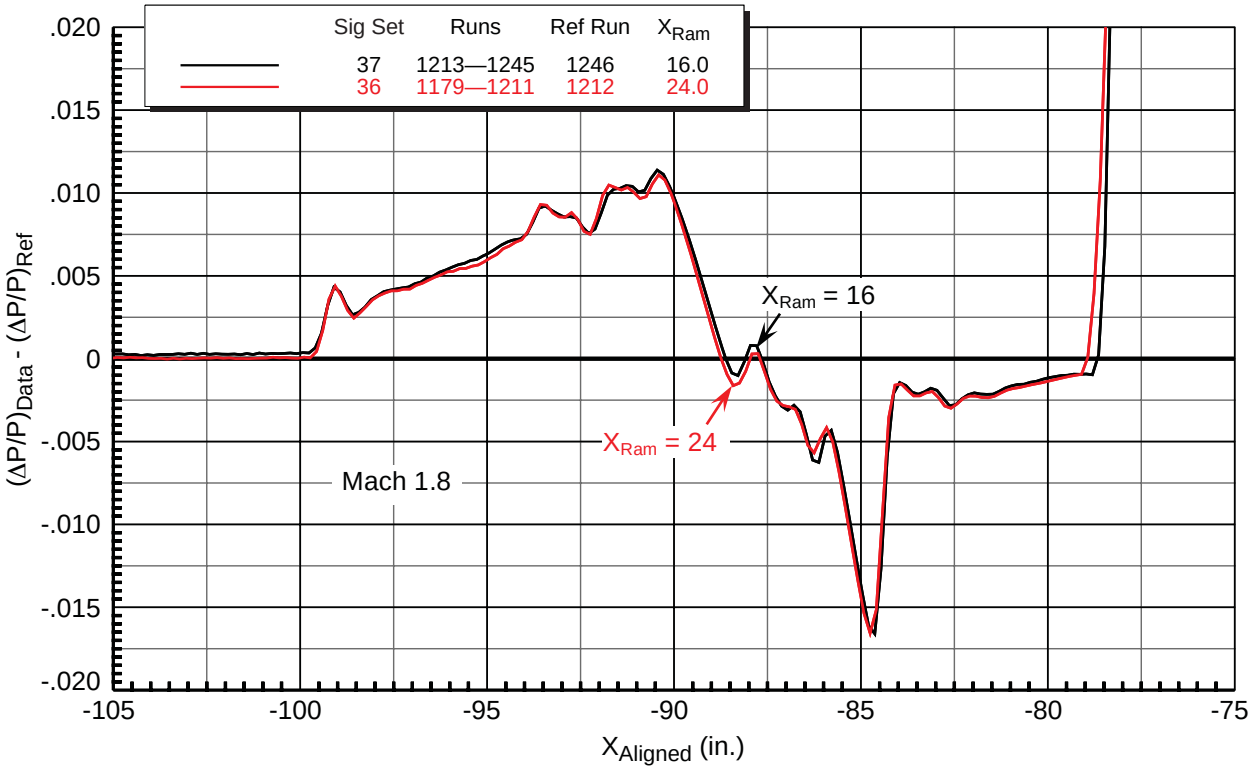

Figure 7–21. Effects of ram position for *Z* sweeps (26” to 34”)
9x7 parametric test, Boom1 VS2 model, 14-in. fwd rail, *M* = 1.80, *HumidAvg*=306 ppm

7.7. Rail Comparisons — 14-in. (RF1) vs. 2 in. Rails

In this section various comparisons of data from the 14-in. and 2-in. rails for the AS2 and Boom1 models are presented. Two primary differences in the effects of the rail on the data were expected between the two rails:

1) Reflection factor: The 14-in. RF1 rail was expected to not amplify the measured pressures at all, whereas the 2-in. rail was expected to cause amplifications between a factor of 1 and 2 (would be 2 for an infinitely-wide flat plate, but lower for this 1.5-in.-wide rail).
2) Contamination of the aft part of the signatures from shock reflections off the wall: The 14-in. height of the RF1 rail was chosen to eliminate this possibility for models up to 33-in. long at a Mach 1.6 (51°) Mach line angle, whereas on the 2-in. rail, the reflected shock passes back over the surface of the rail about 5 in. aft of the incident shock location at Mach 1.6, or possibly less distance aft if the lower Mach line angle closer to the tunnel wall (due to the boundary layer) is taken into account.

Flat-top rails like the 2-in. rail have been used in many sonic boom tests outside of NASA, and users of those rails have developed methods or calibration factors for correcting the data. These corrections are usually based on CFD analyses and/or experience with models of different sizes whose signatures are well known. However, in the present NASA studies discussed herein, no such corrections have been generated, and the data from both rails will be presented as they were taken, with the exception of reflection factors for the 2-in. rail data computed to get the best overall match of the whole signature with the 14-in. rail data.

Figure 7–22 shows a comparison between the sonic boom signatures acquired with the 14-in. rail and 2-in. rail for the AS2 body of revolution in *X* sweeps at a height of 30 in. at Mach 1.6 and $\alpha = 0°$. The 2-in. rail data with no reflection factor correction (RF = 1) is quite high relative to the data acquired with the 14-in. rail, probably as one would expect. But the aft "flat" portion of the signature, which is fairly horizontal in the 14-in. data, is sloped upward in the 2-in. data, which may be due to a reflection of the nose shock off the tunnel wall that is contaminating the aft portion of the signature.

To see what the 2-in. rail data would look like with a correction, a reflection factor of 1.7 ($\Delta P/P$ / 1.7) was applied to match the nose shock strength of the 14-in. rail—see the second sig set 54 curve, with RF 1.7. The nose shock strength now matches that of the 14-in. rail data, but the correlation with the 14-in. data in the aft flat area is poor. From these data and other sources, it is surmised that the correction for reflection factor should not be applied evenly over the entire signature, but a thorough study of how it should be applied has not been conducted by the authors, and so the data will remain as presented herein for now. Similar data for the AS2 model obtained with *Z* sweeps shown in Figure 7–23 shows similar results.

Rail comparisons for data from the Boom1 VS2 model from both tunnels at various heights are shown in Figures 7–24 through –27. Data from the 9x7 tunnel for *Z* and *X* sweeps at a model height of 30 in. and Mach 1.6 are shown in the first two figures. In the *Z* sweep data in Figure 7–24, as with the AS2 data, the unadjusted signatures from the two rails show similar trends, though the 2-in. rail data shows more rounding and less definition of the pressure waves between the shocks. The adjustment of the 2-in. rail data for a reflection factor of 1.7 brings that data down to the level of the 14-in. rail data for the front half of the signature, but in the rear half (after $\Delta P/P$ crosses zero), the adjusted 2-in. rail data have significantly higher pressure levels than the 14-in. data. This could be due to the shock reflections off the wall contaminating the rear part of the signature, but as stated earlier, based strictly on the shocks following the Mach line angle, one might expect the contamination to start about 5 in. aft of the nose

shock. The 2-in. rail data shows no or very little deviation from the 14-in. data at 5 in. back (around X = -110), but the major differences start around 11 in. back (X = -104).

In the X sweep data in Figure 7–25, there are slightly greater differences between the magnitudes of the pressure data for the two rails, even after applying the reflection factor of 1.7 to the 2-in. rail data. All other run parameters (M, h, α) are the same in these data versus those in the previous figure aside from the sweep type, but it doesn't seem likely that sweep type would account for these differences given the findings in Section 7.5.

Rail comparisons for the same model from X sweeps in the 8x6 wind tunnel are shown in Figures 7–26 and –27 for heights of 59 and 49 in. and at Mach numbers of 1.56 and 1.78, respectively. In both figures, the adjusted 2-in. data with RF = 1.7 applied match up fairly well with the 14-in. rail data, though better at the lower height (49 in.). Also, the leading zero pressures for all of the runs in these two figures are below the zero $\Delta P/P$ line, indicating that there were probably some significant differences in the tunnel flow between the reference and data runs. All of the data from the 8x6 tunnel presented in this report were acquired during the second week of testing, after the smooth windows (no holes) were moved to the forward part of the test section and the Mach number was being held to a tighter tolerance, so the poorer data quality issues encountered during the first week are not a factor in these plots.

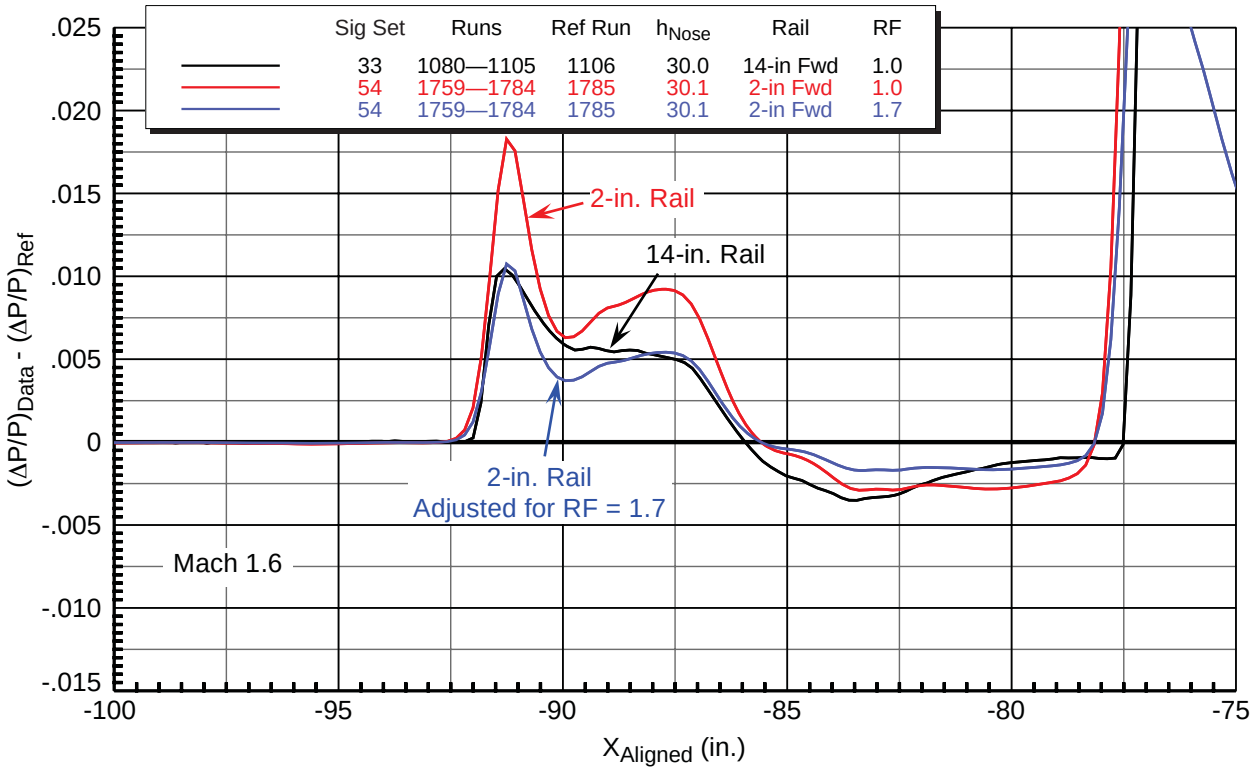

Figure 7–22. Rail comparisons, *X* sweeps (8” to 24”)
9x7 parametric test, AS2 model, *M* = 1.60, *HumidAvg* = 302 ppm

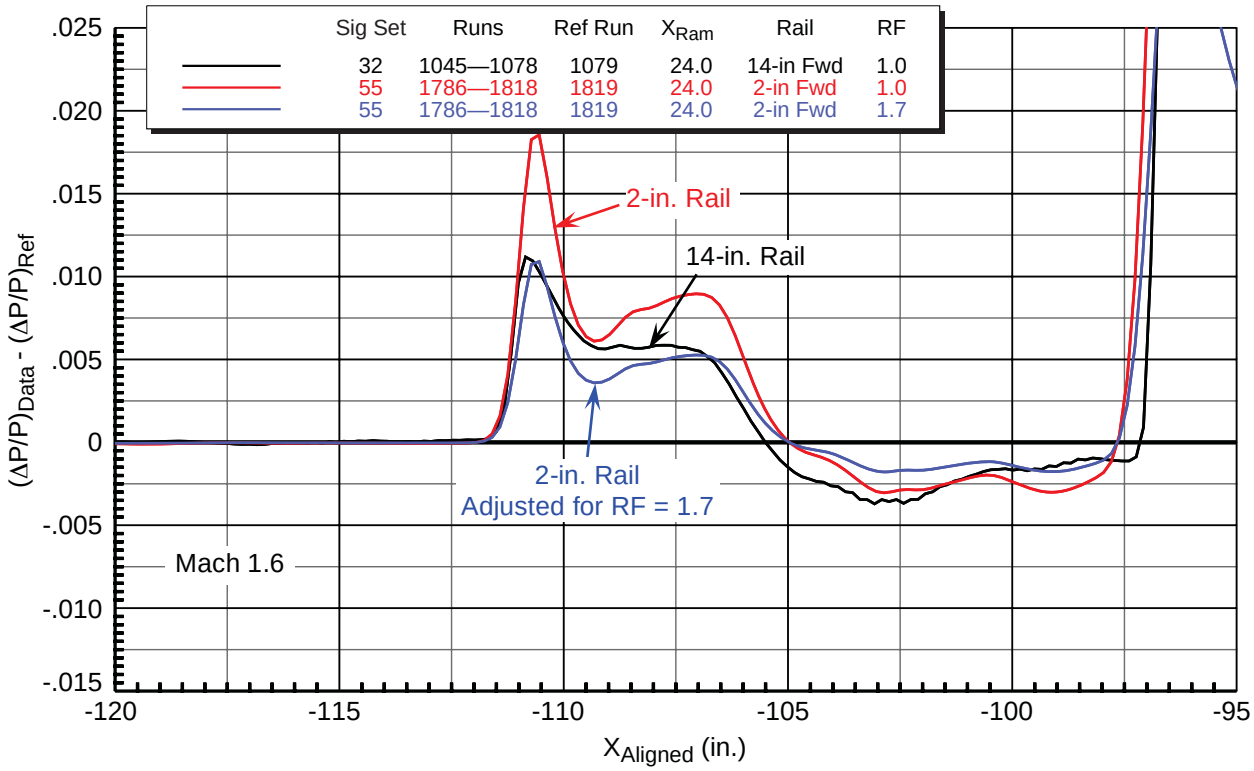

Figure 7–23. Rail comparisons, *Z* sweeps (26” to 34”)
9x7 parametric test, AS2 model, *M* = 1.60, *HumidAvg* = 301 ppm

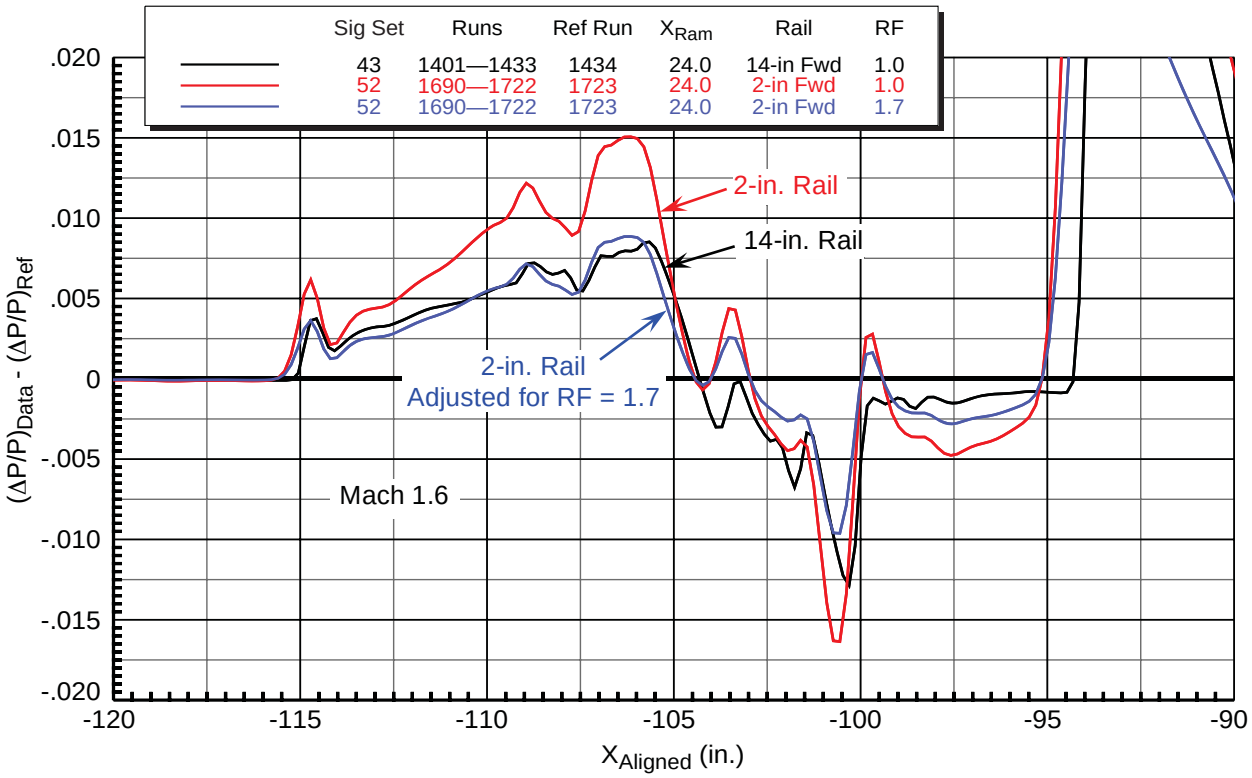

Figure 7–24. Rail comparisons, *Z* sweeps (26” to 34”)
9x7 parametric test, Boom1 VS2 model, *M* = 1.60, *HumidAvg* = 313 ppm

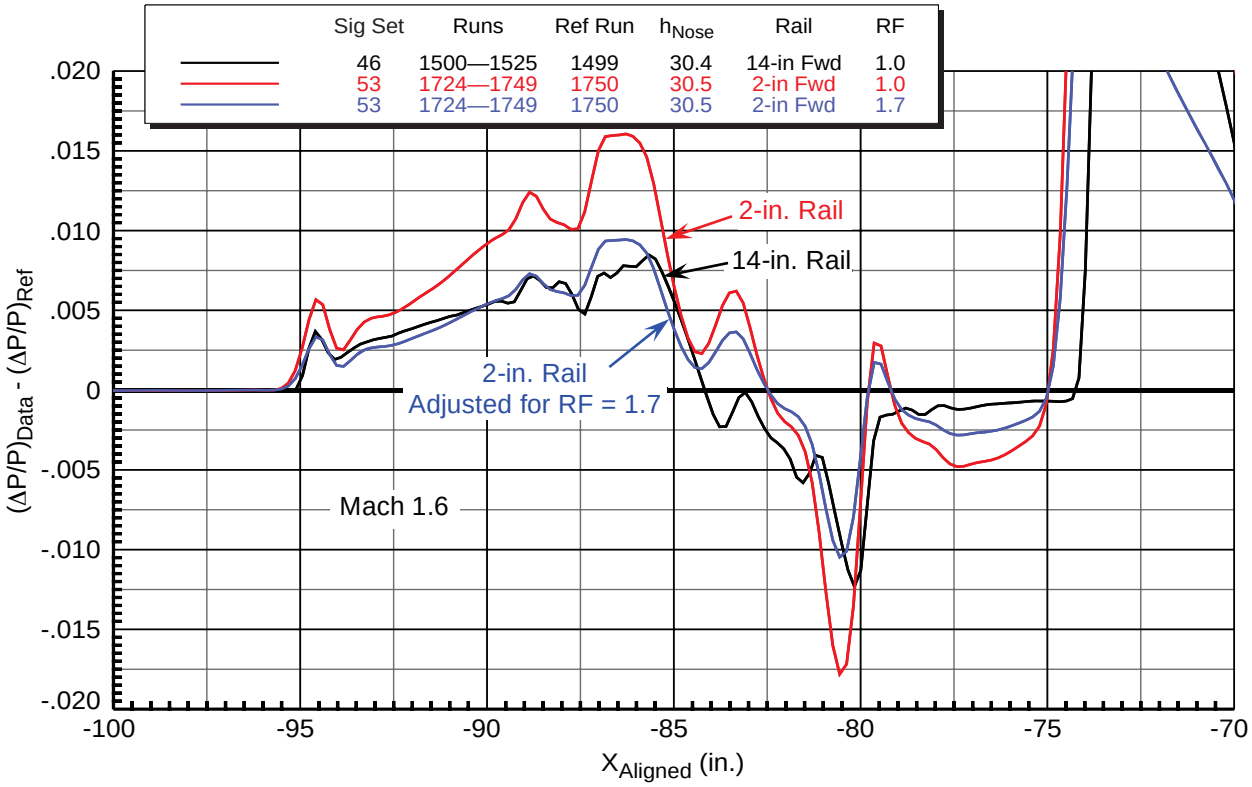

Figure 7–25. Rail comparisons, *X* sweeps (8” to 24”)
9x7 parametric test, Boom1 VS2 model, *M* = 1.60, *HumidAvg* = 319 ppm

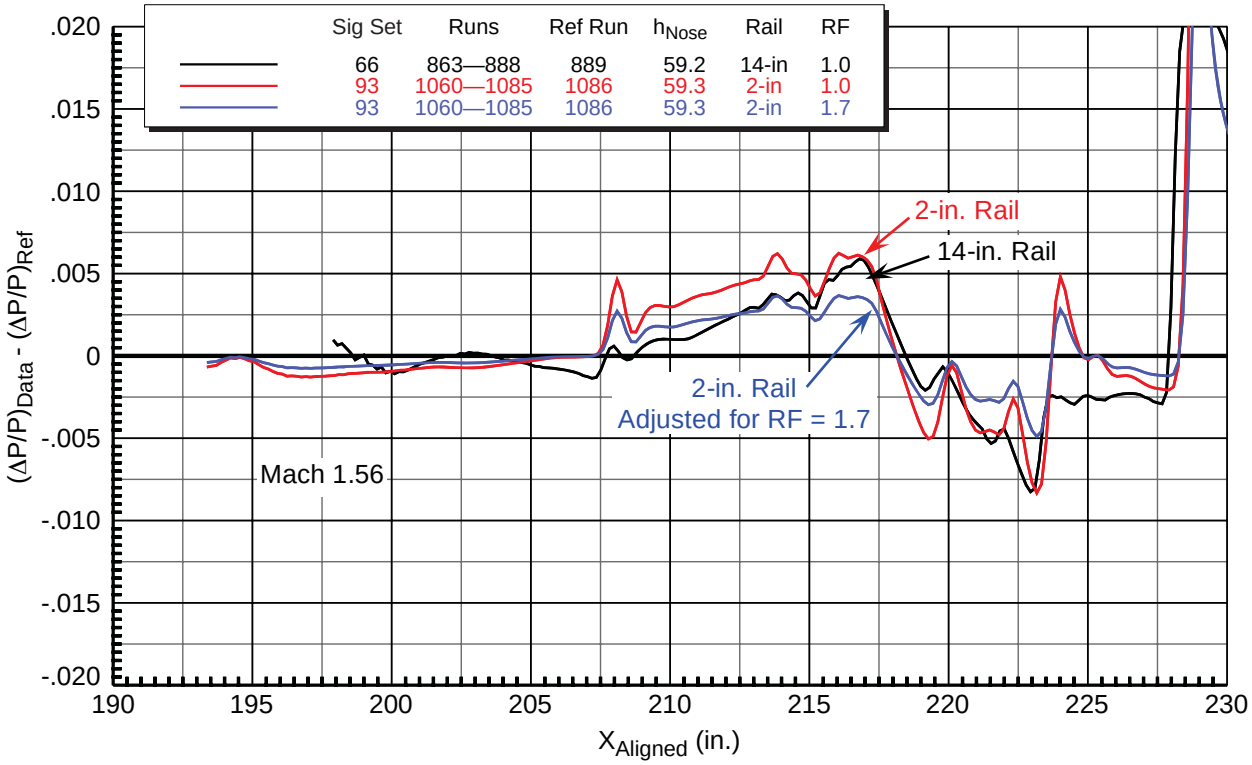

Figure 7–26. Rail comparisons, *X* sweeps (0” to 8”)
8x6 TBC3 test, Boom1 VS2 model, *M* = 1.56, *HumidAvg* = 111 ppm

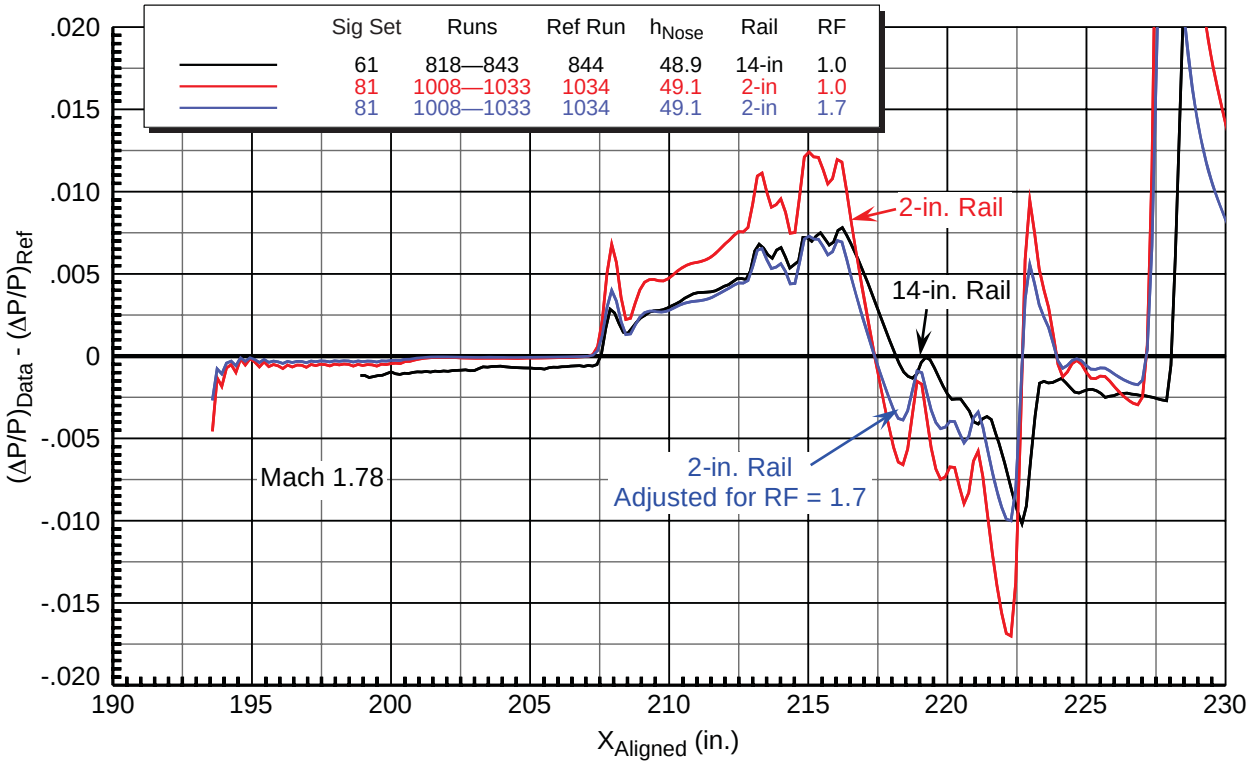

Figure 7–27. Rail comparisons, *X* sweeps (0” to 8”)
8x6 TBC3 test, Boom1 VS2 model, *M* = 1.78, *HumidAvg* = 77 ppm

7.8. Effect of Mounting Strut on Boom Model Signatures

The four different mounting struts, VS1 through VS4, were used with the Boom models (Boom1 or Boom2 with VS1 or VS2, and Boom3 with VS3 or VS4) in the various tests (see Figures 4–20 and –21), but the VS1 strut was only used in the 9x7 TBC1 test. This test was conducted before *X* or *Z* sweeps were employed to permit spatial averaging, therefore, the Boom1 model with VS1 will not be included in the comparisons with the other three struts since the individual signature data does not have the tunnel spatial flow variations removed, and thus is of poorer quality. The Boom1 model was run only with the VS2 strut in the TBC1, 9x7 parametric, and the 8x6 TBC3 tests, and the Boom3 model was run with both the VS3 and VS4 struts in the 9x7 TBC4 test—see Table 5 for the combinations of boom models and struts tested. Recall from the model description section that the Boom3 model has the same aerodynamic lines as the Boom1 model aside for provisions for mounting on the new VS3 and VS4 struts, so comparing the Boom3 model with its struts with the Boom1 model with its struts is valid for illustrating strut effects. Boom1 VS2 data from the 8x6 test will not be included because such data are available from the 9x7 parametric test.

Table 6. Combinations of Boom Models and Struts Tested

Test	*Model*	*Strut*	*Strut shape*	*Spatial averaging* *
9x7 TBC1	Boom1	VS1	Swept forward, short	No
9x7 TBC1	Boom1	VS2	Swept forward, mid	No
9x7 TBC1	Boom2	VS2	Swept forward, mid	No
9x7 Parametric	Boom1	VS2	Swept forward, mid	Yes
8x6 TBC3	Boom1	VS2	Swept forward, mid	Yes
9x7 TBC4	Boom3	VS3	Swept forward, long	Yes
9x7 TBC4	Boom3	VS4	Swept aft, straight sting	Yes

* *Red text: No spatial averaging done in TBC1 test*
Black text: Spatial averaging done in 9x7 Parametric and TBC4 tests
Blue text: Spatial averaging done in 8x6 TBC3 test

Signature comparisons for the Boom1 VS2, Boom3 VS3, and Boom3 VS4 models are made in Figures 7–28 and –29 at Mach 1.6 and 1.8, respectively, at model heights of approximately 60 in. The three signatures for each Mach number are very similar, as expected, in the forward parts up to near the maximum overpressure point, and aft of that there are differences as influenced by the struts. It seems odd though, that in the expansions just aft of the peaks in the Mach 1.6 data, the pressures from the VS3 and VS4 struts look very similar, while the pressures from VS2 are lower; it is VS2 and VS3 that are the upper swept struts, which allow the underside and back ends of the models to remain clean, so they should be more similar. The VS3 strut is longer than VS2 because it has a more forward mounting point on the model, and thus it probably has less influence on the pressure signature below the model, resulting in a cleaner signature that is likely more representative of the real airplane signature.

The VS4 strut has a straight sting that compromises the lower aft end of the Boom3 model, but apparently the effects due to this compromise are not seen in this part of the signature at Mach 1.6. The strongest effect of the VS4 strut is in the large shock at X = -60 in the Mach 1.6 plot, and at -46 in the Mach 1.8 plot, which is from the swept section of the strut that supports the sting. It was learned in the testing that this swept section was not far enough aft to keep its shock from overtaking the signature from the aft end of the model by the time the pressure field reached the rail, thus this strut was deemed unusable.

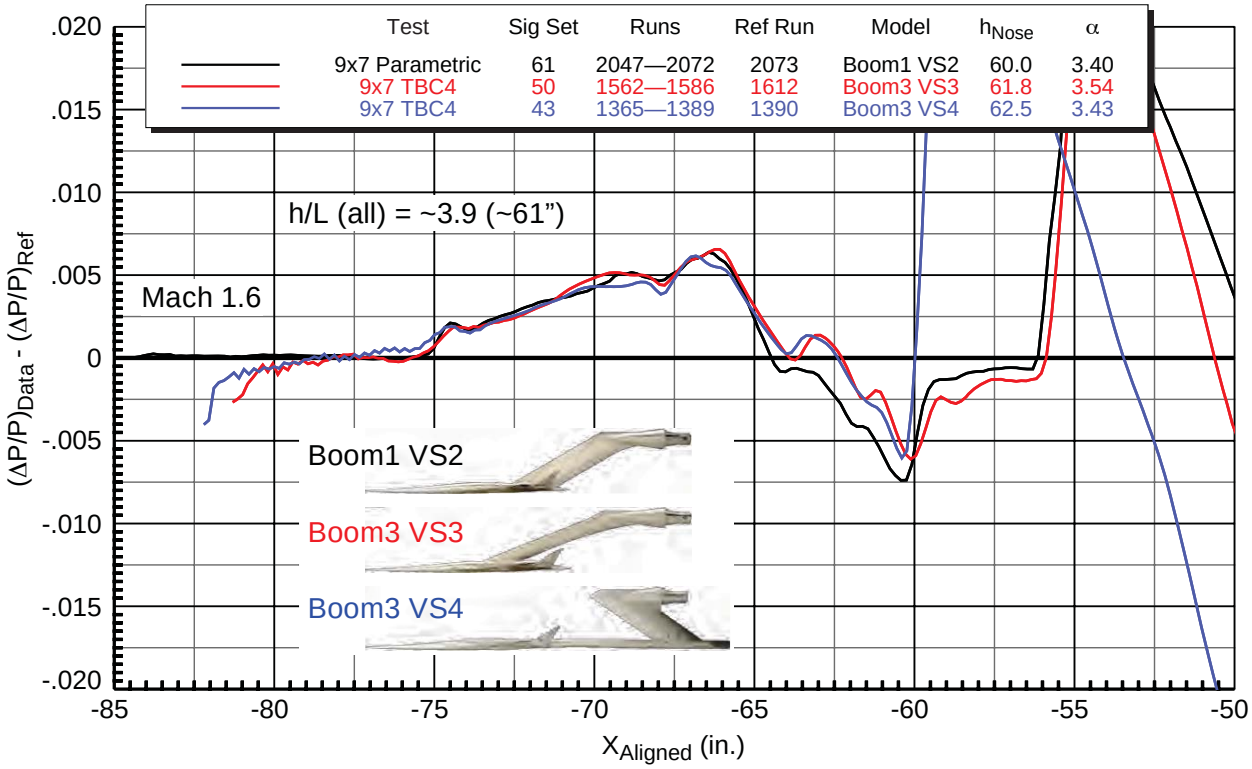

Figure 7–28. Boom model mounting strut effects, *X* and *Z* sweeps 14-in. aft rail, *M* = 1.60, *HumidAvg* = 245 ppm

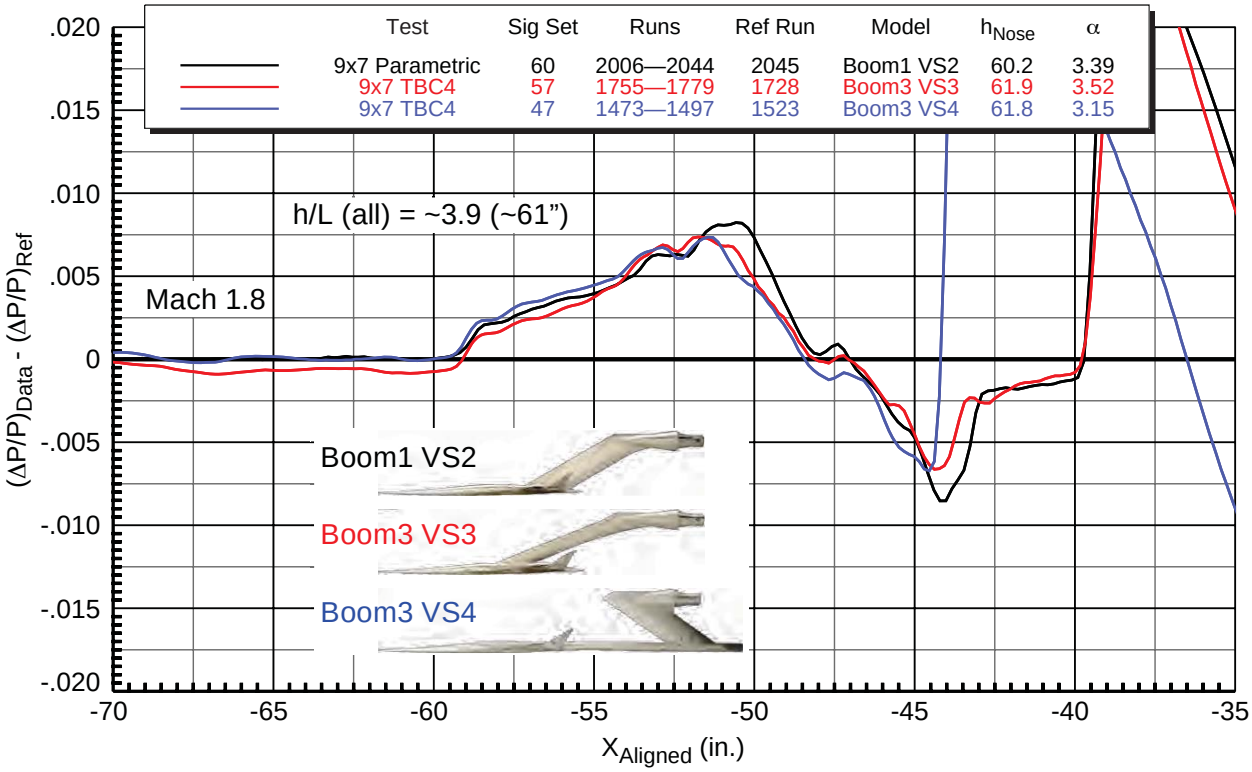

Figure 7–29. Boom model mounting strut effects, *X* and *Z* sweeps 14-in. aft rail, *M* = 1.80, *HumidAvg* = 243 ppm

7.9. Effect of Nacelles and Vertical Tails

The Boom1 model was run with nacelles and vertical tails off (abbreviated "n/v off" herein) only in the 8x6 TBC3 test—refer to Figure 4–15 for CAD views of these components with the model. Comparison plots of these components on and off are presented in Figures 7–30 and –31 with 14-in. rail data at Mach 1.56 and 1.78 and at heights of 59 and 49 in., respectively. In the first figure, the n/v-off signature has an overall higher pressure level than the signature for the full configuration, but this is believed to be just an artifact of the tunnel flow variations between these sets of runs, since there is no reason why the model signature should be different ahead of the vertical tails, and many of the 8x6 runs had similar offsets. The shock from the verticals is apparent near the rear of the signature at X = 217 in the full-configuration curve. This shock is considered to be primarily from the verticals and not the nacelles, since the latter are shielded by the wing. In the second figure, at Mach 1.78, the full-configuration and n/v-off curves do overlap for most of the signature until the shock from the tails at X = 216.

The Boom3 model was run with baseline N1 nacelles and alternate nacelles N3 and N4 in the 9x7 TBC4 test at Mach 1.6, and a comparison plot of these three nacelle configurations is shown in Figures 7–32. The significant differences among the nacelles are visible around X = -60. The shocks for the alternate nacelles occur a little earlier in the signature relative to the shock for the baseline nacelles.

Alternate nacelles N3 and N4 of the same design were also fabricated for the Performance model, and a comparison plot of these with the baseline nacelle N1 is given in Figure 7–33. The primary effect of the nacelles is very subtle in this figure—the N3 and N4 nacelles create slight rises in pressure in the main expansion region (X = -54 to -46), and possibly have continued effects aft of this, but the differences among the signatures forward of this region are not likely due to the nacelle variations.

In the following figure, 7–34, the inlet and nozzle portions of the N3 and N4 nacelles are switched: one combination (sig set 24) has the inlet (NI4) for the N4 nacelle with the nozzle (NN3) for the N3 nacelle, and the other (sig set 37) has the opposite combination, NI3 NN4. The plot shows the same baseline N1 nacelle runs as in the previous figure for reference. The latter combination of inlet and nozzle sections, NI3 NN4, did not make much difference relative to a pure N4 nacelle configuration (compare to Figure 7–33), but the NI4 NN3 combination did cause a significant rise in pressure along the main expansion, particularly near X = -52. This rise, having been measured at roughly 60 in. from the rail, was probably a small shock wave coming from some part of the nacelle, which would be seen if a closer measurement had been taken (all the signatures in the TBC4 test were measured at nominally 60 in.).

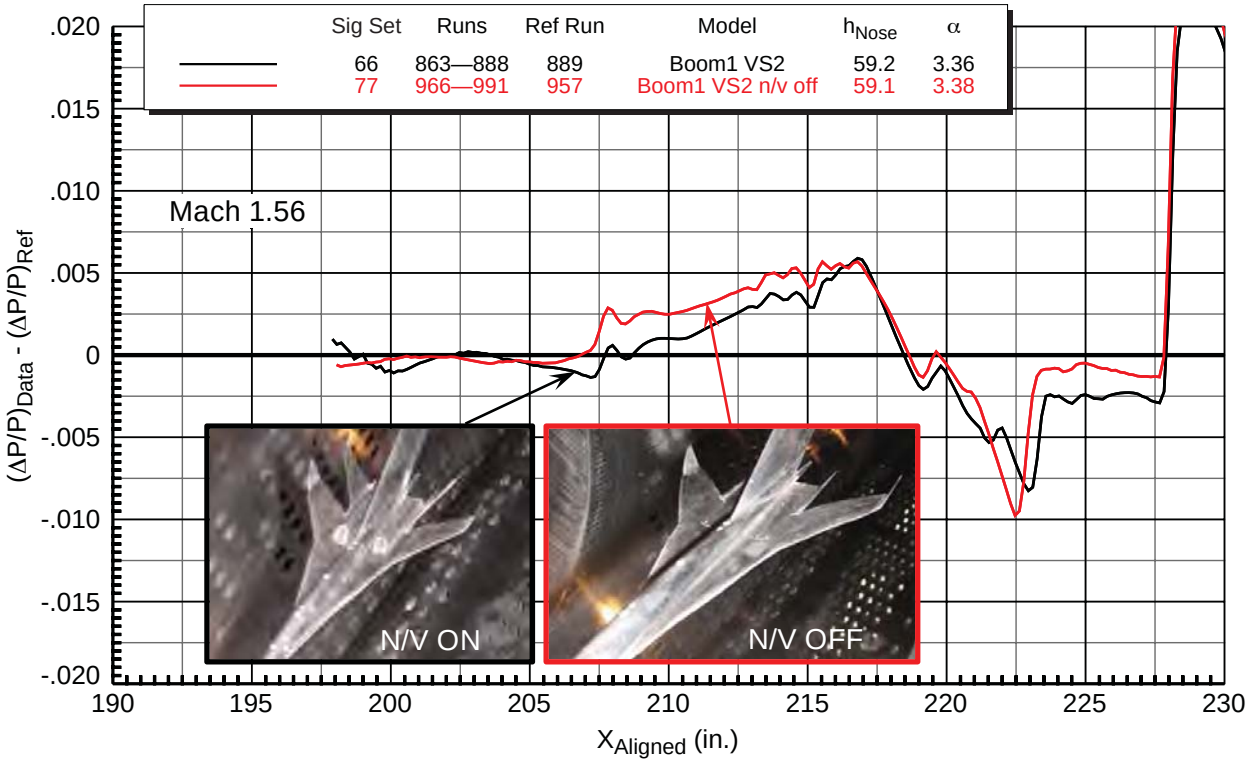

Figure 7–30. Effects of Boom1 model nacelles and vertical tails, *X* sweeps (0” to 12”, 0” to 8”) 8x6 TBC3 test, 14-in. rail, *M* = 1.56, *HumidAvg* = 181 ppm

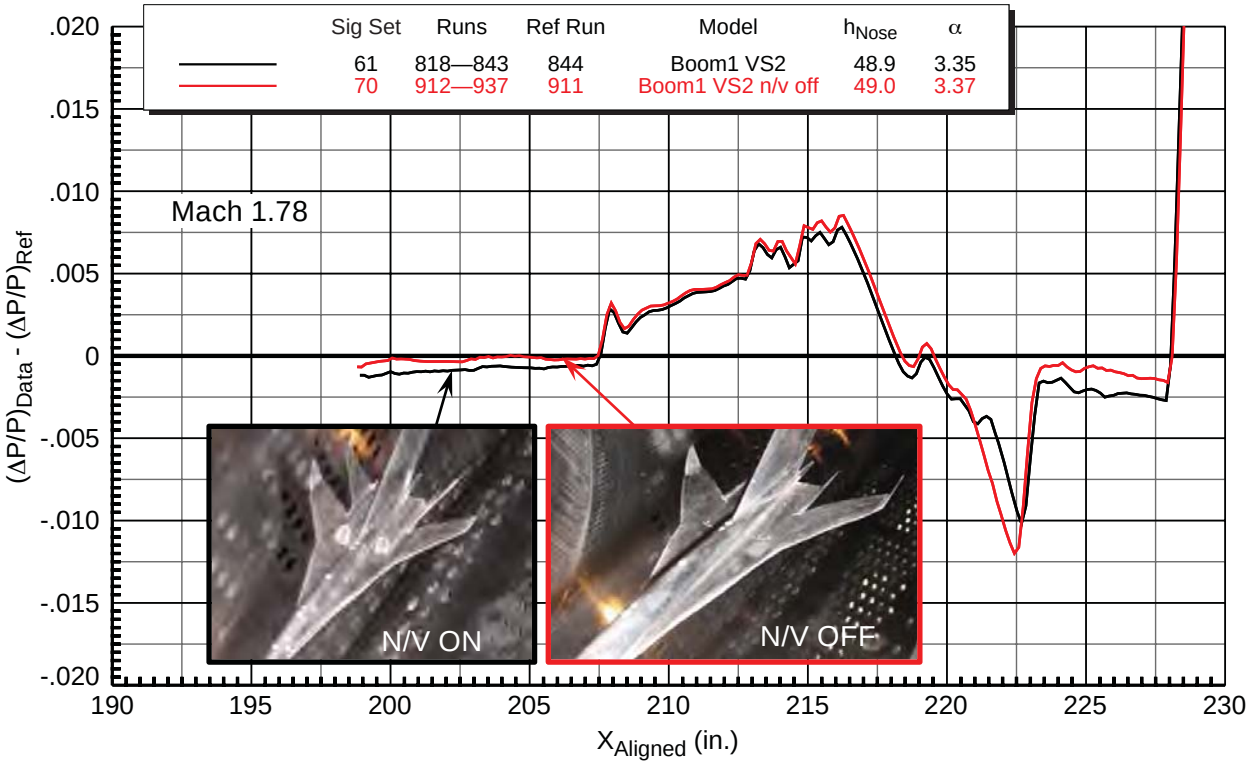

Figure 7–31. Effects of Boom1 model nacelles and vertical tails, *X* sweeps (0” to 8”) 8x6 TBC3 test, 14-in. rail, *M* = 1.78, *HumidAvg* = 81 ppm

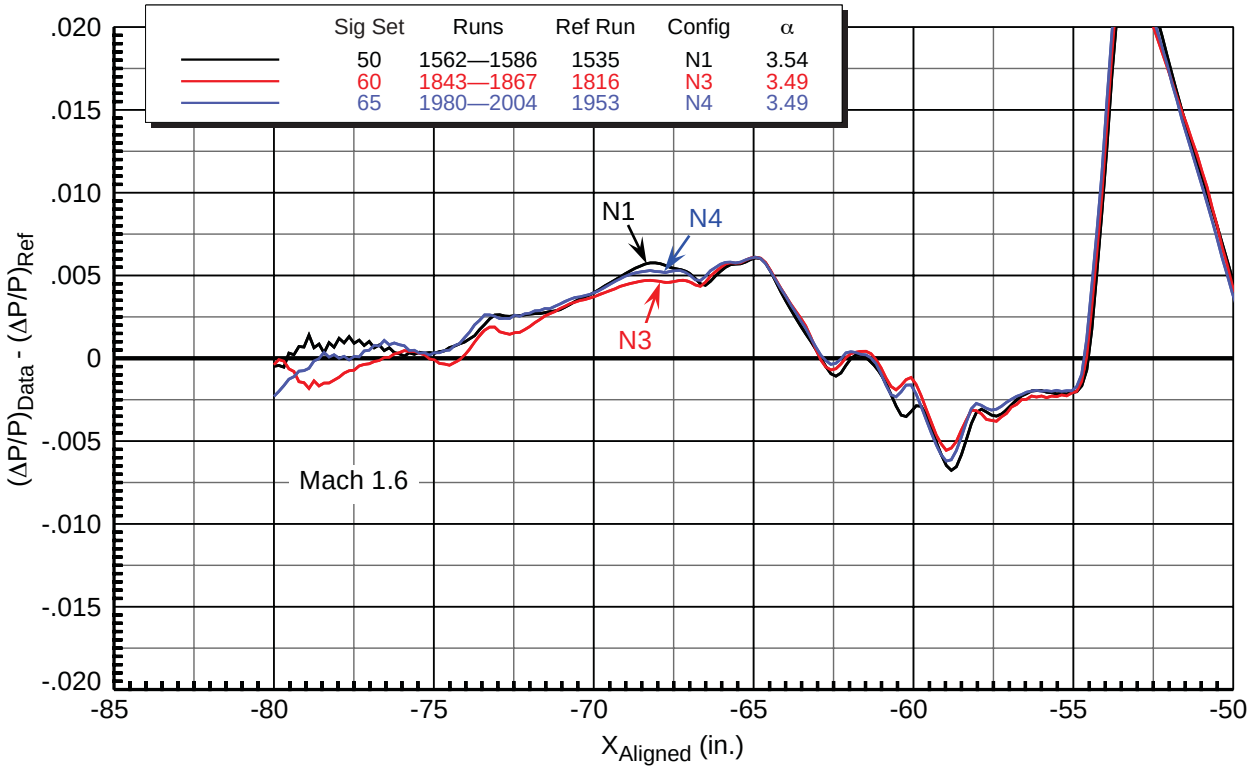

Figure 7–32. Effects of Boom3 model nacelle variations(N1, N3, N4), *Z* sweeps (59” to 65”) 9x7 TBC4 test, 14-in. aft rail, *M* = 1.60, *HumidAvg* = 225 ppm

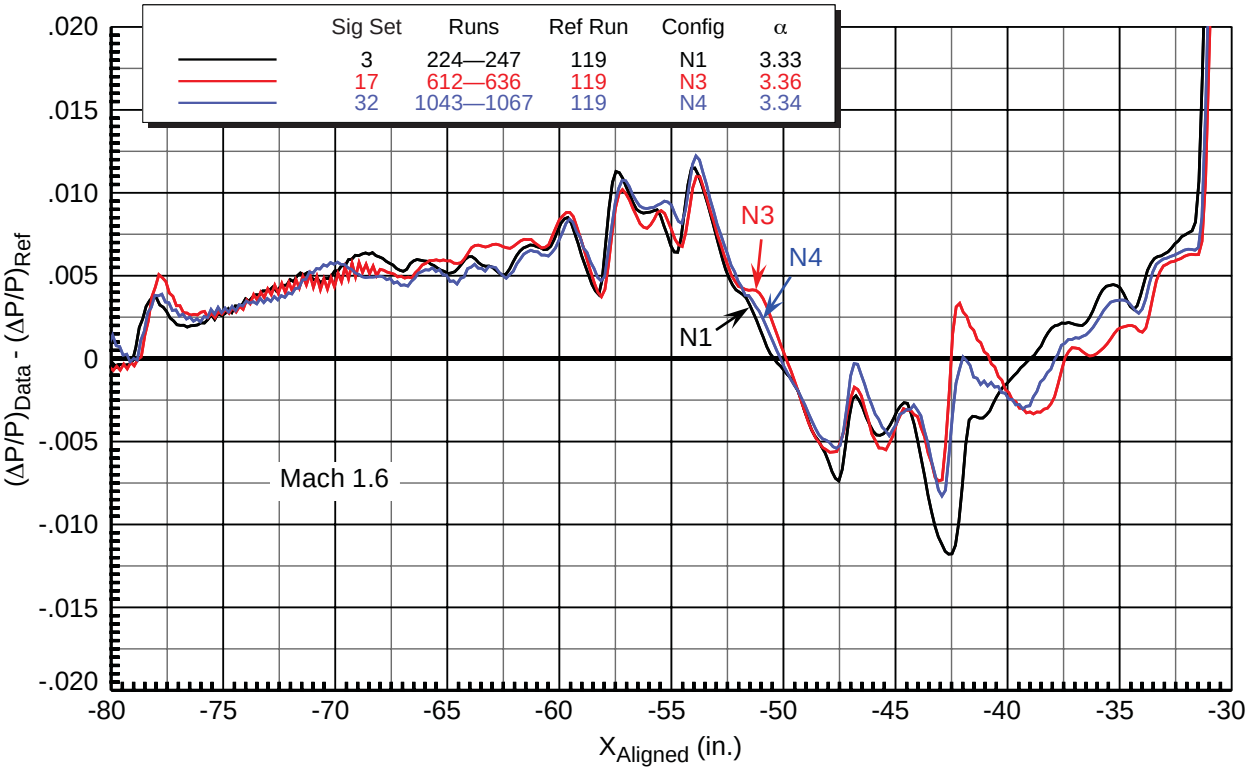

Figure 7–33. Effects of Performance model nacelle variations (N1, N3, N4), *Z* sweeps (59” to 65”) 9x7 TBC4 test, 14-in. aft rail, *M* = 1.60, *HumidAvg* = 220 ppm

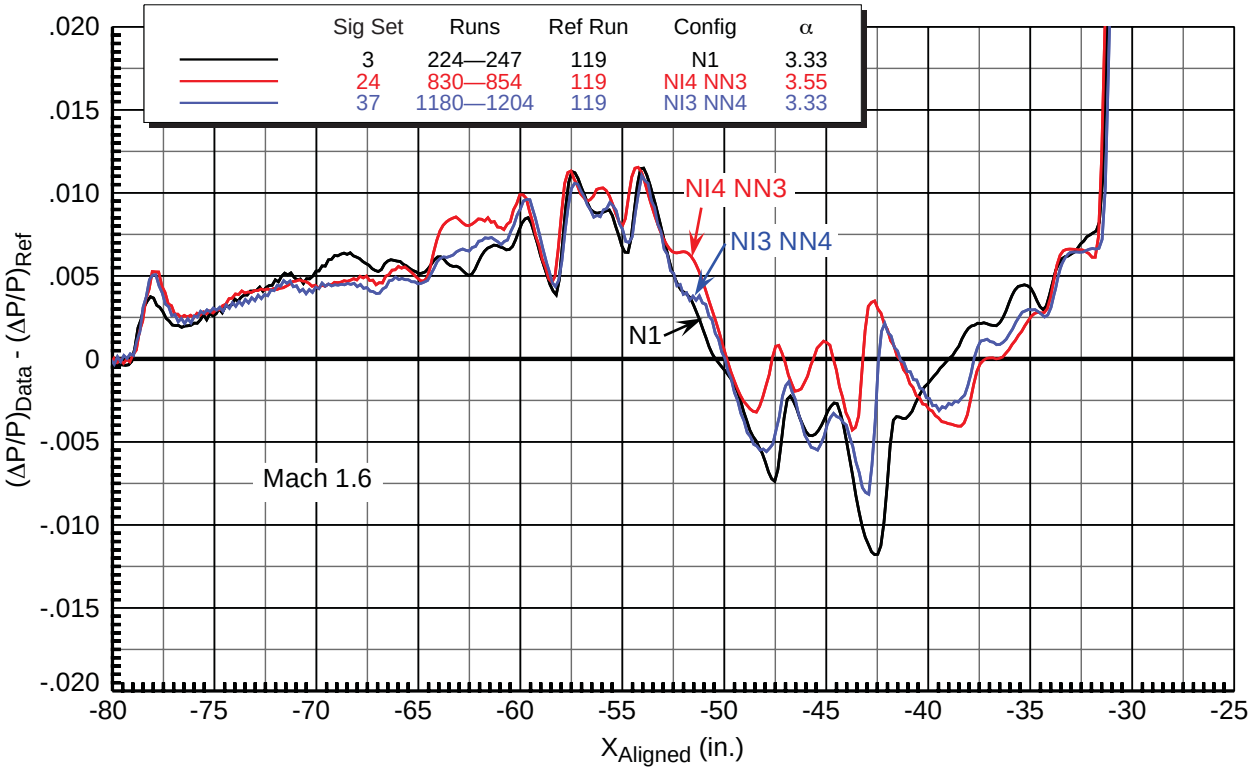

Figure 7–34. Effects of Performance model nacelle variations (N1, NI4-NN3, NI3-NN4) *Z* sweeps (59” to 65”), 9x7 TBC4 test, 14-in. aft rail, *M* = 1.60, *HumidAvg* = 236 ppm

7.10. Effect of Mach Number

The effect of Mach number (1.6 and 1.8) on the sonic boom signatures of Boom1 VS2, Boom3 VS3, and Performance models from the two 9x7 tests are presented in Figures 7–35 through –39. The first three figures are from *X* sweeps of the Boom1 model in the 9x7 parametric test on the three different rail configurations run in this test: the 14-in. forward rail, the 2-in. forward rail, and the 14-in. aft rail. All of these figures show the overall higher pressure levels and shock peaks in the Mach 1.8 data as expected.

The latter two figures are from *Z* sweeps of the Boom3 and Performance models in the 9x7 TBC4 test on the 14-in. aft rail. The Boom3 data in Figure 7–38 show higher pressure peaks for Mach 1.8, but the overall level difference between the two Mach numbers is not present as it is in the three previous figures. One might be led to believe that the higher model height (60 in., vs. 30 in. for Figures 7–35 and –36) would be the reason why there is not a greater difference in overall pressure levels, but the last previous figure (7–37) for the Boom1 model is also at 60-in. height above the rail, so it is puzzling as to why the Boom3 model did not show a similar distinction.

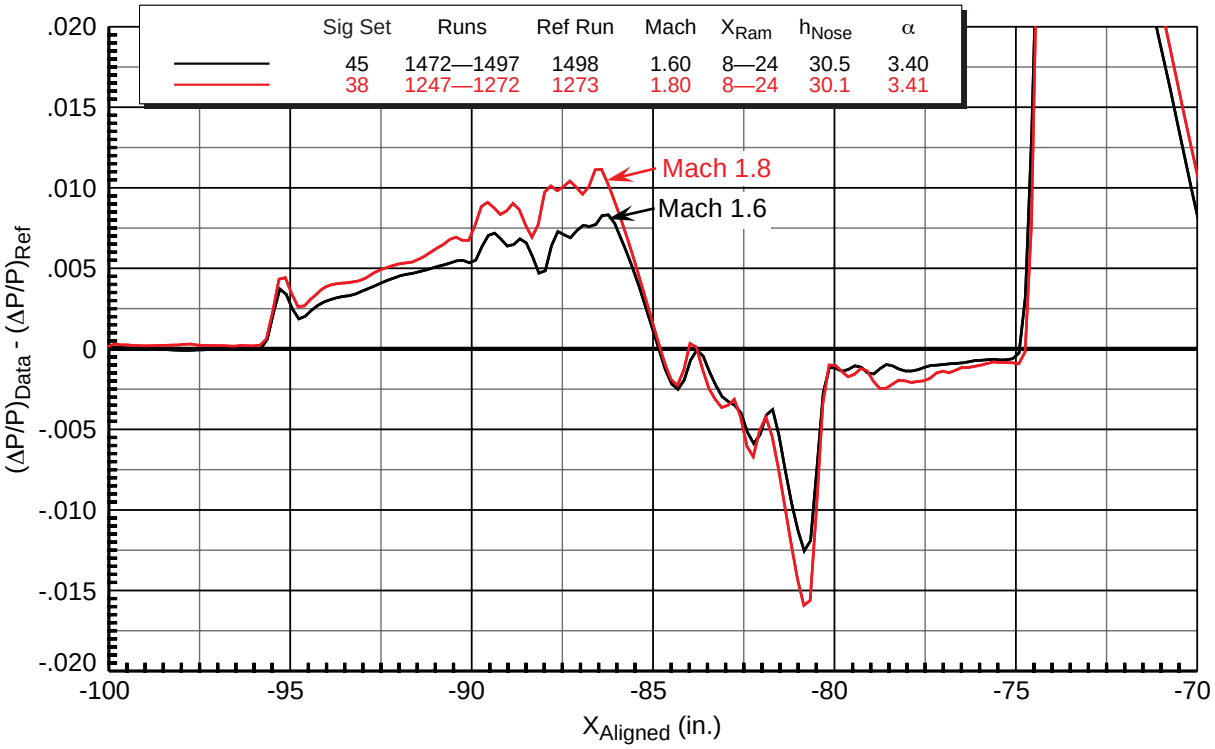

Figure 7–35. Effect of Mach number for Boom1 VS2 model, *X* sweeps (8" to 24") 9x7 parametric test, 14-in. forward rail, *h* = 30 in., *HumidAvg* = 308 ppm

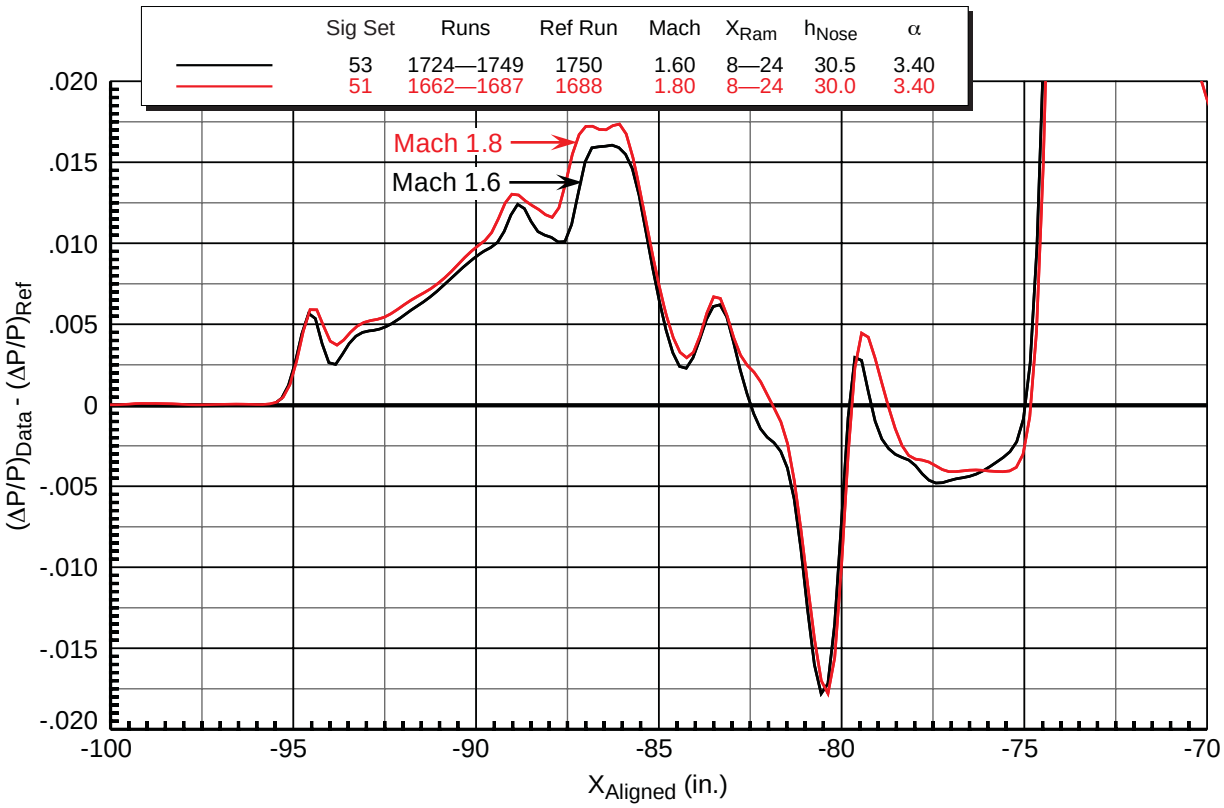

Figure 7–36. Effect of Mach number for Boom1 VS2 model, *X* sweeps (8" to 24") 9x7 parametric test, 2-in. forward rail, *h* = 30 in., *HumidAvg* = 320 ppm

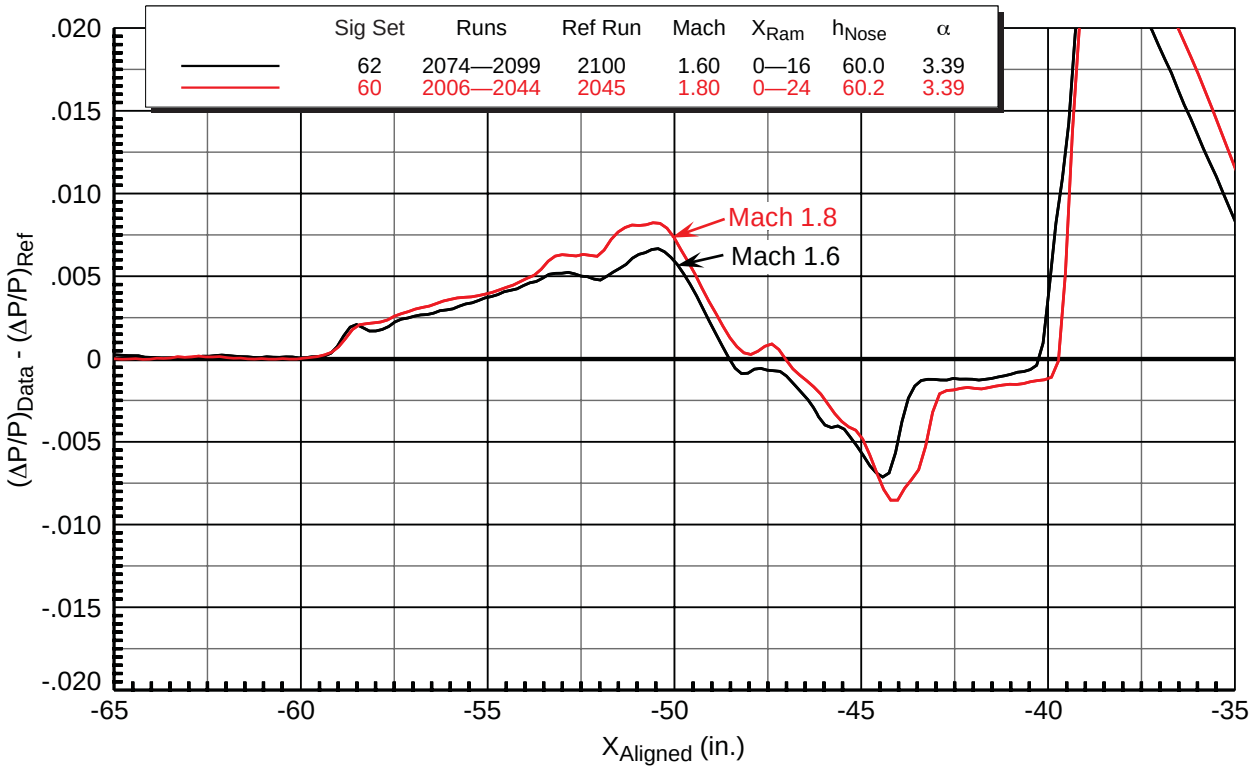

Figure 7–37. Effect of Mach number for Boom1 VS2 model, *X* sweeps (0” to 16”, 0” to 24”) 9x7 parametric test, 14-in. aft rail, *h* = 60 in., *HumidAvg* = 287 ppm

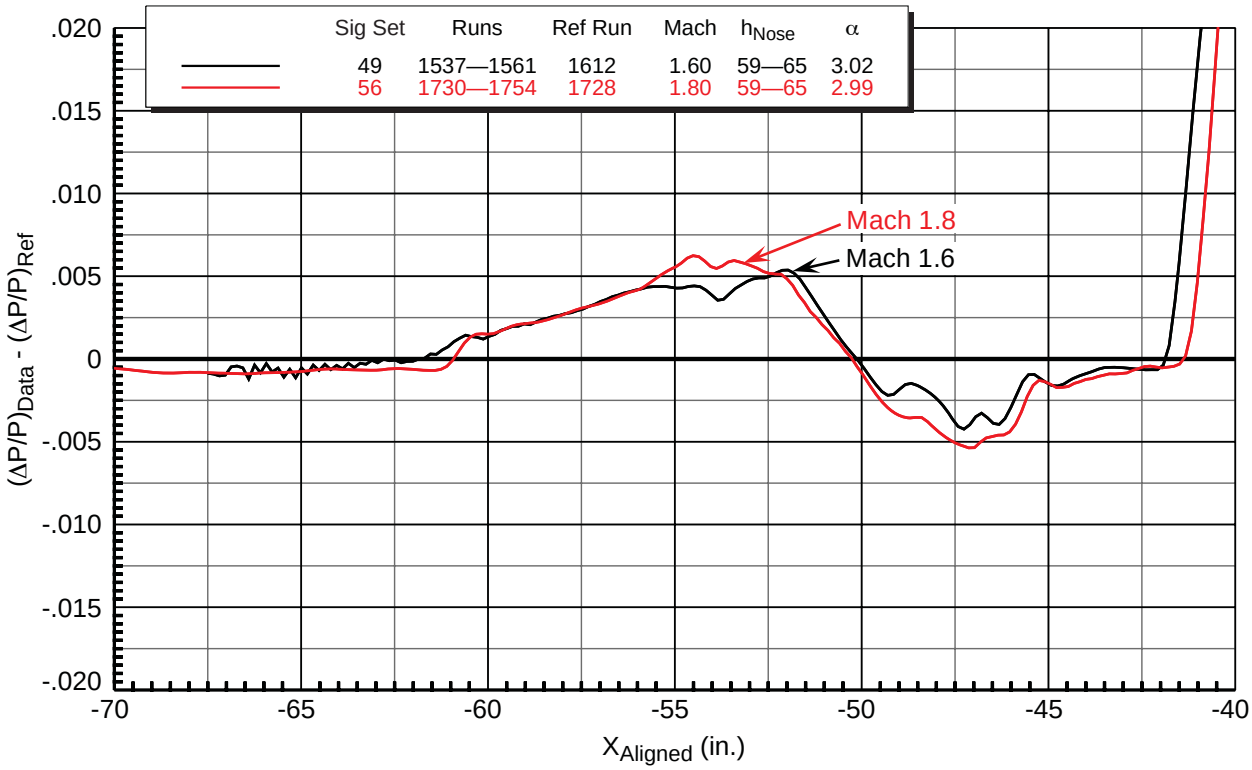

Figure 7–38. Effect of Mach number for Boom3 VS3 model, *Z* sweeps (59” to 65”) 9x7 TBC4 test, 14-in. aft rail, *HumidAvg* = 227 ppm

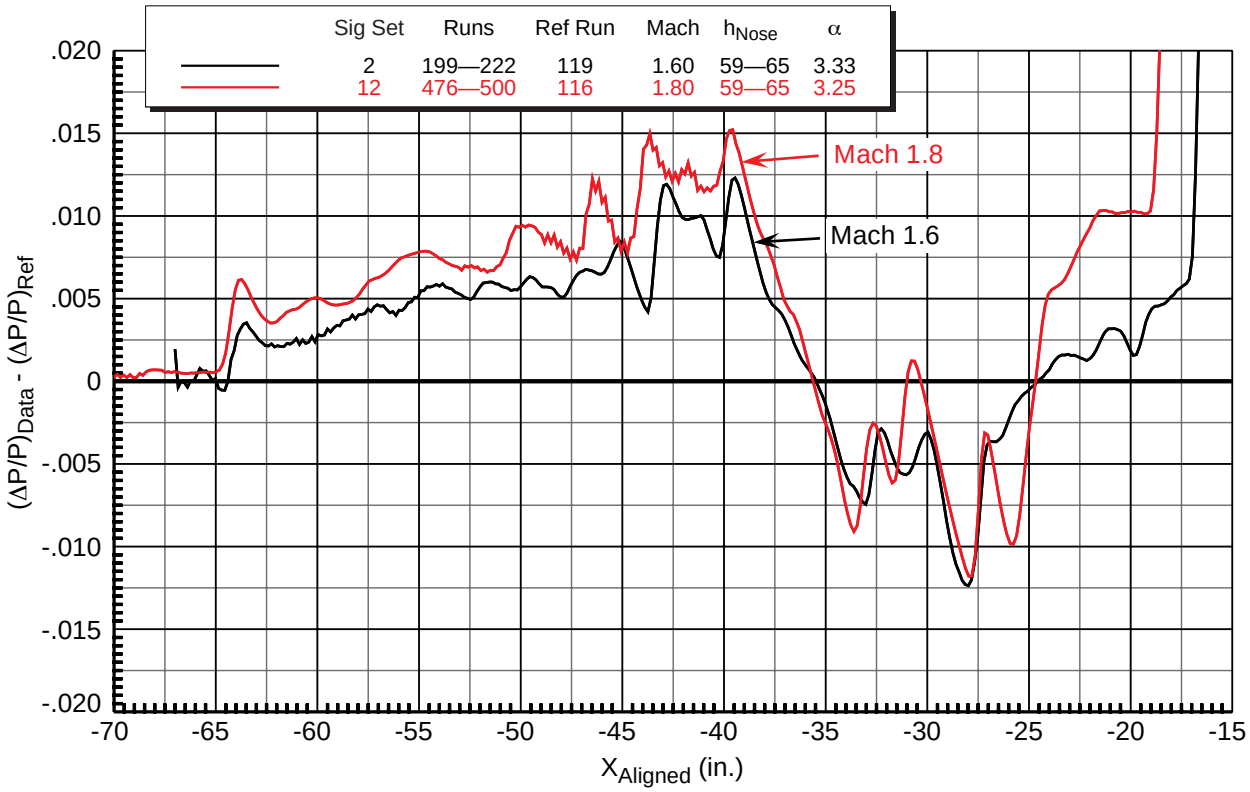

Figure 7–39. Effect of Mach number for Performance sting+contour model, *Z* sweeps (59” to 65”) 9x7 TBC4 test, 14-in. aft rail, *HumidAvg* = 292 ppm

7.11. Effect of Total Pressure

Figure 7–40 shows the effect of total pressure in the 9x7 wind tunnel on the sonic boom signatures of the Boom1 VS2 model at a Mach number of 1.6 and a nominal height of 30 in. from the 14-in. forward rail. Data at pressures of 1450 and 2300 psf are shown. Overall, the agreement between the two signatures is very good, though the higher-pressure run does show slightly higher shock peaks throughout the signature. As discussed in Section 6.3.2, the higher pressure gives a higher Reynolds number, and in general, less flow separation, so it seems reasonable that these would be the causes of the higher shock peaks.

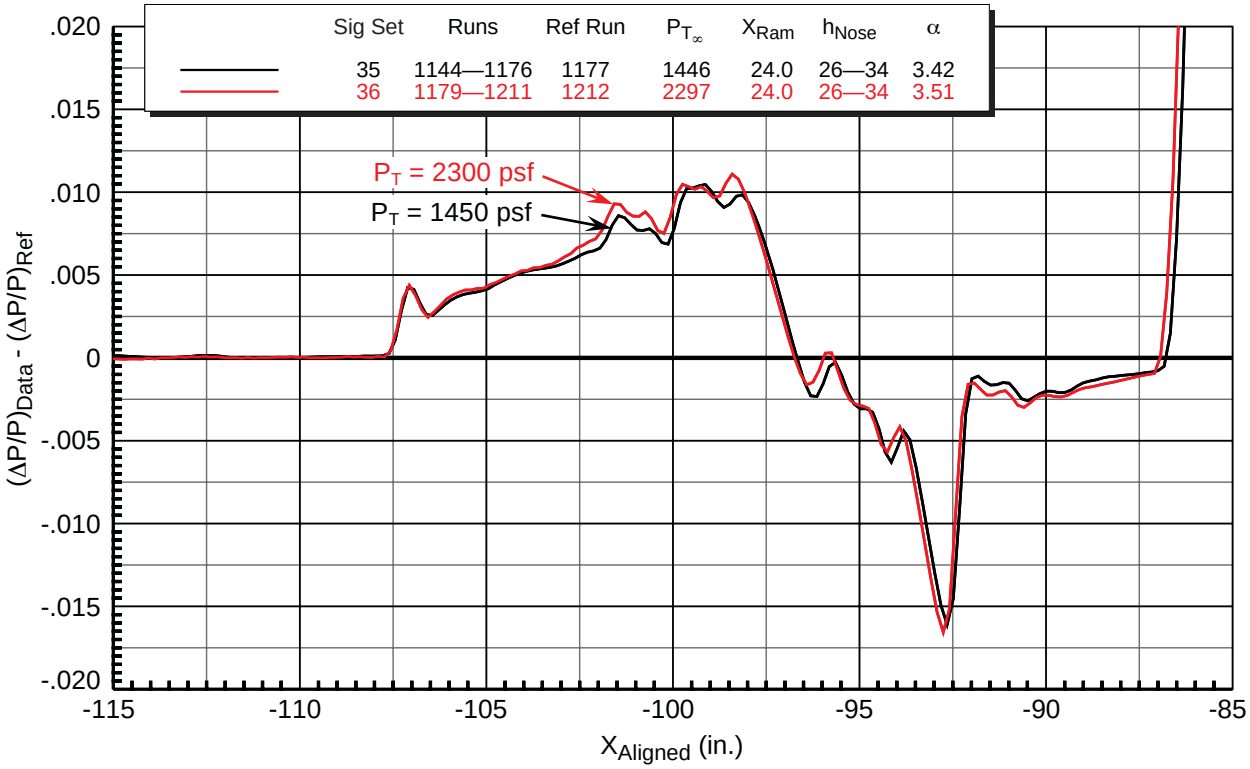

Figure 7–40. Effect of total pressure for Boom1 VS2 model, *Z* sweeps (26” to 34”) 9x7 parametric test, 14-in. forward rail, *M* = 1.6, *HumidAvg* = 298 ppm

7.12. Effect of Angle of Attack

Figures 7–41 through –43 show the effects of angle of attack on the sonic boom signatures of the Boom3 and Performance models from *Z* sweeps (59–65 in.) in the 9x7 TBC4 test. Angles from 2.5° to 4° are shown for the Boom3 model at Mach 1.6 in the first figure, and the trends of the overall pressure levels and shock peaks for the lifting parts of the model (i.e., aft of the nose shock) are consistent with the increasing lift causing stronger sonic boom signatures. Also note that the small shock at the bottom of the main expansion (X = -61) for the lowest angle of attack grows in strength and moves forward in the signature as the angle is increased.

Similar trends of increasing pressure levels and shock peaks with angles of attack from 2.8° to 3.8° for the Performance model at Mach 1.6 are observed in Figure 7–42, and at Mach 1.8 in Figure 7–43 for angles from 3.3° to 3.8°.

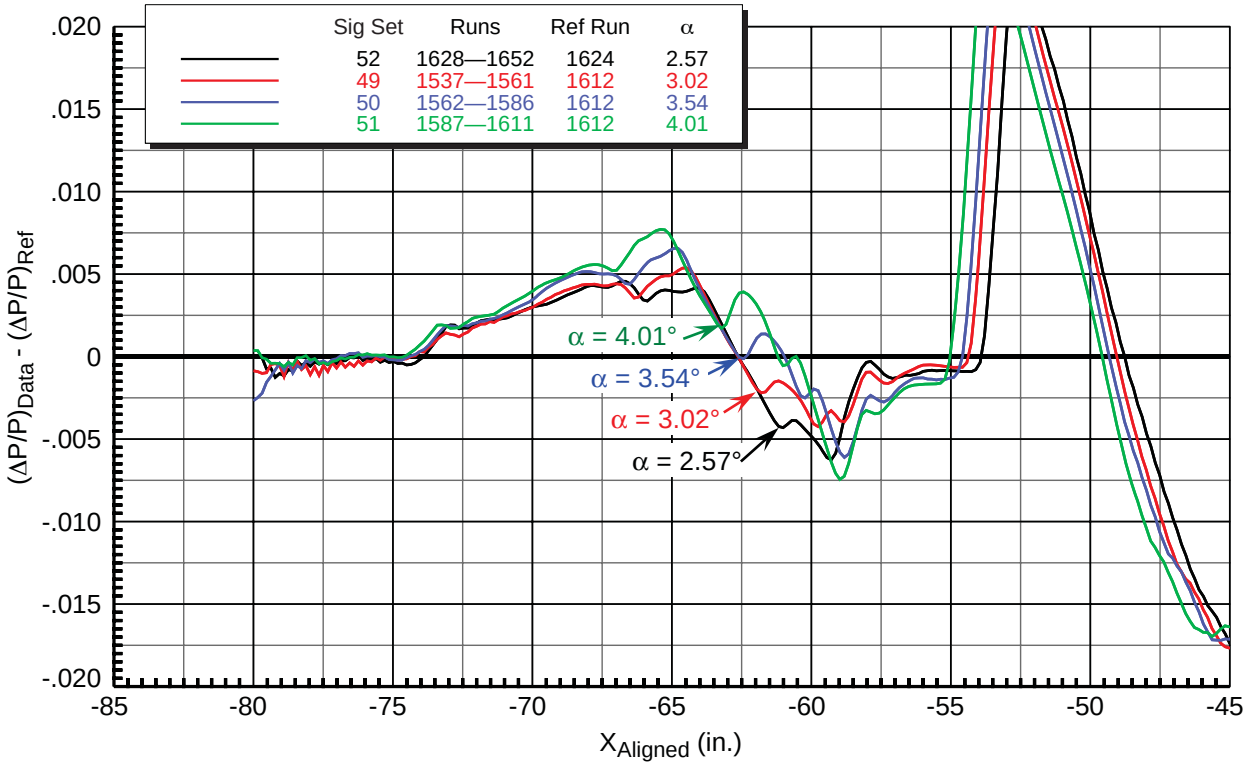

Figure 7–41. Effect of angle of attack for Boom3 VS3 model, *Z* sweeps (59” to 65”) 9x7 TBC4 test, 14-in. aft rail, *M* = 1.60, *HumidAvg* = 230 ppm

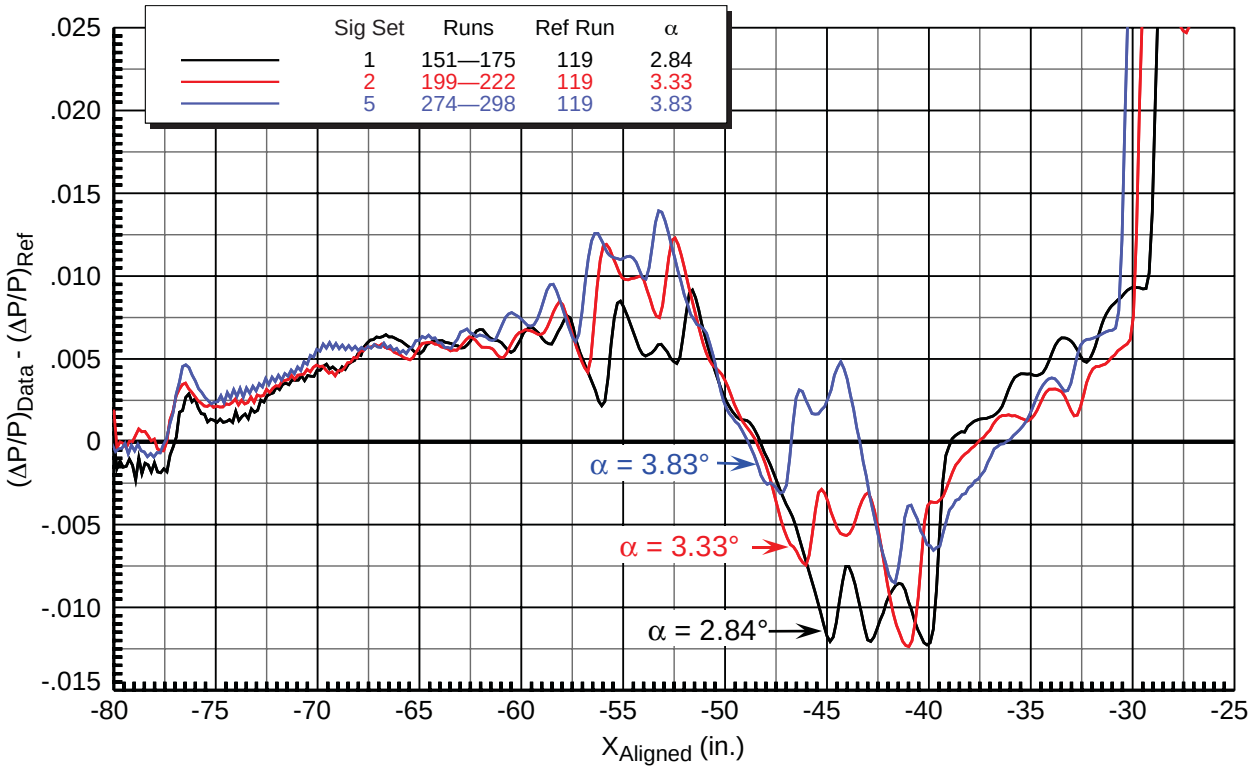

Figure 7–42. Effect of angle of attack for Performance sting+contour model, *Z* sweeps (59” to 65”) 9x7 TBC4 test, 14-in. aft rail, *M* = 1.60, *HumidAvg* = 278 ppm

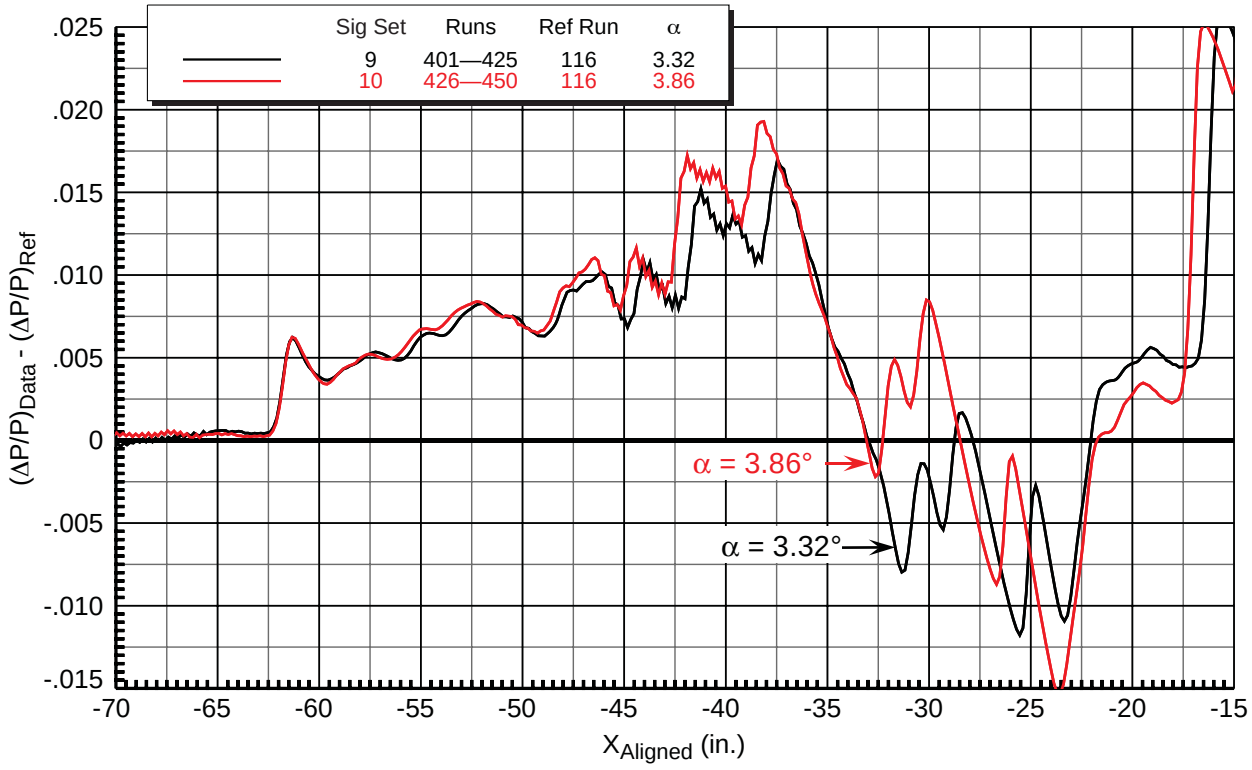

Figure 7–43. Effect of angle of attack for Performance sting+contour model, *Z* sweeps (59” to 65”) 9x7 TBC4 test, 14-in. aft rail, *M* = 1.80, *HumidAvg* = 237 ppm

7.13. Effect of Off-Track Angle

The boom loudness is not only critical for the ground track under the flight path, but also off to both sides of the ground track. Signatures at off-track angles up to 45° are compared to the 0° on-track signatures for the Boom1, Boom3, and Performance models in Figures 7–44 through –47. The first figure shows the signatures for the Boom1 model at a height of 30 in., Mach 1.8, for angles of 0°, 20°, 30°, and 40°, where the off-track angle signatures all have higher maximum pressure peaks than the on-track signature, and the gradients in the main expansions after the maximum peaks are also steeper for the off-track angles. Note also that the on-track signature shows small shocks just after the main expansion, probably for the nacelles and vertical tails, whereas none of the off-track signatures show these.

Figure 7–45 shows signatures for the Boom3 model at a height of 60 in. (nominally), Mach 1.6, for angles of 0°, 15°, 30°, and 45°. Again, the off-track signatures have slightly higher maximum pressure peaks and do not show the small shocks just after the main expansion.

On- and off-track signatures for the Performance model are shown for the same height and angles as for the Boom3 model, at Mach 1.6 and 1.8 in Figures 7–46 and –47, respectively. The same comments as for the other two models apply here as well, but in particular for the Mach 1.8 data, Figure 7–47, the maximum and minimum pressure peaks for the 30° and 45° off-track angles are substantially higher than those for the two lower angles, indicating that the boom loudnesses for these 30° and 45° angles are probably a bit higher also.

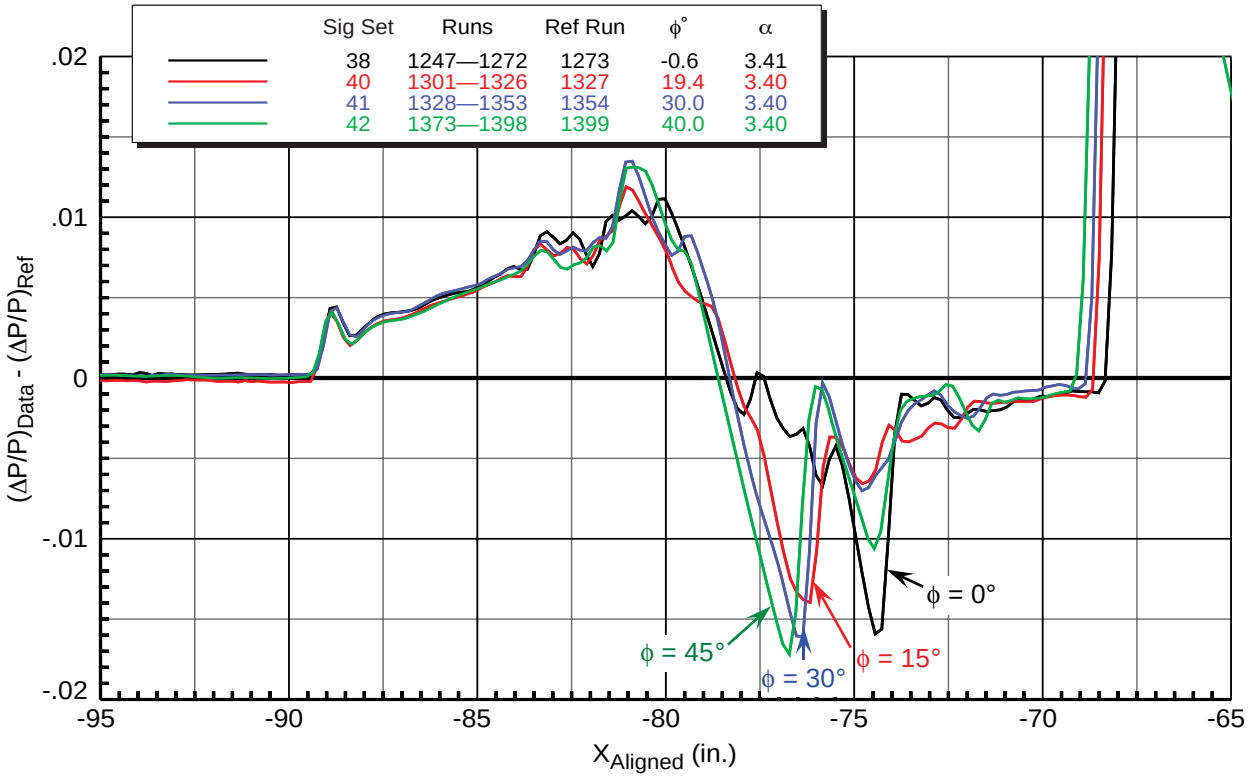

Figure 7–44. Effect of off-track angle for Boom1 VS2 model, *X* sweeps (8" to 24"), h_{Nose} = 30.1 in. 9x7 parametric test, 14-in. forward rail, *M* = 1.80, *HumidAvg* = 306 ppm

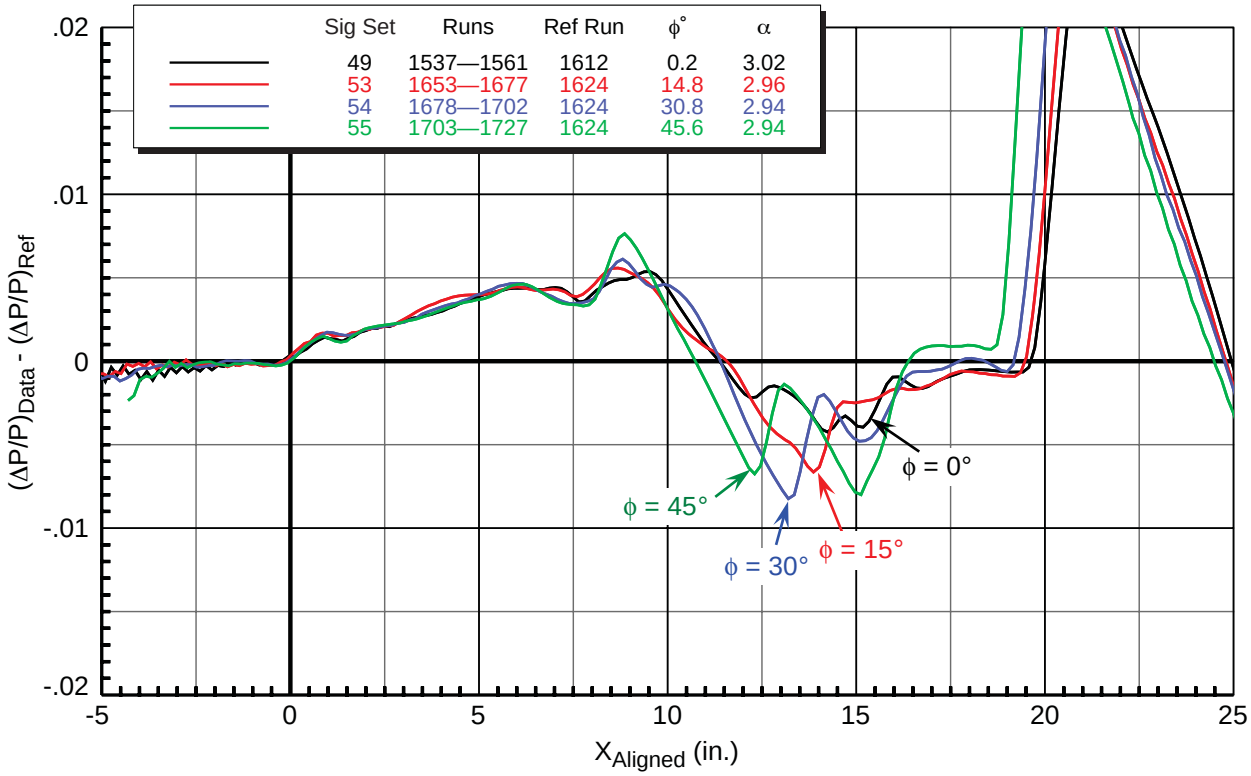

Figure 7–45. Effect of off-track angle for Boom3 VS3 model, *Z* sweeps (59” to 65”) 9x7 TBC4 test, 14-in. aft rail, *M* = 1.60, *HumidAvg* = 226 ppm

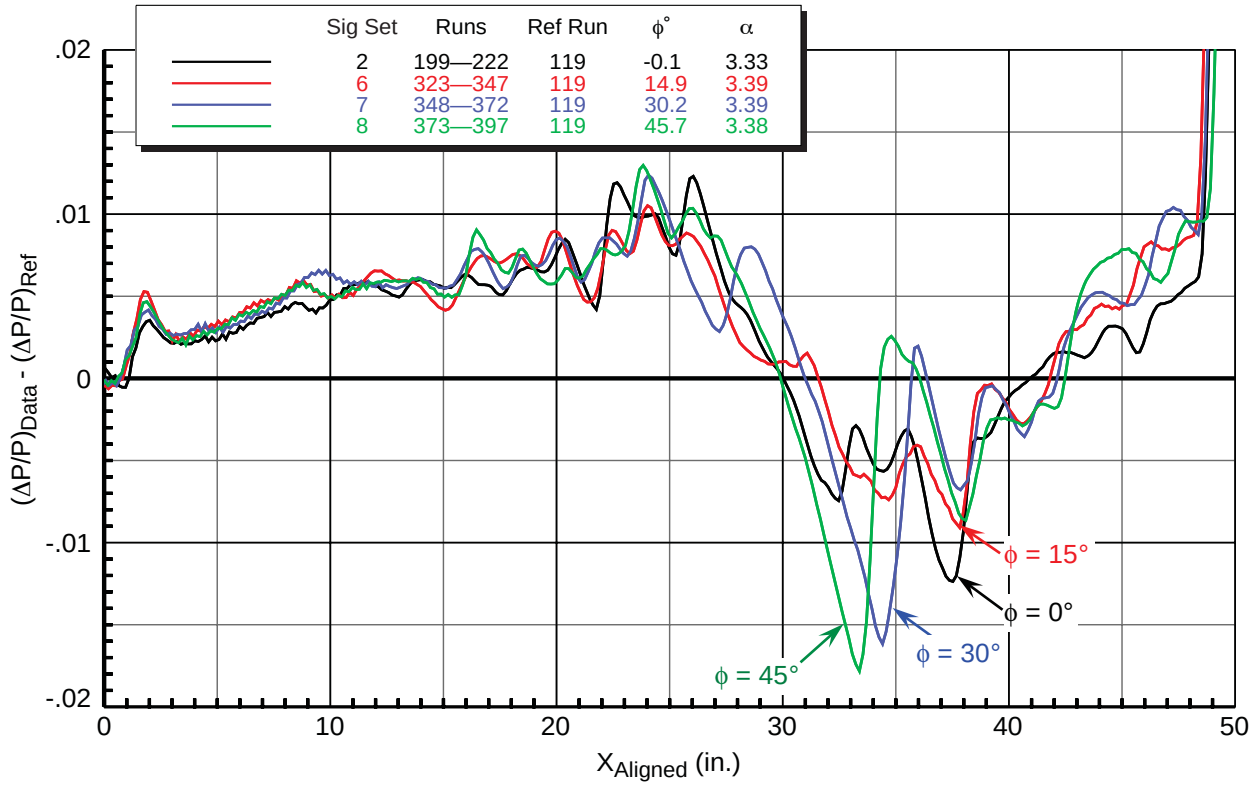

Figure 7–46. Effect of off-track angle for Performance sting+contour model, *Z* sweeps (59” to 65”) 9x7 TBC4 test, 14-in. aft rail, *M* = 1.60, *HumidAvg* = 265 ppm

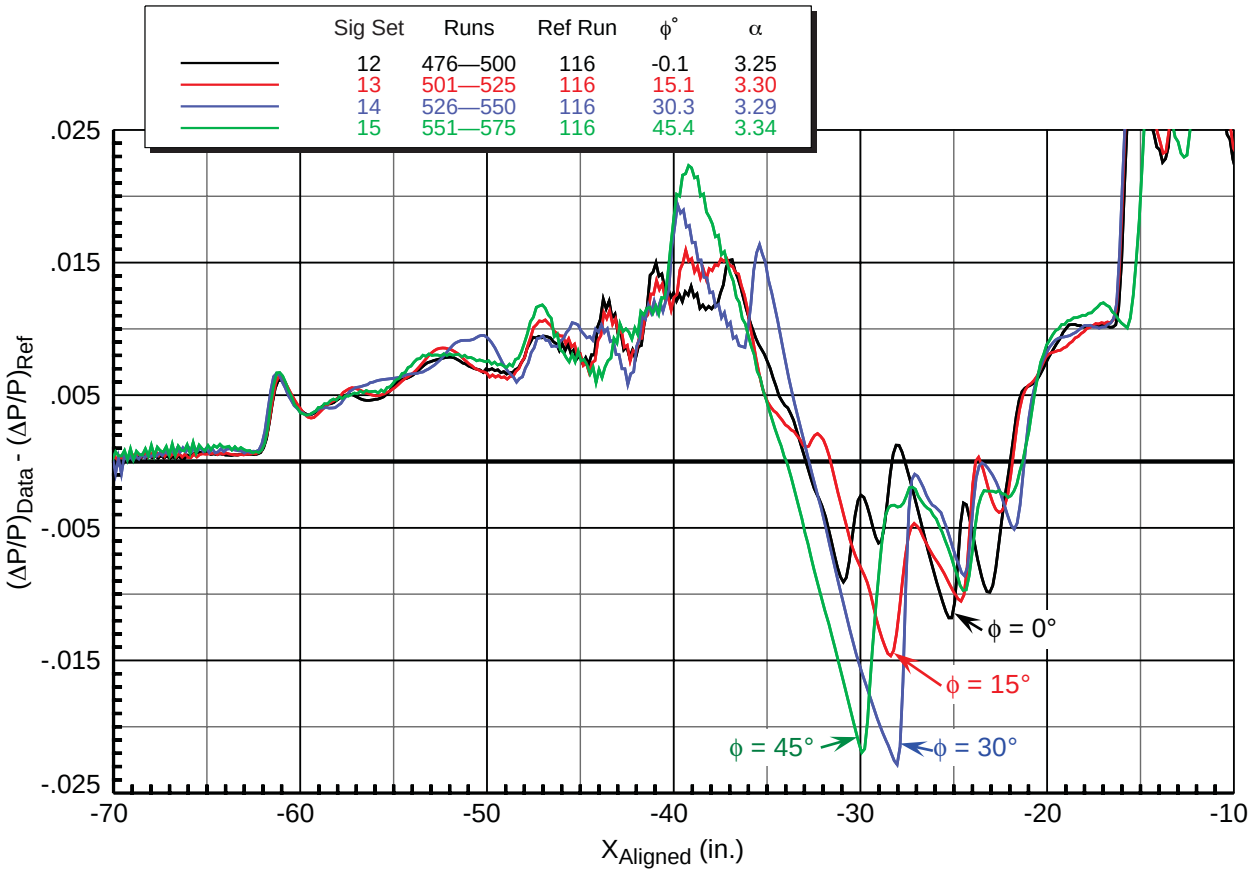

Figure 7–47. Effect of off-track angle for Performance sting+contour model, *Z* sweeps (59” to 65”) 9x7 TBC4 test, 14-in. aft rail, *M* = 1.80, *HumidAvg* = 237 ppm

7.14. Comparisons of Boom1 Model Signatures from 9x7 and 8x6 Tunnels

A few comparison run series between the 9x7 and 8x6 wind tunnels for the Boom1 VS2 model are given in this section in Figures 7–48 through –51, though only in the first figure do the model heights above the rail match. In the latter three figures, the heights do not match so the comparisons presented are meant to be more qualitative, as the runs in these four figures are the only ones available for direct or quasi-direct comparisons between the two facilities for the Boeing models. The 14-in. rail was positioned longitudinally in the 8x6 tunnel such that Boom model heights from approximately 45 to 60 in. could be run while allowing for *X* or *Z* sweeps, so direct comparisons at a height of 30 in. as obtained in many 9x7 runs were not possible.

Figure 7–48 shows the only direct comparison of the Boom1 model signatures measured by the 14-in. rail at an approximate height of 60 in. at a nominal Mach number of 1.6 (1.56 in the 8x6 vs. 1.6 in the 9x7). The 8x6 signature has a lot of waviness and small spikes that are not seen in the 9x7 signature, consistent with data from this rail shown in Figures 7–27 and –28 and others, but the overall shape of the 8x6 curve is similar to that of the 9x7. With *some* of the leading-zero points of the 8x6 curve being below the zero $\Delta P/P$ line, one could argue that the entire curve could be shifted upwards a small amount, which would give a better match with the 9x7 data, but the leading-zero points are not consistent enough to justify this adjustment.

In Figure 7–49, two curves from the 9x7 at heights of 30 and 60 in. are shown for comparison to the 8x6 curve at 49 in. for the Boom1 model signature comparisons at a nominal Mach number of 1.8. Given these substantial height differences, one does not expect the data to match, but one would expect the 49-in. data to lie roughly in between the 30- and 60-in. data. This is not the case, however, as it is generally lower in the front half of the signature than the two curves from the 9x7, although shifting it upward by the amount that the leading-zero points are low would put it in a more reasonable position (aside from the numerous small spikes in the curve).

Comparisons of 9x7 and 8x6 data for the Boom1 model using the 2-in. rail are presented in Figures 7–50 and –51 at nominal Mach numbers of 1.6 and 1.8, respectively. As previously stated, these are not direct comparisons at the same height for each tunnel: in the first figure, the 9x7 data are at a height of 30 in. and the 8x6 at 60 in., and in the second figure, the 9x7 data are at a height of 30 in. and the 8x6 at 49 in. Nonetheless, qualitative comparisons of the runs do show what appear to be reasonable reductions in signature and shock magnitudes from the 30-in. to greater heights, though the reductions here are *greater* than those observed in Figures 7–12 and –13 for the 30- to 60-in. height comparisons from 9x7 data. This is consistent with the low overall levels of the 8x6 signatures in Figures 7–48 and –49 from the 14-in. rail data.

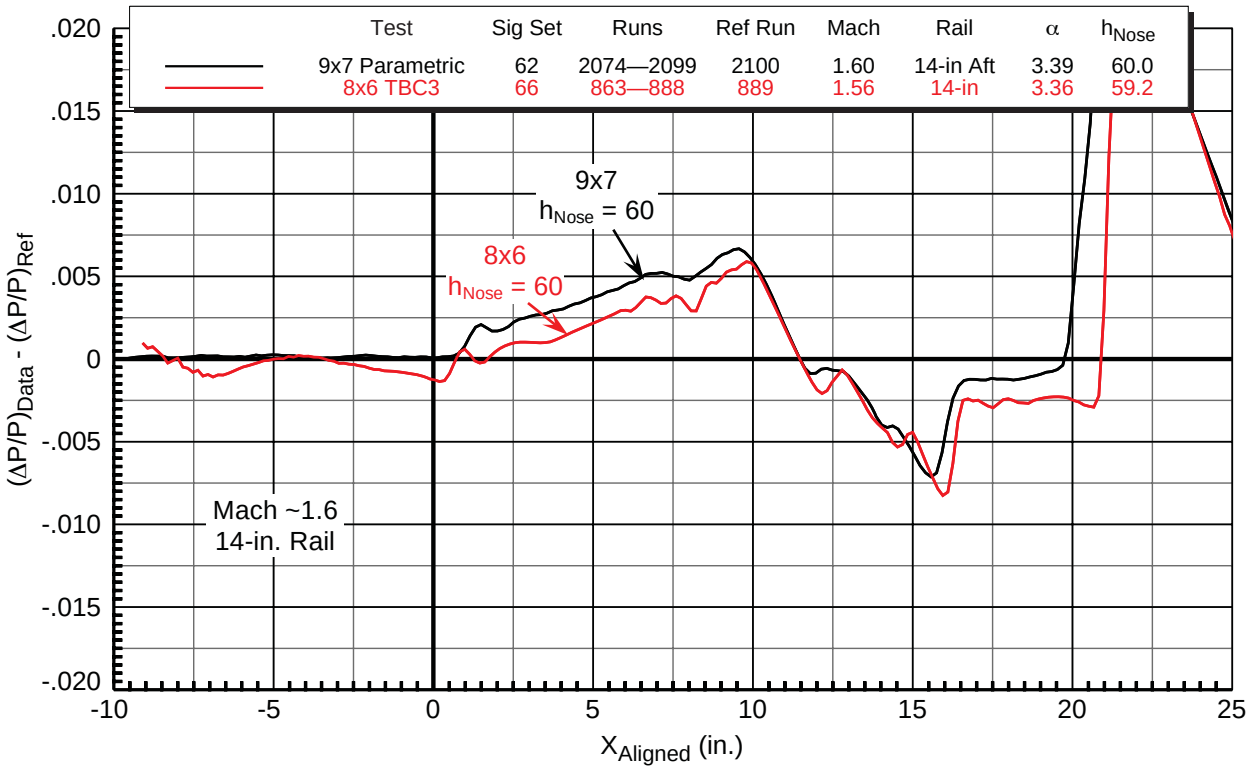

Figure 7–48. Comparison of Boom1 VS2 model signatures from 9x7 and 8x6 wind tunnels 14-in. rail, M = ~1.6, h_{Nose} = 60 in.

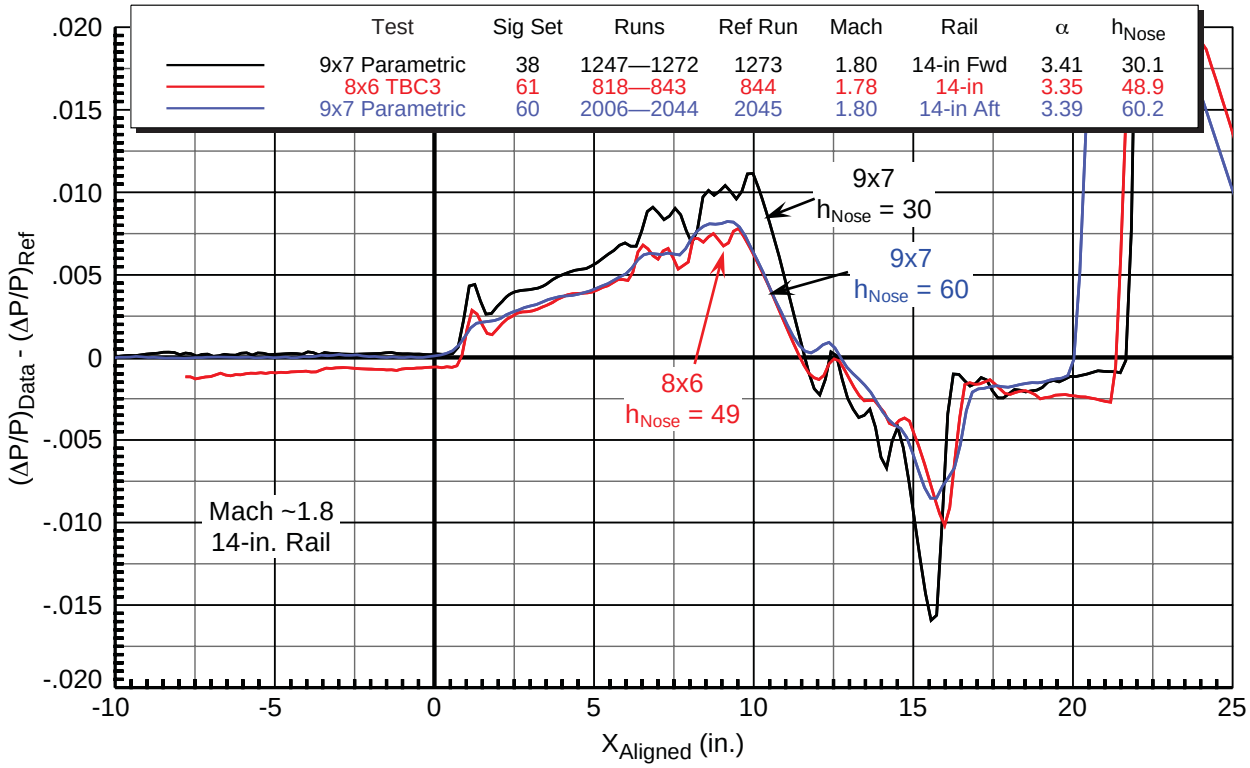

Figure 7–49. Comparison of Boom1 VS2 model signatures from 9x7 and 8x6 wind tunnels 14-in. rail, M = ~1.8, h_{Nose} = 30 to 60 in.

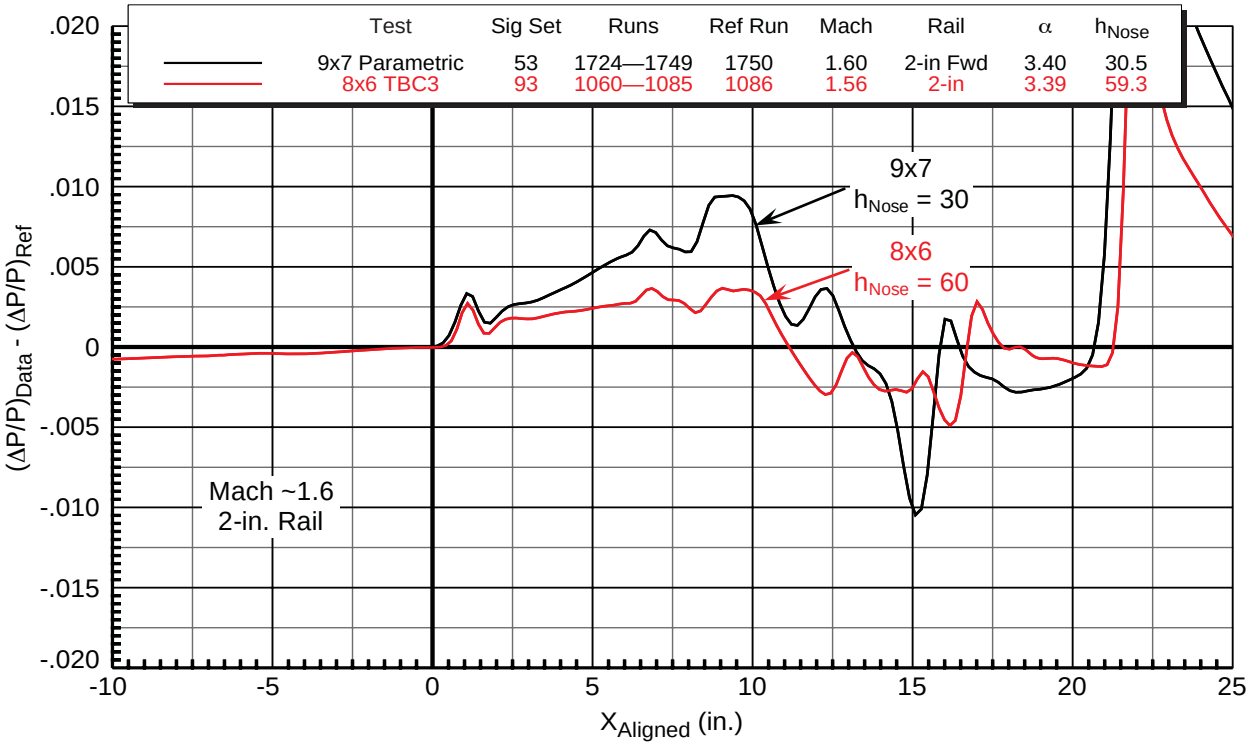

Figure 7–50. Comparison of Boom1 VS2 model signatures from 9x7 and 8x6 wind tunnels 2-in. rail, M = ~1.6, h_{Nose} = 30 to 60 in.

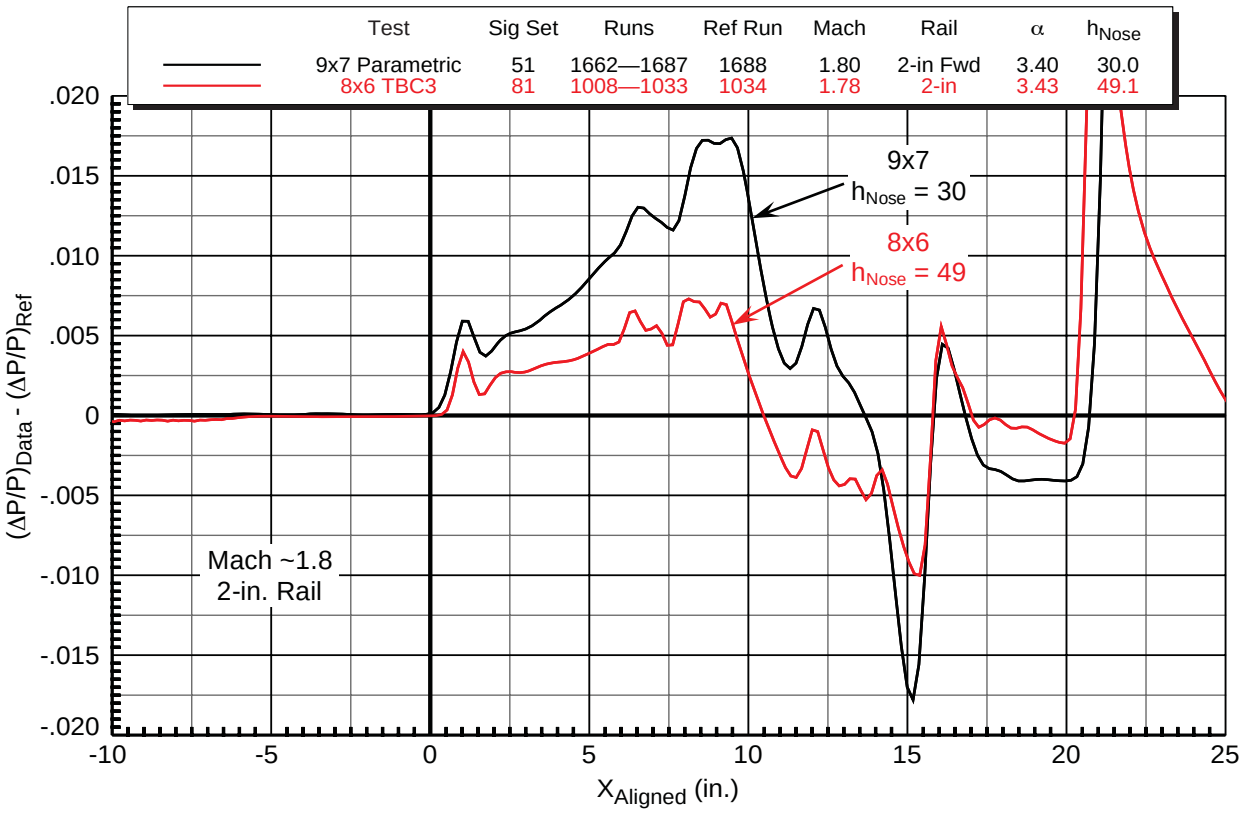

Figure 7–51. Comparison of Boom1 VS2 model signatures from 9x7 and 8x6 wind tunnels 2-in. rail, M = ~1.8, h_{Nose} = 30 to 50 in.

7.15. Reference Run Comparisons and Effects of Humidity

Up to this point, the data presented herein have mostly been the model signatures *corrected* with the reference run pressures, with the exception of the sample reference run shown in Figure 6–11 and the before- and after-reference-run comparisons shown in Figure 6–16. Various comparisons of reference runs will be shown in this section to quantify the magnitude of pressure variations due to the tunnel flow itself, as well as illustrating the effects of changing Mach number, humidity, porous window blank placement in the 8x6 tunnel, and comparisons between tunnels, tests, and rails.

An ideal reference run signature in a wind tunnel would be flat, at zero $\Delta P/P$, meaning no static pressure variation over the length of the rail. Then when a model is positioned such that its shock waves fall on the rail, the resulting pressure distribution would be that of just the model alone. The reference run would not contribute to any errors in the model signature, and this would yield the most consistent and reliable data sets. However, *all* wind tunnels have some amount of static pressure variation throughout the test section, and the presence of a rail itself causes further pressure variations due to its influence on the tunnel flow. If the reference pressure gradients along the rail are small, then the corrected model signatures will be more accurate than if these gradients are large. Large gradients over a small number of orifices adversely affect the model signatures in that various factors (tunnel Mach number variation, turbulence, humidity, and model vibration) cause the model shock waves to shift back and forth over small ranges of orifices during "constant" conditions. With a large reference pressure gradient, a shift of a model shock over a distance of just a few orifices can easily result in a corrected model pressure error on the order of 0.01 to 0.02 in $\Delta P/P$. Clearly, this is highly undesirable when the typical magnitudes of the model shocks being measured are usually less than 0.005 $\Delta P/P$.

Plots of various reference runs are provided in Figures 7–52 through –69. The plots are all made to same $\Delta P/P$ scale so that relative magnitudes can be compared among plots, and the X scales are in tunnel station inches except when comparing the pressures between the 9x7 and 8x6 tunnels, where rail orifice numbers are used instead because of the different tunnel station origins used.

7.15.1. Reference Run Repeatability at Constant and Varying Humidity

The initial set of reference run plots is intended to show the repeatability of various reference runs and the effects of humidity where humidity varies among the runs. Figure 7–52 shows four reference runs from the 9x7 parametric test at Mach 1.6 with humidity essentially constant (296 to 301 ppm). The pressure profiles are all nearly identical (to within ~0.002 $\Delta P/P$), indicating excellent repeatability. A small layout schematic below the plot shows the model and rail positions for these runs in the 9x7 wind tunnel, and the model nose shock is projected at the Mach line angle (51.3° for Mach 1.6) to strike the rail within a few inches aft of the line of rail orifices. Given that the shocks tend to spread slightly with distance from the model, and the uncertainty in shock location due to flow variations and model vibration, the model shocks are likely to fall on some of the aft orifices on the rail. Nonetheless, there is no apparent increase in the scatter of the reference run pressures toward the aft end of the signature.

Note that a new model configuration, "LM 1021, blade," is identified in the legend of Figure 7–52. This is the Lockheed-Martin 1021 configuration,[37] mounted with a blade strut (as opposed to a sting mount) that was run in the 9x7 parametric test. The layout in the figure shows an outline of this model and its blade strut. Note also that the 9x7 window blank locations are shown as thick gray lines at the bottom of the layout image. The window blanks do not protrude *into* the tunnel as indicated by the gray lines, but the lines are shown merely to point out their locations in the tunnel north wall.

Three runs from the 9x7 parametric test having a humidity spread from 199 to 512 ppm are plotted in Figure 7–53. In contrast to the previous figure, there is a definite, though slight, spread of the three

signatures, with the highest signature being the one with the highest humidity. A trend of higher pressures with higher humidity has also been reported in Reference 1.

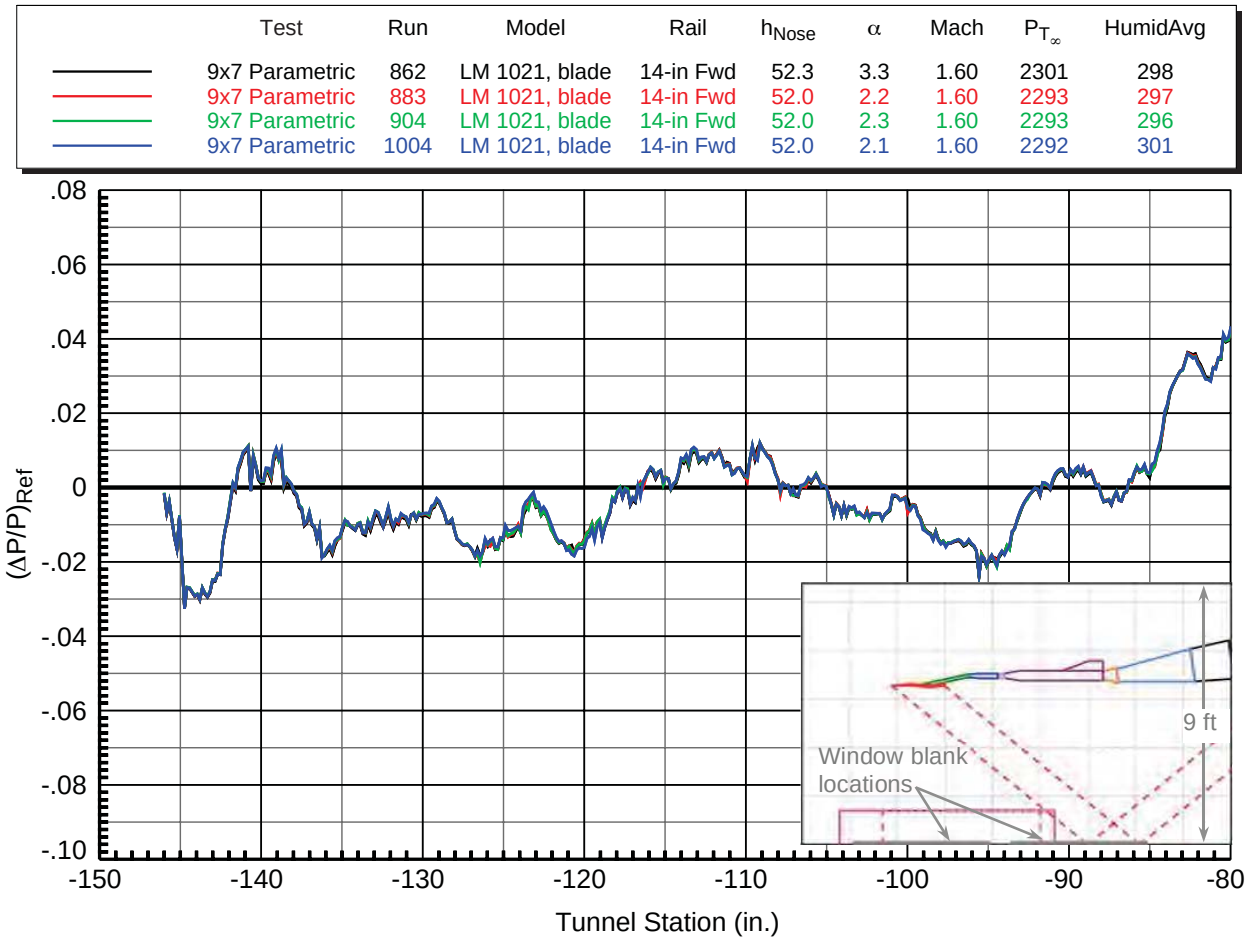

Figure 7–52. 9x7 reference run comparisons, 14-in. rail, *M* = 1.60, constant humidity

Figure 7–53. 9x7 reference run comparisons, 14-in. rail, *M* = 1.60, varying humidity

Reference runs at Mach 1.8 from the same 9x7 test are shown in Figure 7–54, where the humidity spread is only 3 ppm. The repeatability is excellent here too, though not quite as good (generally within ~0.003 *ΔP/P*) as at Mach 1.6. A plot of runs at Mach 1.8 with humidity varying by 300 ppm is given in the next figure, 7–55, and here the humidity effect is dramatic: pressures vary by up to 0.015 *ΔP/P* between the lowest- and highest-humidity runs, with the higher-humidity runs generally having the highest pressures.

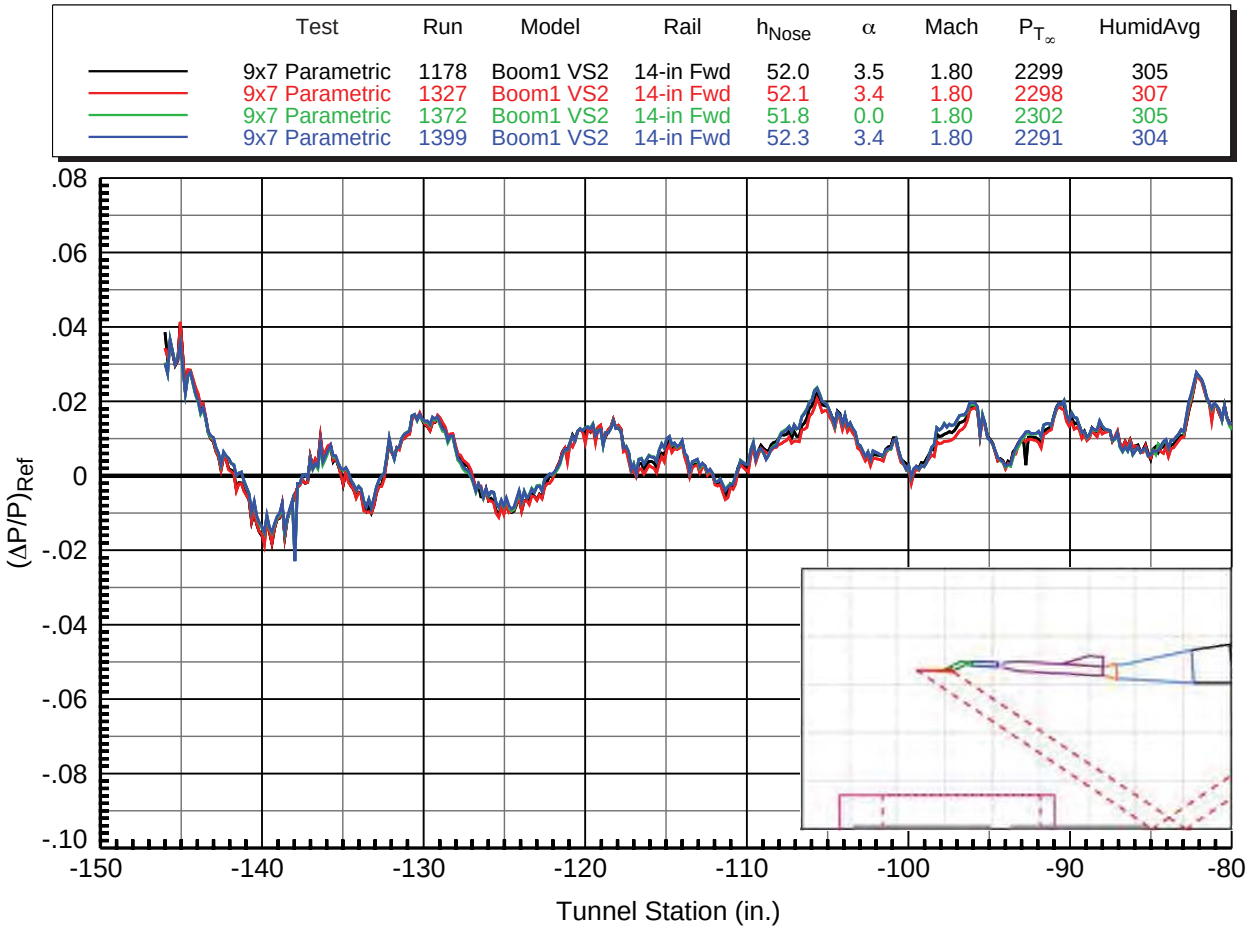

Figure 7–54. 9x7 reference run comparisons, 14-in. rail, *M* = 1.80, constant humidity

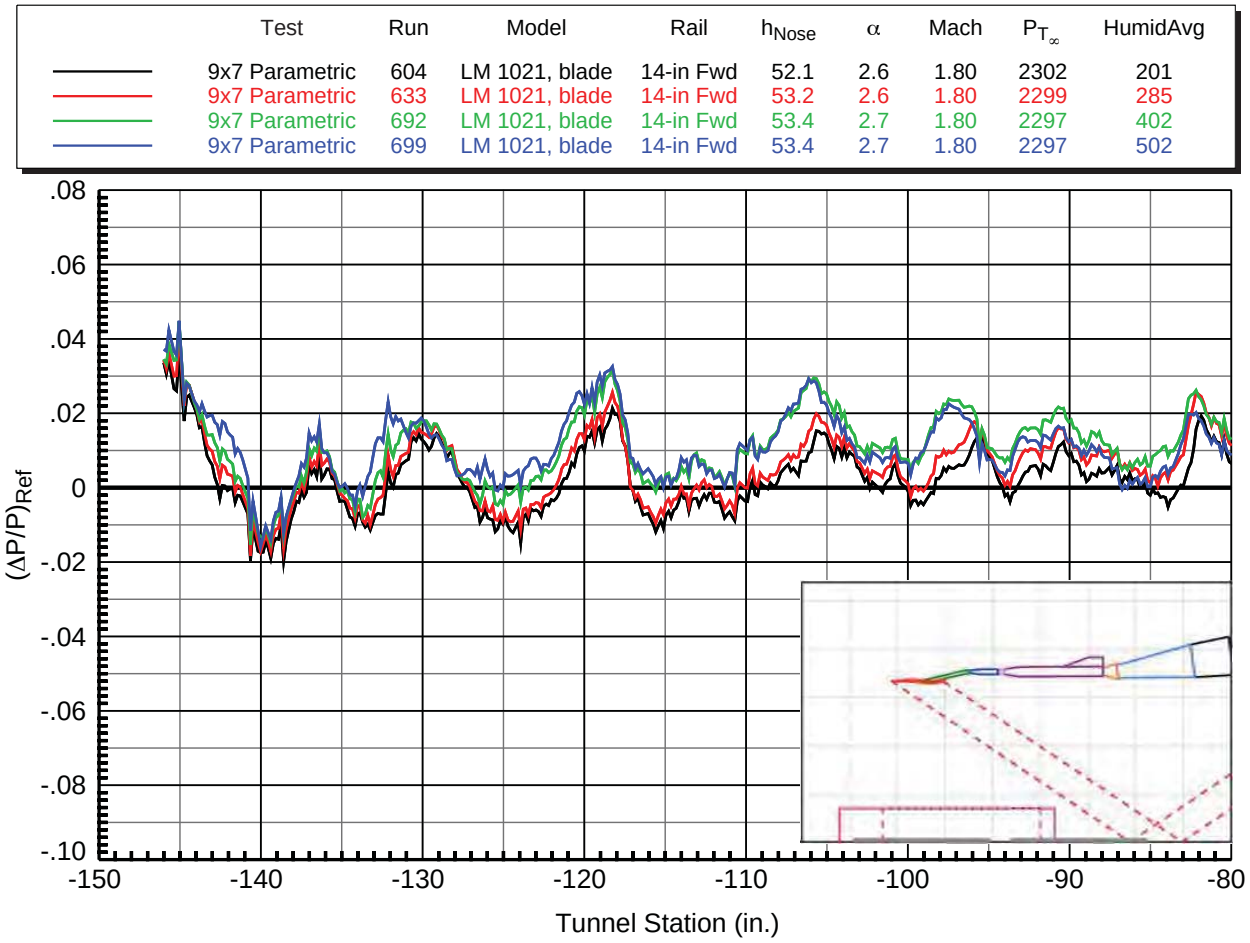

Figure 7–55. 9x7 reference run comparisons, 14-in. rail, *M* = 1.80, varying humidity

Similar sets of runs with constant and varying humidity from the TBC3 8x6 wind tunnel test are shown in Figures 7–56 through –58. The gray window outline shown in the left side of the wind tunnel layout inset image is the downstream window in the 8x6 tunnel; the upstream window is located further to the left relative to this image and is out of view. In the first figure, at Mach 1.56, four runs are plotted, where the first two have nearly identical humidity levels (73 and 78 ppm), and the latter two have higher levels (208 and 330 ppm). The constant- and varying-humidity runs were combined on one plot because it was found that there is almost no variation in pressure among them, indicating that for this set of runs, there seems to be essentially no effect of humidity. In the next figure, 7–57, two runs at Mach 1.78 at very close humidity levels show excellent repeatability. Runs with humidity levels ranging from 184 to 687 ppm are shown in Figure 7–58 at Mach 1.78, and these runs do show an effect of humidity (up to ~0.01 *ΔP/P* difference), though not as much an effect as observed in the 9x7 data at Mach 1.8 (Figure 7–55).

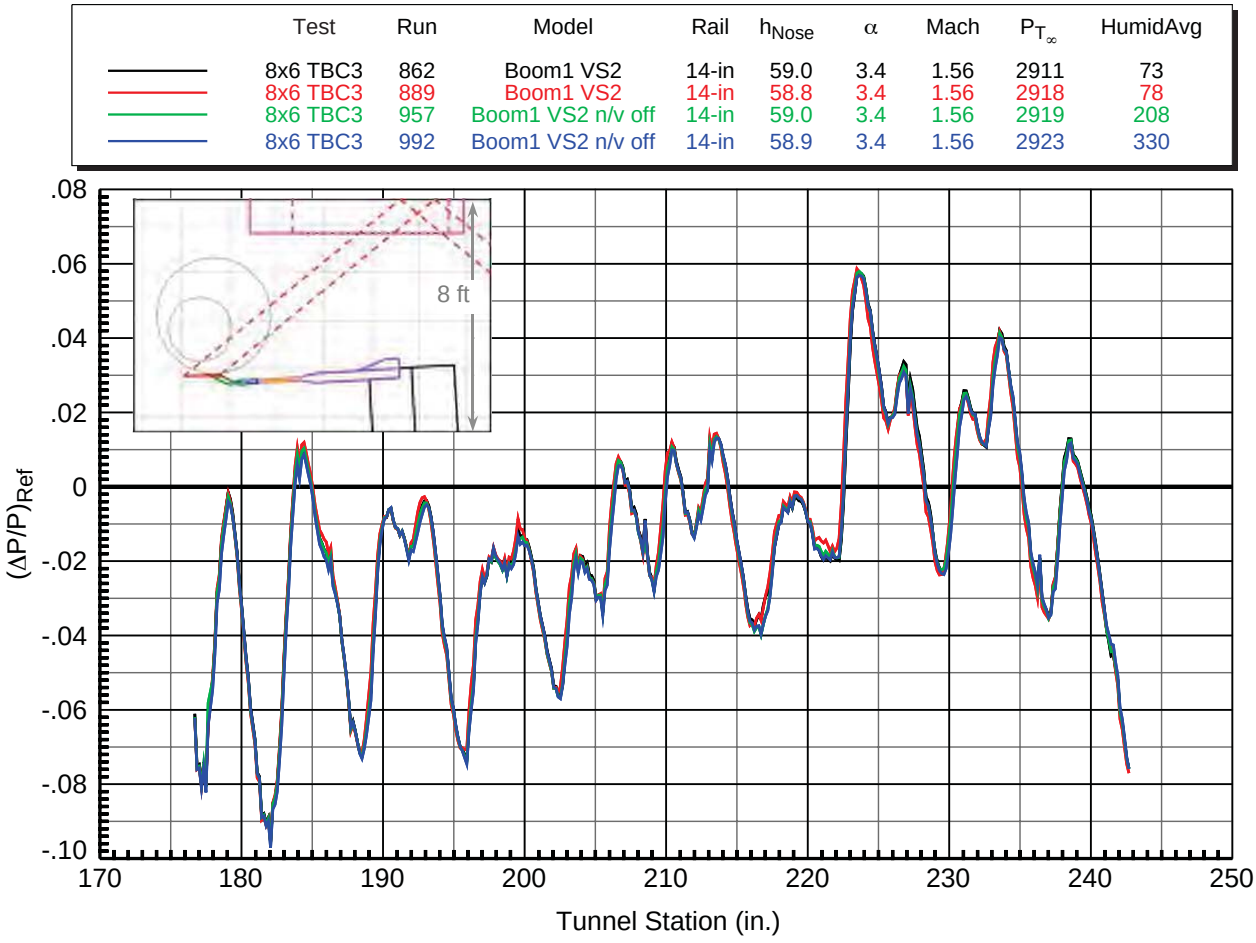

Figure 7–56. 8x6 reference run comparisons, 14-in. rail, *M* = 1.56, varying humidity

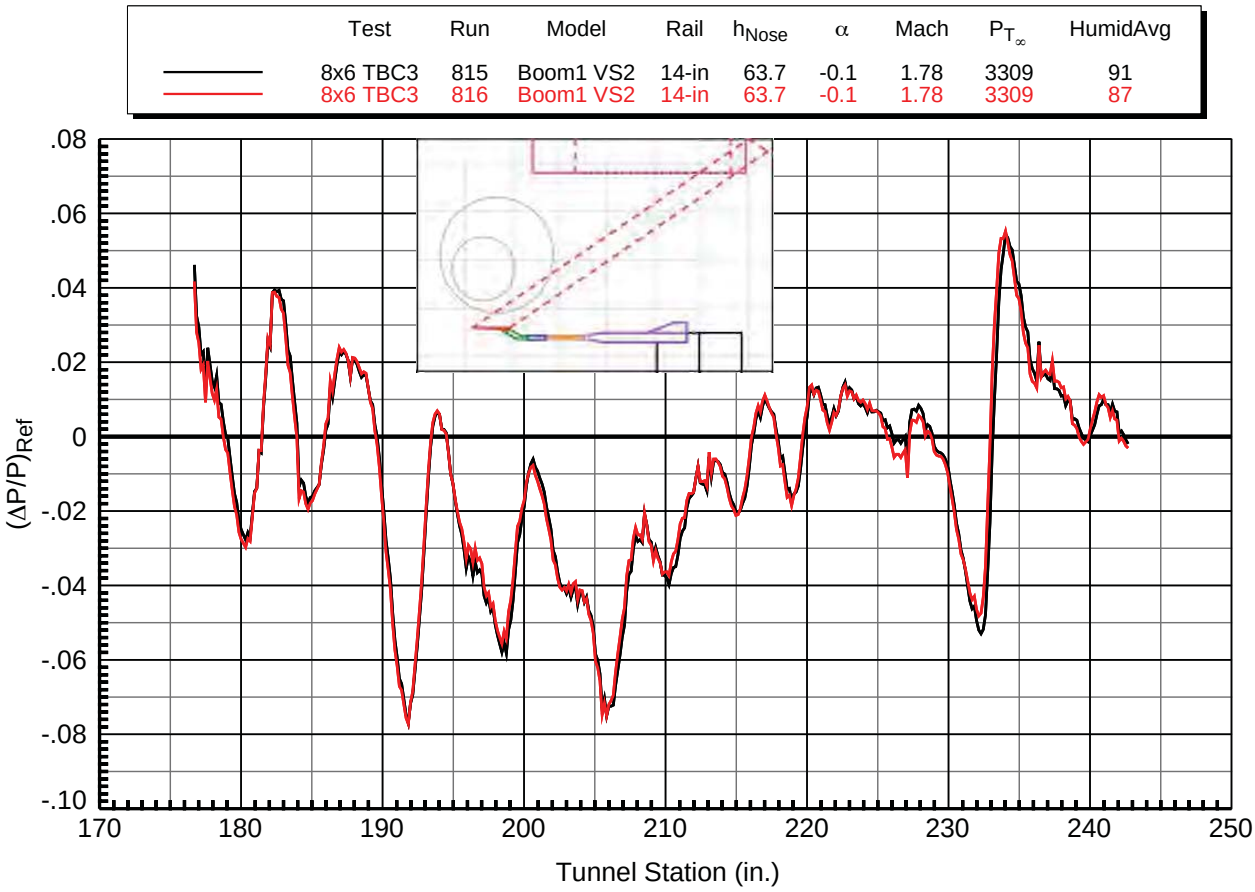

Figure 7–57. 8x6 reference run comparisons, 14-in. rail, *M* = 1.78, constant humidity

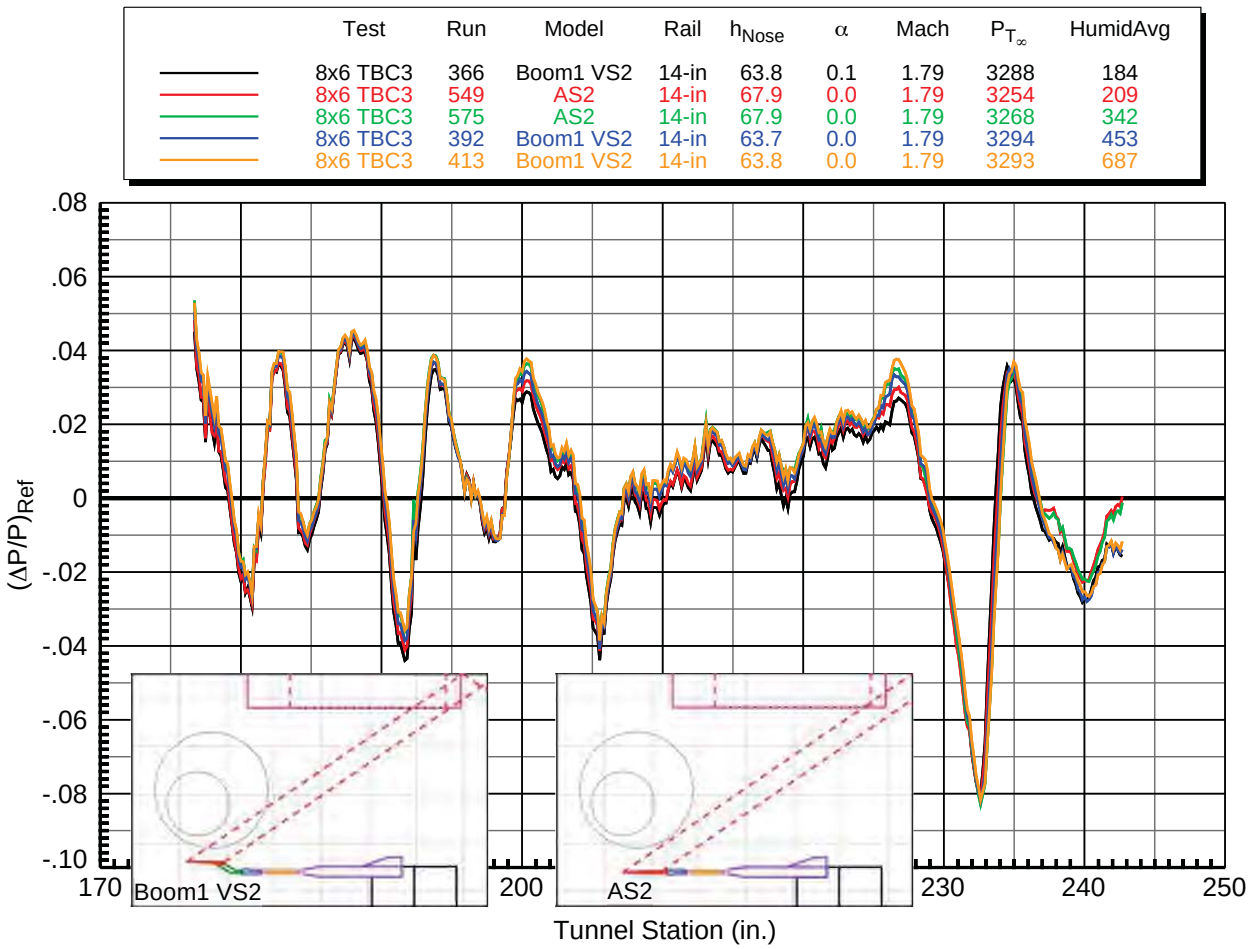

Figure 7–58. 8x6 reference run comparisons, 14-in. rail, *M* = 1.79, varying humidity

7.15.2. Reference Pressure Changes Due to Swapping of Window Blanks

The two prior figures containing 8x6 reference runs at Mach 1.78 show a shift in the pressure levels relative to each other. One run from each of the figures, runs 366 and 815, were selected to plot against each other in Figure 7–59 to clearly show these differences. The run conditions, model, and model and rail positions are identical, and though there is a 90 ppm difference in humidity between them, the differences between the curves are far greater than one would expect for this humidity difference. The major difference between these two runs is the window configuration of the wind tunnel. In Section 3, it was stated that the Schlieren windows were in the downstream position during the first week of the test, with the porous window blanks in the upstream position. Before the start of the second week, the Schlieren windows and the porous blanks were swapped. This is believed to be the cause of the difference between the two reference pressure signatures, as the air flow patterns in the test section would be expected to change with the repositioning of the porous blanks. There should be little or no effect of this on the model pressure signatures since the standard procedure in NASA sonic boom testing is to take a reference run either just before or just after a run series when possible. However, model signatures at the same conditions taken in the first and second weeks of the test are not available to enable a direct comparison.

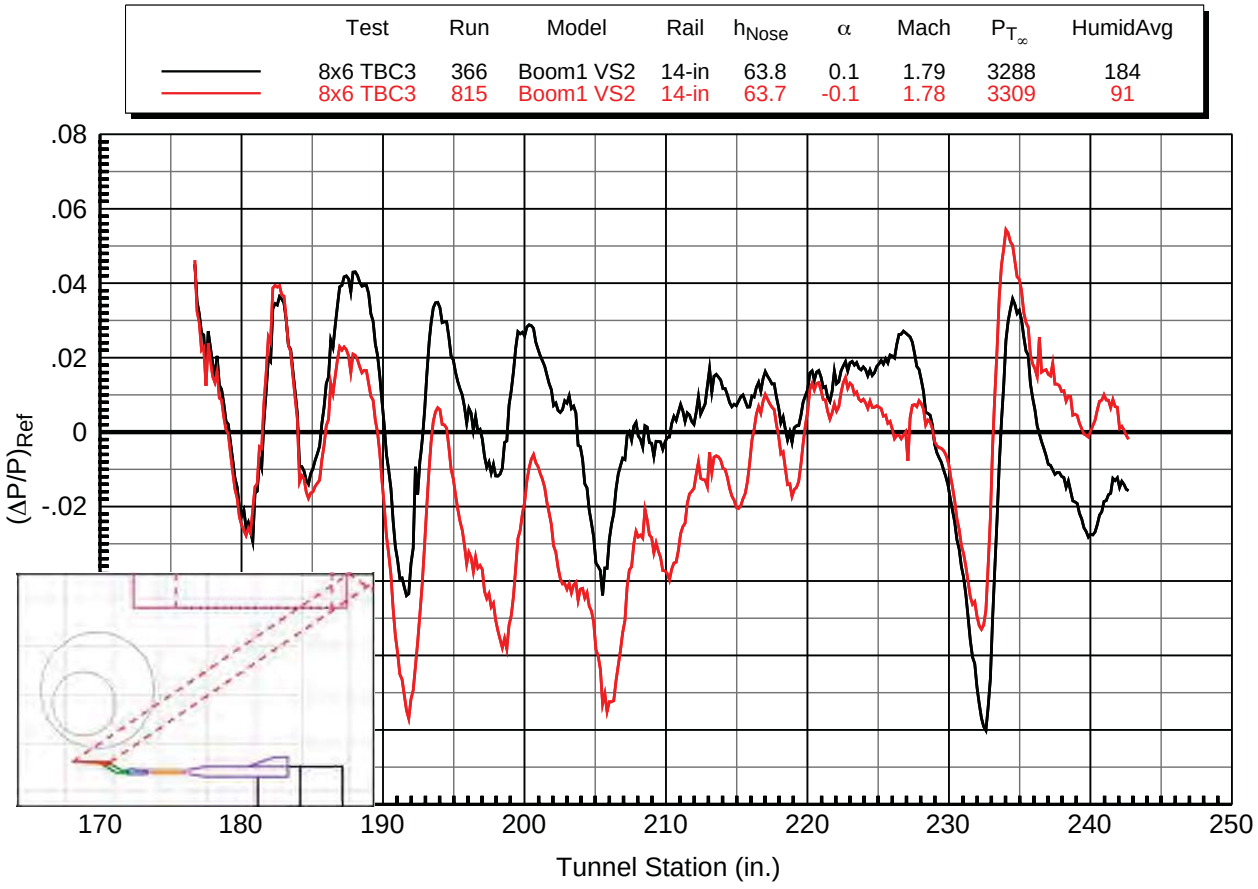

Figure 7–59. 8x6 reference run comparisons, 14-in. rail, *M* = 1.79
Schlieren windows downstream (week 1, runs up to 605), Schlieren windows upstream (week 2, runs 630 and after)

7.15.3. Comparison of Reference Pressures in 9x7 and 8x6 Tunnels Using 14-in. Rail

Reference runs measured on the 14-in. rail installed in the two wind tunnels are compared in Figures 7–60 and –61 for nominal Mach numbers of 1.6 and 1.8, respectively. Data at Mach ~1.6 from the rail in both forward and aft positions in the 9x7 are presented, as are the data for the rail mounted in the one position in the 8x6. The layout diagrams below the plot show that the three reference runs plotted were acquired with three different models: the LM 1021, Boom1, and the cone fairing. Shocks from the latter two models were predicted by the layouts to fall on the rear portion of the instrumented section of the rail, so the portion of the reference run signatures in the plot aft of where the most forward model shocks are (for the Boom1 model, in the vicinity of orifice number 300) are considered not valid for comparison. Ahead of this point however, the curves are considered valid representations of the empty-tunnel pressure signatures. The major points that can be drawn from this plot are 1) that the magnitudes of the pressure variations in the 9x7 tunnel are about twice as high for the aft rail position (±0.030) than for the forward position (±0.015), and 2) the magnitude of the variations for the 8x6 tunnel are significantly higher (±0.040) than either of the 9x7 rail positions. Note also that the 8x6 curve is mostly below the $\Delta P/P = 0$ line—this merely indicates that the static pressures of the rail were lower than the tunnel static pressure reference. In the 8x6 tunnel, this reference static is measured in the "balance house," which is a large plenum chamber surrounding the test section. A choice of a different static pressure would shift the rail pressure curve up or down accordingly.

Pressure data from the 14-in. rail in both tunnels at Mach ~1.8 are presented in Figure 7–61. Again, data from the same three models are used, except at this higher speed, the model shocks were predicted to mostly *not* fall on the instrumented section of the rail, though there is a large shock from the Boom1 model toward the rear of the signature (at orifice number 400). The same general conclusions from the previous figure can also be drawn from this one: the 9x7 reference signature has more variation with the rail in the aft position than in the forward position, and the 8x6 signature variation is significantly higher than either of those from the 9x7.

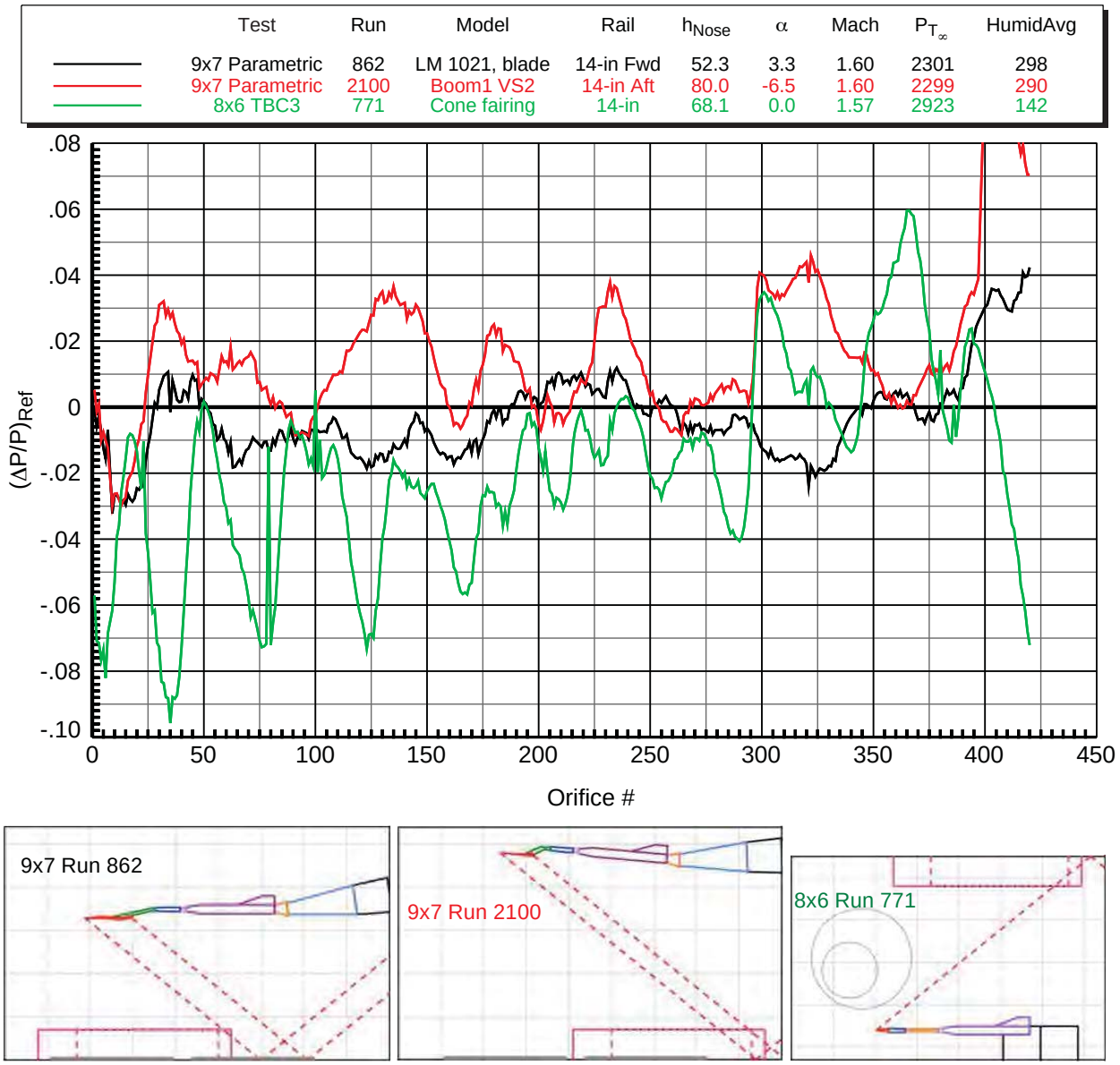

Figure 7–60. 9x7 and 8x6 reference run comparisons, 14-in. rail, *M* = ~1.6

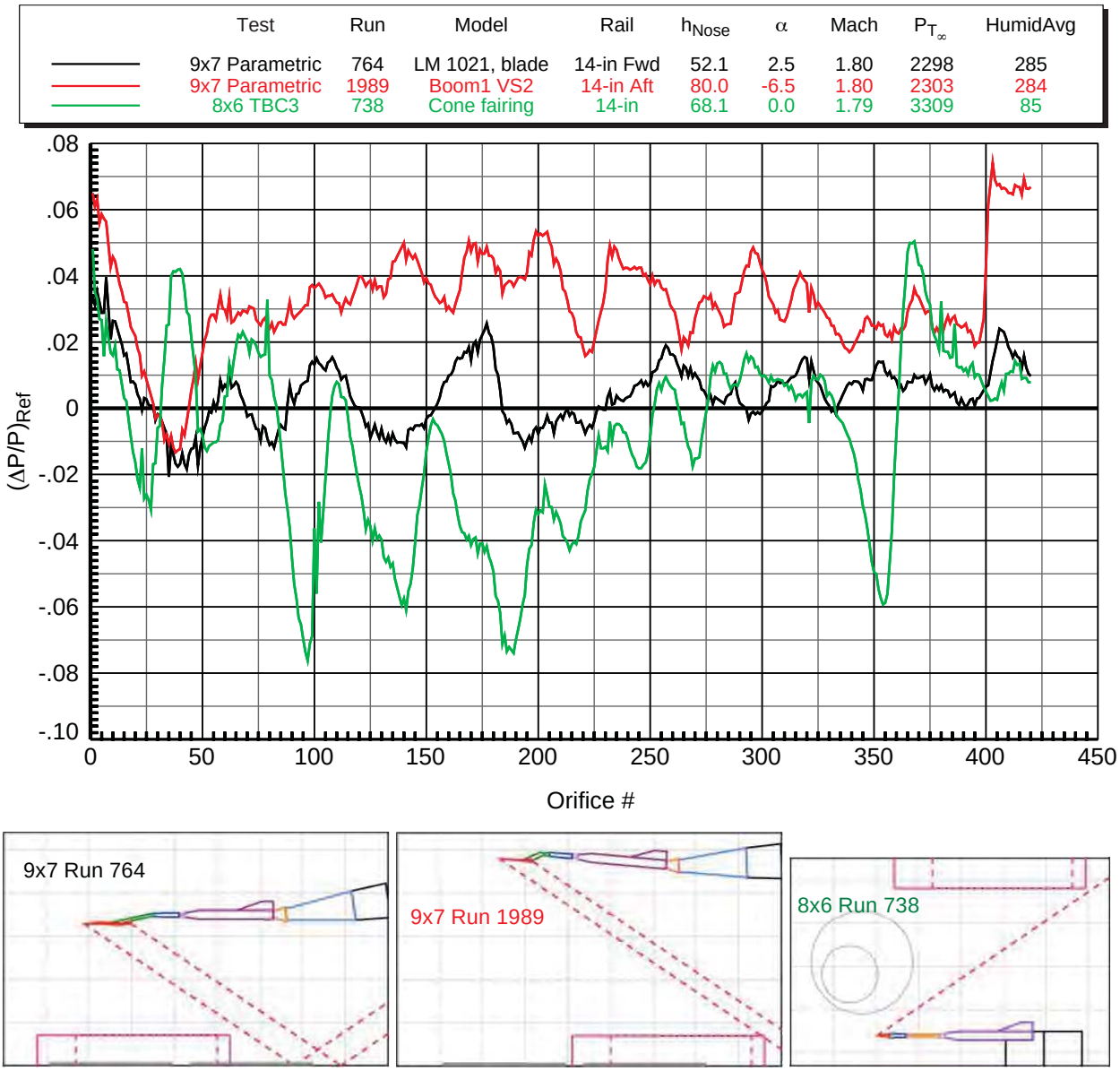

Figure 7–61. 9x7 and 8x6 reference run comparisons, 14-in. rail, *M* = ~1.8

7.15.4. Comparison of Reference Pressures in 9x7 and 8x6 Tunnels Using 2-in. Rail

A similar pair of plots comparing the 9x7 and 8x6 reference run signatures at nominal Mach numbers of 1.6 and 1.8 is presented in Figures 7–62 and –63 with data from the 2-in. rail. However, this rail was not run in the aft position in the 9x7 tunnel during the subject tests, so only one curve from the 9x7 is given in each of these figures. The results are similar to the prior two figures, except that the variation in the 9x7 forward rail position is slightly lower (±0.010 at both Mach numbers) than for the 14-in. rail, and that the variation in the 8x6 tunnel is a bit higher (roughly ±0.050 at Mach 1.56 to ±0.060 at Mach 1.78). Note that the Boom1 model shocks fall on the rail starting at about 2/3 of the length of the rail in the 8x6 test, but the model signature is not discernable at all in the midst of the large peak-to-peak variations in both plots.

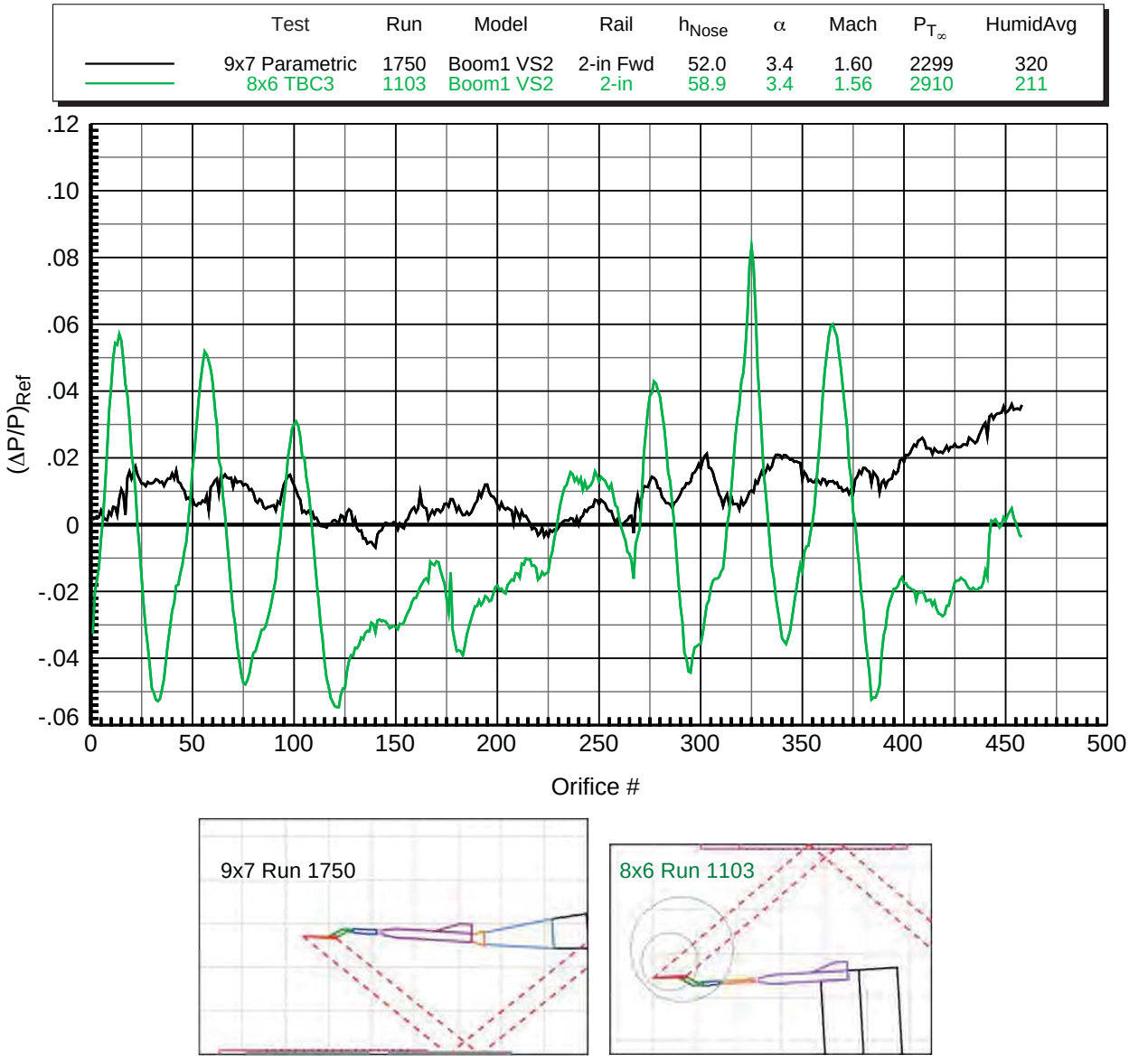

Figure 7–62. 9x7 and 8x6 reference run comparisons, 2-in. rail, *M* = ~1.6

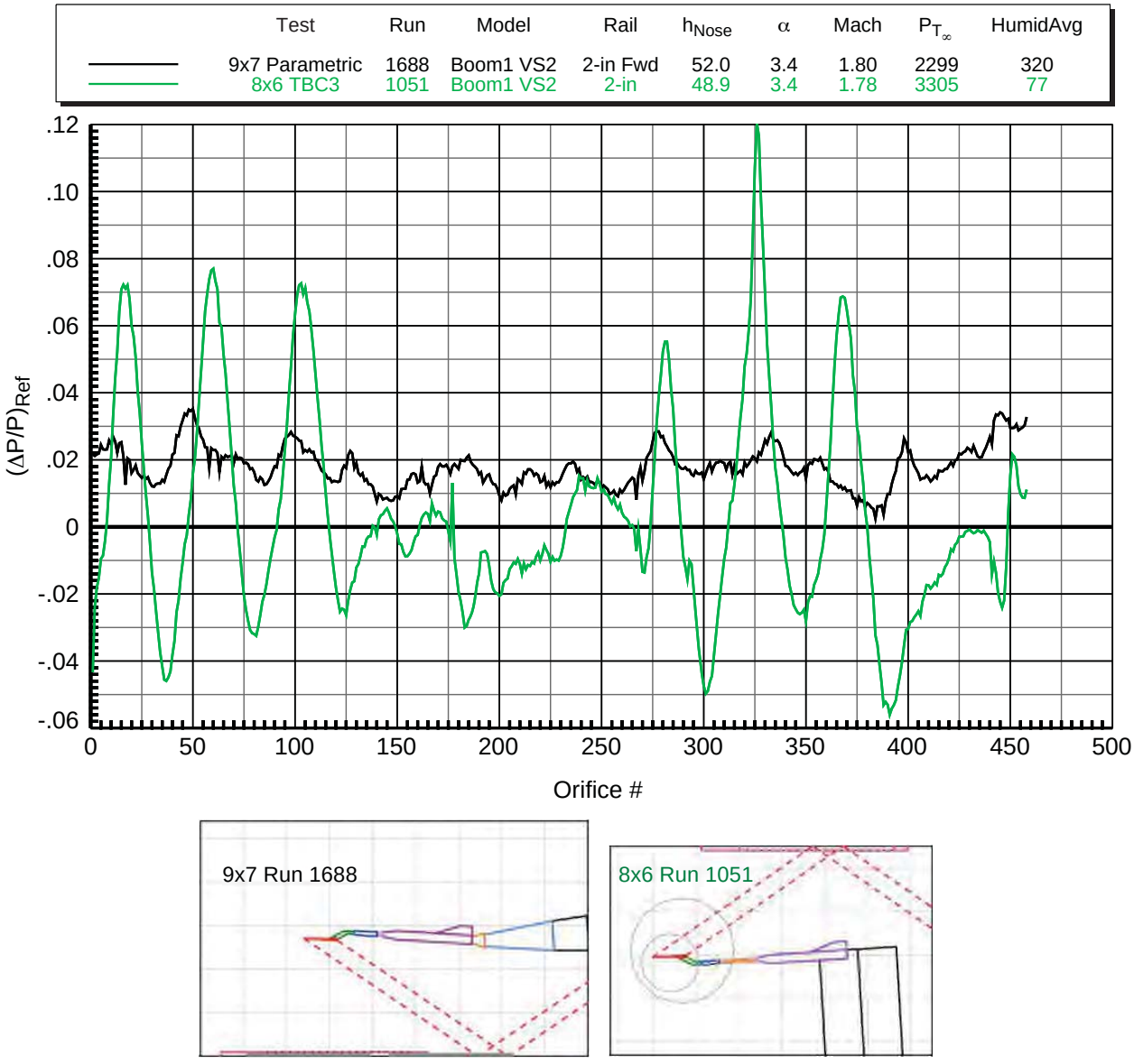

Figure 7–63. 9x7 and 8x6 reference run comparisons, 2-in. rail, *M* = ~1.8

7.15.5. Comparison of Reference Pressures in 9x7 Parametric and TBC4 Tests Using 14-in. Rail

Repeatability of rail pressures at constant conditions *within* a test has been shown in prior figures (7–52, –54, 56, 57), but in the following two figures (7–64 and –65), repeatability from one test to another in the same tunnel will be shown. Two short-term repeat runs from each of the 9x7 parametric and TBC4 tests are shown in Figure 7–64 at Mach 1.6, where the short-term repeatability within each pair of runs is excellent (note the dashed lines showing one curve on top of the other). From the parametric test, the Boom1 model shocks are on the rail aft of tunnel station -34, but ahead of this point the comparison with the tunnel strut cone data (where the cone shock is well aft of the rail) from TBC4 is valid. The test-to-test repeatability (ahead of tunnel station -34) is fairly good, with differences up to 0.015 in $\Delta P/P$ that appear consistent with the slightly higher humidity of the parametric test runs (~290 ppm) versus that of the TBC4 test runs (~230 ppm). At Mach 1.8 in Figure 7–65, the differences in the reference run pressures between the two tests is greater overall, and more consistent through the length of the signature, than at Mach 1.6. The humidity differences are about the same as for the Mach 1.6 data, so this does not necessarily explain the greater differences here. It is interesting, and not obvious why, when the same hardware is put in the same tunnel, and run at almost identical test conditions, that the "empty" tunnel reference signatures are not more similar. There was about a year of separation between the two tests, but time should not be a factor in contributing to the differences unless some changes were made to the tunnel during the interim (and no changes were made which would affect the air flow).

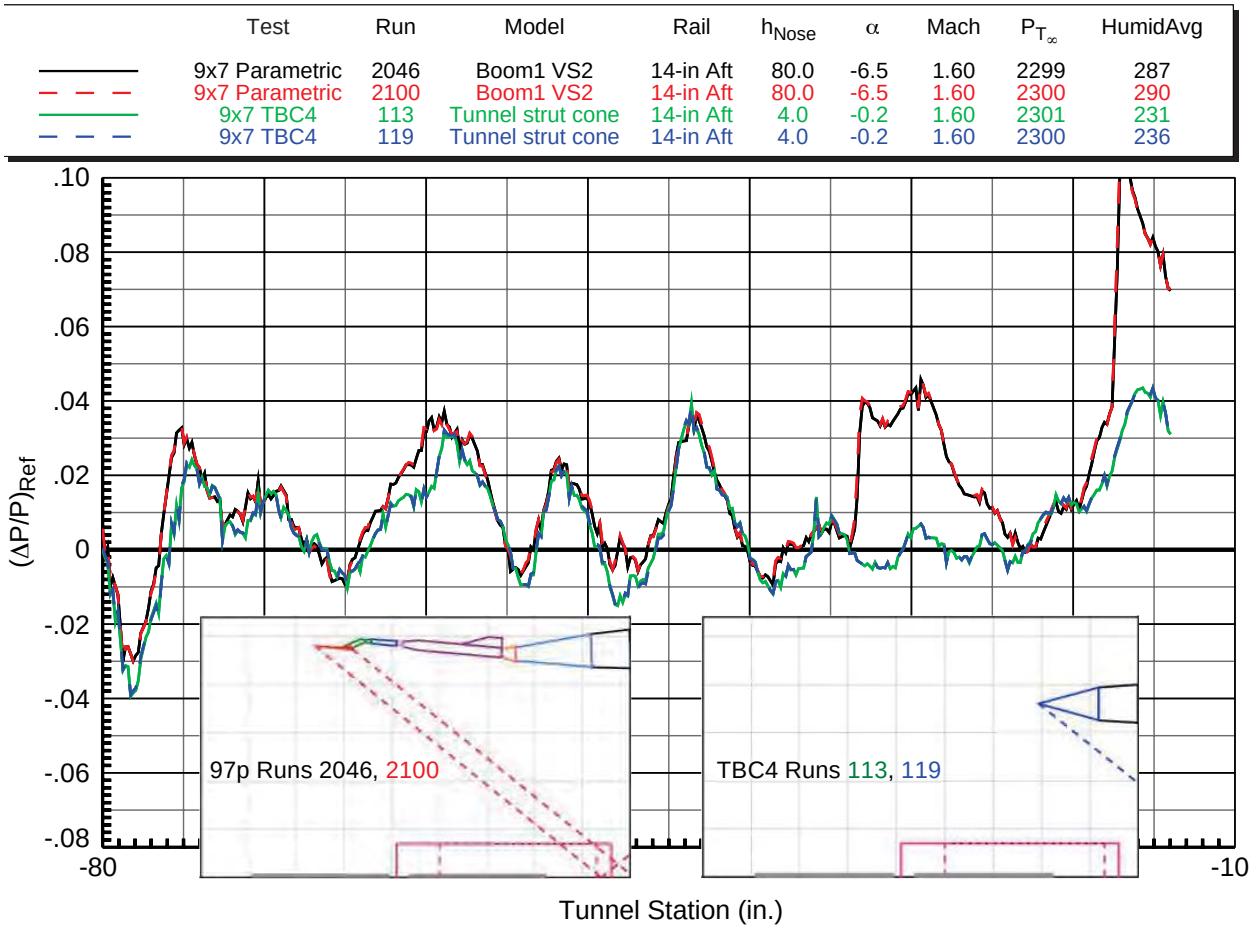

Figure 7–64. 9x7 parametric test and TBC4 test reference run comparisons, 14-in. aft rail, M = 1.60

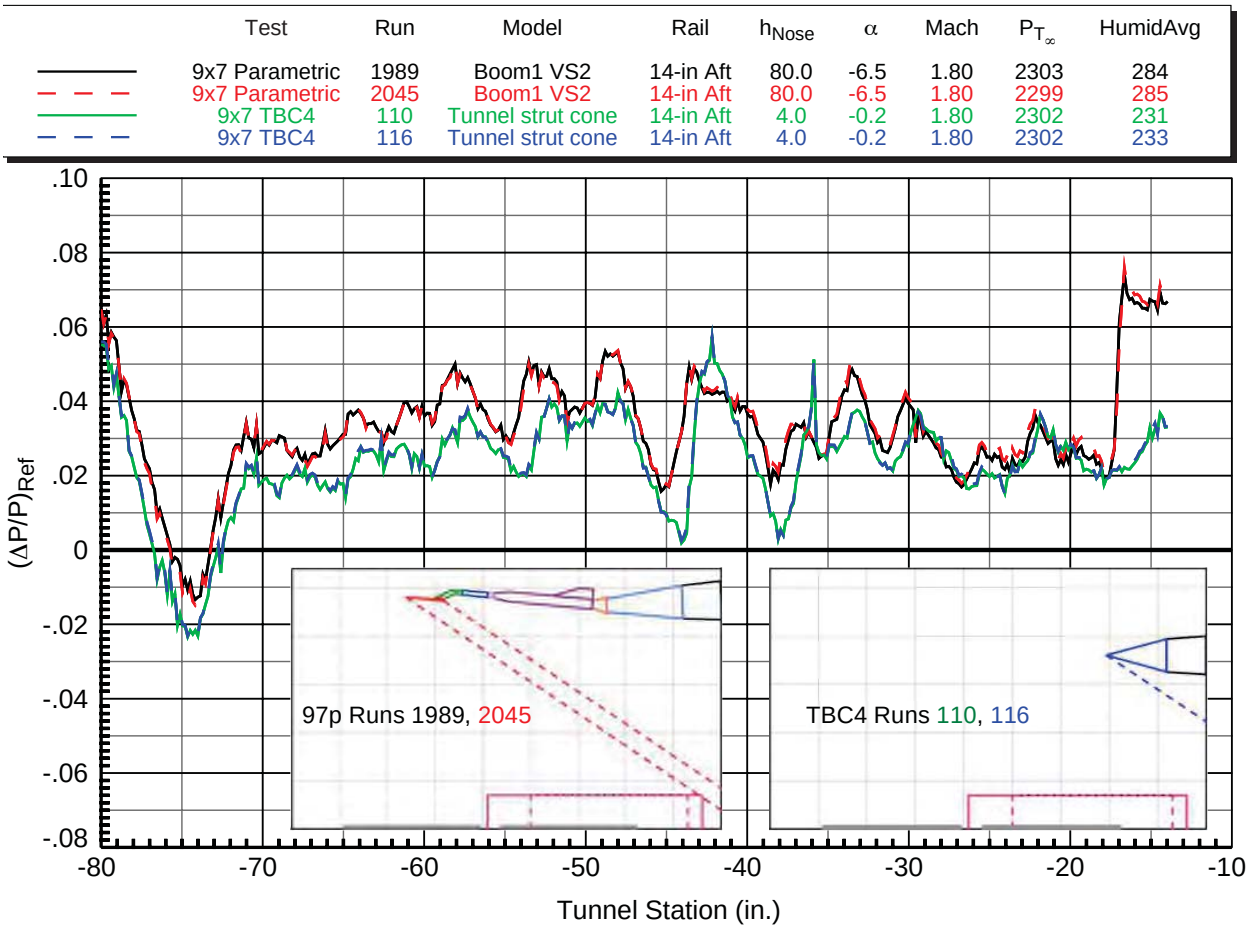

Figure 7–65. 9x7 parametric test and TBC4 test reference run comparisons, 14-in. aft rail, *M* = 1.80

7.15.6. Comparison of Reference Pressures for 14-in. and 2-in. Rails in 9x7 Parametric Test

9x7 parametric test data from the two pressure rails are compared in the next two figures, 7–66 and –67. The 14-in. and 2-in. rails were mounted in the same forward window blank location, and the reference runs were acquired at the same tunnel conditions for both Mach numbers, 1.6 and 1.8. The models were different (LM 1021 and Boom1) between the two runs in each figure, but with their shocks almost entirely off the rails, the use of the different models should not make a difference in the reference run comparisons.

Qualitatively, there is very little difference between the data from the two rails at either Mach number, though the maximum $\Delta P/P$ variation is a little higher for the 14-in. rail (±0.02) than for the 2-in. rail (±0.012).

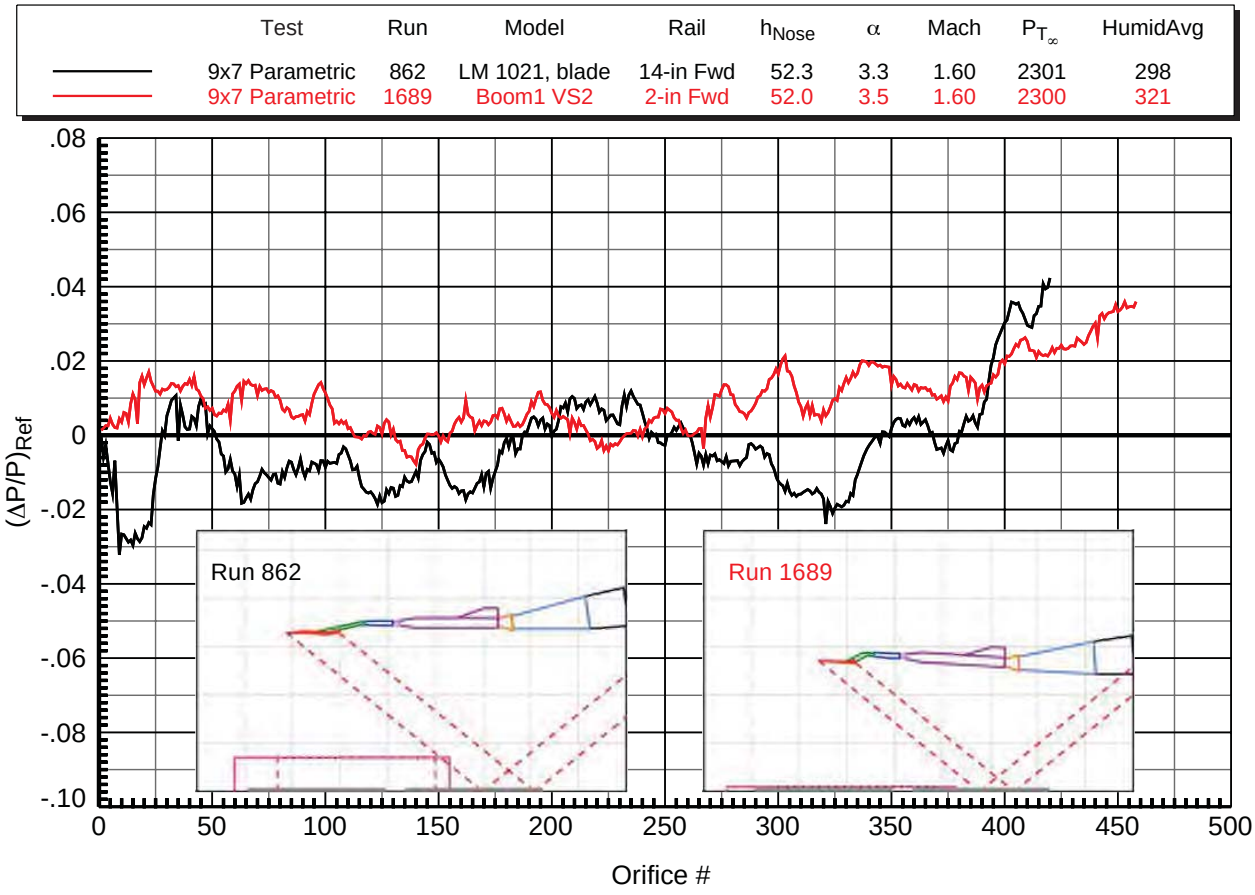

Figure 7–66. 14-in. and 2-in. forward rail reference run comparisons, 9x7 parametric test, *M* = 1.60

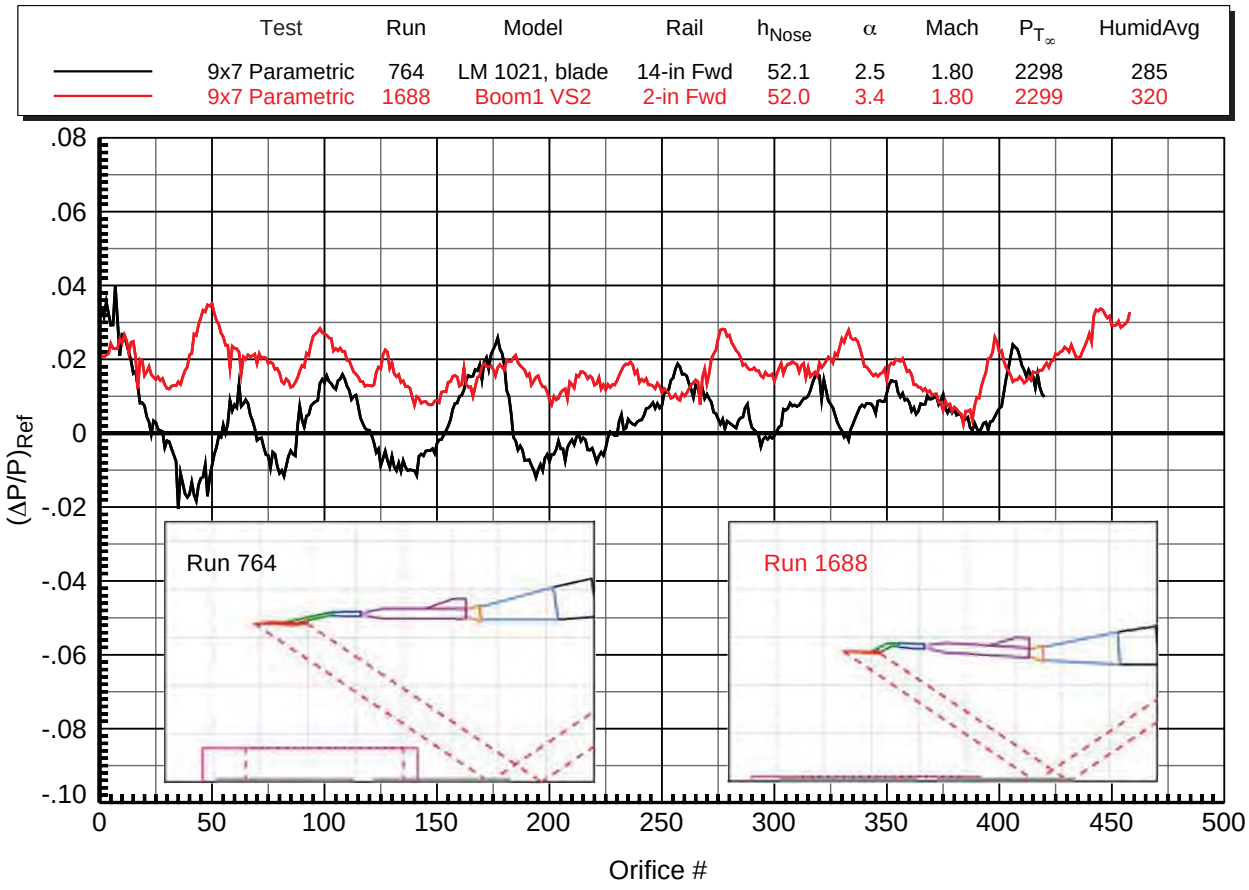

Figure 7–67. 14-in. and 2-in. forward rail reference run comparisons, 9x7 parametric test, *M* = 1.80

7.15.7. Comparison of Reference Pressures for 14-in. and 2-in. Rails in 8x6 TBC3 Test

The same rail comparisons are plotted from the 8x6 wind tunnel data in Figures 7–68 and –69, where the runs with the Boom1 model are in-line reference runs. The much larger peak-to-peak pressure variations in the 8x6 relative to the 9x7 are obvious, and so the differences in the pressures between the two rails are somewhat magnified. It is puzzling to observe, however, that in this tunnel, the 2-in. rail data show slightly *greater* variation (±0.06) than the 14-in. rail data (±0.05).

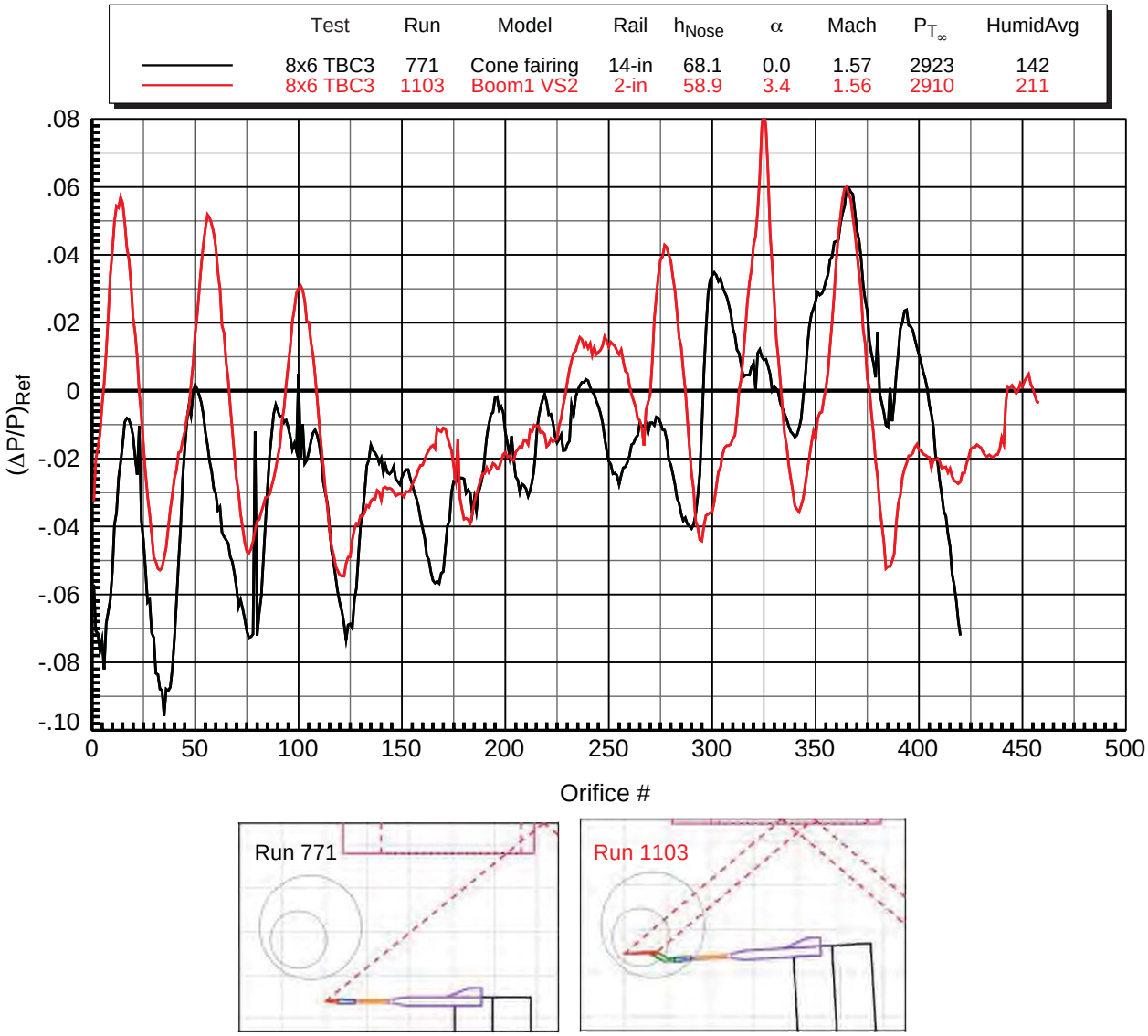

Figure 7–68. 14-in. and 2-in. rail reference run comparisons, 8x6 TBC3 test, *M* = 1.57

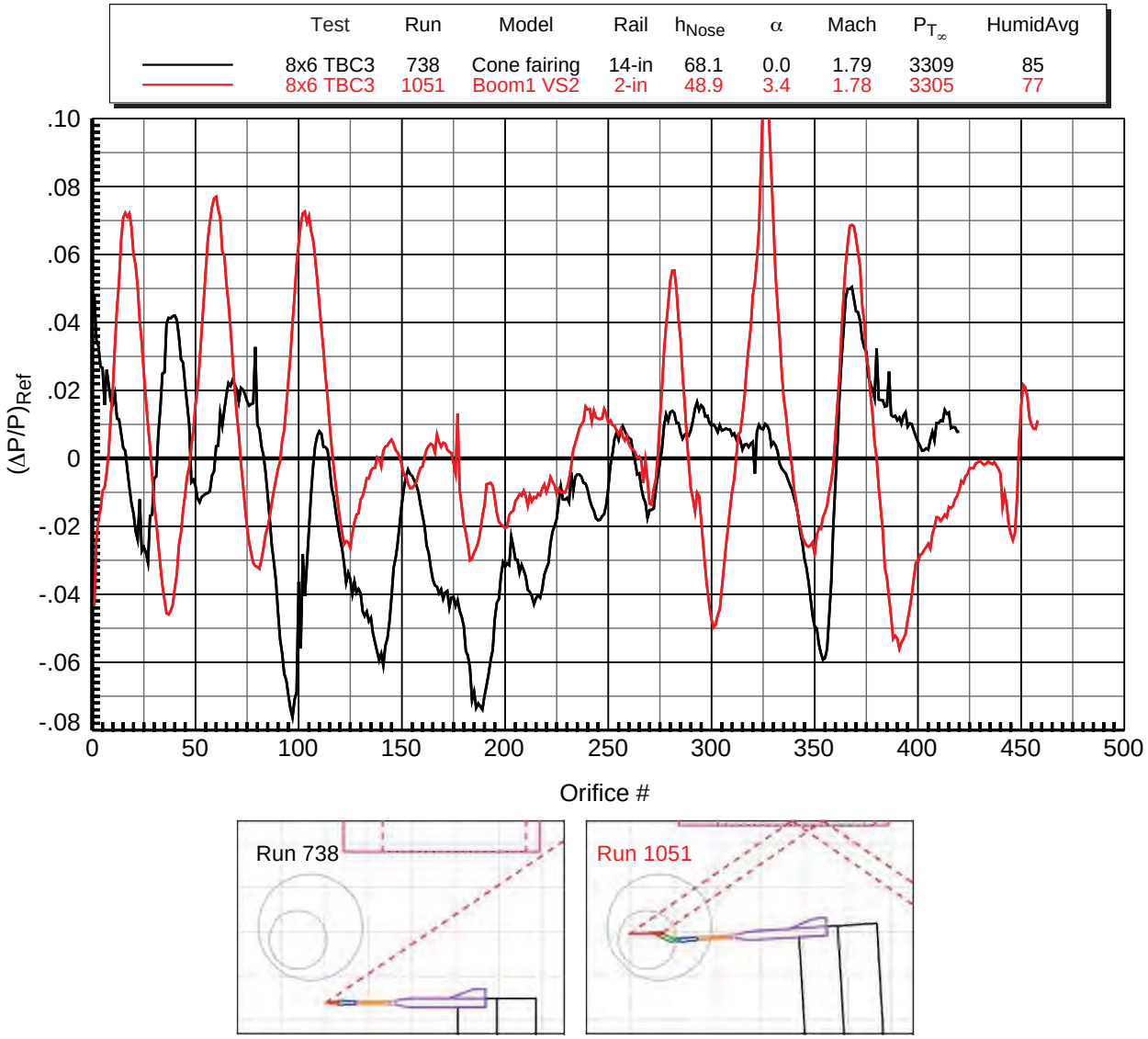

Figure 7–69. 14-in. and 2-in. rail reference run comparisons, 8x6 TBC3 test, *M* = 1.79

8. Computational Methods

8.1. Flow Solvers

Three high-fidelity NASA CFD codes where used to compute the flow around and sonic boom signatures for the Boeing models: *USM3D, Cart3D,* and *OVERFLOW. USM3D* was the default code used in this study, and selected cases were computed using the other two codes. Propagation of the sonic boom signatures to the ground was done using *sBOOM*. In this section a brief description of each of the CFD codes is given.

8.1.1. USM3D

USM3D[42,43] is a tetrahedral cell-centered, finite volume Euler and Navier-Stokes (N-S) method. It provides a variety of options for solving the flow equations and several turbulence models for closure of the N-S equations. For the current study, Roe's flux difference splitting scheme was used with a CFL number of 20. Flux limiters were used to preclude oscillations due to shocks and discontinuities by limiting the values of the spatial derivatives. For the present study, at the start of a new solution, the *USM3D* code ran with first order spatial accuracy for 10,000 iterations, and then ran for an additional 20,000 iterations with second-order spatial accuracy. Obtaining a well converged, first-order accurate solution before switching to second order significantly improves the chance of convergence with the code, but it is sometimes not necessary. *USM3D* has been successfully used to compute sonic boom studies.[28,29] The flow on the models is not expected to be a fully turbulent flow but in some transient state between laminar and fully turbulent flow. Thus, in addition to the turbulent simulations, some selected laminar flow computations were also made. Pointwise grid generation methods were used for inviscid flow simulations with *USM3D*, and *VGrid* methods were used for laminar and turbulent (using the Spalart-Allmaras turbulence model) viscous flow simulations.

8.1.2. Cart3D / AERO

Cart3D[19-21,38] is a high-fidelity inviscid analysis package for conceptual and preliminary aerodynamic design. It allows users to perform automated CFD analysis on complex geometry. The package includes utilities for geometry import, surface modeling, mesh generation, flow simulation and post-processing of results. The main simulation code, *FlowCart*, runs in parallel both in shared memory (OpenMP) and distributed memory (MPI) with excellent scalability. The package is highly automated so that geometry acquisition, and mesh generation can usually be performed within a few minutes on current desktop computers.

The *Cart3D* simulation package comes with an internal mesher called *Cubes* and geometric models are imported into the package as watertight surface triangulations. *Cart3D* uses adaptively-refined Cartesian grids to discretize the space surrounding the models, and cuts the geometry out of the set of "cutcells" which actually intersect the surface triangulation. *Cubes* then produces a topologically-unstructured, adaptively-refined Cartesian grid. The *Cart3D* Adjoint Error Optimization *(AERO)* module was also used. This module uses the method of adjoint-weighted residuals to drive mesh adaptation. Once a user specifies outputs of interest, (lift, drag, etc.) with a corresponding error tolerance, this module automatically refines the mesh to drive the remaining numerical errors in the outputs below the requested tolerance.

FlowCart is the current solver being released with *Cart3D*. It is a scalable, multilevel, linearly-exact upwind solver and uses domain-decomposition to achieve very good scalability. On most modern desktop machines it can converge well over 2 million cells-per-hour-per processor, and it does very well on multi-core CPUs. *FlowCart* is very tightly integrated into *Cart3D* and all of the automation tools are built

around it. Since it is a multilevel code, it converges very quickly and includes the state of the art work on low-dissipation approaches, solid wall boundaries, mesh interfaces and limiters. Both the parallelization and multigrid are completely transparent to the user and are turned on by simple command line arguments to encourage their use. In the present study, *FlowCart* used cell-centered, finite-volume, upwind differencing. The Barth–Jespersen limiter was used to preserve monotonicity. Time integration was performed by an unstructured, nested multigrid procedure.

8.1.3. Overflow

OVERFLOW[44,45] is the *OVER*set structured grid *FLOW* solver that was used by Boeing for their inviscid and viscous simulations[8] presented in this paper. The turbulence model that was used was the Spalart-Allmaras (SA) model, and the dissipation scheme was *TLNS3D*. The simulation was run until the residuals reduced to near zero and this took approximately 5000 time steps.

8.1.4. sBOOM

A recently-developed NASA sonic boom prediction code, *sBOOM*,[46] was used to propagate sonic boom signatures to the ground. *sBOOM* solves the augmented Burger's equation numerically and takes into account effects such as non-linearity, molecular relaxation and thermo-viscous absorption into the propagation process. The thickness of the shocks is predicted analytically, which avoids artificial smoothing and empirical shock thickening during loudness calculation. *sBOOM* can predict on-track and off-track ground signatures with or without wind effects, along with consideration for aircraft maneuvers.

Ground signatures extrapolated with *sBOOM* have been run in the present study through a loudness code based on the procedures laid out by Shepherd and Sullivan.[47] The code estimates the boom loudness levels in *PLdB, dBA,* and *dBC,* but only the *PLdB* results will be presented herein since this metric is the perceived level as heard by humans.

8.2. Grid Generation

Customized off-body volume grids for supersonic flow are fundamental to the prediction of accurate sonic boom pressure signatures. The various grid generation methods—Mach cone aligned prism *(MCAP)* meshes, Boom Grid *(BG)* Generation Method, Inflate Generation Method, and a solution adaptive Cartesian method—are discussed in this section.

8.2.1. Grid Extrusion Method: Mach Cone Aligned Prism

The Mach Cone Aligned Prism *(MCAP)* collar grid method,[3,27,28] was used with the *USM3D* flow solver for accurate sonic boom computations. *MCAP* appends geometrically-similar prism cell meshes to an interior tetrahedral mesh with cylindrical boundaries. The shearing angle of the appended prism mesh is adjusted for the angle of attack and Mach angle to allow for both on- and off-track aligned grids. The *MCAP* algorithm provides a mesh composed entirely of tetrahedral cells and an automated process to construct grids suited to obtain accurate sonic boom pressure signatures. Sonic boom pressure signatures can be obtained on configurations of any level of geometric complexity provided a refined volume grid of tetrahedra within the near body cylindrical boundary of surface triangles is supplied. The inner cylindrical meshes were developed using *TetRUSS*[48] (*GridTool* and *VGrid*)[49] or *Pointwise*[50,51] grid generation methods. Thin, anisotropic cells near the configuration surfaces were developed to support viscous computations at the wind tunnel Reynolds number. The mesh density was increased within the sonic boom zone of influence below the model to off-track angles of 90 degrees to accurately capture the sonic boom signature out to the cylindrical boundary. The inner cylindrical boundaries were then used as input to the *MCAP* software and projected in the radial direction and sheared to align with the Mach angle with

a series of prism layers to the far field. The projected prism collar grid maintains the highly refined grid spacing in the axial direction of the inner cylindrical mesh to the far field. By simply increasing the distance of radial projection, as successive prism layers are appended to the grid, radial stretching of the cells is accomplished, and this greatly reduces the number of grid points required, while also reducing the effects of numerical dissipation. Shearing to align the prism cells with the Mach cone angle around the aircraft model improves the accuracy of both on- and off-track computations. When the angle of attack is non-zero, an additional asymmetrical shear is applied and a cosine function is used to smoothly transition the differences in shear angle from the lower to upper symmetry planes.

8.2.2. Grid Extrusion Method: Boom Grid (BG)

The Boom Grid *(BG)* method[30] is similar to other "extrusion" grid generation approaches in that the new grid is created by extending lines from grid points on a boundary surface for an existing grid in a direction approximately normal to that surface. The *Q2D* (Quasi-two-dimensional) grid generation code, from which the *BG* code evolved, was developed using this approach to provide a rapid airfoil analysis capability. The *Q2D* method uses a point numbering system that automatically provides matching faces when the extruded prisms are split into tetrahedral cells, eliminating the need to post-process the cells to meet this requirement, and thus reducing grid generation times dramatically.

The *BG* method utilizes the same efficient cell-splitting method used in *Q2D*, but has several requirements that resulted in it being developed as a separate code. First, instead of using the symmetry plane as the starting surface, the new cells are extruded through the outer, typically cylindrical, far-field boundary of an existing "core" 3-D grid around a configuration, creating a "collar" grid. The extension direction is approximately normal to the original surface points when viewed from the front, but the new grid lines are swept in the stream-wise direction. This grid line shearing, along with stretching of the distance between subsequent layers, creates high-aspect ratio cell faces that are closely aligned with the Mach angle so that the dissipation of the boom signature is reduced. Depending on the desired location for extracting a sonic boom signature, anywhere from 20 to more than 100 layers of cells may need to be generated. Another difference from *Q2D* is that these cells then need to be merged with the core grid, which requires converting the old outer boundary faces to field faces and renumbering the points, cells and faces to reflect flow solver requirements.

The collar grid lines are often extruded normal to the original core grid outer boundary when viewed from the front. If the outer boundary is a cylinder, then all of the extruded grid lines meet at the center of the circle (front view of the cylinder) as a radial reference point. If the core grid has the configuration located at this reference point, then boom signature propagation lines will be approximately aligned with the radial grid lines, as desired. The weakness of this approach, however, is that in generating a core grid with the outer cylinder outside of the wing tip, there can be a significant distance from the bottom of the fuselage to the beginning of the collar grid. As the grid is not sheared and stretched in this region, the signal can get dissipated before reaching the collar grid.

If only on-track signatures are needed, then the above problem can be resolved (though with some additional cost due to more grid cells) by simply increasing the size of the outer core grid circle to allow the configuration to be shifted down closer to the lower boundary. For off-track signatures, however, this approach gives poor alignment of the grid lines and signal propagation direction. The *BG* method attempts to address this problem by using a variable radial reference point instead of the standard center of the circle. This allows the configuration to be shifted down closer to the outer boundary, using either a larger circle or an arbitrary-shaped boundary, and still have the radial lines emanate from the configuration for better signal propagation. It has also been found that the location of the radial reference point can be calibrated to focus the grid lines in a desired off-track direction to provide good signal resolution with very little degradation of the on-track signature.

8.2.3. Solution-Adaptive Cartesian Grids

Solution-adaptive cartesian grids are used by *Cart3D*, and are generated by the *Cubes* and *AERO* modules as described above in section 8.1.2.

8.2.4. Initial and Boundary Conditions

For all viscous simulations, a no-slip viscous boundary condition (BC) was used on all solid surfaces of the models. A supersonic inflow BC was used at the domain inflow face and an extrapolation BC was used at the downstream outflow face of the domain. A characteristic inflow and outflow BC was used along the far field, lateral faces of the outer domain. For the inviscid flow simulation *Cart3D* used an inviscid aerodynamic surface BC on all solid surfaces.

9. Comparison of Experimental Data and Computational Simulations

Data from selected wind tunnel runs of the Boeing AS2, Boom1, Boom3, and Performance models are compared to predictions from the three CFD codes described above in this section.

9.1. AS2 Body of Revolution

All three CFD codes were used to compute the pressure signatures for the AS2 model at distances of 30 and 60 in. below the model. As an example of an adapted grid and pressure contours from *Cart3D*, Figure 9–1 shows the adjoint-adapted grid at Mach 1.6 after 13 levels of adaptation, and the sensor lines are shown in orange at 30- and 60- in. heights. The refinement pattern is driven by the features of the adjoint solution. Figure 9–2 shows the symmetry plane pressure contours.

Inviscid and viscous predictions of AS2 signatures are compared with 9x7 wind tunnel data in Figure 9–3 at a height of 30 in., and with 8x6 wind tunnel data in Figure 9–4 at a height of 60 in. The data from the 9x7 were acquired at Mach 1.6 with the 14-in. rail, while the 8x6 data were acquired at Mach 1.56 with the 2-in. rail. The CFD predictions were run at Mach 1.6 and a Reynolds number of 4.1 million per foot, which is a little lower than the 9x7 wind tunnel Reynolds number of 4.5 million per foot at M = 1.6 and P_T = 2300 psf.

The wind tunnel data in these plots are shown in the dark gray curves with circle symbols, and the predictions are shown in the colored curves without symbols. Note that the y-axis labels, *(ΔP/P)Data – (ΔP/P)Ref*, apply exclusively to the experimental data; there is no need for "reference" runs in the CFD, so the labels for the CFD cases would be just *ΔP/P*.

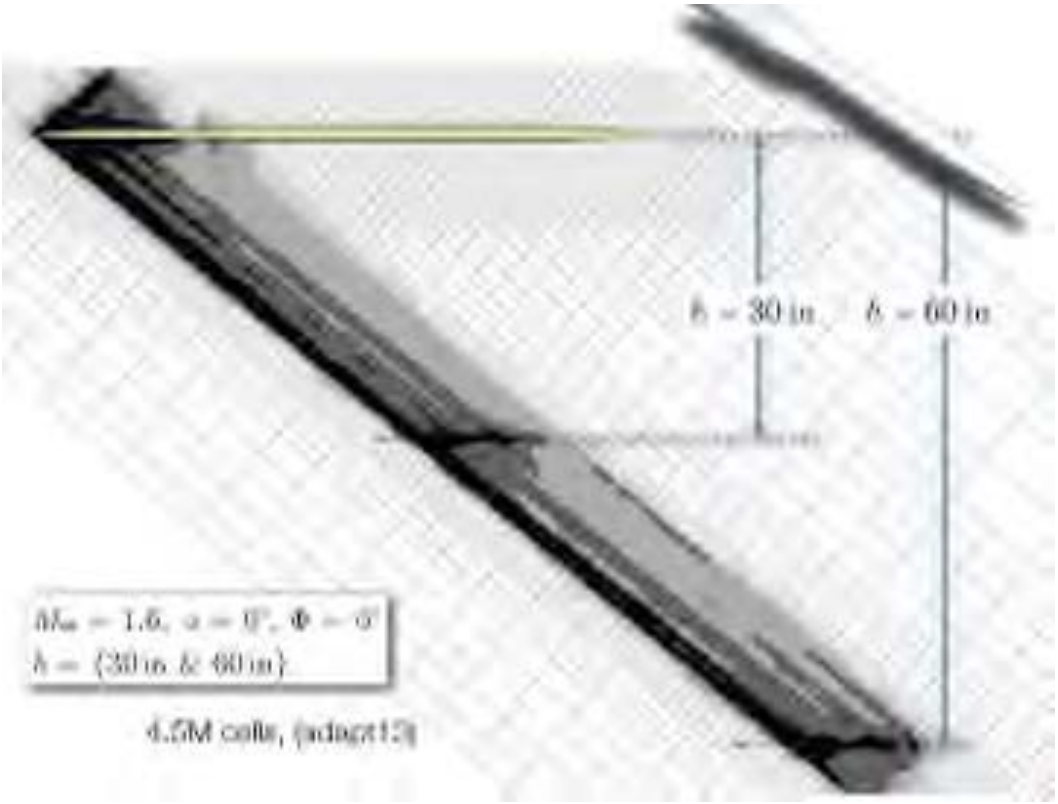

Figure 9–1. Symmetry plane *CART3D* adjoint-adapted grid for AS2 model, M = 1.6, α = 0°

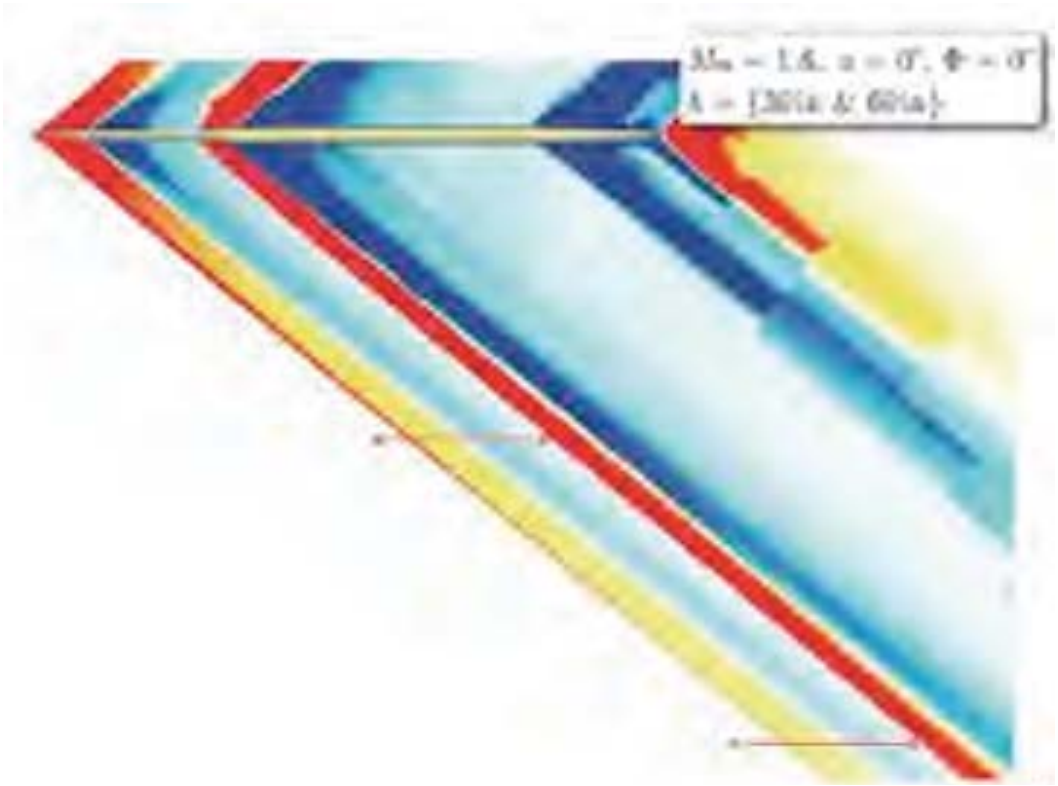

Figure 9–2. Symmetry plane pressure contours for AS2 model, *Cart3D*, M = 1.6, α = 0°

Two inviscid CFD predictions, *Cart3D* and *USM3D*, and two viscous CFD predictions, *Cart3D* and *USM3D SA* (Spalart-Allmaras turbulence model) and *OVERFLOW*, are compared to AS2 model data from the 9x7 parametric test at a height of 30 in. above the rail in Figure 9–3. All of the codes predict nose shock peaks between 20% and 60% higher than the experimental data peak and much faster rise times. The experimental data are from the 14-in. RF1 rail, so there is no amplification of the measured shock peak by any reflection factor. There is good agreement of all three codes with experimental data in the flat region behind the nose shock, but all of the codes over-predict the main expansion in the aft portion of the signature. The reason for this discrepancy is not known, though the same discrepancy was noted for the Lockheed Seeb body-of-revolution model.[3,37] It was surmised that the leading shock from the pressure rail striking the curved part of the AS2 model was the cause for the discrepancy, but upon further review of the 26 individual signatures in the X sweep for the 1080–1105 run series from the 9x7 parametric test, it was determined that this is not the likely cause. For the first few inches of the 16-in. *X* sweep, the rail nose shock does pass over the curved nose section of the AS2 model, but the model pressures in the main expansion are nearly the same as those from the latter part of the *X* sweep, indicating that the rail shock does not significantly influence model signature. The two inviscid and viscous CFD results in Figure 9–3 match the flat portion of the signature fairly well, though the viscous *OVERFLOW* result (sig set 34) has a bit of an undershoot at the start of the shocks for the model nose (X = 1) and the balance adapter (X = 15.5).

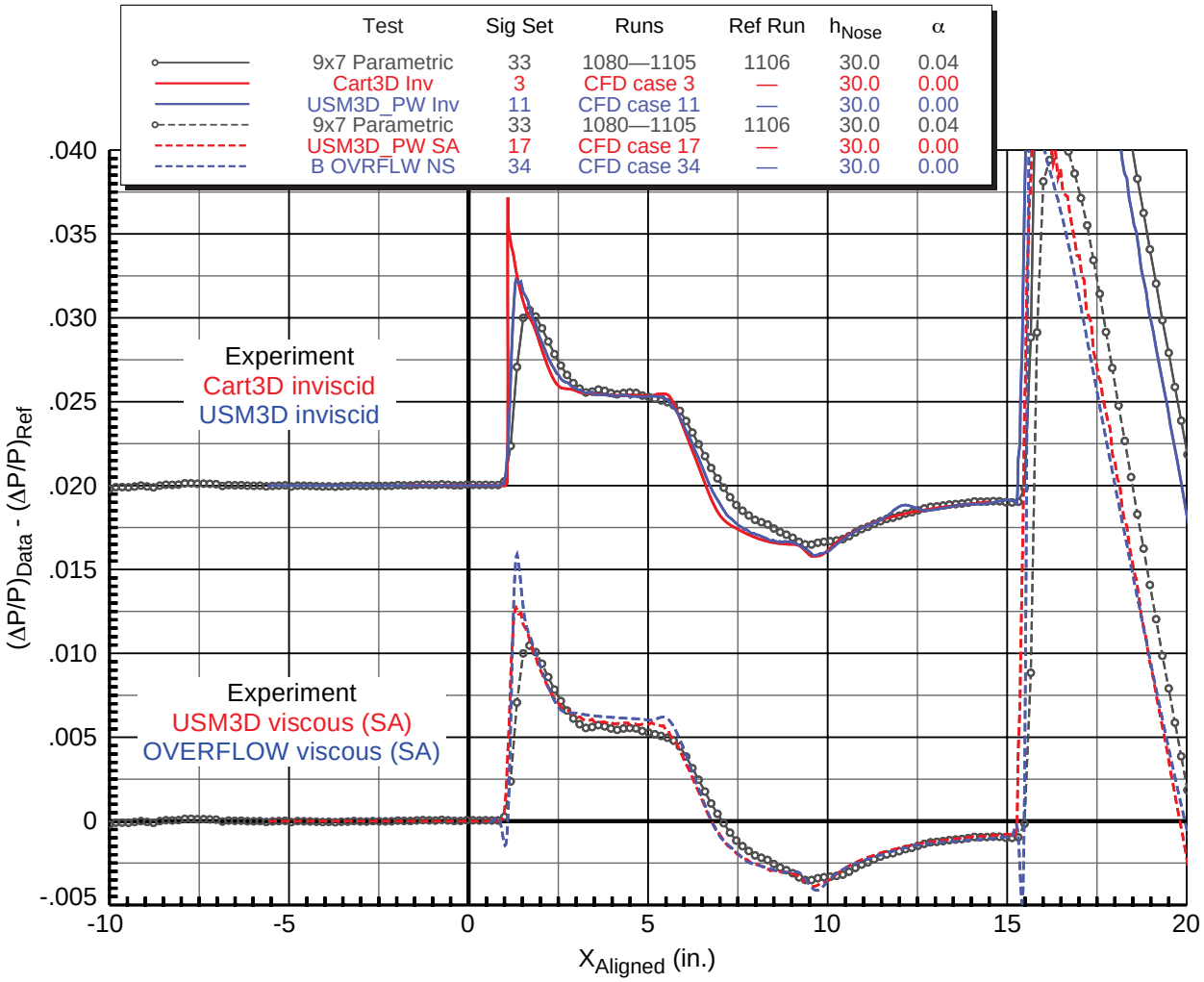

Figure 9–3. Experiment/CFD comparisons for AS2 model 9x7 parametric test, 14-in. forward rail, M = 1.60, h_{Nose} = 30 in., α = 0°

Figure 9–4 below shows experiment and inviscid/viscous CFD comparisons for the AS2 model at heights of 60 in. from the 2-in. rail in the 8x6 wind tunnel. In contrast to the prior figure with the 14-in.-rail data, the nose shock peaks are substantially higher than the CFD-predicted peaks. This is consistent with the rail comparison findings in the earlier section, in which the reflection factor for the 2-in. rail abnormally amplifies the shock peaks. The experimental data in Figure 9–4 also show a slight bump in the flat portion of the signature around $X = 3.5$. It is possible that this bump could be the reflection of the nose shock off the tunnel wall, though it is just over 2 in. aft of the nose shock in this Mach 1.56 signature, whereas a shock reflection in a Mach 1.6 flow is expected to affect the model signature a little less than 5 in. downstream of the incident shock as discussed above.

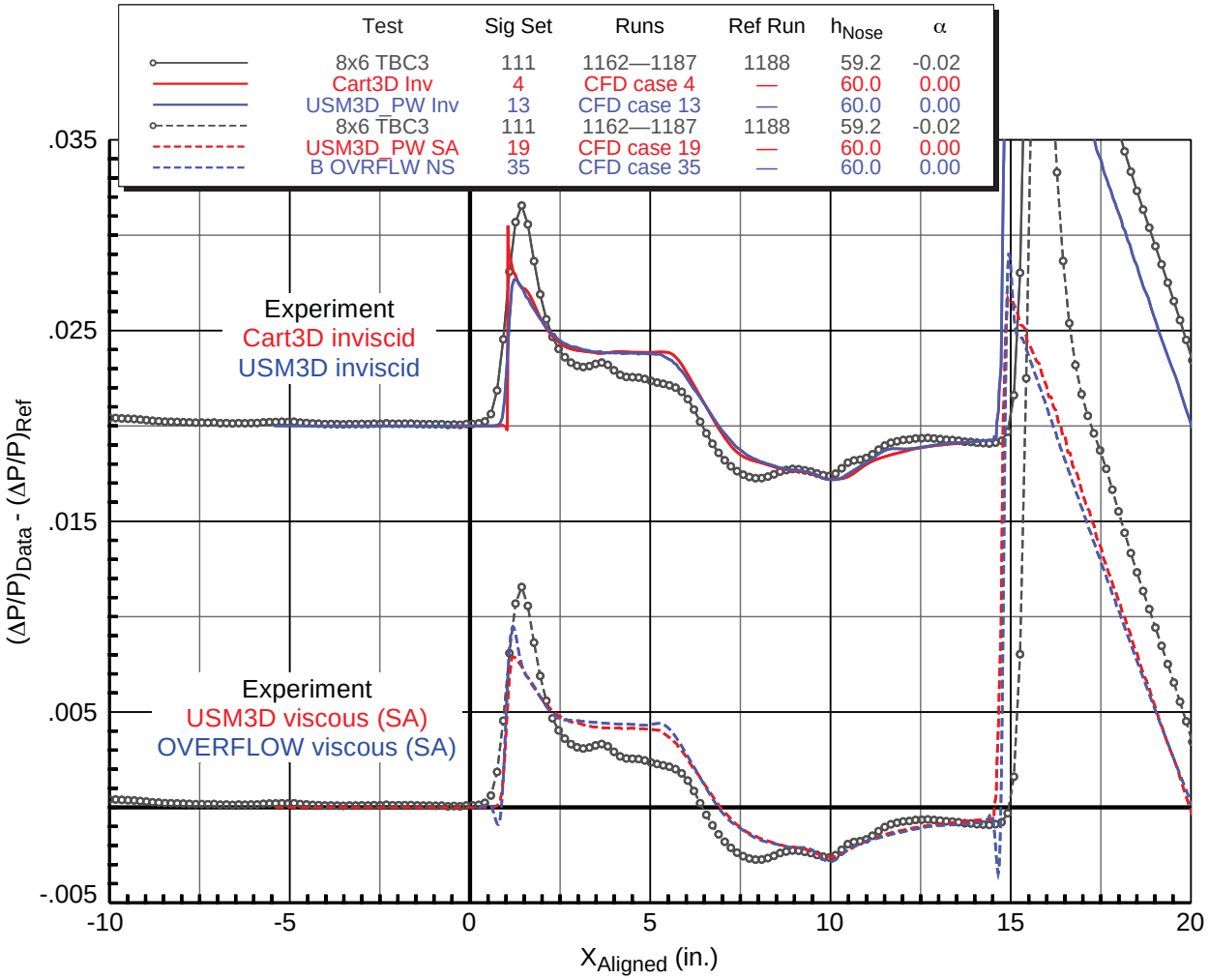

Figure 9–4. Experiment/CFD comparisons for AS2 model
8x6 TBC3 test, 2-in. rail, M = 1.56 (WT), 1.60 (CFD), h_{Nose} = 60 in., α = 0°

9.2. Boeing Boom1 Model

The flow field around the Boom1 VS2 was computed using all three codes for a free-stream Mach number of 1.6, angle of attack of 3.4,º and Reynolds number of 4.1 million per foot. Figure 9–5 shows pressure coefficient contours on the surface of the Boom1 VS2 model as computed by *USM3D* with a laminar boundary layer, and Figure 9–6 shows the symmetry plane pressure contours below the model for a *Cart3D* solution after 14 levels of adaption. The refinement pattern is driven by the features of the adjoint solution. As with the AS2 model predictions, the sonic boom signatures were extracted at a distances of 30 and 60 in. below the model nose for comparisons with the wind tunnel data, as indicated by the orange lines in the figure.

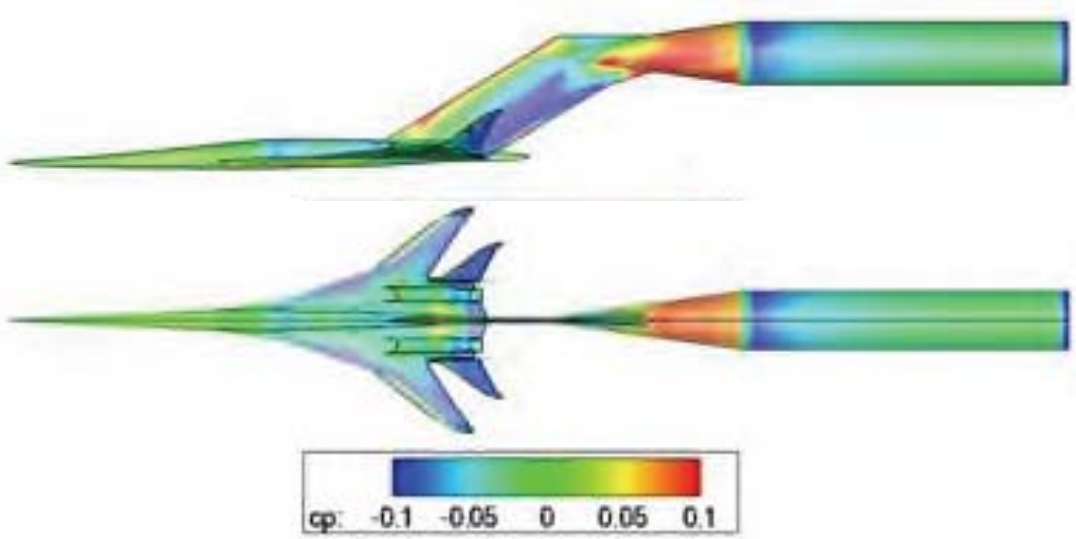

Figure 9–5. Surface pressure contours for Boom1 VS2 model, *USM3D* laminar results, M = 1.6, α = 3.4°

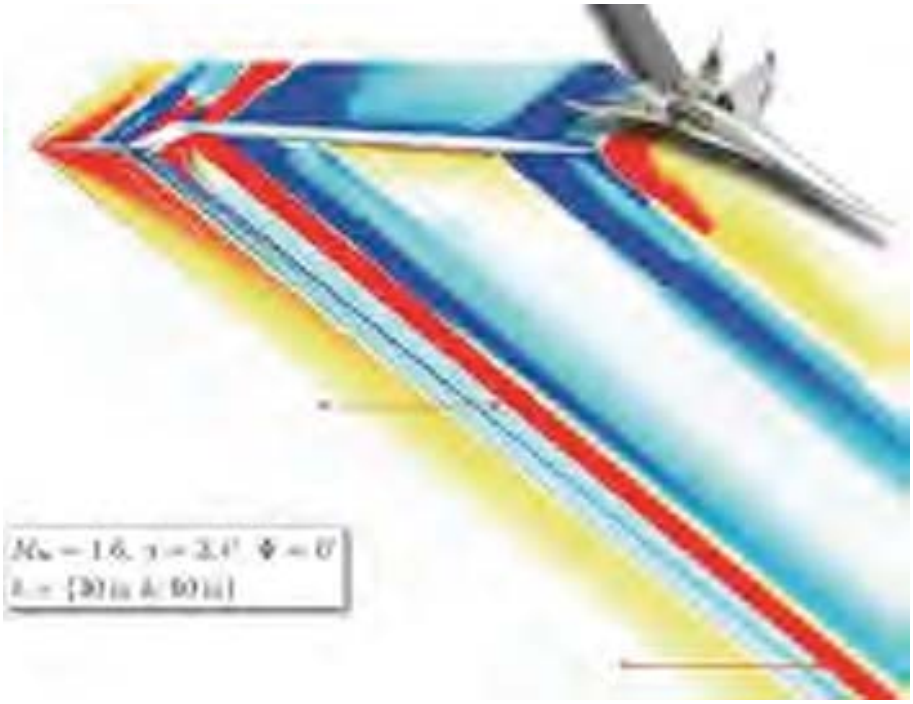

Figure 9–6. Symmetry plane pressure contours for Boom1 VS2 model, *Cart3D*, M = 1.6, α = 3.4°

Inviscid *Cart3D* and *OVERFLOW* predictions for Boom1 VS2 are compared with wind tunnel data in Figure 9–7 at α = 3.4° and h_{Nose} = 30 in. There is very good agreement between the CFD results and wind tunnel data along the flat portions of the signature, but both CFD codes predict stronger shocks at every location along the experimental data signature where there is some waviness or a rounded shock peak. The rounding is not surprising since the temporal and spatial variations in the wind tunnel flow cause individual pressure signatures in an *X* or *Z* sweep to have varying degrees of shock peak amplitudes that become somewhat washed out in the averaging. The greatest differences between the CFD and experimental data are aft of the main expansion, where the codes predict some very strong shocks from the region around the nacelles and vertical tails. The absence of a boundary layer is the cause of the discrepancy with experiment.

Viscous *OVERFLOW* and *USM3D* laminar predictions for this model at the same conditions provide a better match with the wind tunnel data than the inviscid predictions, and the shock peaks are not nearly as amplified as for the inviscid predictions as well. Note that the *OVERFLOW* prediction captures more of the small-shock details than the *USM3D* prediction does just forward of the main expansion, but which are not seen in the experimental data.

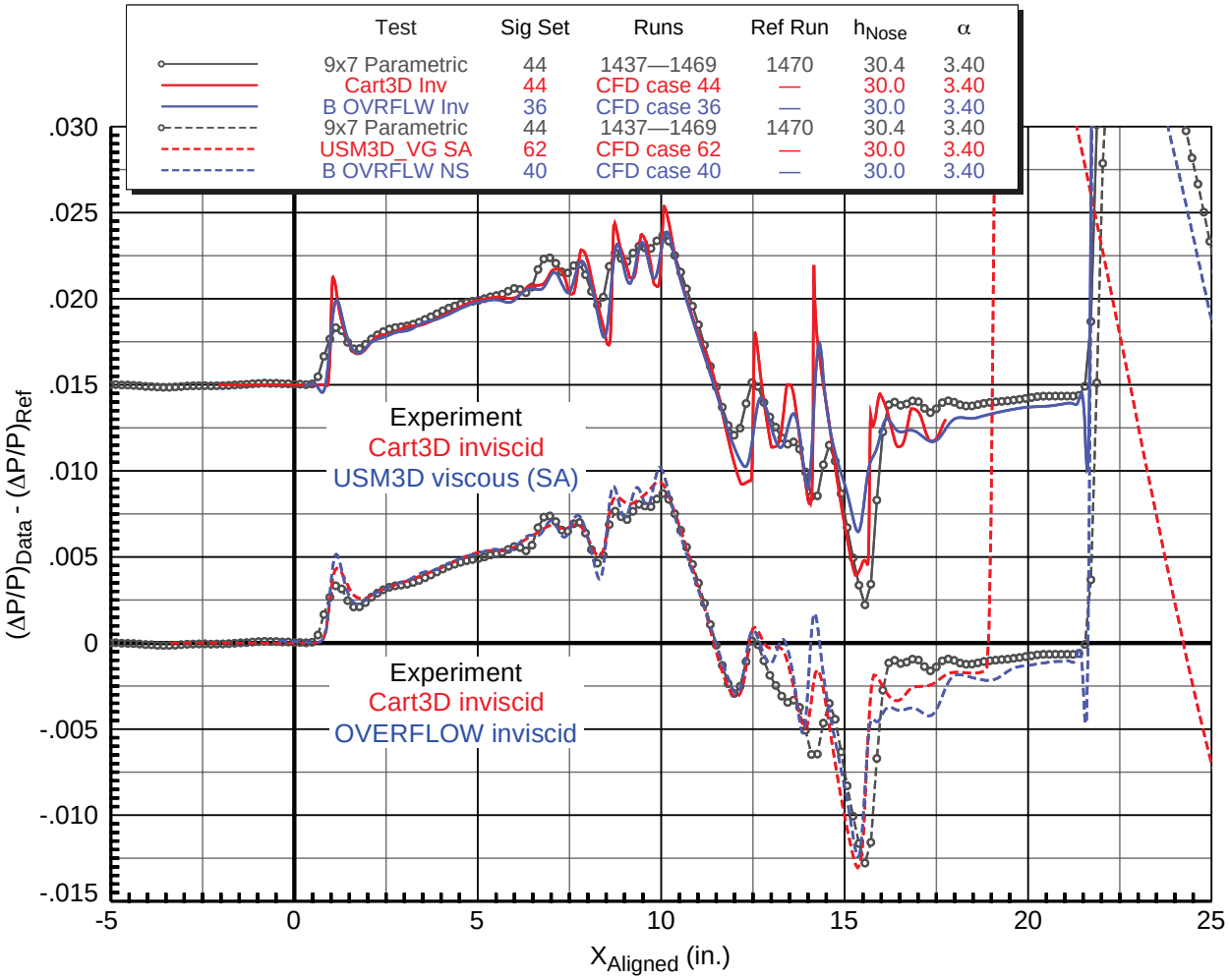

Figure 9–7. Experiment/CFD comparisons for Boom1 VS2 model 9x7 parametric test, 14-in. forward rail, M = 1.60, h_{Nose} = 30 in., α = 3.4°

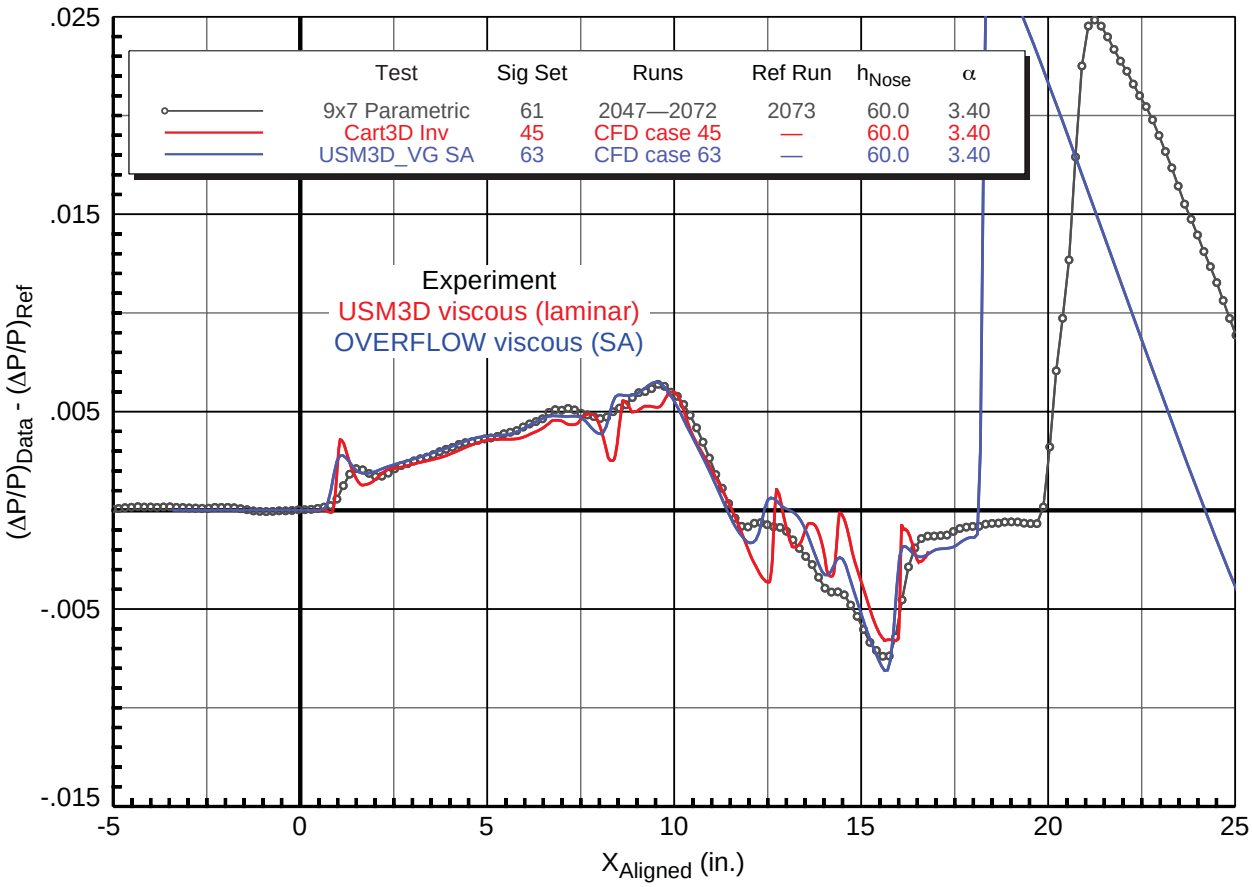

Figure 9–8. Experiment/CFD comparisons for Boom1 VS2 model 9x7 parametric test, 14-in. aft rail, M = 1.60, h_{Nose} = 60 in., α = 3.4°

CFD/experiment comparisons at h = 60 in. are shown in Figure 9–8. One inviscid solution is given from *Cart3D* and one viscous turbulent solution is given from *USM3D* with the Spalart-Allmaras turbulence model. As with the comparisons at 30 in., the agreement is generally very good, with the shock peaks from the predictions being somewhat higher than those from the wind tunnel, especially for the inviscid solution. Note that the greatest discrepancies between the experimental and CFD data occur in the aft part of the signature, with the viscous solution being closer to the wind tunnel data than the inviscid solution.

Comparing the overall pressure level between this figure and that of the previous two figures confirms that the CFD codes did very well in capturing the effects of model height.

9.3. Boeing Boom3 Model

Laminar and turbulent *USM3D* predictions were made for the Boom3 VS3 model at Mach 1.6, a Reynolds number of 4.1 million per foot, α = 3.1º, and off-track angles of 15°, 30°, and 45° in addition to the on-track angle of 0°. Figure 9–9 shows the surface pressure contours on this model for a *USM3D* laminar solution, and the symmetry plane flow field pressure contours down to a height of 60 in. are shown in Figure 9–10.

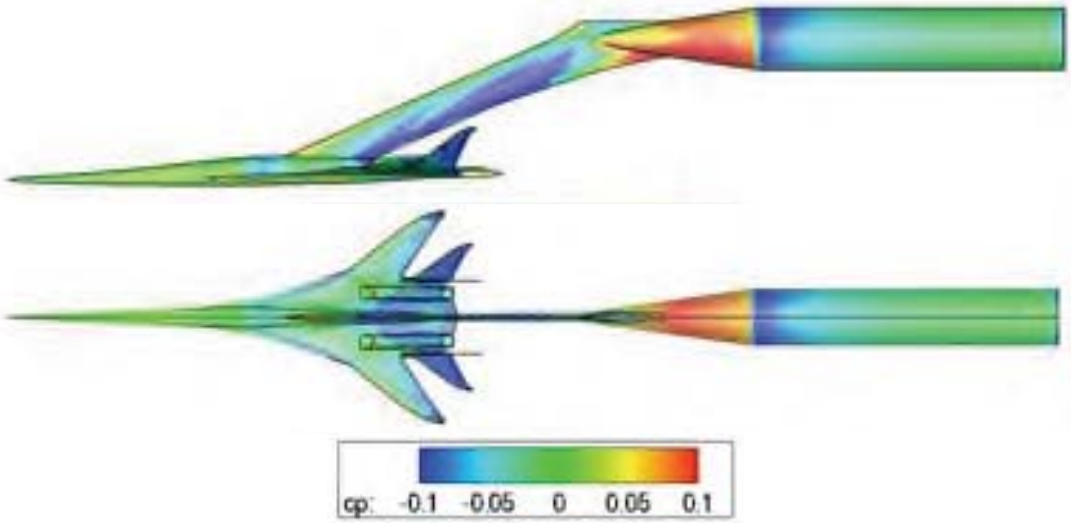

Figure 9–9. Surface pressure contours for Boom3 VS3 model, *USM3D* laminar results, $M = 1.6, \alpha = 3.1°$

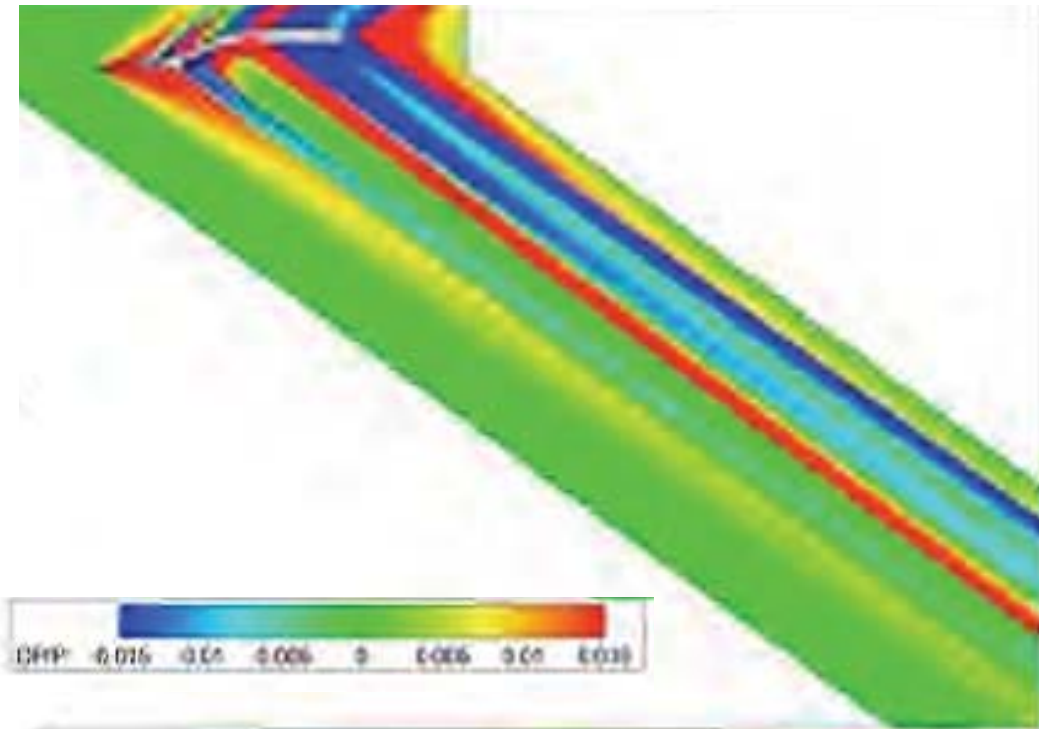

Figure 9–10. Symmetry plane pressure contours for Boom3 VS3 model, *USM3D* laminar results, $M = 1.6, \alpha = 3.1°$

The experiment/CFD comparison plots that follow are for each of the on-track and off-track angles at a model height of 60 in., but first a plot of just the *USM3D-SA* predictions at the four track angles is given in Figure 9–11 to clearly illustrate the differences in the signatures at these angles. Note that the four signatures are very similar in the forward region (as expected since the geometry here is mostly a body of revolution), with the exception that the nose shock is predominant in the $\varphi = 0°$ case and becomes smaller until flat in the $\varphi = 45°$ case. The reason for this could be due to the flow field grid being of finer resolution below the model than off to the sides, but this is being looked into at the time of this writing. The primary differences in the signatures occur from the lifting surfaces of the model, from the wings aft. The main expansion becomes deeper and moves forward with off-track angle, and the aft shocks become stronger. The same is generally true for the experimental data at these four track angles shown in Figure 33, but the nose shock signature shape stays very consistent with off-track angle, as would be expected.

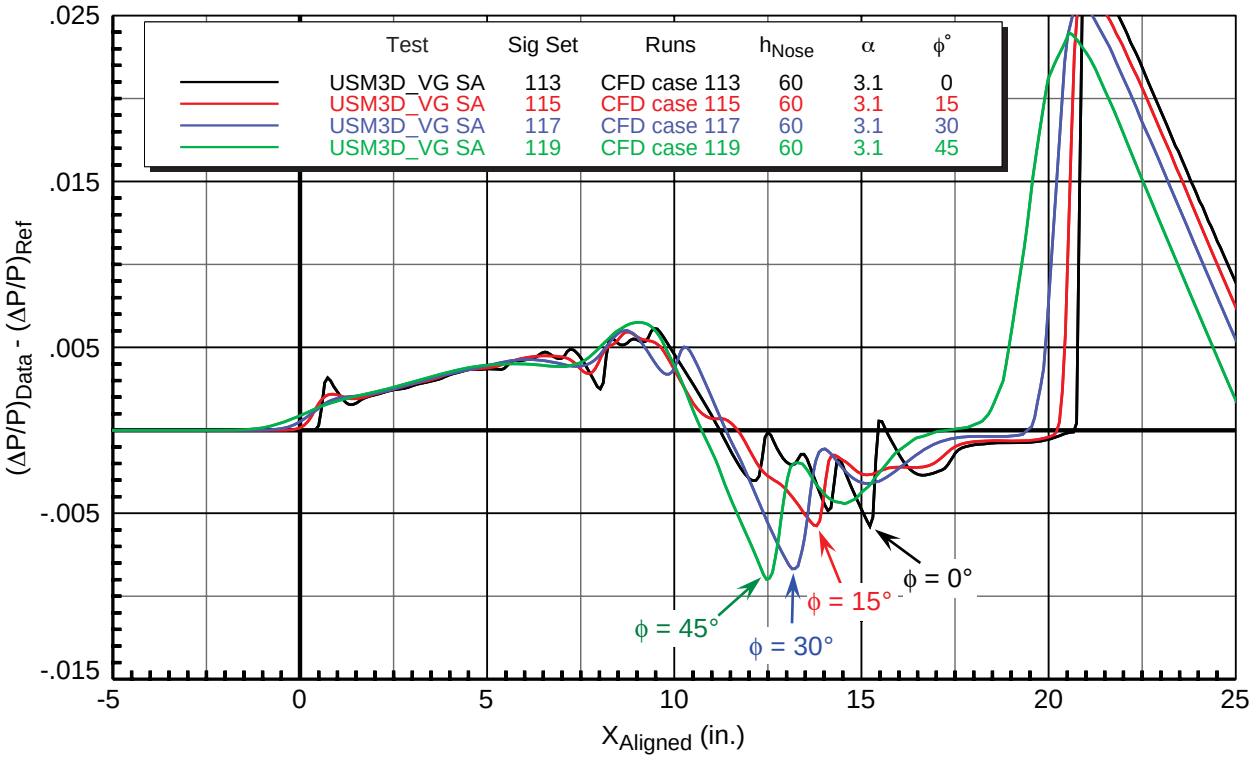

Figure 9–11. CFD predictions for effect of off-track angle for Boom3 VS3 model, *USM3D SA* turbulent results, $M = 1.6$, $h_{Nose} = 60$ in., $\alpha = 3.1°$

The four sets of curves in Figure 9–12 show comparisons between the experimental data and viscous CFD results (*USM3D* laminar and turbulent SA) for this model at the conditions specified above. Note the 0.02 $\Delta P/P$ offsets for the upper three sets of curves. In general there is good agreement between the experimental and CFD results in the front part of the signatures at all track angles, though not as good for capturing the nose and wing shocks at the 45° off-track angle. In the $\varphi = 0°$ case, the laminar and turbulent *USM3D* results agree with each other from the front through the main expansion, but aft of this they differ. Both *USM3D* methods predict stronger nose shocks under track, which appears smeared in the experimental data, and they also overpredict the strength of some of the aft shocks under track after the main expansion. The 15° and 30° off-track CFD predictions match the wind tunnel data very well overall, with little difference between the laminar and turbulent solutions.

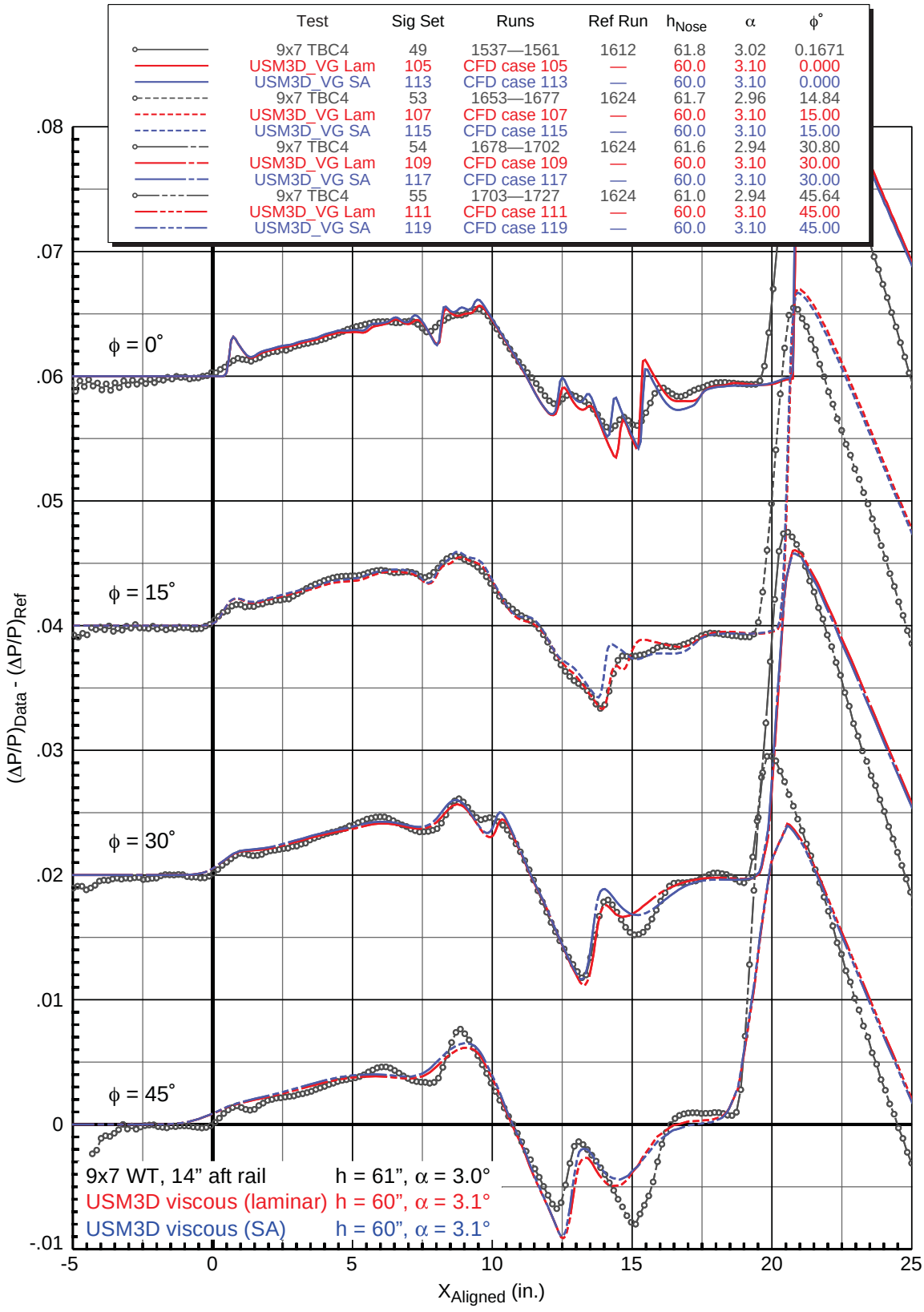

Figure 9–12. Experiment/CFD predictions for Boom3 VS3 model at various off-track angles 9x7 TBC4 test, 14-in. aft rail, M = 1.60, h_{Nose} = ~60 in., α = ~3.1°

9.4. Performance Model

Similar laminar and turbulent *USM3D* predictions were made by NASA for the larger Performance model as for the Boom3 VS3 model, at the same conditions of Mach 1.6, a Reynolds number of 4.1 million per foot, a height of 60 in., and for the track angles of 0°, 15°, 30°, and 45°. The angle of attack for these predictions though was 3.4° since this configuration is of the same design as the Boom1 model aside from the difference in mounting provisions. Figure 9–13 shows the surface pressure contours on this model for a *USM3D* turbulent solution, and the symmetry plane flow field pressure contours down to a height of 60 in. are shown in Figure 9–14.

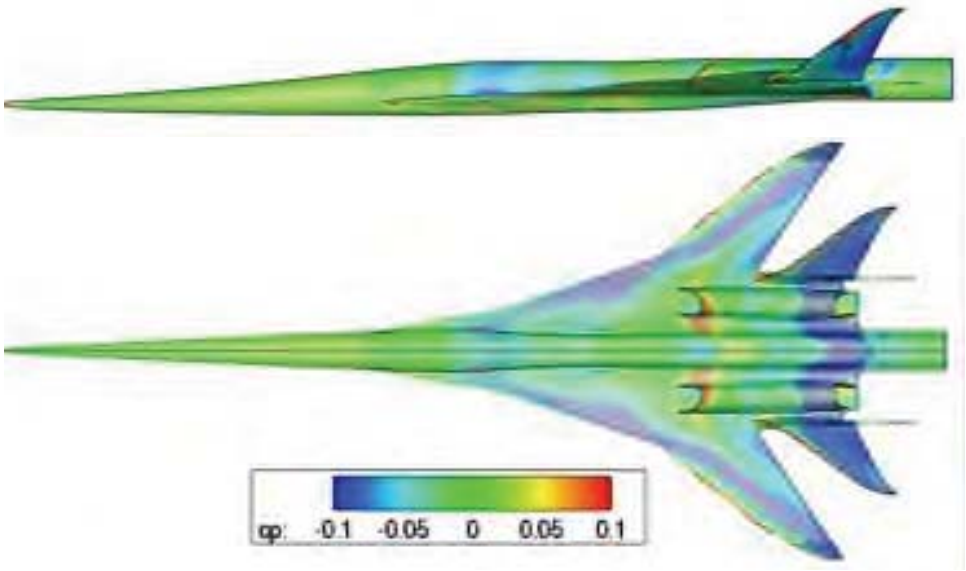

Figure 9–13. Surface pressure contours for Performance model, *USM3D SA* turbulent results, M=1.6, α=3.4°

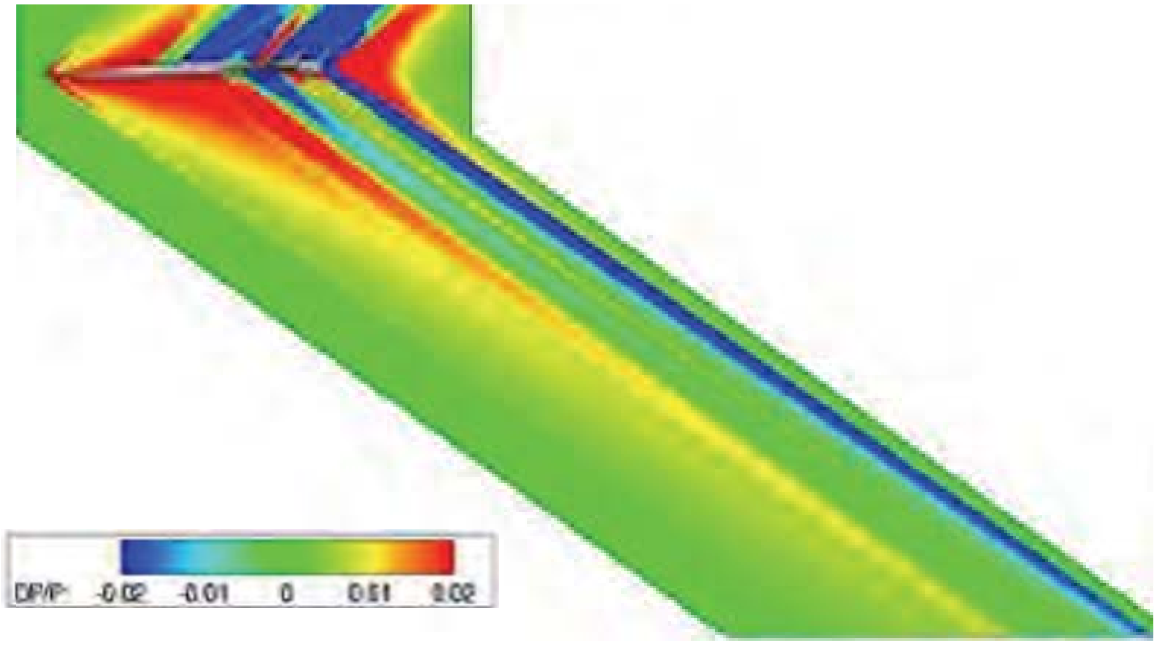

Figure 9–14. Symmetry plane pressure contours for Performance model, *USM3D SA* turbulent results, M=1.6, α=3.4°

Note that as shown in these figures, the configuration was modeled in CFD with the sting can at the aft end and *not* the tailored dummy sting (refer to Figures 4–6 and –7). As stated in Section 4.2.1, the experimental data presented herein were acquired with the tailored dummy sting, so this represents a configuration mis-match in the experiment/CFD comparisons to be presented. The dummy sting surface mesh was not available in time for preparation of those results for this report, so the comparisons are presented as they are to show the differences/similarities in the front halves of the signatures.

A set of plots similar to those presented above for the Boom3 model showing the predicted effects of off-track angle and comparisons with experimental data are shown in Figures 9–15 and –16. The first plot, Figure 9–15, shows the *USM3D-SA* predictions at the four track angles from 0° to 45°. In this case, however, unlike the Boom3 model predictions, the shape and magnitude of the nose shock at all four angles are identical, and the signatures overlap up to the start of the wing shock, as one would expect. Aft of this point, similar to Boom3, the main expansion pressures become deeper and move forward with off-track angle.

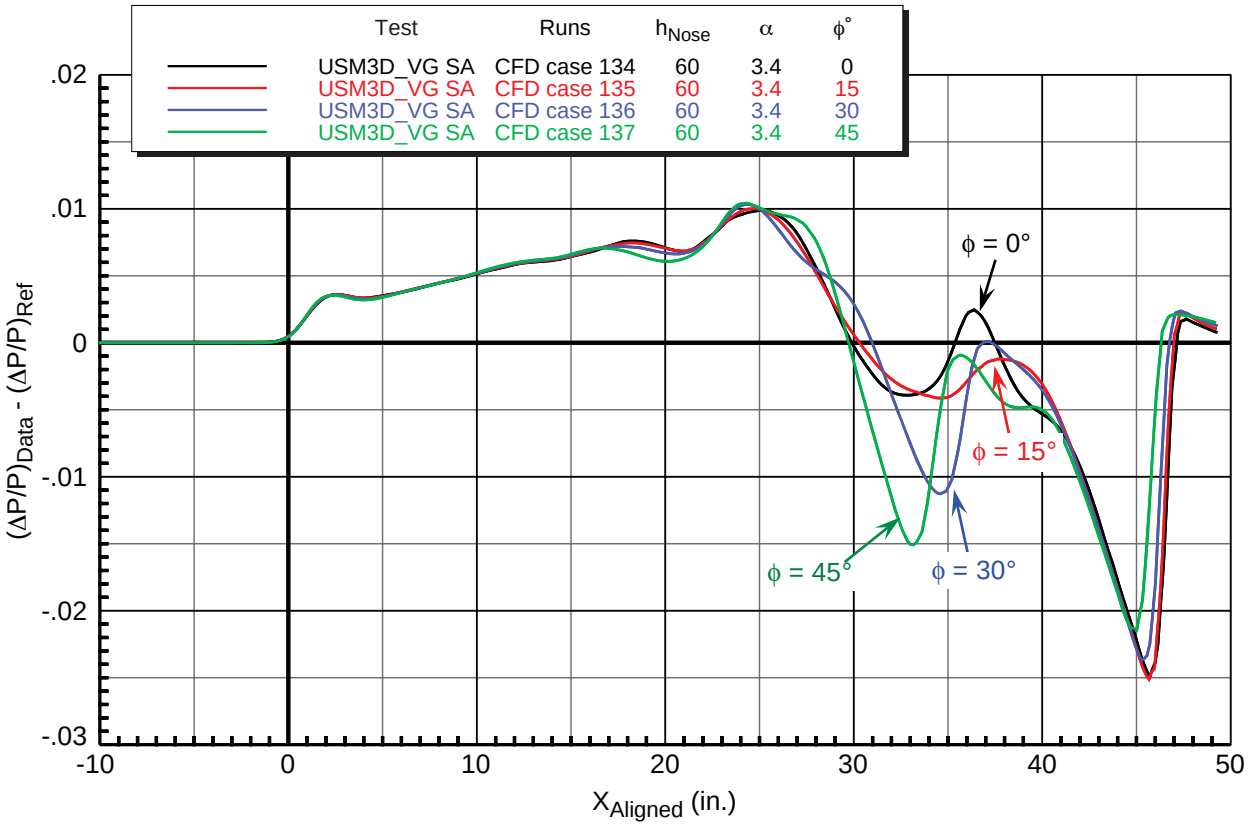

Figure 9–15. CFD predictions for effect of off-track angle for Performance model, *USM3D SA* turbulent results, M = 1.6, h_{Nose} = 60 in., α = 3.1°

Comparisons between the experimental data and CFD results (USM3D turbulent SA) for this model are presented in Figure 9–16, with the caveat as stated above that the tailored dummy sting was used in the experiment and the sting can was used in the CFD. The CFD predictions did not match the experimental data in the front half of the signature (ahead of the *y0* point—where the mail expansion after the highest peak crosses the y = 0 line) nearly as well for this model as they did for the Boom3 model. In these Performance model plots, the experimental data show a lot of definition of the small shocks along the length of the model that the CFD did not capture. There may be too much variation, however, in the measured data for this model, in that the ramp from the nose shock to the wing shock is fairly smooth in the Boom1 and Boom3 signatures, leading to some questions about the validity of the data for this model.

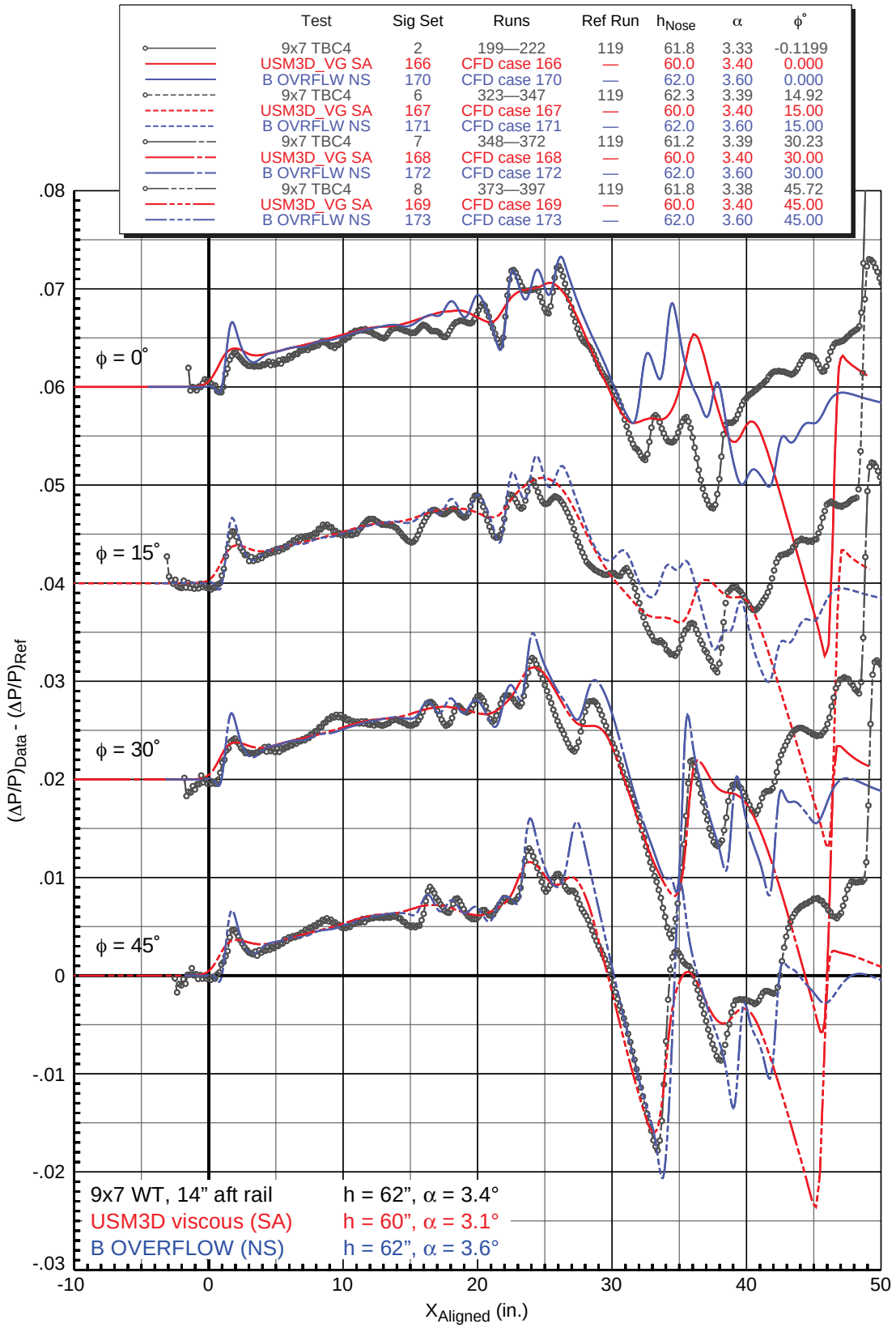

Figure 9–16. Experiment/CFD predictions for Performance model at various off-track angles 9x7 TBC4 test, 14-in. aft rail, M = 1.60, h_{Nose} = ~60 in., α = 3.1° to 3.6°

Despite this, however, it is clear from the plots that the overall trends of the signature variations with off-track angle; in particular, matching the main expansions quite well in the 30° and 45° off-track angle cases.

The expansions and shocks aft of the *y0* point show significant disagreements between the CFD and experimental data, as expected due to the sting can vs. tailored dummy sting differences, though it is surprising to see better agreement as the off-track angle is increased.

10. Propagated Signatures to Ground Level

Selected near-field pressure signatures from the measured data for the Boom1, Boom3, and Performance models were extrapolated to ground level by the *sBOOM*[46] code and their loudnesses estimated using a code based on the procedure by Shepherd.[47] Flight altitudes of 47,500 ft were assumed for all cases since that is the cruise altitude chosen by Boeing in their studies, and the signatures were scaled up in *X* by the inverse of the model scale before being processed in *sBOOM.*

No adjustments were made to the measured signatures for input to *sBOOM* other than truncating them so that they began and ended at zero *ΔP/P*, and ensuring that none of the portions of the signature associated with the model support system were included. It is recognized that without correcting the signatures to a flight configuration—replacing the model aft end and support system flow field pressures with estimated pressures for the full airplane with propulsion system effects—the absolute levels of the predicted sonic boom loudnesses will not be right. The low experimental Reynolds number (1 million at Mach 1.6 based on Boom1 model chord) relative to that in cruising flight (72 million at Mach 1.6, 47,500 ft) also contributes to errors in the loudness levels estimated from wind tunnel measurements. However, it is the intent in this report to show the estimated ground signatures for the various configurations and to highlight their *differences* both in terms of the signature shapes and the loudness levels. No inferences should be made about the *PLdB* levels quoted for the extrapolated signatures being the final levels expected for the selected configurations. Modeling the full-scale vehicle at flight conditions in CFD is required for more accurate estimation of the real sonic boom loudness levels.

10.1. Repeatability

Near-field signatures showing the repeatability of three *Z*-sweep run series acquired back-to-back for the Performance model in the TBC4 test were shown in Figure 7–8, and these signatures extrapolated to ground level are shown in Figure 10–1. The data were acquired at Mach 1.6 in the 9x7 wind tunnel, with the model approximately 62 in. from the 14-in. rail at 3.3° angle of attack. The small differences in the near-field signatures cause some differences in the ground signatures, particularly in the front ramp portions. The first curve, sig set 2, has the highest pressure peak and the greatest loudness by 3 dB over the other two curves, indicating the sensitivity of the loudness metric to the small shape differences among the repeat runs.

10.2. Effect of Mach Number

Two *X*-sweep run series for the Boom1 model in the 9x7 parametric test showing the signature differences between Mach 1.6 and 1.8 were presented in Figure 7–35, and the signatures extrapolated to the ground for these run series are presented in Figure 10–2. In the near-field signatures, there was a significant increase in the overall pressure levels and shock peaks at Mach 1.8 relative to Mach 1.6, and this is also true for ground signatures, where the higher-Mach-number case has a sound level 4.5 dB higher than at the lower Mach number.

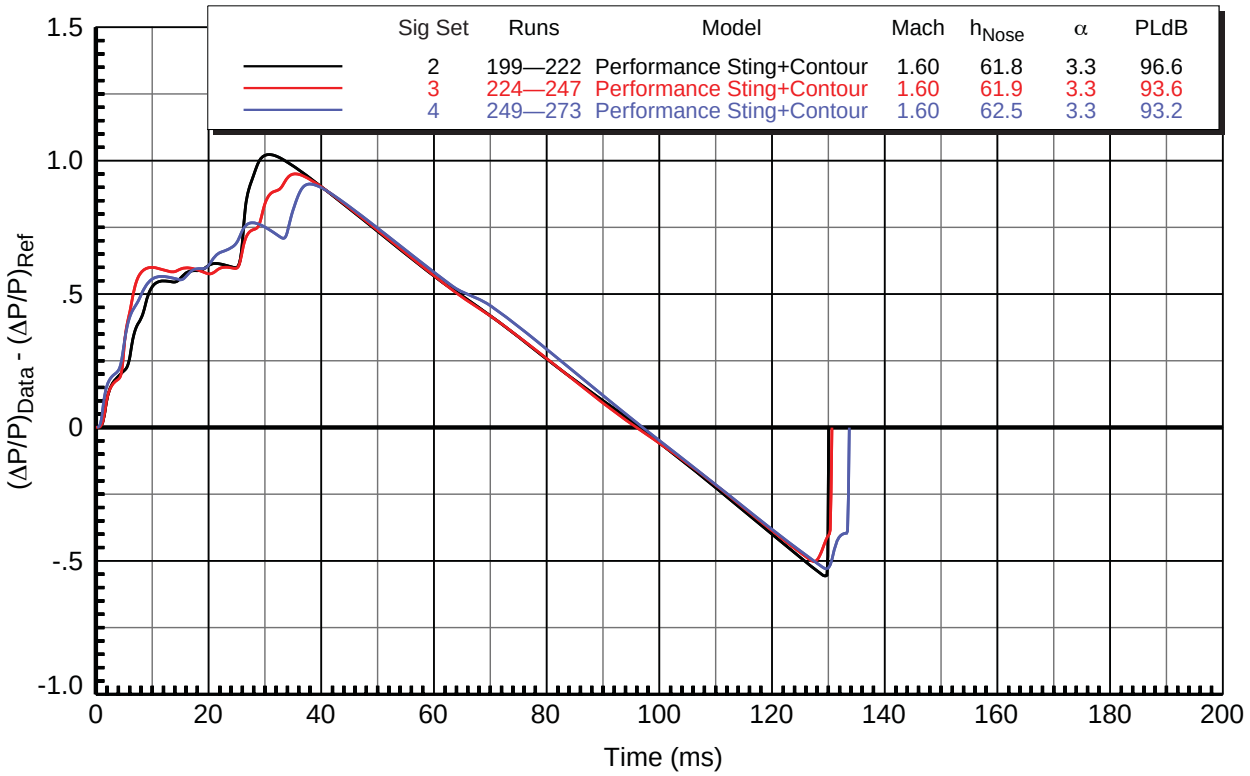

Figure 10–1. Repeatability of *sBOOM*-extrapolated signatures for Performance model 9x7 TBC4 test, 14-in. aft rail, M = 1.60, h_{Nose} = ~62 in., α = 3.3°

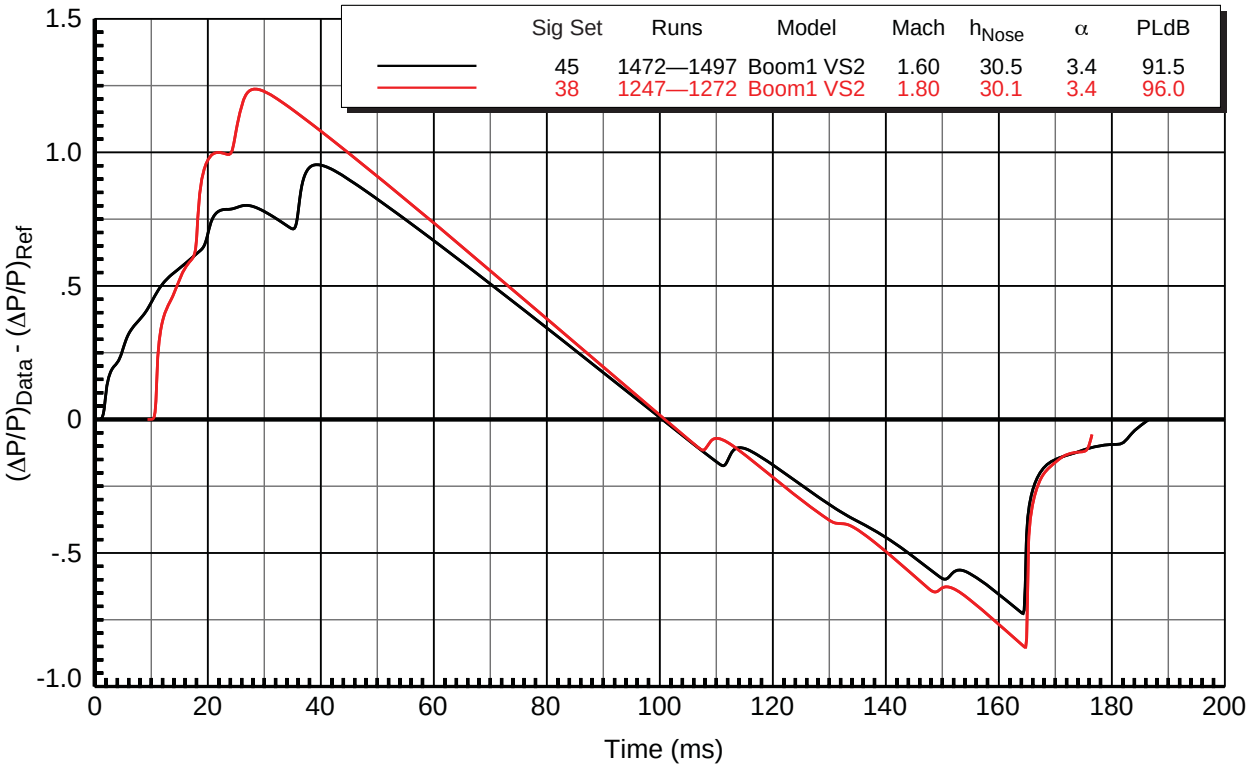

Figure 10–2. Effect of Mach number in *sBOOM*-extrapolated signatures for Boom1 VS2 model 9x7 parametric test, 14-in. forward rail, M = 1.60, h_{Nose} = 30 in., α = 3.4°

10.3. Effect of Off-Track Angle

Boom3 model pressure signatures at 60 in. from the rail at three different off-track angles, 15°, 30°, and 45°, as well as undertrack, 0°, were presented in Figure 9–12, and those signatures extrapolated to ground level are presented in Figure 10–3. The primary differences among the near-field signatures are in the highest pressure peaks just before the main expansions, and in the shocks right after the main expansions. In the ground signatures, these differences are apparent in the locations and magnitudes of the coalesced shocks toward the front and in the rear shocks. There is a spread of sound levels of around 7 dB among these signatures, with the 30°- and 45°-angle data having the highest levels.

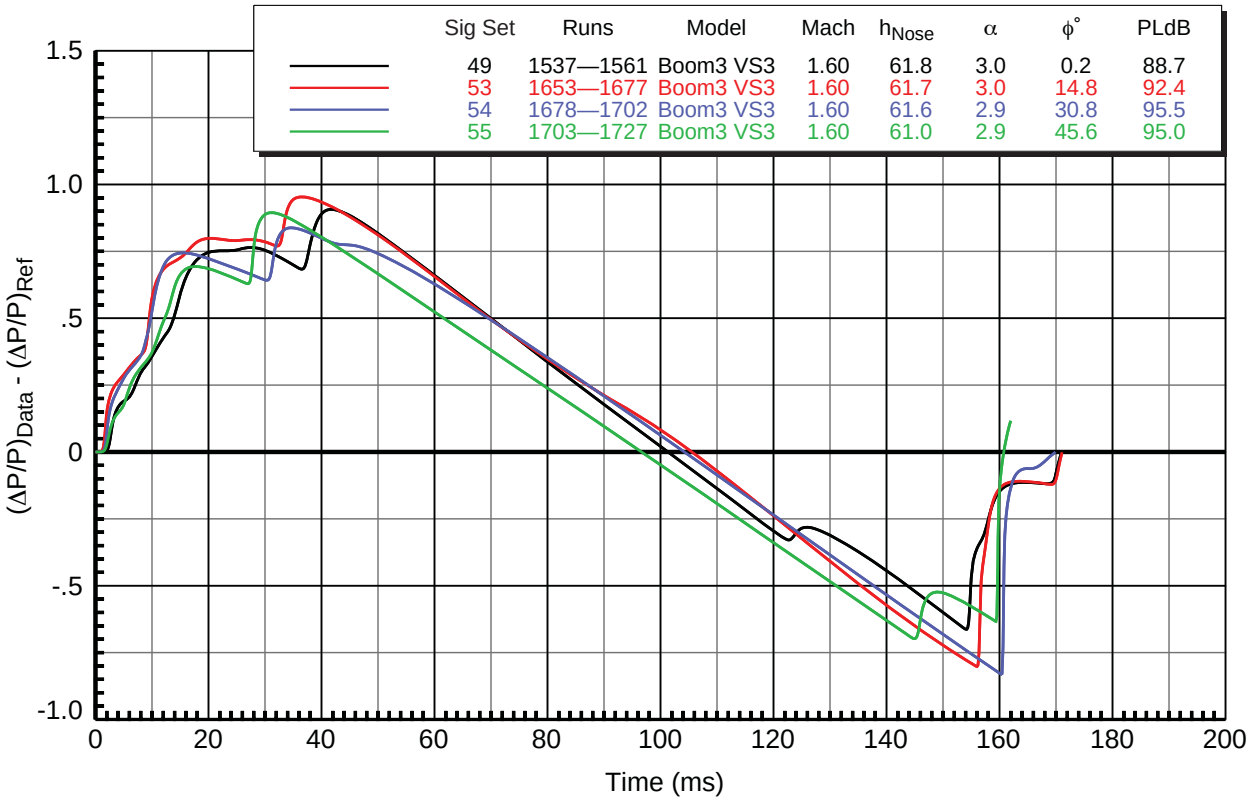

Figure 10–3. Effect of off-track angle in *sBOOM*-extrapolated signatures for Boom3 VS3 model 9x7 TBC4 test, 14-in. aft rail, M = 1.60, h_{Nose} = ~62 in., α = ~3.0°

11. Performance Model Drag Comparisons

As part of the evaluation of NASA in-house prediction capability for supersonic transports, CFD drag predictions were made for the Boeing Performance model (with the sting can at the rear, not the tailored dummy sting). The code used was *USM3D*, and the grids were generated using *VGrid.*[49] The grid was optimized for drag prediction (thus with a viscous solution), and it was not stretched or extended to obtain a boom signature at some distance from the model. *OVERFLOW* predictions from Boeing were also included in the study for comparison.

Drag polar comparisons of experimental data with the *USM3D* and *OVERFLOW* predictions are shown in Figure 11–1 for the Performance model at M = 1.6, α = 2.75º. The *USM3D* results compare well with the experimental and differ by a maximum of 6 counts of drag (0.0006). Additionally, the *USM3D* results are in closer agreement to wind tunnel data than the Boeing-supplied *OVERFLOW* results.

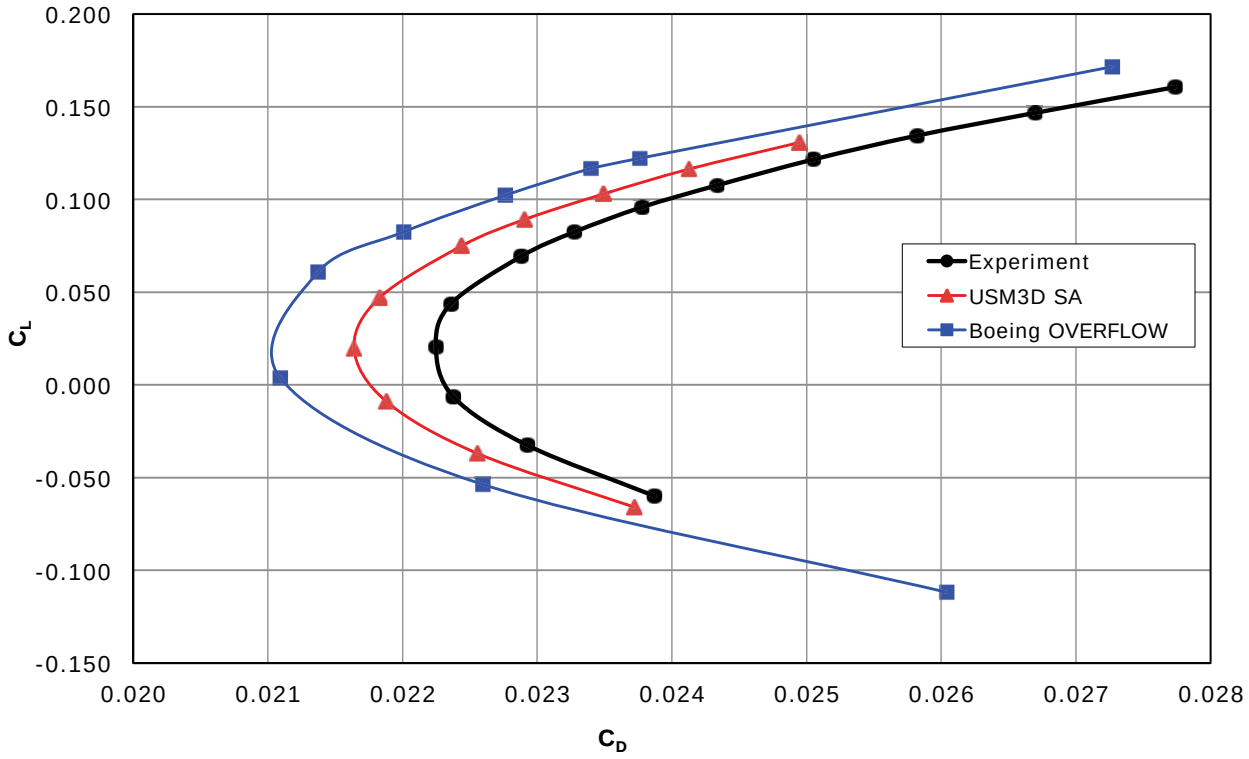

Figure 11–1. Experiment/CFD comparisons of drag polars for Performance model, M = 1.6, α = 2.75°

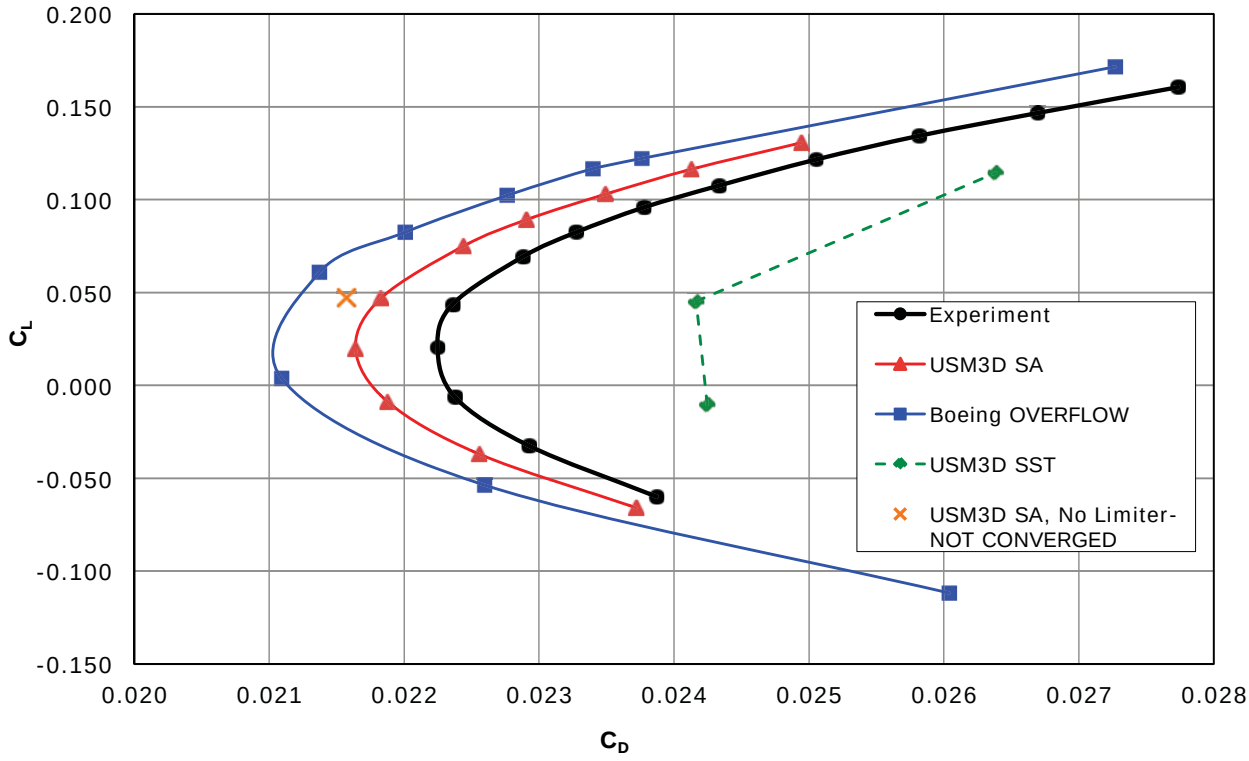

Figure 11–2. Experiment/CFD comparisons of turbulence models for Performance model, M = 1.6, α = 2.75°

A study of the standard turbulence models used for supersonic testing was also conducted. The bulk of the study was conducted with the Spalart-Allmaras *(SA)* turbulence model.[48] Additionally, Menter's Sheer Stress Transport *(SST)* turbulence model[48] has shown promise for supersonic predictions, so three runs using this model were also made. Figure 11–2 shows the effect of turbulence modeling on the computed drag polar. *USM3D SA* results were closer to the wind tunnel data than Boeing *OVERFLOW* and *USM3D SST* results. For this case, the *SST* model did a poor job predicting the drag and was considerably different from all of the other results. Also included in the figure are the results from an *SA* run with out the *MINMOD* limiter. This limiter is needed for most supersonic flow cases to avoid numerical oscillations that result in the code being unable to compute results (NaNs). Historically, the use of a limiter has incorrectly predicted the skin-friction drag. Several runs were conducted without the use of the limiter. However, none of the runs were fully successful in that the code reported errors and terminated. The furthest-processed data point (closest to convergence) is shown, and as can be seen, it further deviates from the experimental data than the *USM3D SA* case with the limiter. In all of the limiter-off cases, the drag value moved away from the *USM3D* results and closer to the Boeing *OVERFLOW* predictions.

A grid convergence study using *USM3D SA* was conducted as part this computational analysis of the Boeing Performance model. The locations of the sourcing remained constant, although the size of the grid cell dictated by the source was altered both up and down by an overall scaling factor. Five grids were created ranging from 26.5 to 72.2 million grid cells. Figure 11–3 shows that as the grid size increased the code converged to a smaller drag number for the given point. The difference between the 68.9- and 72.2-million-point grids was less that 0.1 percent. Consequently, the 68.9-million-point grid was used for the study (this was the original grid produced).

Finally, a comparison of results from a grid designed for boom prediction and a grid designed for drag prediction was made. The boom-stretched grid was created by *VGrid,* then sourced by *AUTOSRC* and *SSGRID* to stretch the grid. These methods were introduced in 2008 as part of the NASA Fundamental Aeronautics Program Sonic Boom Prediction Workshop.[52] The grid had 34 million grid cells and was stretched for the case at Mach 1.6 with an angle of attack of 2.75°. The results are compared to the baseline 68.9-million-point grid in Figure 11–4 and differed by over 2.4 counts of drag although the lift coefficient did increase slightly. An additional grid was therefore made to try to reduce this difference. This new grid used the sourcing from the baseline case, but had a volume source inserted under the model (as *AUTOSRC* adds) and a smaller outer boundary. *SSGRID* was then used to stretch the grid for the same Mach 1.6, angle of attack 2.75° case. The resultant grid had approximately 67 million cells, and the drag results are much closer to the baseline results, differing by less than one-tenth of a drag count.

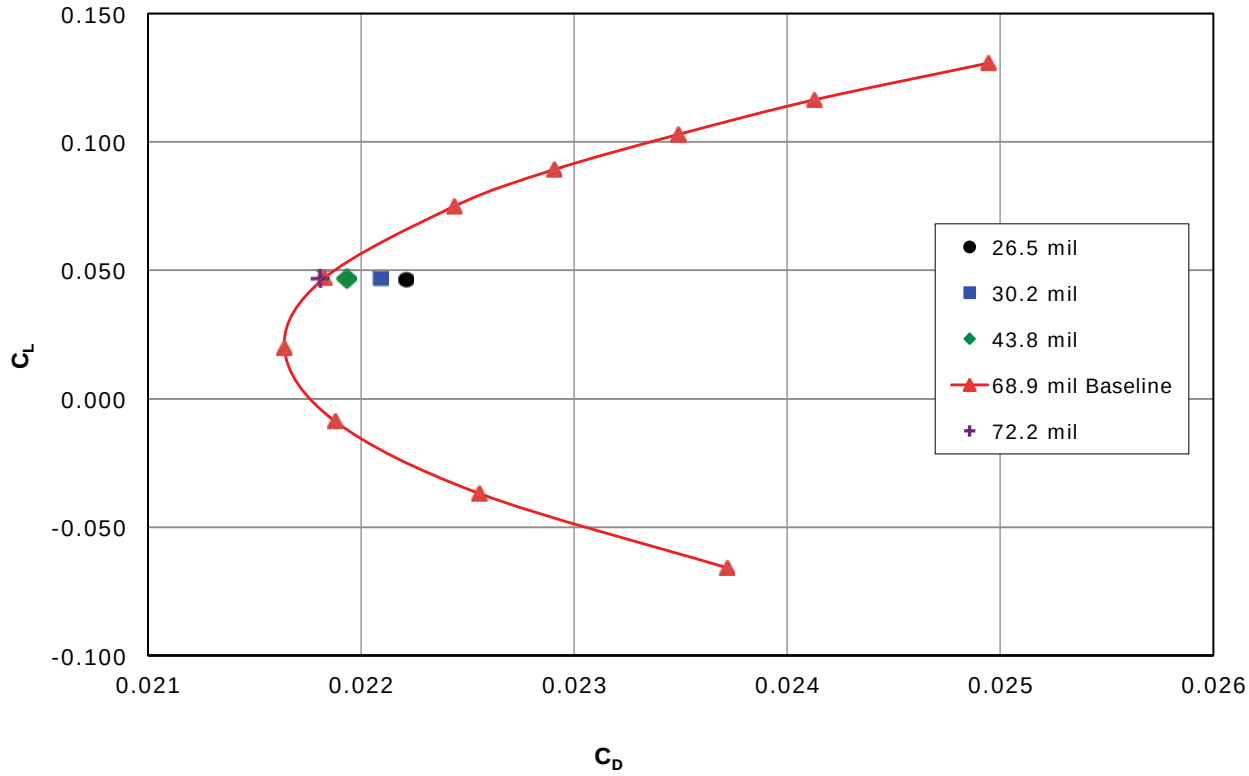

Figure 11–3. Grid convergence study for Performance model, M = 1.6, α = 2.75º

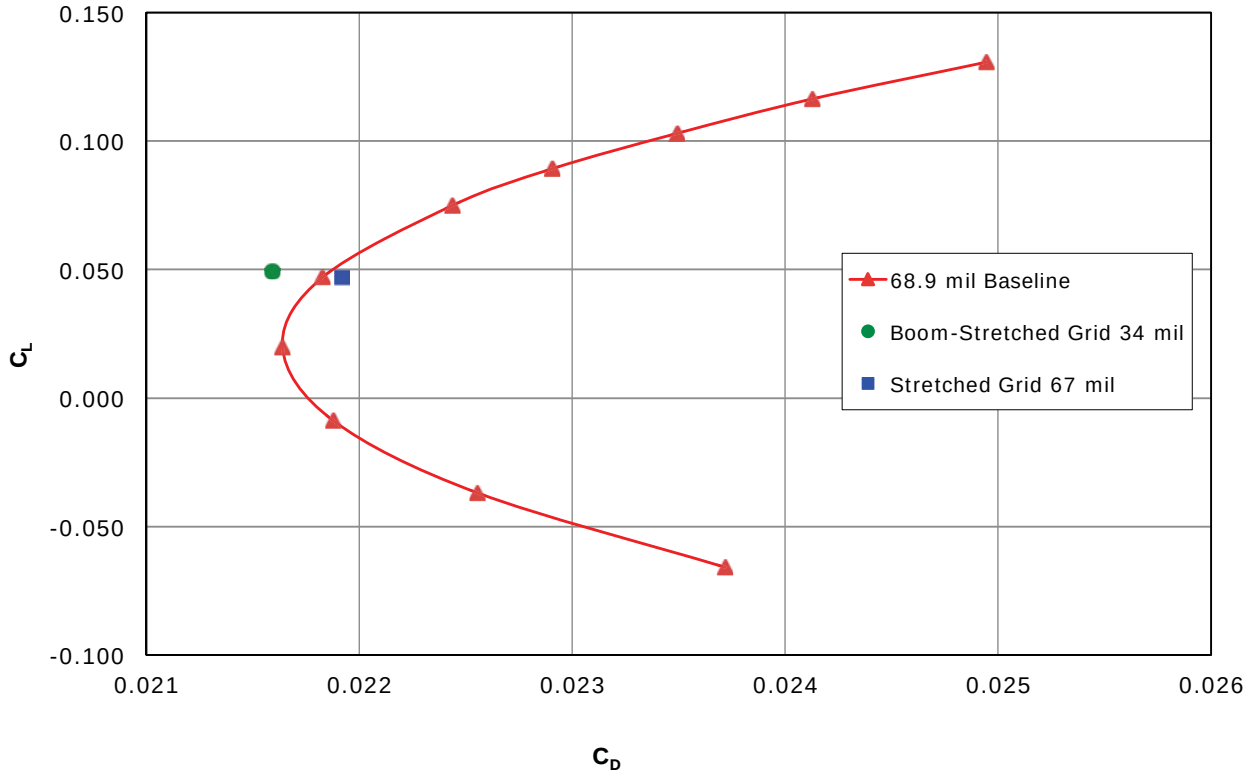

Figure 11–4. Effect of gridding style on drag prediction for Performance model, M = 1.6, α = 2.75º

12. Concluding Remarks

Near-field pressure signatures were measured and computational predictions made for three models representing Boeing's Quiet Experimental Validation Concept (QEVC) supersonic transport as well as for an axisymmetric calibration model. Experimental sonic boom pressure signatures were acquired primarily at Mach 1.6 and 1.8 in wind tunnel tests conducted during Phases I and II of a NASA Research Announcement (NRA) contract for Experimental Systems Validations for N+2 Supersonic Commercial Transport Aircraft, which was led by the NASA High Speed Project under the Fundamental Aeronautics Program.

The sonic boom test data were obtained using a 14-in. tapered "RF1" rail and a 2-in. flat-top rail. Both rails captured an entire pressure signature in one data point, and successive signatures at varying positions along or above the rail were used to improve data quality through spatial averaging. The sonic boom data obtained by the rails were validated with high-fidelity numerical simulations of off-body pressures. The test results generally showed good agreement between the computational and experimental data when a variety of testing techniques including spatial averaging of a series of pressure signatures were employed. The two wind tunnels generally produced comparable data.

The spatially-averaged sonic boom test data generally showed good agreement with computational predictions. The use of the RF1 rail combined with spatial averaging of aligned signatures with different axial positions and constant altitude masked the wind tunnel distortions seen in the individual pressure signatures at most fixed model positions in the wind tunnel. The rail data were, as predicted, free from model shock reflections for the boom model. The data from these wind tunnel tests proved that accurate data with reasonable acquisition time is obtainable in the Ames 9x7 and Glenn 8x6 supersonic wind tunnels.

In summary, the wind tunnel test provided validation data that provides the confidence in the CFD methods to predict the sonic boom pressures of complex vehicles. CFD, regardless of flow solver, with an Mach aligned mesh, is able to fairly accurately predict the sonic boom levels and the next step towards realization of civilian supersonic transportation would be the design and CFD evaluation of flight vehicles with vehicle flight demonstration testing with true atmospheric effects.

The high-fidelity sonic boom pressure data from the recent tests will aid in the development of improved computational and grid generation techniques for sonic boom analysis in the future by providing the data and model geometries to the supersonic aircraft development community.

13. References

1. Durston, Donald A., Cliff, Susan E., Wayman, Thomas R., Merret Jason M., Elmiligui, Alaa A., and Bangert, Linda S.: *Near-Field Sonic Boom Test on Two Low-Boom Configurations Using Multiple Measurement Techniques at NASA Ames*. AIAA 2011-3333, 29th AIAA Applied Aerodynamics Conference, Honolulu HI, June 2011

2. Wilcox, Floyd J., Jr.; and Elmiligui, Alaa A.: Experimental Measurements of Sonic Boom Signatures Using a Continuous Data Acquisition Technique. NASA TP-2013-218035, August 2013

3. Cliff, S., Elmiligui, A., Aftosmis, A., Thomas, S., Morgenstern, J., and Durston, D.: *Design and Evaluation of a Pressure Rail for Sonic Boom Measurements in Wind Tunnels.* ICCFD7-2006, Seventh International Conference on Computational Fluid Dynamics (ICCFD7), Big Island HI, July 2012

4. Morgenstern, John M.: *Distortion Correction for Low Sonic Boom Measurement in Wind Tunnels*. AIAA-2012-3216, 30th AIAA Applied Aerodynamics Conference, New Orleans LA, June 2012

5. Morgenstern, John M.: *How to Accurately Measure Low Sonic Boom or Model Surface Pressures in Supersonic Wind Tunnels.* AIAA-2012-3215, 30th AIAA Applied Aerodynamics Conference, New Orleans LA, June 2012

6. NASA Langley Research Center Supersonics Project: Request for Proposal for Potential Order for System-Level Experimental Validations for Supersonic Commercial Transport Aircraft Entering Service in the 2018–2020 Time Period. NASA Program Announcement Number NNH08ZEA001N-SUP3, August 2009

7. Cliff, Susan E., Durston, Donald A., Elmiligui, Alaa E., Walker, Eric L., and Carter, Melissa B.: *Experimental and Computational Sonic Boom Assessment of Lockheed-Martin N+2 Low Boom Models.* NASA TP (to be published)

8. Magee, Todd E., Wilcox, Peter A., Fugal, Spencer R., Acheson, Kurt E., Adamson, Eric E., Bidwell, Alicia L., and Shaw, Stephen G.: *System-Level Experimental Validations for Supersonic Commercial Transport Aircraft Entering Service in the 2018–2020 Time Period, Phase I Final Report.* NASA CR-2013-217797, February 2013

9. Magee, Todd E., Shaw, Stephen G., and Fugal, Spencer R.: *Experimental Validations of a Low-Boom Aircraft Design.* AIAA 2013-0646, 51st AIAA Aerospace Sciences Meeting, Dallas TX, January 2013

10. Magee, Todd E., Fugal, Spencer R., Fink, Lawrence E., Adamson, Eric E., and Shaw, Stephen G.: System-Level Experimental Validations for Supersonic Commercial Transport Aircraft Entering Service in the 2018–2020 Time Period, Phase II Final Report. NASA CR (to be published)

11. Magee, Todd E., Fink, Lawrence E., Fugal, Spencer R., Adamson, Eric E., and Shaw, Stephen G.: *Boeing N+2 Supersonic Experimental Validation Phase II Program.* AIAA 2014–2137, 32nd AIAA Applied Aerodynamics Conference, Atlanta GA, June 2014

12. Trefny, Charles J., Hirt, Stefanie M., Anderson, Bernhard H., Fink, Lawrence E., and Magee, Todd E.: *Performance of a Supersonic Over-Wing Inlet with Application to a Low-Sonic-Boom Aircraft.* AIAA 2014-3802, 50th AIAA/ASME/SAE/ASEE Joint Propulsion Conference, Cleveland OH, July 2014

13. Cliff, S. E., Thomas, S. D., McMullen, M. S., Melton, J. E., and Durston, D. A.: Assessment of Unstructured Euler Methods for Sonic Boom Pressure Signatures Using Grid Refinement and Domain Rotation Methods. NASA TM-2008-214568, September 2008

14. Choi, S., Alonso, J. J., and Van der Weide, E.: *Numerical and Mesh Resolution Requirements for Accurate Sonic Boom Prediction.* AIAA Journal of Aircraft, vol. 46, no. 4, July–August 2009

15. Carter, Melissa B., and Deere, Karen A.: *Grid Sourcing and Adaptation Study Using Unstructured Grids for Supersonic Boom Prediction.* AIAA Paper 2008-6595, 26th AIAA Applied Aerodynamics Conference, Honolulu HI, August 2008

16. Jones, W.T., Nielsen, E. J., and Park M. A.: *Validation of 3D Adjoint Based Error Estimation and Mesh Adaption for Sonic Boom Prediction.* AIAA Paper 2006-1150, 44th AIAA Aerospace Sciences Meeting and Exhibit, Reno NV, January 2006

17. Park M. A., and Darmofal, D. L.: Validation of an Output-Adaptive Tetrahedral Cut-Cell Method for Sonic Boom Prediction. AIAA Journal, vol. 48, no. 9, September 2010

18. Park, Michael A.: *Low Boom Configuration Analysis with FUN3D Adjoint Simulation Framework*. AIAA-2011-3337, 29th AIAA Applied Aerodynamics Conference, Honolulu HI, June 2011

19. Aftosmis, M. J., and Berger, M. J.: *Multilevel Error Estimation and Adaptive h-Refinement for Cartesian meshes with embedded boundaries*. AIAA Paper 2002-0863, 40th AIAA Aerospace Sciences Meeting, Reno NV, January 2002

20. Nemec, M., and Aftosmis, M.: *Adjoint Error Estimation and Adaptive Refinement for Embedded-Boundary Cartesian Meshes.* AIAA Paper 2007-4187, 18th AIAA Computational Fluid Dynamics Conference, Miami FL, June 2007

21. Wintzer, Mathias, Nemec, Marian, and Aftosmis, Michael J.: *Adjoint-based Adaptive Mesh Refinement for Sonic Boom Prediction.* AIAA Paper 2008-6593, 26th AIAA Applied Aerodynamics Conference, Honolulu HI, August 2008

22. Louisville, A., Dervieux, A., and Alauzet, F.: *Fully Anisotropic Goal-Oriented Mesh Adaptation for 3D Steady Euler Equations.* Journal of Computational Physics, vol. 229, isue 8, pp. 2866-2897, April 2010

23. Haering, E., Murray, J., Purifoy, D., Graham, D., Meredith, K., Ashburn, C., and Stucky, M.: *Airborne Shaped Sonic Boom Demonstration Pressure Measurements with Computational Fluid Dynamics Comparisons.* AIAA Paper 2005-0009, 43rd AIAA Aerospace Sciences Meeting, Reno NV, January 2005

24. Laflin, Kelly R., Klausmeyer, Steven M., and Chaffin, Mark: *A Hybrid Computational Fluid Dynamics Procedure for Sonic Boom Prediction.* AIAA Paper 2006-3168, 24th AIAA Applied Aerodynamics Conference, San Francisco CA, June 2006

25. Waithe, Kendrick A.: *Application of USM3D for Sonic Boom Prediction by Utilizing a Hybrid Procedure*. AIAA Paper 2008-0129, 46th AIAA Aerospace Sciences Meeting, Reno NV, January 2008

26. Howe, Donald C.: *Hybrid Cart3D/OVERFLOW Near-Field Analysis of a Low Boom Configuration with Wind Tunnel Comparisons.* AIAA Paper-2011-3336, 29th AIAA Applied Aerodynamics Conference, Honolulu HI, June 2011

27. Campbell, Richard L., Carter, Melissa B., Deere, Karen A. and Waithe, Kenrick A.: *Efficient Unstructured Grid Adaptation Methods for Sonic Boom Prediction.* AIAA Paper 2008-7327, 26th AIAA Applied Aerodynamics Conference, Honolulu HI, August 2008

28. Cliff, Susan E., Elmiligui, Alaa A., Campbell, Richard L., and Thomas, Scott D.: *Evaluation of Refined Tetrahedral Mesh with Projected, Stretched, and Sheared Prism Layers for Sonic Boom Analysis.* AIAA-2011-3338, 29th AIAA Applied Aerodynamics Conference, Honolulu, HI, June 2011

29. Cliff, Susan E., Elmiligui, Alaa A., Campbell, Richard L., and Thomas, Scott D.: *Refined Tetrahedral Meshes with Mach Cone Aligned Prisms for Sonic Boom Analysis*. Journal of Aircraft, vol. 50, no. 3, May–June 2013

30. Park, Michael A., Campbell, Richard L., Elmiligui, Alaa A., Cliff, Susan E., and Nayani, Sudheer N.: *Specialized CFD Grid Generation Methods for Near-Field Sonic Boom Prediction*, AIAA-0115, 52nd Aerospace Sciences Meeting, National Harbor MD, January 2014.

31. *Test Planning Guide for High Speed Wind Tunnels,* *http://www.nasa.gov/sites/default/files/643643main_HSpeedTestPlanGuide.pdf.* NASA Ames Wind Tunnel Operations Division report number A027-9391-XB2, rev. 5, April 27, 2005

32. Reed, T. D., Pope, T. C., and Cooksey, J. M.: *Calibration of Transonic and Supersonic Wind Tunnels.* NASA CR-2920, November 1977

33. Soeder, Ronald H., NASA Lewis 8- by 6-Foot Supersonic Wind Tunnel User Manual. NASA TM-105771, February 1993

34. Arrington, E. Allen, Pickett, Mark T., and Soeder, Ronald H.: Baseline Calibration of the NASA Lewis 8- by 6-Foot Supersonic Wind Tunnel (1991 and 1992 Tests), NASA TM-97-107431, January 1998

35. George, A. R., and Seebass, R.: *Sonic Boom Minimization Including Both Front and Rear Shocks.* AIAA Journal, vol. 9, no. 10, pp. 2091-2093, October 1971

36. Darden, Christine M.: Sonic Boom Minimization with Nose-Bluntness Relaxation, NASA TP-1348, January 1979

37. Morgenstern, John, Norstrud, Nicole, Sokhey Jack, Martens, Steve, and Alonso, Juan: Advanced Concept Studies for Supersonic Commercial Transports Entering Service in the 2018 to 2020 Period, Phase I Final Report. NASA/CR—2013-217820, February 2013

38. Aftosmis, Michael J., Nemec, Marian, and Cliff, Susan E.: *Adjoint-based Low Boom Design with Cart3D*, AIAA 2011-3500, 29th AIAA Applied Aerodynamics Conference, Honolulu HI, June 2011

39. Morgenstern, John M.: *Wind Tunnel Testing of a Sonic Boom Minimized Tail-Braced Wing Transport Configuration*, AIAA 2004-4536, 10th AIAA/ISSMO Multidisciplinary Analysis and Optimization Conference, Albany NY, September 2004

40. Heineck, James T., Schairer, Edward T., Walker, Louise A., and Kushner, Laura K.: *Retroreflective Background Oriented Schlieren (RBOS)*, ISFV14-140, 14th Int'l Symposium on Flow Visualization, Daegu, Korea, June 2010

41. Walker, Eric L.: Statistical Calibration and Validation of a Homogeneous Ventilated Wall-Interference Correction Method for the National Transonic Facility. NASA TP-2005-213947, December 2005

42. Frink, N. T., Pirzadeh, S. Z., Parikh, P. C., Pandya, M. J., and Bhat, M. K.: *The NASA Tetrahedral Unstructured Software System*, The Aeronautical Journal, vol. 104, no. 1040, pp. 491-499, October 2000

43. Frink, Neal T.: *Assessment of an Unstructured-Grid Method for Predicting 3-D Turbulent Viscous Flows.* AIAA 96-0292, 34th AIAA Aerospace Sciences Meeting, Reno NV, January 1996

44. Nichols, R., and Buning, P.: *User's Manual for OVERFLOW 2.1, Version 2.1t*, http://people.nas.nasa.gov/~pulliam/Overflow/Overflow_Manuals.html, August 2008

45. Nichols, R. H., Tramel, R. W., and Buning, P. G.: *Solver and Turbulence Model Upgrades to OVERFLOW 2 for Unsteady and High-Speed Applications.* AIAA 2006-2824, 24th AIAA Applied Aerodynamics Conference, San Francisco CA, June 2006

46. Rallabhandi, Sriram K.: *Advanced Sonic Boom Prediction Using Augmented Burger's Equation,* AIAA-2011-1278, 49th AIAA Aerospace Sciences Meeting, Orlando FL, January 2011

47. Shepherd, Kevin P., and Sullivan, Brenda M.: *A Loudness Calculation Procedure Applied to Shaped Sonic Booms.* NASA TP-3134, November 1991

48. Abdol-Hamid, Khaled S., Frink, Neal T., Deere, Karen A., and Pandya, Mohagna J.: *Propulsion Simulations Using Advanced Turbulence Models with the Unstructured-Grid CFD Tool, TetrUSS.* AIAA 2004-0714, 42nd AIAA Aerospace Sciences Meeting, Reno NV, January 2004

49. Pirzadeh, Shahyar: *Advanced Unstructured Grid Generation for Complex Aerodynamics Applications*, AIAA 2008-7178, 26th AIAA Applied Aerodynamics Conference, Honolulu HI, August 2008

50. *Pointwise Software, http://www.pointwise.com*, 213 South Jennings Avenue, Fort Worth, Texas 76104

51. Steinbrenner, John P. and Abelanet, J. P.: *Anisotropic Tetrahedral Meshing Based on Surface Deformation Techniques*, AIAA 2007-0554, AIAA 45th Aerospace Sciences Meeting, Reno NV, January 2007

52. Park, Michael A., Aftosmis, Michael J., Campbell, Richard L., Carter, Melissa B., Cliff, Susan E., and Bangert, Linda S.: *Summary of the 2008 NASA Fundamental Aeronautics Program Sonic Boom Prediction Workshop,* AIAA 2013-0649, 51st AIAA Aerospace Sciences Meeting, Dallas TX, January 2013

Appendix A

Listing of Experimental Run Sweeps Plotted

Test	Model	Rail	Swp	Mach	h_{Nose} *(in.)*	X_{Ram} *(in.)*	α°	φ°	Sig Set	Run Sweeps*	Figures
97p	AS2	14" Fwd	X	1.6	30	7.9–23.8	0	0	33	1080–1105: 1079	6-12,13,14,15
97p	AS2	14" Fwd	X	1.6	30	7.9–23.8	0	0	33	1080–1105: 1106	6-13,14,15; 7-6,14,22; 9-3
97p	AS2	14" Fwd	X	1.6	31.8	8–23.8	0	0	34	1107–1132: 1133	7-6
97p	AS2	14" Fwd	Z	1.6	26–34	16	0	0	31	1010–1043: 1009	7-1
97p	AS2	14" Fwd	Z	1.6	26–34	16	0	0	31	1010–1043: 1044	7-6,14,19
97p	AS2	14" Fwd	Z	1.6	26–34	24	0	0	32	1045–1078: 1079	7-6,14,19,23
97p	AS2	2" Fwd	X	1.6	30	8–23.8	0	0	54	1759–1784: 1785	7-22
97p	AS2	2" Fwd	Z	1.6	26–34	24	0	0	55	1786–1818: 1819	7-23
97p	Boom1 VS2	14" Fwd	X	1.6	30	8–23.8	3.4	0	45	1472–1497: 1498	6-4; 7-10,35
97p	Boom1 VS2	14" Fwd	X	1.6	30	8–23.8	3.4	0	46	1500–1525: 1499	7-10,12,15,25
97p	Boom1 VS2	14" Fwd	X	1.6	30	8–23.8	3.4	0	47	1526–1551: 1552	7-10
97p	Boom1 VS2	14" Fwd	X	1.8	30	8–23.8	3.4	0	38	1247–1272: 1273	6-4; 7-11,35,44,49
97p	Boom1 VS2	14" Fwd	X	1.8	30	8–23.8	3.4	0	39	1274–1299: 1300	7-11,13,16
97p	Boom1 VS2	14" Fwd	X	1.8	30	8–23.8	3.4	20	40	1301–1326: 1327	7-44
97p	Boom1 VS2	14" Fwd	X	1.8	30	8–23.8	3.4	30	41	1328–1353: 1354	7-44
97p	Boom1 VS2	14" Fwd	X	1.8	30	8–23.8	3.4	40	42	1373–1398: 1399	7-44
97p	Boom1 VS2	14" Fwd	Z	1.6	26–34	24	3.4	0	43	1401–1433: 1434	6-6; 7-15,20,24
97p	Boom1 VS2	14" Fwd	Z	1.6	26–34	16	3.4	0	44	1437–1469: 1470	6-6; 7-15,20; 9-7
97p	Boom1 VS2	14" Fwd	Z	1.8	26–34	24	3.4	0	35	1144–1176: 1177	7-40
97p	Boom1 VS2	14" Fwd	Z	1.8	26–34	24	3.4	0	36	1179–1211: 1212	6-6; 7-21,40
97p	Boom1 VS2	14" Fwd	Z	1.8	26–34	16	3.4	0	37	1213–1245: 1246	6-6; 7-16,21
97p	Boom1 VS2	14" Aft	X	1.6	60	0–15.8	3.4	0	61	2047–2072: 2073	6-4; 7-3,7,12,28; 9-8
97p	Boom1 VS2	14" Aft	X	1.6	60	0–15.8	3.4	0	62	2074–2099: 2100	7-7,37,48

Test	Model	Rail	Swp	Mach	h_{Nose} *(in.)*	X_{Ram} *(in.)*	α°	φ°	Sig Set	Run Sweeps*	Figures
97p	Boom1 VS2	14" Aft	X	1.8	60	0–23.9	3.4	0	60	2006–2044: 2045	6-4,13; 7-13,29,37,49
97p	Boom1 VS2	2" Fwd	X	1.6	30	8–23.8	3.4	0	53	1724–1749: 1750	6-4; 7-17,25,36,50
97p	Boom1 VS2	2" Fwd	X	1.8	30	8–23.8	3.4	0	51	1662–1687: 1688	6-4; 7-18,36,51
97p	Boom1 VS2	2" Fwd	Z	1.6	26–34	24	3.4	0	52	1690–1722: 1723	6-6; 7-17,24
97p	Boom1 VS2	2" Fwd	Z	1.8	26–34	24	3.4	0	48	1567–1599: 1600	6-6
97p	Boom1 VS2	2" Fwd	Z	1.8	26–34	16	3.4	0	49	1601–1633: 1634	7-18
TBC3	AS2	2"	X	1.56	59	16–23.9	0	–	111	1162–1187: 1188	7-2; 9-4
TBC3	Boom1 VS2	14"	X	1.56	59	0–7.9	3.4	–	66	863–888: 862	7-30
TBC3	Boom1 VS2	14"	X	1.56	59	0–7.9	3.4	–	66	863–888: 889	6-5; 7-26,48
TBC3	Boom1 VS2	14"	X	1.56	59	0–7.9	3.4	–	77	966–991: 957	7-30
TBC3	Boom1 VS2	14"	X	1.56	59	0–7.9	3.4	–	77	966–991: 992	6-5
TBC3	Boom1 VS2	14"	X	1.78	49	0–7.9	3.4	–	61	818–843: 817	7-31
TBC3	Boom1 VS2	14"	X	1.78	49	0–7.9	3.4	–	61	818–843: 844	6-5,13; 7-27,49
TBC3	Boom1 VS2	14"	X	1.78	49	0–7.9	3.4	–	70	912–937: 911	7-31
TBC3	Boom1 VS2	14"	X	1.78	49	0–7.9	3.4	–	70	912–937: 938	6-5
TBC3	Boom1 VS2	14"	Z	1.78	39.5–44.6	0	3.4	–	36	443–467: 468	6-7
TBC3	Boom1 VS2	14"	Z	1.78	39.6–44.5	0	3.4	–	31	367–391: 392	6-7
TBC3	Boom1 VS2	14"	Z	1.78	46.1–64	0	3.4	–	40	500–536: 499	6-7
TBC3	Boom1 VS2	2"	X	1.56	59	0–7.9	3.4	–	93	1060–1085: 1086	6-5; 7-26,50
TBC3	Boom1 VS2	2"	X	1.78	49	0–7.9	3.4	–	81	1008–1033: 1034	6-5; 7-27,51
TBC4	Boom3 VS3	14" aft	Z	1.6	58.6–64.7	0	4	0	51	1587–1611: 1612	7-41
TBC4	Boom3 VS3	14" aft	Z	1.6	58.8–64.8	0	3	0	49	1537–1561: 1612	7-38,41,45; 9-12
TBC4	Boom3 VS3	14" aft	Z	1.6	58.8–64.8	0	3.5	0	50	1562–1586: 1535	7-32
TBC4	Boom3 VS3	14" aft	Z	1.6	58.8–64.8	0	3.5	0	50	1562–1586: 1612	7-28,41
TBC4	Boom3 VS3	14" aft	Z	1.6	59–65	0	2.6	0	52	1628–1652: 1624	7-4,41
TBC4	Boom3 VS3	14" aft	Z	1.6	59–65	0	3	15	53	1653–1677: 1624	7-45; 9-12

Test	Model	Rail	Swp	Mach	h_{Nose} *(in.)*	X_{Ram} *(in.)*	α°	φ°	Sig Set	Run Sweeps*	Figures
TBC4	Boom3 VS3	14" aft	Z	1.6	59–65	0	3	30	54	1678–1702: 1624	7-45; 9-12
TBC4	Boom3 VS3	14" aft	Z	1.6	59–65	0	3	45	55	1703–1727: 1624	7-45; 9-12
TBC4	Boom3 VS3	14" aft	Z	1.6	59–65	0	3.5	0	60	1843–1867: 1816	7-32
TBC4	Boom3 VS3	14" aft	Z	1.6	59–65	0	3.5	0	65	1980–2004: 1953	7-32
TBC4	Boom3 VS3	14" aft	Z	1.8	59.5–64.5	0	3	0	56	1730–1754: 1728	7-38
TBC4	Boom3 VS3	14" aft	Z	1.8	59.5–64.5	0	3.5	0	57	1755–1779: 1728	7-29
TBC4	Boom3 VS4	14" aft	Z	1.6	59.5–65.6	0	3.4	0	43	1365–1389: 1390	7-28
TBC4	Boom3 VS4	14" aft	Z	1.8	59.3–64.3	0	3.1	0	47	1473–1497: 1523	7-29
TBC4	Perf sting + contour	14" aft	Z	1.6	58.2–64.3	0	3.3	30	7	348–372: 119	7-46; 9-16
TBC4	Perf sting + contour	14" aft	Z	1.6	58.3–64.3	0	3.3	0	32	1043–1067: 119	7-33
TBC4	Perf sting + contour	14" aft	Z	1.6	58.7–64.7	0	3.8	0	5	274–298: 119	7-42
TBC4	Perf sting + contour	14" aft	Z	1.6	58.8–64.9	0	3.3	45	8	373–397: 119	7-46; 9-16
TBC4	Perf sting + contour	14" aft	Z	1.6	59.3–65.4	0	3.3	15	6	323–347: 119	7-46; 9-16
TBC4	Perf sting + contour	14" aft	Z	1.6	59.6–64.1	0	3.3	0	2	199–222: 119	7-8,39,42,46; 9-16
TBC4	Perf sting + contour	14" aft	Z	1.6	59.6–64.1	0	3.3	0	3	224–247: 119	7-8,33,34
TBC4	Perf sting + contour	14" aft	Z	1.6	59.6–65.5	0	3.3	0	4	249–273: 119	7-8
TBC4	Perf sting + contour	14" aft	Z	1.6	59.6–65.6	0	3.3	0	37	1180–1204: 119	7-34
TBC4	Perf sting + contour	14" aft	Z	1.6	59.6–64.4	0	2.8	0	1	151–175: 119	7-42
TBC4	Perf sting + contour	14" aft	Z	1.6	59.7–65.7	0	3.3	0	17	612–636: 119	7-33
TBC4	Perf sting + contour	14" aft	Z	1.6	60.2–66.3	0	3.6	0	24	830–854: 119	7-34
TBC4	Perf sting + contour	14" aft	Z	1.8	58.1–63.1	0	3.3	30	14	526–550: 116	7-47
TBC4	Perf sting + contour	14" aft	Z	1.8	58.6–63.7	0	3.3	45	15	551–575: 116	7-47
TBC4	Perf sting + contour	14" aft	Z	1.8	59–64.1	0	3.3	0	9	401–425: 116	7-9,42
TBC4	Perf sting + contour	14" aft	Z	1.8	59.2–64.2	0	3.3	15	13	501–525: 116	7-47
TBC4	Perf sting + contour	14" aft	Z	1.8	59.2–64.3	0	3.9	0	10	426–450: 116	7-42
TBC4	Perf sting + contour	14" aft	Z	1.8	59.4–64.5	0	3.3	0	12	476–500: 116	7-9,39,47

* *Run sweeps nomenclature: sweep start–end: reference*

Appendix B

Listing of Reference Runs Plotted

Test	Model	Rail	Mach	h_{Nose} *(in.)*	X_{Ram} *(in.)*	α°	φ°	Runs	Figure
97p	Boom1 VS2	14" Fwd	1.8	52	0	3.4	0	1178	54
97p	Boom1 VS2	14" Fwd	1.8	52	0	3.4	20	1327	54
97p	Boom1 VS2	14" Fwd	1.8	52	0	3.4	30	1372	54
97p	Boom1 VS2	14" Fwd	1.8	52	0	3.4	40	1399	54
97p	Boom1 VS2	14" Aft	1.6	82	0	5	0	2100	60
97p	Boom1 VS2	14" Aft	1.6	82	0	5	0	2046	64
97p	Boom1 VS2	14" Aft	1.6	82	0	5	0	2100	64
97p	Boom1 VS2	14" Aft	1.8	82	0	5	0	1989	61
97p	Boom1 VS2	14" Aft	1.8	82	0	5	0	1989	65
97p	Boom1 VS2	14" Aft	1.8	82	0	5	0	2045	65
97p	Boom1 VS2	2" Fwd	1.6	52	0	3.4	0	1750	62
97p	Boom1 VS2	2" Fwd	1.6	52	0	3.4	0	1689	66
97p	Boom1 VS2	2" Fwd	1.8	52	0	3.4	0	1688	63
97p	Boom1 VS2	2" Fwd	1.8	52	0	3.4	0	1688	67
97p	LB 1021, blade	14" Fwd	1.6	52	0	2.3	0	862	52
97p	LB 1021, blade	14" Fwd	1.6	52	0	2.3	0	1004	52
97p	LB 1021, blade	14" Fwd	1.6	52	0	2.3	0	397	53
97p	LB 1021, blade	14" Fwd	1.6	52	0	2.3	0	831	53
97p	LB 1021, blade	14" Fwd	1.6	52	0	2.3	0	862	60
97p	LB 1021, blade	14" Fwd	1.6	52	0	2.3	0	862	66
97p	LB 1021, blade	14" Fwd	1.6	52	0	2.3	20	883	52
97p	LB 1021, blade	14" Fwd	1.6	52	0	2.3	30	904	52
97p	LB 1021, blade	14" Fwd	1.6	53	0	2.3	0	564	53
97p	LB 1021, blade	14" Fwd	1.8	52	0	2.3	0	764	61
97p	LB 1021, blade	14" Fwd	1.8	52	0	2.3	0	764	67
97p	LB 1021, blade	14" Fwd	1.8	53	0	2.3	0	604	55
97p	LB 1021, blade	14" Fwd	1.8	53	0	2.3	0	633	55
97p	LB 1021, blade	14" Fwd	1.8	53	0	2.3	0	692	55
97p	LB 1021, blade	14" Fwd	1.8	53	0	2.3	0	699	55
TBC3	AS2	14"	1.8	67.86	0	0	—	549	58
TBC3	AS2	14"	1.8	67.9	0	0	—	575	58
TBC3	Boom1 VS2	14"	1.6	59	0	3.4	—	862	56
TBC3	Boom1 VS2	14"	1.6	59	0	3.4	—	889	56
TBC3	Boom1 VS2	14"	1.6	59	0	3.4	—	957	56
TBC3	Boom1 VS2	14"	1.6	59	0	3.4	—	992	56
TBC3	Boom1 VS2	14"	1.8	63.68	0	0	—	392	58
TBC3	Boom1 VS2	14"	1.8	63.83	0	0	—	366	58
TBC3	Boom1 VS2	14"	1.8	63.83	0	0	—	413	58
TBC3	Boom1 VS2	14"	1.8	63.83	0	0	—	366	59
TBC3	Boom1 VS2	14"	1.8	64	0	0	—	815	57
TBC3	Boom1 VS2	14"	1.8	64	0	0	—	816	57
TBC3	Boom1 VS2	14"	1.8	64	0	0	—	815	59
TBC3	Boom1 VS2	2"	1.557	59	0	3.4	—	1103	62
TBC3	Boom1 VS2	2"	1.557	59	0	3.4	—	1103	68
TBC3	Boom1 VS2	2"	1.775	49	0	3.4	—	1051	63
TBC3	Boom1 VS2	2"	1.775	49	0	3.4	—	1051	69
TBC3	Cone fairing	14"	1.6	68	0	0	—	771	60

Test	Model	Rail	Mach	h_{Nose} *(in.)*	X_{Ram} *(in.)*	α°	φ°	Runs	Figure
TBC3	Cone fairing	14"	1.6	68	0	0	—	771	68
TBC3	Cone fairing	14"	1.8	68	0	0	—	738	61
TBC3	Cone fairing	14"	1.8	68	0	0	—	738	69
TBC4	Strut cone	14" aft	1.6	58	0	-7.5	0	113	64
TBC4	Strut cone	14" aft	1.6	58	0	-7.5	0	119	64
TBC4	Strut cone	14" aft	1.8	58	0	-7.5	0	110	65
TBC4	Strut cone	14" aft	1.8	58	0	-7.5	0	116	65